ABSTRACT

BOUNDARY INTEGRAL EQUATION METHODS
FOR SUPERHYDROPHOBIC FLOW AND INTEGRATED
PHOTONICS

by
Kosuke Sugita

This dissertation presents fast integral equation methods (FIEMs) for solving two important problems encountered in practical engineering applications.

The first problem involves the mixed boundary value problem in two-dimensional Stokes flow, which appears commonly in computational fluid mechanics. This problem is particularly relevant to the design of microfluidic devices, especially those involving superhydrophobic (SH) flows over surfaces made of composite solid materials with alternating solid portions, grooves, or air pockets, leading to enhanced slip.

The second problem addresses waveguide devices in two dimensions, governed by the Helmholtz equation with Dirichlet conditions imposed on the boundary. This problem serves as a model for photonic devices, and the systematic investigation focuses on the scattering matrix formulation, in both analysis and numerical algorithms. This research represents an important step towards achieving efficient and accurate simulations of more complex photonic devices with straight waveguides as input and output channels, and Maxwell's equations in three dimensions as the governing equations.

Numerically, both problems pose significant challenges due to the following reasons. First, the problems are typically defined in infinite domains, necessitating the use of artificial boundary conditions when employing volumetric methods such as finite difference or finite element methods. Second, the solutions often exhibit singular behavior, characterized by corner singularities in the geometry or abrupt changes in boundary conditions, even when the underlying geometry is smooth. Analyzing the exact nature of these singularities at corners or transition points is extremely difficult.

Existing methods often resort to adaptive refinement, resulting in large linear systems, numerical instability, low accuracy, and extensive computational costs.

Under the hood, fast integral equation methods serve as the common engine for solving both problems. First, by utilizing the constant-coefficient nature of the governing partial differential equations (PDEs) in both problems and the availability of free-space Green's functions, the solutions are represented via proper combination of layer potentials. By construction, the representation satisfies the governing PDEs within the volumetric domain and appropriate conditions at infinity. The combination of boundary conditions and jump relations of the layer potentials then leads to boundary integral equations (BIEs) with unknowns defined only on the boundary. This reduces dimensionality of the problem by one in the solve phase. Second, the kernels of the layer potentials often contain logarithmic, singular, and hypersingular terms. High-order kernel-split quadratures are employed to handle these weakly singular, singular, and hypersingular integrals for self-interactions, as well as nearly weakly singular, nearly singular, and nearly hypersingular integrals for near-interactions and close evaluations. Third, the recursively compressed inverse preconditioning (RCIP) method is applied to treat the unknown singularity in the density around corners and transition points. Finally, the celebrated fast multipole method (FMM) is applied to accelerate the scheme in both the solve and evaluation phases. In summary, high-order numerical schemes of linear complexity have been developed to solve both problems often with ten digits of accuracy, as illustrated by extensive numerical examples.

BOUNDARY INTEGRAL EQUATION METHODS FOR SUPERHYDROPHOBIC FLOW AND INTEGRATED PHOTONICS

by
Kosuke Sugita

A Dissertation
Submitted to the Faculty of
New Jersey Institute of Technology and
Rutgers, The State University of New Jersey – Newark
in Partial Fulfillment of the Requirements for the Degree of
Doctor of Philosophy in Mathematical Sciences

Department of Mathematical Sciences
Department of Mathematics and Computer Science, Rutgers-Newark

August 2023

BOUNDARY INTEGRAL EQUATION METHODS FOR SUPERHYDROPHOBIC FLOW AND INTEGRATED PHOTONICS

Kosuke Sugita

Shidong Jiang, Dissertation Co-Advisor   Date
Professor, Department of Mathematical Sciences,
New Jersey Institute of Technology

Michael Siegel, Dissertation Co-Advisor   Date
Professor, Department of Mathematical Sciences,
New Jersey Institute of Technology

Travis Askham, Committee Member   Date
Assistant Professor, Department of Mathematical Sciences,
New Jersey Institute of Technology

David Shirokoff, Committee Member   Date
Assistant Professor, Department of Mathematical Sciences,
New Jersey Institute of Technology

Manas Rachh, Committee Member   Date
Research Scientist, Center for Computational Mathematics,
Flatiron Institute, New York City, New York

BIOGRAPHICAL SKETCH

Author:	Kosuke Sugita
Degree:	Doctor of Philosophy
Date:	August 2023

Undergraduate and Graduate Education:

- Doctor of Philosophy in Mathematical Sciences,
  New Jersey Institute of Technology, Newark, NJ, 2023

- Master of Science in Applied Mathematics,
  Aoyama Gakuin University, Sagamihara City, Kanagawa, Japan, 2017

- Master of Science in Mathematics,
  Kyoto University, Kyoto City, Kyoto, Japan, 2007

- Bachelor of Science in Mathematics,
  Tohoku University, Sendai City, Miyagi, Japan, 2005

Major:	Mathematical Sciences

Presentations and Publications:

S. Jiang, and M. Siegel, and K. Sugita, "A Boundary Integral Equation Method and Applications to Superhydrophobic Flow," in preparation.

K. Sugita, S. Jiang, and M. Rachh, "A Boundary Integral Equation Method for Integrated Photonics," in preparation.

Y. Zhang, Z. Song, K. Sugita, S. Xue, and W. Zhang, "Impacts of Nanobubbles in Pore Water on Heavy Metal Pollutant Release from Contaminated Soil Columns," *Nanomaterials*, Vol 13(10), 1671, 2023.

H. Kohashi, K. Sugita, M. Sugihara, and T. Hoshi, "Efficient methods for computing integrals in electronic structure calculations," *JSIAM Letters*, Vol 9, pp. 81-84, 2017.

Dedicated to my parents.

ACKNOWLEDGMENT

TABLE OF CONTENTS

Chapter   **Page**

LIST OF TABLES

LIST OF FIGURES

Figure **Page**

Figure   **Page**

CHAPTER 1

INTRODUCTION

The first part of this dissertation is concerned with the accurate and efficient computation of velocities, pressure, and tractions (surface forces) in flows over superhydrophobic surfaces, sometimes referred to as superhydrophobic (SH) flow.

When a rough hydrophobic solid is submerged in a fluid, gas bubbles can become trapped within the grooves in the solid surface, resulting in a stable mixed state known as Cassie state. This leads to the formation of a superhydrophobic surface, which is of great interest within the fluid mechanics community due to its tendency to exhibit reduced resistance to liquid motion (Quéré [70]). The study of flows over SH surfaces typically focuses on two types of canonical problems. The first problem involves an idealized scenario of externally imposed shear flow over a single SH surface (Philip [68]). The second problem, which is more representative of realistic configurations, involves pressure-driven flow within SH channels (Rothstein[74]). In both cases, the focus is not on the intricate details of the flow, but rather on a suitable aggregated or coarse-grained quantity that represents the decreased friction resulting from superhydrophobicity. In the first case, this quantity is represented by the intrinsic slip length (Davis and Lauga [22]), which is solely determined by the geometric characteristics of the surface. In the second case, it is represented by the effective slip length (Lauga and Stone [59]), which accounts for the excess volumetric flow in the channel. As part of this work, we develop an efficient method for computing these coarse-grained quantities over complex and highly irregular surfaces.

SH surfaces appear not only in the engineering development of nano-fluidic devices, but also in nature. Some examples of naturally occurring SH surfaces are shown in Figure 1.1. This figure also shows SH surfaces that have been manufactured

for nano-fluidic applications. An idealized model of flow in a channel with one or more SH surfaces is shown in Figures 2.12 and 2.13 in Chapter 2.

(a) surface 1: $a_0 = 15$ μm, $\phi = 0.08$, $r_m = 2.64$ (b) surface 3: $a_0 = 13$ μm, $\phi = 0.15$, $r_m = 4.47$
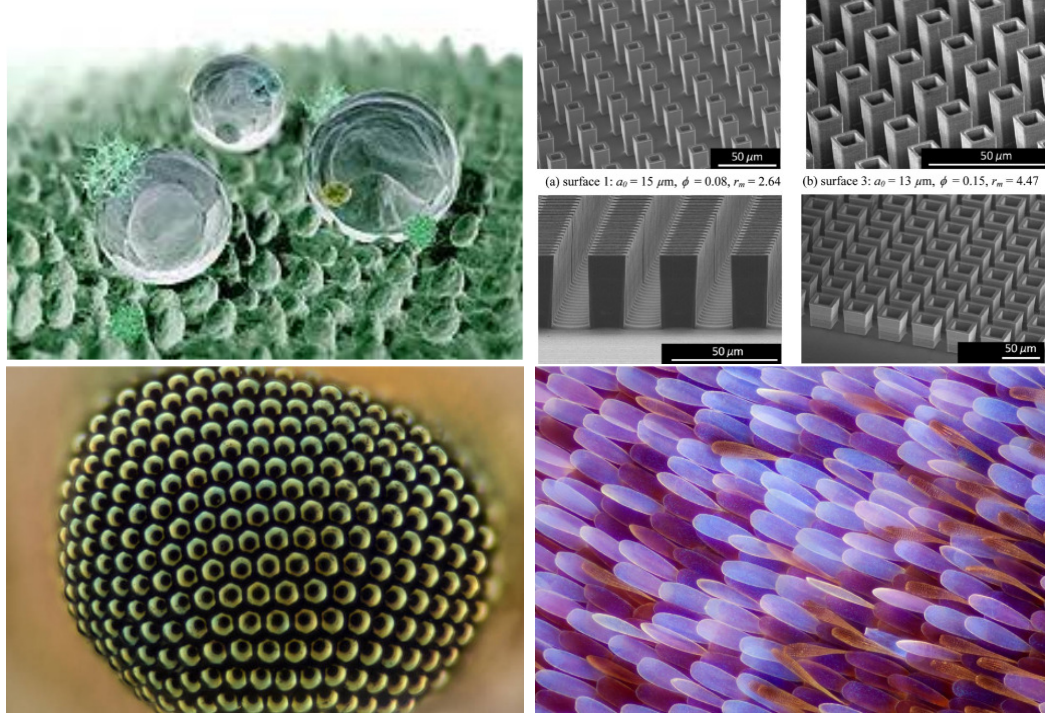
Figure 1.1 Examples of superhydrophobic surfaces. Top left: a surface of a lotus leaf [78]. Top right: manufactured hollow hybrid superhydrophobic surfaces (from Dash et al. [21]). Bottom left: a magnified mosquito eye [1]. Bottom right: a magnified surface of a butterfly wing [29].

There is a vast literature on SH flow problems. We review some of the prior work that is relevant to the current study. An important early theoretical investigation is the seminal work of Philip [68], who mathematically derived exact solutions to various SH flow problems subject to mixed boundary conditions for a flat or undeformed interface. Since then, there have been many theoretical and numerical investigations of flow over SH surfaces in different geometries. For example, Teo and Khoo [77] numerically investigated the effects of interface curvature on the transverse SH flow through micro-scale channels and tubes. Yariv and Siegel [83] analyzed the rotation of an infinite cylinder with air-bubbles or grooves as a model of the rigid-body motion of an SH particle in a viscous liquid. Crowdy [20] mathematically analyzed longitudinal

shear flow over a no-slip surface with partial slip circular bubbles. Yariv and Schnitzer [82] studied a similar longitudinal flow with closely spaced circular bubbles using asymptotic analysis. Nearly all of the numerical studies involve a regular periodic geometry, where the solution needs only to be computed over a single solid-groove cell. In contrast, the method developed here will be capable of computing over irregular geometries with many cells.

In the above studies, two types of flow alignment are typically considered: longitudinal flow or transverse flow. Longitudinal flow refers to the case where the fluid motion is parallel to the gas-filled grooves, while transverse flow involves fluid motion which is perpendicular to the grooves. A relatively small number of mathematical and numerical studies have focused on the transverse flow compared with the longitudinal flow. Hence, we concentrate in this work on the development of a numerical method for transverse flow. However, the algorithm developed here, with modifications, also applies to the case of longitudinal flow.

The presence of mixed boundary conditions and corners on the boundary of a given domain introduces significant difficulties for numerical computations. The existence of corners and boundary transition points, where boundary conditions change type, leads to flow singularities, i.e., singularities in the velocity and stress fields. A standard approach to dealing with the singularities, adaptive mesh refinement, leads to numerous unknowns, ill-conditioned linear systems, and a loss of accuracy. Previous approaches based on the finite element method (FEM) have been implemented and studied (e.g., Teo and Khoo [77], Lam et al. [58], and Kirk et al. [50]) and some software packages are available. The reported numerical results show a few digits of accuracy. A drawback of these methods is the need to discretize the whole computational domain with a large number of elements (10^5-10^6 elements per a single solid-groove cell). Another approach that applies to Stokes flow over SH surfaces is the Boundary Integral Equation (BIE) method, which has the potential

to achieve high accuracy. However, there has been much less work applying BIE methods to SH flow, with Kelmanson [49], Yariv and Schnitzer [82] among the few studies. In the BIE method, one only needs to discretize the boundary of the domain, so that the dimension of the problem is reduced by one in the solve phase. When applied to mixed boundary value problems, however, the BIE methods require either adaptive refinement or special techniques to achieve high accuracy due to the presence of corners and boundary transition points. Whereas research efforts to develop the BIE methods on Stokes equations on complex geometries are ongoing, with recent work including Askham and Rachh [4], Rachh and Askham [71], Helsing and Jiang [39], Rachh and Serkh [72], and Wu et al. [80], the boundary conditions discussed in their work do not include mixed boundary conditions.

Related work on adaptive mesh refinement for mixed boundary value problems in the context of Laplace's equation is given by Helsing [37] who develops the Recursively Compressed Inverse Preconditioning (RCIP) method (Helsing and Ojala [42]) for that application. A significant part of the current dissertation is to extend for the first time the RCIP method to mixed boundary value problems of the Stokes flow. We also adapt the RCIP method to SH flow problems. An additional challenge in the latter case arises due to the nonstandard 'hybrid' form of boundary conditions for SH flow, which is described in section 2.2.6. We will reformulate the discrete problem for the SH flow so that it is compatible with the RCIP method.

In the first part of this dissertation, we develop an accurate and fast numerical method based on the BIE method for interior mixed boundary value problems for Stokes equations, and apply it to the SH flow. Our method allows the boundary of a given computational domain to have corners and mixed boundary conditions that occur at the juncture between solid surfaces and bubble menisci in SH flow. The proposed numerical method in this work is summarized as follows. First, we choose a layer potential representation for the solution and derive the associated

boundary integral equations. Then, we design a numerical method that makes use of or adapts the following numerical techniques: the RCIP method, a matrix scaling technique, kernel-split quadratures, and the Stokes FMM. The combination of these methods has several advantages. The RCIP method, introduced in Helsing and Ojala [42] and further described in Helsing [37], Helsing and Holst [38], Helsing and Jiang [39], and Helsing [36], can accurately handle flow singularities at corners and boundary transition points and leads to an optimal number of unknowns in the discretization. Singular and nearly singular integrals are calculated via high-order kernel-split quadratures in [37] which gives high accuracy, even for the evaluation of nearly singular layer potentials at target points close to the boundary. A matrix scaling technique is adapted from Helsing and Jiang [39] to stabilize the linear system obtained by discretizing the BIEs. The fast multipole method (FMM) by Greengard and Rokhlin [34] is incorporated to accelerate the computations of matrix-vector products for evaluating layer potentials and reduces the space complexity and CPU time of the numerical simulations. We illustrate the combined method by computing challenging examples of SH flow in geometries with corners and boundary transition points. The examples show that the method is able to achieve high accuracy and linear scaling complexity, and can handle geometries with hundreds of cells.

The second half of this dissertation is focused on computational electromagnetics and its applications to integrated photonics, discussed in Chapter 3. Our objective is to devise an efficient and accurate numerical method that is capable of handling large-scale simulations for the development of integrated photonics.

In the photonics industry, there is high demand on efficient and accurate simulations on the propagation of electromagnetic waves for designing integrated photonic devices. In integrated photonics, the optical circuits consists of basic components such as star couplers, arrayed-waveguide gratings, reconfigurable optical add/drop multiplexers (ROADM), matrix switches, lattice-form programmable dispersion

equalizers, etc. Figure 1.2 shows one typical device and its schematic interior design, and Figure 1.3 shows the images of computational domains for two kinds of waveguides. While the integrated photonics industry has been growing rapidly, the lack of efficient and reliable design software has become one of the bottlenecks for its development. This is an extremely difficult problem in computational mathematics. Unlike integrated eletronic circuits that admit a simplified model, one has to solve three-dimensional Maxwell's equations for photonic devices. The wavelength of the incident wave in integrated photonic devices is about 1.55 micrometers, while the devices are usually on the scale of centimeters in two-dimensional plane and at least tens of micrometers in thickness. Thus, when measured in terms of wavelength, the size of the device is about $10 \times 1000 \times 1000$. By the Nyquist–Shannon sampling theorem that states at least two points per wavelength are required to resolve an oscillatory signal, it is easy to see that one needs *hundreds of millions* of discretization points for a very low-accuracy calculation. All existing software packages for integrated photonics rely on either the finite difference time domain (FDTD) method or the finite element method (FEM), both of which require the discretization for the whole volume. And accurate numerical simulations become impractical even if the design engineers have some of the most powerful computers at their hands.
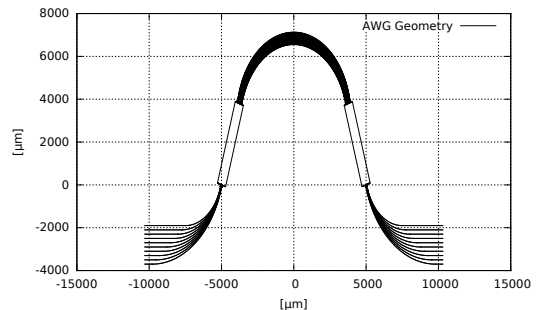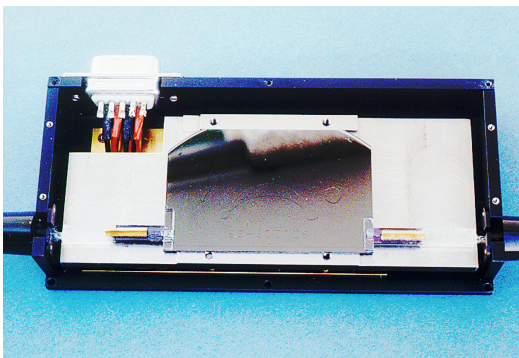
Figure 1.2 Left: a packaged arrayed waveguide grating (AWG) module [24]. Right: a plane geometry of an AWG [66].
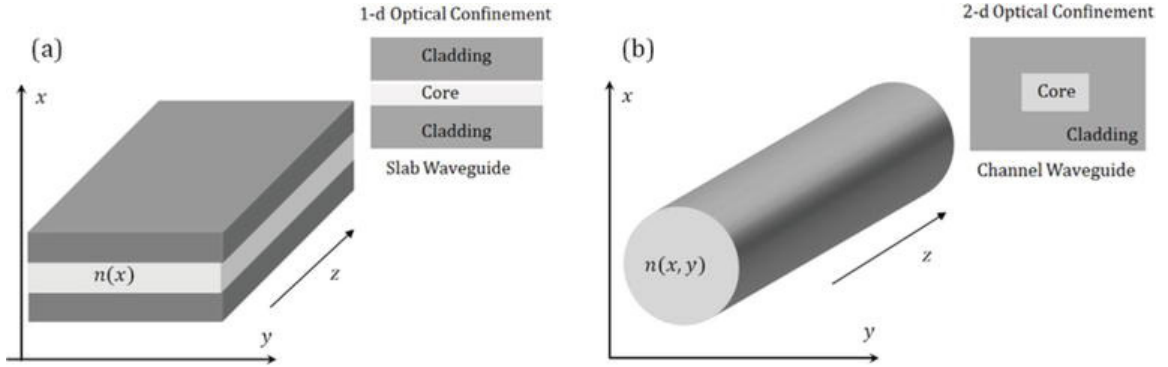
Figure 1.3 Modeled images of waveguides from [88]. Left: a planar optical waveguide. Right: an optical fiber.

Here we propose a scattering matrix formulation for the simulation of photonic devices. By design, the input and output channels of photonic components consists of straight waveguides that admit a finite number of so-called propagating modes. The scattering matrix is a matrix of finite dimension converting the incoming propagating waves to reflected and transmitted outgoing propagating waves. It is clear that the scattering matrix provides all information of a photonic device. In practice, various functional components inside a photonic device are well separated from each other so that the interference between any two components can be neglected. Thus, the scattering matrix for each component offers a black-box characterization of its functions, and the scattering matrix for the whole device can be constructed to satisfactory accuracy by assembling the scattering matrices of each component together. To the best of our knowledge, a systematic study of the scattering matrix formulation has not been carried out for photonic devices. In this dissertation, we study the scattering matrix formulation for the simplified model problem - waveguide structures in two dimensions with the Helmholtz equation as the governing equation and the boundary condition being the zero Dirichlet condition. We analyse the mathematical properties of the scattering matrix and present detailed numerical investigation of the scattering matrix formulation for the model problem. Once again, we apply fast integral equation methods to solve this problem, and state-of-art

numerical tools such as the kernel-split quadrature for close evaluation, generalized Gaussian quadrature for self and near interactions when building the system matrix, the RCIP method for point singularities, and the fast algorithms such as the fast multipole methods and its descendants, are used to achieve 10+ digits of accuracy within minutes for large-scale simulations.

The rest of this dissertation is organized as follows. Chapter 2 is focused on SH flow, and Chapter 3 on integrated photonics. In both Chapters 2 and 3, we present the mathematical formulations to be used, our numerical methods, and numerical examples as sections in this order, respectively. Finally, we conclude this dissertation in Chapter 4.

CHAPTER 2

FLUID DYNAMICS AND SUPERHYDROPHOBIC FLOW

2.1 Mathematical Formulation

2.1.1 Governing equations and boundary conditions

We first present the primitive or PDE formulation for multiply-connected interior Stokes flow in 2D bounded geometries. The mathematical formulation and numerical method can be easily generalized to exterior flow in unbounded geometries. The domain is allowed to have nonsmooth boundaries and mixed boundary conditions, and the numerical method is specially tailored to accurately handle such conditions.

The fluid domain Ω (an illustration is given in Figure 2.1) is taken to be a multiply-connected region bounded by M closed curves, Γ_i, for $i = 1, \ldots, M$. We denote the outermost or enclosing boundary by Γ_1, and let $\Gamma = \cup_{i=1}^{M} \Gamma_i$ be the entire boundary. Each closed curve Γ_i is composed of N_i piecewise smooth curves $\Gamma_i^{(j)}$ for $j = 1, \ldots, N_i$, so that $\Gamma_i = \cup_{j=1}^{N_i} \Gamma_i^{(j)}$. Different boundary conditions (e.g., Dirichlet or Neumann) will be allowed on the different boundary components $\Gamma_i^{(j)}$.

The boundary value problem for incompressible 2D Stokes flow in the domain Ω with boundary Γ is written

$$-\mu \Delta \boldsymbol{u} + \nabla p = \boldsymbol{0} \text{ and } \nabla \cdot \boldsymbol{u} = 0 \text{ for } \boldsymbol{x} \in \Omega, \tag{2.1}$$

$$\mathcal{B}_i^{(j)}(\boldsymbol{u}, p) = 0 \text{ for } \boldsymbol{x} \in \Gamma_i^{(j)}, \ i = 1, \ldots, M \text{ and } j = 1, \ldots, N_i. \tag{2.2}$$

Here $\boldsymbol{u}$ is the fluid velocity, p is the pressure, and μ is the viscosity which is taken to be constant in Ω. The functional $\mathcal{B}_i^{(j)}(\boldsymbol{u}, p)$ (which can also depend on derivatives of velocity and pressure) prescribes the boundary condition on boundary component $\Gamma_i^{(j)}$. This will typically be either a Dirichlet condition on the velocity $\boldsymbol{u} = \boldsymbol{g}_i^{(j)}(\boldsymbol{x})$ or a Neumann condition on the surface force $\boldsymbol{f} = \boldsymbol{h}_i^{(j)}(\boldsymbol{x})$, where $\boldsymbol{x} \in \Gamma_i^{(j)}$ and $\boldsymbol{f}$

is the surface force or traction $\boldsymbol{f} = \boldsymbol{\sigma n}$. Here $\boldsymbol{\sigma}$ is the stress tensor defined as $\boldsymbol{\sigma} = \sigma_{ij} := -\delta_{ij}p + \mu\left(\frac{\partial u_i}{\partial x_j} + \frac{\partial u_j}{\partial x_i}\right)$ and $\boldsymbol{n}$ is the unit normal vector pointing outwards on the boundary, i.e., into the fluid domain Ω on the embedded objects, and away from the fluid on the external boundary. Example geometries with mixed boundary conditions are shown in Figure 2.2.
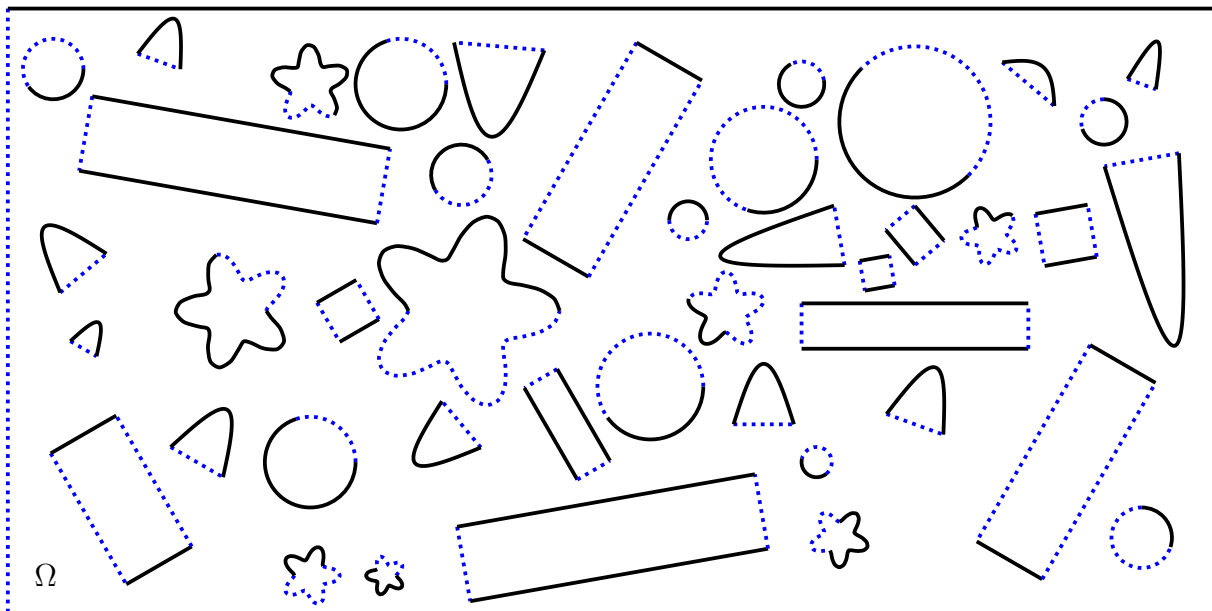
Figure 2.1 A schematic computational domain where objects with piecewise smooth boundary curves are non-uniformly placed inside the bounding box. The fluid region Ω is the interior of the bounding box, exterior to the objects.
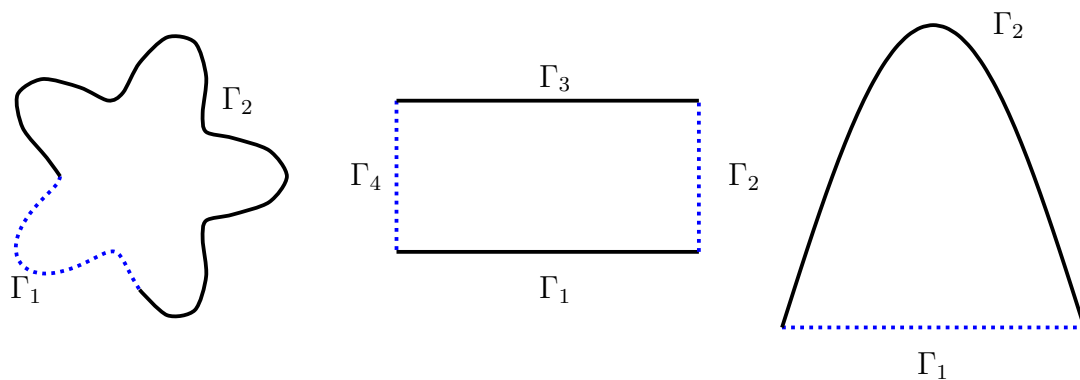
Figure 2.2 Extracted samples of boundary pieces in Figure 2.1. The black lines correspond to Dirichlet boundary condition, and blue dotted lines Neumann condition respectively.

The mixed boundary value problem corresponding to superhydrophobic flow is discussed in Subsection 2.2.6.

2.1.2 Notation and nomenclature

The notation used throughout this chapter is similar to Helsing and Jiang [39], Wu et al. [80], and Klinteberg et al. [51]. In two-dimensional space $\mathbb{R}^2$, we write boundary integral kernels in the form $K(\boldsymbol{x}, \boldsymbol{y})$, and refer to $\boldsymbol{x} = (x_1, x_2)$ as the *target* point and $\boldsymbol{y} = (y_1, y_2)$ as the *source* point, respectively. We define $\boldsymbol{r} := \boldsymbol{x} - \boldsymbol{y}$ and $r := |\boldsymbol{r}|$, and denote by $\boldsymbol{n_x}$ and $\boldsymbol{n_y}$ the unit normal vectors on the boundary Γ pointing outward at $\boldsymbol{x}$ and $\boldsymbol{y}$, respectively. The outward normal sometimes is denoted by $\boldsymbol{n}$ if the context is clear. In a slight abuse of notation, we use the same boldface letter to denote an integral operator, its kernel, and the associated matrix after discretization, with the meaning clear from context.

In some parts of the presentation (e.g., Section 2.2.3) it will be convenient to use complex numbers to represent points and vectors in $\mathbb{R}^2$. This employs the natural representation $a_1 + ia_2$ for the vector $\boldsymbol{a} = (a_1, a_2)$ and we use the complex number $\nu = n_1 + in_2$ to represent the normal vector $\boldsymbol{n}$. Note that in complex notation the dot product of two vectors is represented by $\boldsymbol{a} \cdot \boldsymbol{b} = Re(a\bar{b})$.

We shall refer to a point $\boldsymbol{s} \in \Gamma$ for which the boundary conditions change type of $\boldsymbol{s}$ as a *boundary transition point*. The surface Γ can be either smooth or have a corner at a boundary transition point. We also use $\boldsymbol{s}$ to denote a corner point where the boundary conditions do not change type.

2.1.3 Integral equation formulation

Stokes layer potentials   We now reformulate the problem (Equations (2.2)) in terms of boundary integral equations (BIEs). Different approaches are available to write this problem in terms of BIEs, see e.g. Pozrikidis [69]. We will make use of a

combined-field BIE representation Wu et al. [80] that leads to a non-rank deficient linear system.

For simplicity, we first consider mixed boundary conditions in which the boundary Γ is composed of a set of curves $\Gamma_D = \{\Gamma_i^{(j)} : (i,j) \in \mathcal{I}\}$ on which Dirichlet conditions are imposed, and a set of curves $\Gamma_N = \Gamma - \Gamma_D$ on which Neumann conditions are applied. Here $\mathcal{I}$ denotes the set of indices (i,j) for which a Dirichlet condition is applied on boundary component $\Gamma_i^{(j)}$. Later, the more complex boundary conditions for superhydrophobic flow will be considered.

In a standard way, we write the velocity $\boldsymbol{u}$ and stress $\boldsymbol{f}$ at $\boldsymbol{x} \in \Omega$ as a sum of Stokes single and double layer potentials acting on an unknown density vector $\boldsymbol{\rho}$:

$$\boldsymbol{u}(\boldsymbol{x}) = \boldsymbol{S}_{\Gamma_N}[\boldsymbol{\rho}](\boldsymbol{x}) + \boldsymbol{D}_{\Gamma_D}[\boldsymbol{\rho}](\boldsymbol{x}), \tag{2.3}$$

$$\boldsymbol{f}(\boldsymbol{x}) = \boldsymbol{S}'_{\Gamma_N}[\boldsymbol{\rho}](\boldsymbol{x}) + \boldsymbol{D}'_{\Gamma_D}[\boldsymbol{\rho}](\boldsymbol{x}). \tag{2.4}$$

Here $\boldsymbol{S}_\Gamma$ and $\boldsymbol{D}_\Gamma$ are, respectively, the velocity single and double layer potentials over a boundary component Γ, and $\boldsymbol{S}'_\Gamma$ and $\boldsymbol{D}'_\Gamma$ are the traction single and double layer potentials (cf. Equations (2.6)-(2.9) below). The subscripts Γ_N and Γ_D are used to indicate that we use the single layer representation (i.e., Equations (2.6) and (2.8) below) on parts of the boundary where a Neumann condition is enforced, and the double layer representations (2.7) and (2.9) on boundary components where the Dirichlet condition is imposed. Later, we consider examples involving pressure-driven flow in a channel for which pressure boundary conditions are imposed on part of the boundary, denoted by Γ_P. A layer potential representation of the pressure is given by

$$p(\boldsymbol{x}) = S^p_{\Gamma_N}[\boldsymbol{\rho}](\boldsymbol{x}) + D^p_{\Gamma_D}[\boldsymbol{\rho}](\boldsymbol{x}) + S^p_{\Gamma_P}[\boldsymbol{\rho}](\boldsymbol{x}) + D^p_{\Gamma_P}[\boldsymbol{\rho}](\boldsymbol{x}), \tag{2.5}$$

where S^p_Γ and D^p_Γ are the pressure single and double layer potentials over Γ. Note that we use the single layer representation of the pressure over Γ_N, the double layer

representation over Γ_D, and the total combined field representation over Γ_P. The density $\boldsymbol{\rho}$ is determined by the boundary conditions, as detailed below.

The layer potentials in Equations (2.3)-(2.4) are given by

$$S_\Gamma[\boldsymbol{\rho}]_i(\boldsymbol{x}) := \frac{1}{4\pi\mu} \int_\Gamma G_{ij}(\boldsymbol{x}, \boldsymbol{y}) \rho_j(\boldsymbol{y}) dS_{\boldsymbol{y}}, \tag{2.6}$$

$$D_\Gamma[\boldsymbol{\rho}]_i(\boldsymbol{x}) := \frac{1}{4\pi} \int_\Gamma T_{ijk}(\boldsymbol{x}, \boldsymbol{y}) \rho_j(\boldsymbol{y}) n_{\boldsymbol{y},k} dS_{\boldsymbol{y}}, \tag{2.7}$$

$$S'_\Gamma[\boldsymbol{\rho}]_i(\boldsymbol{x}) := -\frac{1}{4\pi} \int_\Gamma T_{ijk}(\boldsymbol{x}, \boldsymbol{y}) \rho_j(\boldsymbol{y}) n_{\boldsymbol{x},k} dS_{\boldsymbol{y}}, \tag{2.8}$$

$$D'_\Gamma[\boldsymbol{\rho}]_i(\boldsymbol{x}) := \frac{\mu}{4\pi} \int_\Gamma \left[\frac{\partial}{\partial x_l} T_{ijk} + \frac{\partial}{\partial x_i} T_{ljk} - \delta_{il}\Pi_{kj} \right] \rho_j(\boldsymbol{y}) n_{\boldsymbol{y},k} n_{\boldsymbol{x},l} dS_{\boldsymbol{y}}, \tag{2.9}$$

$$S^p_\Gamma[\boldsymbol{\rho}](\boldsymbol{x}) := \frac{1}{4\pi\mu} \int_\Gamma G^p_j(\boldsymbol{x}, \boldsymbol{y}) \rho_j(\boldsymbol{y}) dS_{\boldsymbol{y}}, \tag{2.10}$$

$$D^p_\Gamma[\boldsymbol{\rho}](\boldsymbol{x}) := \frac{\mu}{4\pi} \int_\Gamma \Pi^p_{kj}(\boldsymbol{x}, \boldsymbol{y}) \rho_j(\boldsymbol{y}) n_{\boldsymbol{y},k} dS_{\boldsymbol{y}} \tag{2.11}$$

where $dS_{\boldsymbol{y}}$ is an arclength element on boundary component Γ. In the above expressions, $G_{ij}(\boldsymbol{x}, \boldsymbol{y})$ is the velocity fundamental solution or Stokeslet, $T_{ijk}(\boldsymbol{x}, \boldsymbol{y})$ is the associated stress tensor, and $\Pi_{ik}(\boldsymbol{x}, \boldsymbol{y})$ is the pressure kernel. These are given by

$$G_{ij}(\boldsymbol{x}, \boldsymbol{y}) := \delta_{ij} \ln \frac{1}{r} + \frac{1}{r^2} \hat{x}_i \hat{x}_j, \tag{2.12}$$

$$T_{ijk}(\boldsymbol{x}, \boldsymbol{y}) := \frac{4}{r^4} \hat{x}_i \hat{x}_j \hat{x}_k, \tag{2.13}$$

$$\Pi_{ik} := 4 \left(-\frac{1}{r^2} \delta_{ik} + \frac{2}{r^4} \hat{x}_i \hat{x}_k \right), \tag{2.14}$$

$$G^p_j(\boldsymbol{x}, \boldsymbol{y}) := \frac{1}{2\pi} \frac{\hat{x}_j}{r^2}, \tag{2.15}$$

where $\hat{x}_i := (\boldsymbol{x} - \boldsymbol{y})_i$, and $n_{\mathbf{x},k}$ is used denote the kth component of the vector $n_{\boldsymbol{x}}$, etc. Einstein summation notation is used above and throughout, with indices i, j, k, l taking values in the set $\{1, 2\}$ for 2D flow.

For smooth $\boldsymbol{\rho}$ and Γ, the integral in Equation (2.7) is regular (i.e., with a smooth integrand) while Equations (2.6), (2.8) and (2.10) are weakly singular. The

integrals in Equations (2.9) and (2.11) are hypersingular when the target point is on the boundary Γ.

2.1.4 Boundary integral equations

Standard jump relations are used to derive the boundary integral equations from the layer potential representation (2.4). In the simplified situation in which the boundary Γ is decomposed into a region Γ_D on which a Dirichlet boundary condition is applied and a region Γ_N on which a Neumann or surface traction boundary condition is imposed, we apply $\boldsymbol{u}|_{\Gamma_D} = \boldsymbol{g}(\boldsymbol{x})$ on Γ_D and $\boldsymbol{f}|_{\Gamma_N} = \boldsymbol{\sigma}\boldsymbol{n}|_{\Gamma_N}$, for a given surface stress $\boldsymbol{f}$, on Γ_N. Then, the following boundary integral equations can be derived from well-known jump relations for the layer potentials as can be seen in Pozrikidis [69]

$$-\frac{1}{2}\boldsymbol{\rho}(\boldsymbol{x}) + \boldsymbol{D}_{\Gamma_D}[\boldsymbol{\rho}](\boldsymbol{x}) + \boldsymbol{S}_{\Gamma_N}[\boldsymbol{\rho}](\boldsymbol{x}) = \lim_{h\to 0+} \boldsymbol{D}[\boldsymbol{\rho}](\boldsymbol{x} - h\boldsymbol{n_x}) = \boldsymbol{u}|_{\Gamma_D} \quad \boldsymbol{x} \in \Gamma_D, \quad (2.16)$$

$$\frac{1}{2}\boldsymbol{\rho}(\boldsymbol{x}) + \boldsymbol{D}'_{\Gamma_D}[\boldsymbol{\rho}](\boldsymbol{x}) + \boldsymbol{S}'_{\Gamma_N}[\boldsymbol{\rho}](\boldsymbol{x}) = \lim_{h\to 0+} \boldsymbol{S}'[\boldsymbol{\rho}](\boldsymbol{x} - h\boldsymbol{n_x}) = \boldsymbol{f}|_{\Gamma_N} \quad \boldsymbol{x} \in \Gamma_N. \quad (2.17)$$

(Note that the signs in Equations (2.16 and (2.17) are for interior problem, for exterior problem signs on identity terms change.) This system of equations determines the vector density $\boldsymbol{\rho}$. Once $\boldsymbol{\rho}$ is known, velocities and tractions throughout the domain Ω and on the boundary are determined from the layer potential representations (2.3) and (2.4).

We first use the layer potential representations above to formulate an RCIP method for problems with mixed boundary conditions in simple geometries (e.g., those in Figure 2.2), so as to validate the numerical algorithm. Later, in Section 2.2.6, we will adapt the formulation and numerical method to deal with the more complicated boundary conditions exhibited by models of superhydrophobic flow.

2.2 Numerical Methods

We first describe a standard BIE method employing a panel-based Nyströöm discretization scheme, and discuss some difficulties that occur when applying such a standard method to geometries like those shown in Figures 2.1 and 2.2. Then, we describe our numerical scheme into which we incorporate the RCIP method, kernel-split quadratures, a scaling method, and the Stokes FMM to handle the difficulties.

2.2.1 Standard procedure of BIE methods

A standard BIE method based on Nyström discretization typically involves the following set of steps:

1. Formulate the boundary integral equation (BIE) representation of the problem. In our example of the mixed Dirichlet-Neumann boundary value problem for Stokes equations, the BIE representations are (2.16) and (2.17). We assume that the BIE system of n_{eq} integral equations can be written in the standard form

$$(\boldsymbol{I}_c + \boldsymbol{K}_c)\boldsymbol{\rho}_c(\boldsymbol{x}) = \boldsymbol{b}_c(\boldsymbol{x}), \tag{2.18}$$

where $\boldsymbol{I_c}$ is the identity operator, $\boldsymbol{K}_c$ represents the integral operators, $\boldsymbol{\rho}_c$ is the unknown layer density, and $\boldsymbol{b}_c(\boldsymbol{x})$ denotes the boundary data. The subscript c is used to represent continuous (as opposed to discrete) functions and operators.

2. Apply a quadrature method to discretize the BIEs (e.g., Equations (2.16) and (2.17)) to obtain a linear system of the form

$$(\boldsymbol{I} + \boldsymbol{K})\,\boldsymbol{\rho} = \boldsymbol{b}, \tag{2.19}$$

where $\boldsymbol{I}$ is the identity matrix, $\boldsymbol{K}$ is a matrix of discretized layer potentials with quadrature weights, $\boldsymbol{\rho}$ is the unknown density to be solved, and $\boldsymbol{b}$ is the data given by the boundary conditions.

3. Determine the unknown density values $\boldsymbol{\rho}$ by numerically solving the linear system (2.19), typically using an iterative method such as GMRES [76].

4. Evaluate the desired quantities such as the velocities in Ω and surface forces using the layer potential representations, e.g., Equations (2.3) and (2.4).

We use n_{gl} point Gauss-Legendre quadrature nodes and weights for the discretization in the second step, where $n_{gl} = 16$ throughout this paper.

If the boundary Γ is sufficiently smooth and the boundary condition is entirely Dirichlet or Neumann, then BIEs (2.16) and (2.17) involve integral operators that are compact and the associated discrete system (2.19) is well-conditioned. Then, the kernels of the layer potentials contain terms like

$$\frac{\boldsymbol{r} \cdot \boldsymbol{n}_y}{r^2}, \tag{2.20}$$

but when Γ is smooth $\boldsymbol{r} \cdot \boldsymbol{n}_y$ is of order r^2 which makes the integrand of Equation (2.20) bounded, and hence the associated integral operator is compact. If Γ contains a corner vertex $\boldsymbol{p}$, then (2.20) is $O(r^{-1})$ as $\boldsymbol{x}$ and $\boldsymbol{y}$ approach $\boldsymbol{p}$ from different sides. This is similar to the double layer potential operator for Laplace's equation. However, it is shown in Verchota [79] that the Laplace double layer potential is a bounded singular operator on Lipschitz domains. In this case, the associated discrete system (2.19) is also well-conditioned. Wu et al. [80] exploit this fact to obtain accurate solutions to the Dirichlet problem for Stokes equations on domains with corners.

In the current paper, we impose mixed boundary conditions on Γ and in addition the boundary may be nonsmooth. Standard quadrature rules for smooth integrals then results in a loss of accuracy. There are hypersingular integral operators in $\boldsymbol{K}_c$ and the associated discrete system (2.19) is ill-conditioned. Even if Γ is entirely smooth, the presence of boundary transition points where the boundary condition changes type leads to hypersingular and nearly hypersingular integrals in $\boldsymbol{K}_c$ for target points on the interface. Without special treatment, this leads to a loss of accuracy.

Adaptive or graded mesh refinement in the neighborhood of a corner or boundary transition point mitigates the issue. Nevertheless, the size of the discrete problem grows significantly with refinement level, and it can still be difficult to obtain satisfactory accuracy due to the ill-conditioning of the linear system when

standard quadratures are used. Determining an optimal level of refinement to obtain satisfactory accuracy is also problematic. The density $\boldsymbol{\rho}$ will be insufficiently resolved with underrefinement, while overrefinement often leads to numerical instability and loss of accuracy due to the non-uniform spacing of a graded mesh. A numerical example that illustrates the poor performance of standard quadrature and adaptive refinement schemes (compared to the method developed in this paper) is shown in Figure 2.7 below. To resolve these issues, we adapt the recently the developed RCIP method and combine it with kernel-split quadratures, a scaling technique, and the Fast Multipole Method to obtain a fast and accurate numerical scheme. We describe these pieces in order.
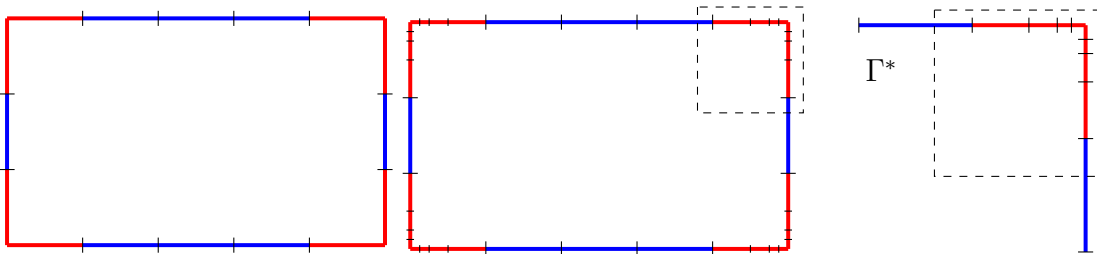
Figure 2.3 Left: rectangular boundary without refinements. Middle: rectangular boundary with dyadic refinements towards corners. Right: zoomed-in top-right refined corner. The four coarse panels in the neighborhood of a corner point are denoted by Γ^*.

2.2.2 The RCIP method

Overview of the method We provide a brief overview of the RCIP (Recursively Compressed Inverse Preconditioning) method, which was originally proposed in Helsing and Ojala [42]. Here, the method is applied at geometric corners and boundary transition points, i.e., where the boundary condition changes type. Such points are referred to as singular points. We first describe the application of RCIP in the neighborhood of a single corner point $\boldsymbol{s} \in \Gamma$ and later modify it for the treatment of a boundary transition point. A detailed exposition of the method applied to Laplace's equation and to integral equations of scattering theory is given in Helsing [36]. We

provide an overview similar to Helsing and Jiang [39] and Helsing and Jiang [40]. One technical difference between the application of the RCIP method to Laplace and Helmholtz equations and the current work is that, in the former, the BIEs are scalar equations, while the corresponding relations for Stokes flow are two-dimensional vector equations.

We assume a discrete system of n_{eq} integral equations of the form of Equation (2.19). The RCIP method employs dyadic mesh refinement toward the singular point, as illustrated in Figure 2.3. The linear system to be solved after refinement is written as

$$(\boldsymbol{I}_{\text{fin}} + \boldsymbol{K}_{\text{fin}})\,\boldsymbol{\rho}_{\text{fin}} = \boldsymbol{b}_{\text{fin}}. \tag{2.21}$$

Define the number of panels on the coarse mesh before refinement as n_p. We denote the number of subdivisions in the neighborhood of a singular point by n_{sub}

The RCIP method employs dyadic mesh refinement toward the singular point, as illustrated in Figure 2.3. The method begins with the decomposition or splitting of the interaction matrix

$$\boldsymbol{K} = \boldsymbol{K}^{\circ} + \boldsymbol{K}^{*} \tag{2.22}$$

where $\boldsymbol{K}^{*}$ is nonzero only when the target and source points are both on the subset Γ^{*} containing the four coarse panels closest to the singular point (cf. Figure 2.3), and $\boldsymbol{K}^{\circ}$ is nonzero when the target and source points are not both on Γ^{*}. Informally, $\boldsymbol{K}^{\circ}$ represents the smooth part of interaction matrix, and $\boldsymbol{K}^{*}$ holds the singular and near singular part due to the presence of the corner. The $*$ and $\circ$ notation is used on other matrices to denote the same splitting.

The compressed linear system which results from the RCIP method is

$$(\boldsymbol{I}_{coa} + \boldsymbol{K}^{\circ}_{coa}\boldsymbol{R})\,\tilde{\boldsymbol{\rho}}_{coa} = \boldsymbol{b}_{coa}, \tag{2.23}$$

where $\boldsymbol{I}_{coa}$ is the identity matrix on the coarse mesh, $\boldsymbol{K}_{coa}^{\circ}$ is $\boldsymbol{K}^{\circ}$ discretized on the coarse mesh, $\boldsymbol{R}$ is a recursively compressed inverse preconditioner (described below), and $\tilde{\boldsymbol{\rho}}_{coa}$ is a transformed density discretized on the coarse mesh. The transformed density is defined by

$$(\boldsymbol{I}_{\text{fin}} + \boldsymbol{K}_{\text{fin}})\,\boldsymbol{\rho}_{fin} = \boldsymbol{P}\tilde{\boldsymbol{\rho}}_{coa}. \tag{2.24}$$

where $\boldsymbol{P}$ is a prolongation matrix which interpolates from points on the coarse grid to points on the fine grid. The fine grid density $\boldsymbol{\rho}_{fin}$ and other quantities of interest can be recovered from $\tilde{\boldsymbol{\rho}}_{coa}$ in a postprocessing step, as described in Helsing [36].

The matrix $\boldsymbol{R}$ is a lossless compression of $\boldsymbol{K}^*$. We summarize its computation, starting with definitions of 'b-type' and 'c-type' meshes. Define a nested sequence of graded meshes Γ_i^c, $i = 1, \ldots, n_{sub}$ with $\Gamma_{i-1}^c \subset \Gamma_i^c$ and Γ_{nsub}^c coinciding with Γ^*, the four panels of the coarse or unrefined mesh that are closest to the singular point $\boldsymbol{s}$. The meshes Γ_i^c for $i = 1, \ldots, n_{sub}-1$ are recursively obtained from Γ_{i+1}^c by subdividing the two panels closest to the singular point and removing the two panels farthest from $\boldsymbol{s}$. Note that Γ_i^c always consists of two panels on either side of the singular point. We define Γ_i^b for $i = 1, \ldots, n_{sub}$ to be the six panels obtained by subdividing the two panels closest to $\boldsymbol{s}$ in Γ_i^c. An illustration of the different mesh types is given in Figure 2.5. We let $n_b = 6*ngl$ and $n_c = 4*n_{gl}$ denote the number of grid points on type b and c meshes, respectively, per singular point. The operator $\boldsymbol{R}$ is an $N_{coa} \times N_{coa}$ matrix, where $N_{coa} = n_{eq}n_p n_{gl}$, and is constructed sequentially from the deepest refinement level $l = 1$ to $l = n_{sub}$ via the recursion relation

$$\boldsymbol{R}_l = \boldsymbol{P}_{Wbc}^T \left(\mathbb{F}[\boldsymbol{R}_{l-1}^{-1}] + \boldsymbol{B}_l^{\circ}\right)^{-1} \boldsymbol{P}_{bc} \quad (1 \le l \le n_{sub}) \tag{2.25}$$

with

$$\boldsymbol{B}_l = \boldsymbol{I}_{l,b} + \boldsymbol{K}_{l,b}. \tag{2.26}$$

Matrices and operators in the above equation are defined as follows. $\boldsymbol{P}_{bc}$ is an $N_b \times N_c$ prolongation matrix, where $N_b = n_{eq}n_b$ and $N_c = n_{eq}n_c$, which interpolates n_{eq} discrete functions (the components of $\boldsymbol{\rho}$) from points on Γ_l^c to the refined mesh Γ_l^b. $\boldsymbol{P}_{Wbc} := \boldsymbol{W}_b \boldsymbol{P}_{bc} \boldsymbol{W}_c^{-1}$ is a $N_b \times N_c$ weighted interpolation matrix, where $\boldsymbol{W}_b$ and $\boldsymbol{W}_c$ are diagonal matrices composed of Gauss-Legendre quadrature weights on type-b and type-c meshes, respectively. The target and source points of $\boldsymbol{K}_{l,b}$ are on Γ_l^b, and $\boldsymbol{K}_{l,b}^\circ$ is an $N_b \times N_b$ matrix obtained from the splitting (2.22) applied to $\boldsymbol{K}_{l,b}$. $\boldsymbol{I}_{l,b}^\circ$ is an $N_b \times N_b$ matrix on Γ_l^b obtained from the splitting of the identity $\boldsymbol{I}_b$. $\mathbb{F}[\,\cdot\,]$ is an operator padding $\boldsymbol{R}_{l-1}^{-1}$ with zeros to expand the matrix size from $N_c \times N_c$ to $N_b \times N_b$ for $l > 1$. The recursion is initialized by setting $\mathbb{F}[\boldsymbol{R}_{l-1}^{-1}] = \boldsymbol{I}_{1,b}^* + \boldsymbol{K}_{1,b}^*$, so that in the first step we invert the operator $\boldsymbol{I}_{1,b} + \boldsymbol{K}_{1,b}$ on the finest type-b mesh Γ_1^b. Figures 2.5 and 2.6 illustrate the recursive computations of $\boldsymbol{R}_l$.
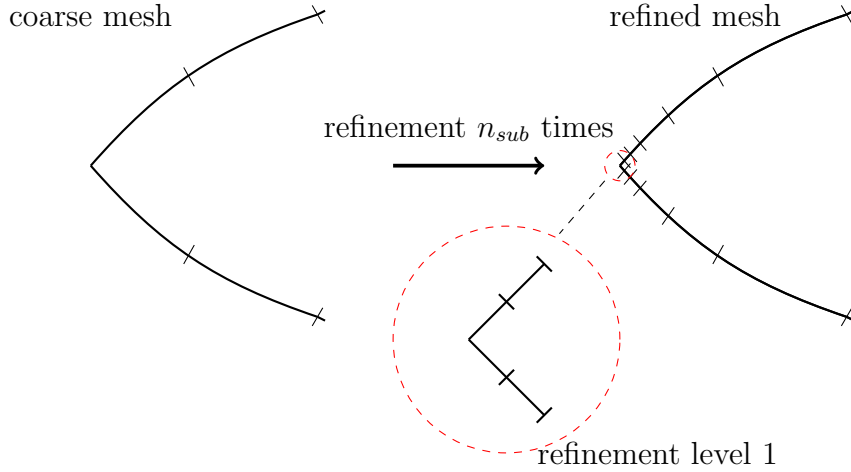
Figure 2.4 Illustration of recursive relation of the RCIP method from refinement level 1 to n_{sub}.

$$\boldsymbol{R}_{l-1}$$

Type-c on Γ_{l-1}

$$\boldsymbol{R}_l = \boldsymbol{P}_{Wbc}^T \left(\mathbb{F}[\boldsymbol{R}_{l-1}^{-1}] + \boldsymbol{I}_b^\circ + \boldsymbol{K}_{l,b}^\circ \right)^{-1} \boldsymbol{P}_{bc}$$

Type-c on Γ_l

$$\boldsymbol{R}_{l-1}^{-1} \qquad \boldsymbol{I}_{l,b}^\circ + \boldsymbol{K}_{l,b}^\circ$$

$$\mathbb{F}[\boldsymbol{R}_{l-1}^{-1}] + \boldsymbol{I}_{l,b}^\circ + \boldsymbol{K}_{l,b}^\circ$$

Type-b on Γ_l Type-b on Γ_l
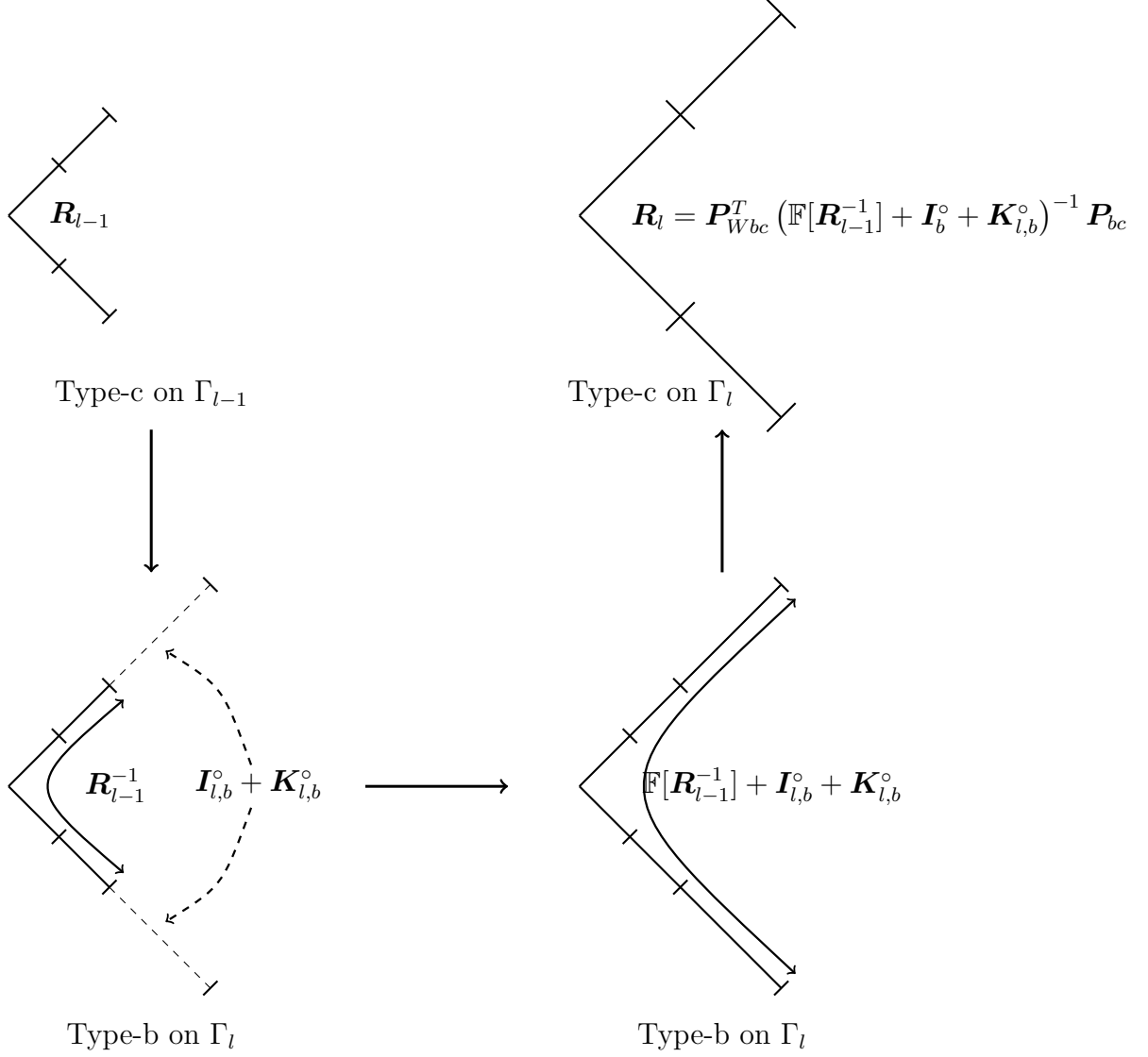
Figure 2.5 Illustration of recursive relation (2.25) of the RCIP method from refinement level $l-1$ to l. $\boldsymbol{R}_l$ on a type-c mesh at level l (top right) is constructed starting with $\boldsymbol{R}_{l-1}$ on type-c mesh (top left) through the intermediate steps on the type-b mesh at level l (bottom).
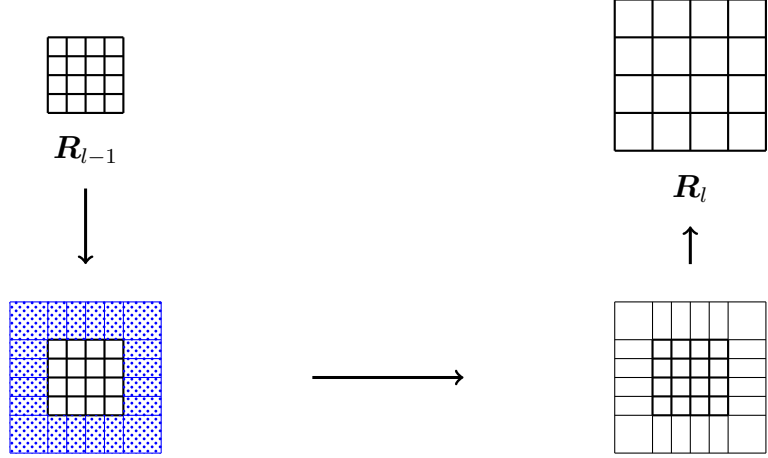
$$\boldsymbol{I}_{l,b}^{\circ} + \boldsymbol{K}_{l,b}^{\circ} \text{ (shaded blue) sorrounding } \boldsymbol{R}_{l-1}^{-1} \qquad \boldsymbol{R}_{l-1}^{-1} + \boldsymbol{I}_{l,b}^{\circ} + \boldsymbol{K}_{l,b}^{\circ}$$

Figure 2.6 Matrix representations corresponding to Figure-2.5 for recursive relation (2.25).

If the boundary Γ contains one singular point, the matrix $\boldsymbol{R}$ coincides with the identity except for an $N_c \times N_c$ block of entries where $\boldsymbol{K}_{coa}^*$ is nonzero. We denote that block by $\boldsymbol{R}^*$. Said another way, $\boldsymbol{K}_{coa}^{\circ}$ has a zero block of size $N_c \times N_c$, which is precisely where $\boldsymbol{R}^*$ is located. Furthermore, $\boldsymbol{R}^*$ is determined by the above iteration as $\boldsymbol{R}^* = \boldsymbol{R}_{nsub}$. $\boldsymbol{R}$ therefore has the following structure:

$$\boldsymbol{R} = \begin{bmatrix} \boldsymbol{I} & & & \\ & \boldsymbol{R}^* & & \\ & & & \\ & & & \boldsymbol{I} \\ & & & \end{bmatrix}. \tag{2.27}$$

When there is more than one singular point $\boldsymbol{R}$ has a similar structure, but there are multiple blocks $\boldsymbol{R}^*$.

After computation of the matrix $\boldsymbol{R}$, the linear system (2.23) is solved for $\tilde{\boldsymbol{\rho}}$ using an iterative method such as GMRES.

Remark 2.2.1. *The matrix $\boldsymbol{B}_l^\circ$ in the Equation (2.25) becomes increasingly ill-conditioned as n_{sub} increases. This is related to the presence of hypersingular kernels at a corner or boundary transition point. We stabilize the inversion $\left(\mathbb{F}[\boldsymbol{R}_{l-1}^{-1}] + \boldsymbol{B}_l^\circ\right)^{-1}$ using the Schur-Banachiewicz block inversion formula in Henderson and Searle [44] as suggested in Helsing [43] (see also Helsing [36]).*

Remark 2.2.2. *Each step of the recursion involves inversion of a $N_b \times N_b$ matrix. Using the Schur-Banachiewicz block inversion formula this is reduced to inverting a $2n_{eq}n_{gl} \times 2n_{eq}n_{gl}$ matrix at each step, which for our values of n_{eq} and n_{gl} amounts to a 64×64 system. This enables extremely efficient calculation of the preconditioner $\boldsymbol{R}$. In our numerical examples, $\boldsymbol{R}$ is computed on the fly in less than 0.01 seconds per singular point even with a level of adaptive refinement up to 100. Additionally, $\boldsymbol{R}$ can be reused for certain geometries, e.g., corners with the same opening angles, assuming the same boundary conditions at each corner. For fixed N_{coa}, the time and space complexities of the RCIP method are proportional to the number of singular points and the deepest level of refinement n_{sub}.*

A numerical example illustrating advantages of the RCIP method in a mixed boundary value problem, compared to standard dyadic mesh refinement, is shown in Figure 2.7. In the numerical experiment, we choose a rectangular domain and set the boundary conditions to Dirichlet on the top and bottom, and Neumann on the left and right sides. The figure plots the condition number of the matrix $(\boldsymbol{I} + \boldsymbol{K})$ in the linear system (2.19), the number of the GMRES iterations to solve for the density, and the relative error in the velocity at a target point $(x, y) = (0.5, 0.1)$ inside of the domain (away from the boundary).
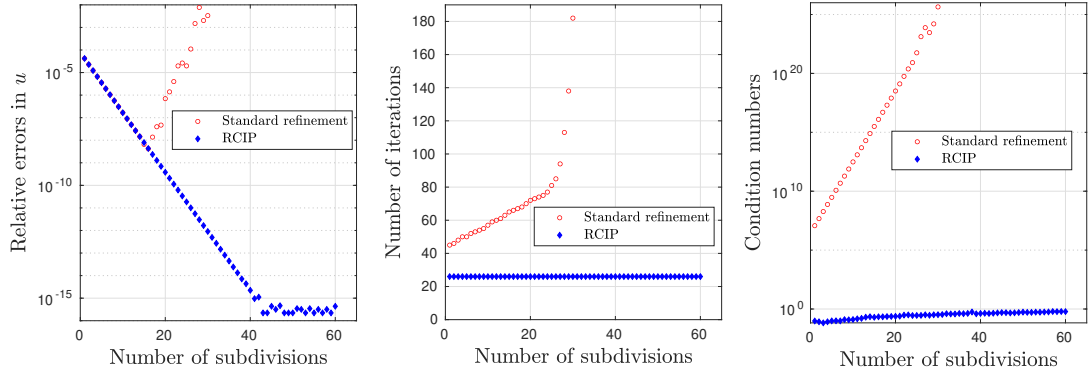
Figure 2.7 Comparisons between the standard refinement method and the RCIP method on relative errors in velocity values on the left, number of GMRES iterations in the middle, and condition numbers on the right. The red circle plots correspond to a standard refinement, and the blue filled plots the RCIP method. The horizontal axis indicates the number of refinements in both methods. The rectangular domain has its height 1, width 2, and the center at the origin. For all evaluations, the target point is set to $(x, y) = (0.5, 0.1)$.

Matrix scaling for the RCIP method. The matrix $\boldsymbol{B}_l$, in addition to being ill-conditioned, is poorly balanced. This leads to a severe loss of accuracy when computing the recursion relation (2.25). Following Helsing and Jiang [39], we employ a scaling technique to improve the stability of the construction of $\boldsymbol{R}$.

The reason $\boldsymbol{B}_l$ becomes more unbalanced as the grid refinement increases (i.e., l decreases) is due to the hypersingular kernel singularities when the target and source point are on different sides of a corner or boundary transition point. We explain the detailed mechanism of the instability. Consider a case in which two sections Γ_1 and Γ_2 of a b-type mesh with n_b total gridpoints meet at a corner. Suppose a Dirichlet condition is imposed on Γ_1 and Neumann condition on Γ_2 as shown in Figure 2.8.
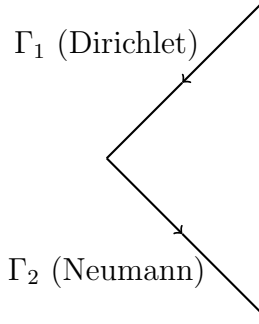
Figure 2.8 A schematic image of boundary transition around a corner at which the boundary condition switches from Dirichlet to Neumann. The first equation of the BIEs in (2.28) corresponds to Γ_1 and the second to Γ_2. The arrows show the direction of $\boldsymbol{x_i}$ for increasing index i.

The boundary conditions are described by the following two BIEs, which are solved on Γ_1 and Γ_2 respectively:

$$-\frac{1}{2}\boldsymbol{\rho}(\boldsymbol{x}) + \boldsymbol{D}_{\Gamma_1}[\boldsymbol{\rho}](\boldsymbol{x}) + \boldsymbol{S}_{\Gamma_2}[\boldsymbol{\rho}](\boldsymbol{x}) = \boldsymbol{u}(\boldsymbol{x}) \quad \boldsymbol{x} \in \Gamma_1,$$
$$\frac{1}{2}\boldsymbol{\rho}(\boldsymbol{x}) + \boldsymbol{D}'_{\Gamma_1}[\boldsymbol{\rho}](\boldsymbol{x}) + \boldsymbol{S}'_{\Gamma_2}[\boldsymbol{\rho}](\boldsymbol{x}) = \boldsymbol{f}(\boldsymbol{x}) \quad \boldsymbol{x} \in \Gamma_2 \tag{2.28}$$

The matrix-vector product $(\boldsymbol{B}_l)_{ij}\rho_j := (\boldsymbol{I}_{b,l} + \boldsymbol{K}_{b,l})_{ij}\rho_j$ is a discrete representation of the left hand sides of BIEs (2.28) on a b-type grid, where ρ_j refers to an array of density values. We assume the first n_b elements of ρ_j correspond to the first component of $\boldsymbol{\rho}$ or ρ_{1j}, and the second n_b elements to ρ_{2j}. It follows that $\boldsymbol{B}_l$ is a $2n_b \times 2n_b$ matrix which can be written as

$$\boldsymbol{B}_l = \boldsymbol{I} + \begin{bmatrix} -2\boldsymbol{D}_{11}^{(1)} & -2\boldsymbol{S}_{12}^{(1)} & -2\boldsymbol{D}_{11}^{(2)} & -2\boldsymbol{S}_{12}^{(2)} \\ 2\boldsymbol{D}_{11}'^{(1)} & 2\boldsymbol{S}_{12}'^{(1)} & 2\boldsymbol{D}_{11}'^{(2)} & 2\boldsymbol{S}_{12}'^{(2)} \\ -2\boldsymbol{D}_{21}^{(1)} & -2\boldsymbol{S}_{22}^{(1)} & -2\boldsymbol{D}_{21}^{(2)} & -2\boldsymbol{S}_{22}^{(2)} \\ 2\boldsymbol{D}_{21}'^{(1)} & 2\boldsymbol{S}_{22}'^{(1)} & 2\boldsymbol{D}_{21}'^{(2)} & 2\boldsymbol{S}_{22}'^{(2)} \end{bmatrix} = \begin{bmatrix} \boldsymbol{B}_{l,11} & \boldsymbol{B}_{l,12} & \boldsymbol{B}_{l,13} & \boldsymbol{B}_{l,14} \\ \boldsymbol{B}_{l,21} & \boldsymbol{B}_{l,22} & \boldsymbol{B}_{l,23} & \boldsymbol{B}_{l,24} \\ \boldsymbol{B}_{l,31} & \boldsymbol{B}_{l,32} & \boldsymbol{B}_{l,33} & \boldsymbol{B}_{l,34} \\ \boldsymbol{B}_{l,41} & \boldsymbol{B}_{l,42} & \boldsymbol{B}_{l,43} & \boldsymbol{B}_{l,44} \end{bmatrix}.$$
$$\tag{2.29}$$

where we have used $\boldsymbol{S}_{km}^{(n)}$, $\boldsymbol{D}_{km}^{(n)}$, etc. to denote $n_b/2 \times n_b/2$ block matrices from the discretization of the single and double layer potentials in (2.28) when the target is on Γ_k, the source is on Γ_m, and the integrand involves the nth component of $\boldsymbol{\rho}$, for $k, m, n \in \{1, 2\}$. The partitioning of $\boldsymbol{B}_l$ into a 4×4 block matrix thus follows naturally

from (1) our representation using single and double layer potentials, (2) the vector nature of $\boldsymbol{\rho}$, and (3) the two BIEs (2.28) describing mixed boundary conditions.

Figure 2.9 shows representative behavior of 2-norms of these blocks. We concentrate on $\boldsymbol{B}_{l,ij}$ for $i = 1, 2$ and $j = 1, 2$, since the other blocks behave similarly. We observe

- Diagonal blocks $\|\boldsymbol{B}_{l,11}\|$ and $\|\boldsymbol{B}_{l,22}\|$ are roughly independent of the refinement level,

- $\|\boldsymbol{B}_{l,12}\|$ roughly halves as the grid is refined by one level (i.e., l decreases by one),

- $\|\boldsymbol{B}_{l,21}\|$ roughly doubles as the grid is refined by one level.

The reason for this behavior is as follows. The kernel of the off-diagonal block $B_{l,21}$ in (2.29) scales like $O(1/r^2)$ around the corner and thus increases by a factor of 4 with grid refinement from level $l + 1$ to level l, while the element of arclength dS_y is simultaneously reduced by a factor of 2. Hence the magnitude of this block doubles at each grid refinement. The kernels of the diagonal blocks scale like $O(1/r)$, and when combined with the scaling of dS_y the magnitude of these blocks are roughly unchanged at each grid refinement. The kernel of $B_{l,12}$ scales like $\ln r$ and thus the magnitude of this block scales like $(1/2) \ln 2$ at each grid refinement.

On the other hand, if the boundary condition transitions from a Neumann condition on Γ_1 to a Dirichlet condition on Γ_2 the off-diagonal blocks behave oppositely, i.e., $\|\boldsymbol{B}_{l,21}\|$ roughly halves and $\|\boldsymbol{B}_{l,12}\|$ roughly doubles as the grid is refined. Figure 2.9 shows the norm ratios of block matrices $\|\boldsymbol{B}_{l,ij}\|/\|\boldsymbol{B}_{l+1,ij}\|(i, j \in \{1, 2\})$.
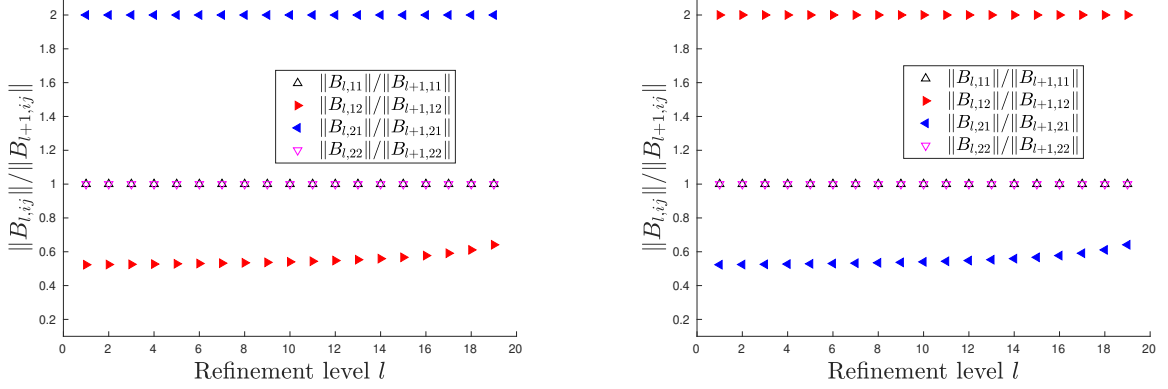
Figure 2.9 Plots of norm ratios $\|\boldsymbol{B}_{l,ij}\|/\|\boldsymbol{B}_{l+1,ij}\|$. The figures show cases of boundary transitions from Dirichlet to Neumann conditions on the left, and from Neumann to Dirichlet on the right.

We apply a scaling technique to remove the instability. The essential idea of the technique is described in Golub and Loan [30] and is similar to that used in Helsing and Jiang [39]. It uses a row-column equilibration to reduce the instability. For each refinement level l, we define the $2n_b \times 2n_b$ scaling matrix

$$\boldsymbol{S}_l := \begin{bmatrix} \boldsymbol{D}_l & O \\ O & \boldsymbol{D}_l \end{bmatrix} \tag{2.30}$$

where

$$\boldsymbol{D}_l := \begin{bmatrix} \boldsymbol{I} & O \\ O & s_l\boldsymbol{I} \end{bmatrix} \tag{2.31}$$

is an $n_b \times n_b$ diagonal block matrix with $\boldsymbol{I}$ an $n_b/2 \times n_b/2$ identity matrix. Here, $s_l = 2^{n_{sub}-l}$ if the first two row blocks correspond to a Dirichlet condition on Γ_1 and the second two row blocks to a Neumann condition on Γ_2. Alternatively, if the first two row blocks correspond to a Neumann condition on Γ_1 and the second two row blocks to a Dirichlet condition on Γ_2, s_l is set to $2^{-(n_{sub}-l)}$. Suppose now that we wish to solve the linear system $\boldsymbol{B}_l x = b$. Then to implement row-column equilibration, we instead solve $\left(\boldsymbol{D}_l^{-1}\boldsymbol{B}_l\boldsymbol{D}_l\right)y = \boldsymbol{D}_l^{-1}b$, and set $x = \boldsymbol{D}_l y$. It is easily verified that $\left(\boldsymbol{D}_l^{-1}\boldsymbol{B}_l\boldsymbol{D}_l\right)$ has no effect on the diagonal blocks of $\boldsymbol{B}_l$ but rescales the

off diagonal blocks so that their matrix norms are roughly independent of refinement level. Similarly, the inverse of $\boldsymbol{B}_l$ is computed as as

$$\boldsymbol{B}_l^{-1} = \boldsymbol{S}_l \left(\boldsymbol{S}_l^{-1} \boldsymbol{B}_l \boldsymbol{S}_l \right)^{-1} \boldsymbol{S}_l^{-1}. \tag{2.32}$$

Figure 2.10 gives examples in which the RCIP method is applied with and without scaling in three representative geometries with mixed Dirichlet-Neumann boundary conditions. The figure shows that the condition number of $\boldsymbol{R}$ increases rapidly without scaling, but remains roughly constant when the above technique is applied.

Construction of ρ_{fin} from $\tilde{\rho}_{coa}$.   Physical quantities in the interior of the domain Ω, such as the velocity $\boldsymbol{u}$ or stress $\boldsymbol{f}$, are computed in a post-processing step using the layer potential representations (2.3) and (2.4). Although we are able to carry out the evaluations to high accuracy in most of Ω using the coarse grid density $\tilde{\boldsymbol{\rho}}_{coa}$, loss of accuracy is observed at target points that are close to a corner or boundary transition point $\boldsymbol{s}$. This due to the evaluation of nearly singular kernels. The loss of accuracy is prevented by using the refined density $\boldsymbol{\rho}_{fin}$ to compute physical quantities in the bulk when the target point is near $\boldsymbol{s}$. An efficient method to reconstruct $\boldsymbol{\rho_{fin}}$ from $\tilde{\boldsymbol{\rho}}_{coa}$, which essentially involves running the recursion relation (2.25) backwards, is given in Helsing [37] (see also Helsing [36]). The computational cost of this technique is proportional to n_{sub} and the number of singular points n_s. The refined density $\boldsymbol{\rho}_{fin}$ is used only for a small fraction of the full function evaluations. Hence, the density reconstruction does not measurably affect the overall computational cost of the post-processing step.
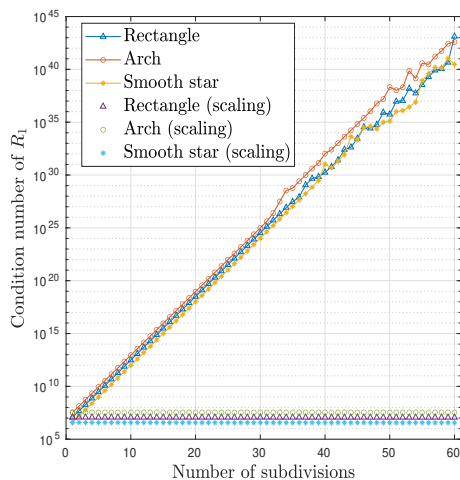
Figure 2.10 Effects of the scaling technique. The horizontal axis corresponds to the number of subdivision n_{sub} of the RCIP method, and the vertical axis corresponds to the condition number of R_1. Three geometries are used: smooth star, rectangle, and arch shown in Figure 2.2. With each geometry, two results are plotted. One is the case of the scaling applied, and the other is without scaling.

2.2.3 Kernel-split quadratures

Overview of the method Kernel-split quadrature is applied to accurately evaluate layer potentials when the target point is close to or on the boundary Γ. If the entire boundary is smooth and the layer potentials are compact operators, then the standard quadrature works well and can achieve high accuracy. In this work, however, the Stokes layer potentials have high-order kernel singularities which imply a loss of compactness. As a result, it is difficult to obtain high accuracy for close and on surface evaluations using the RCIP method alone. We address this difficulty by incorporating kernel-splitting into the RCIP method. Representative references on kernel-split quadrature are Helsing [37], Helsing and Jiang [39], Wu et al. [80], and Klinteberg et al. [51]. These provide details on the derivation and implementation of the method in various settings. We only summarize the main ideas, in particular relying on explicit formulae provided by We et al. [80], who describe the application of kernel splitting to the Stokes layer potentials. We refer the reader to [80] for more details.

The main task in the derivation of kernel-split quadrature is to rewrite the Stokes layer potentials S, D, S', and D' as well as the pressure layer potentials in terms of four canonical complex contour integrals. We first express the kernels of the integral operators in complex notation as

$$K(z_x, z_y) = \phi_0(z_y) + \phi_L(z_y) \log |z_y - z_x| + \frac{\phi_1(z_y)}{z_y - z_x} + \frac{\phi_2(z_y)}{(z_y - z_x)^2} + \frac{\phi_3(z_y)}{(z_y - z_x)^3}, \quad (2.33)$$

where $z_x = x_1 + ix_2$ and $z_y = y_1 + iy_2$ are complex variable representations of the target point $\boldsymbol{x} = (x_1, x_2)$ and the source point $\boldsymbol{y} = (y_1, y_2)$, and ϕ_L and ϕ_i $(i = 0, \cdots, 3)$ are smooth functions determined by the kernels in Equations (2.6)-(2.11). Then the layer potentials can be written in terms of the four fundamental complex contour integrals:

$$I_L[\tau](z_x) := \int_\Gamma \tau(z_y) \log |z_y - z_x| |dz_y|, \quad \text{(real logarithmic)} \quad (2.34)$$

$$I_C[\tau](z_x) := \int_\Gamma \frac{\tau(z_y)}{z_y - z_x} dz_y, \quad \text{(Cauchy)} \quad (2.35)$$

$$I_H[\tau](z_x) := \int_\Gamma \frac{\tau(z_y)}{(z_y - z_x)^2} dz_y, \quad \text{(hypersingular)} \quad (2.36)$$

$$I_S[\tau](z_x) := \int_\Gamma \frac{\tau(z_y)}{(z_y - z_x)^3} dz_y. \quad \text{(supersingular)} \quad (2.37)$$

Here $\tau(z_y)$ is a complex density function on Γ that involves products of the components of $\boldsymbol{\rho}$, ϕ_L, ϕ_i (i=1,...,3), and the outward pointing normal vector ν_y at $y \in \Gamma$ expressed as a complex number. The integrals in Equations (2.35) - (2.37) are interpreted in their principal value or Hadamard finite part sense.

The high accuracy of the method relies on panelwise polynomial approximation of $\tau(z_y)$ and analytical evaluation of the resulting weakly singular and singular integrals. Let Γ_{GL} be a Gauss-Legendre panel on Γ consisting of open arc in the complex plane with starting point on -1 and endpoint 1. A general arc can always be made to have this property by translation, rotation, and scaling. Assuming the (complex) density of the Stokes layer potentials is piecewise smooth on the boundary,

the discretized density is well approximated by panelwise polynomial approximation at Legendre nodes. In particular, we use $(n_{gl} - 1)$th order polynomial interpolation. The coefficients of the polynomial approximation are determined by the solution of a Vandermonde system. Substitution of the polynomial approximation for $\tau(z_y)$ into the complex integrals (2.34)-(2.37) (taking the integration over Γ_{GL}) followed by contour deformation of Γ_{GL} to $[-1, 1]$ then leads to integrals of the form

$$
\begin{aligned}
p_k &= \int_{-1}^{1} t^{k-1} \ln |t - z_x| \, dt, \\
q_k^{(m)} &= \int_{-1}^{1} \frac{t^{k-1}}{(t - z_x)^m} dt, \quad \mathrm{m} = 1, 2, 3,
\end{aligned}
\tag{2.38}
$$

where $k = 1, \ldots, n_{gl}$. There can also be a residue contribution in the case of Cauchy integrals if z_x lies between the arc Γ_{GL} and the real line between $[-1, 1]$. The integrals in Equations (2.38) are analytically evaluated using a recursion. The method gives accurate results when z_x is either on the boundary or close to it. More details are provided in Helsing [37], Wu et al. [80].

Expressions giving the Stokes layer potentials in terms of the complex contour integrals (2.34)-(2.37) are derived in Wu et al. [80]. Here we present the expressions without derivation, and refer the reader to [80] for details. We introduce the complex notation $z = (y_1 - x_1) + (y_2 - x_2)i$, $\nu = n_1 + in_2$ where $\boldsymbol{n} = (n_1, n_2)$ is the outward unit normal to Γ, ν_x and ν_y are the outward normals evaluated at z_x and z_y, and $\tau = \rho_1 + i\rho_2$ with $\boldsymbol{\rho} = (\rho_1, \rho_2)$. The single layer potential $\boldsymbol{S}$ can be written as

$$
\boldsymbol{S}[\tau](z_x) = -\frac{1}{4\pi\mu} \begin{bmatrix} I_L[\mathrm{Re}\,\{\tau\}] \\ I_L[\mathrm{Im}\,\{\tau\}] \end{bmatrix} + \frac{1}{4\pi\mu} \left[\begin{bmatrix} \mathrm{Im}\,\{I_C[\overline{\nu_y} \cdot]\} \\ \mathrm{Re}\,\{I_C[\overline{\nu_y} \cdot]\} \end{bmatrix} \otimes \begin{bmatrix} \mathrm{Re}\,\{z\} \\ \mathrm{Im}\,\{z\} \end{bmatrix} \right] \begin{bmatrix} \mathrm{Re}\,\{\tau\} \\ \mathrm{Im}\,\{\tau\} \end{bmatrix}.
\tag{2.39}
$$

where we use the tensor product notation $\boldsymbol{a} \otimes \boldsymbol{b} = a_i b_j$. In this representation, the Stokes single-layer potential involves both weakly singular and singular contour

integrals. Similarly, the Stokes double layer potential $\boldsymbol{D}$ can be written as

$$\boldsymbol{D}[\tau](z_x) = -\frac{1}{2\pi}\mathrm{Im}\begin{bmatrix} I_C\left[\frac{\mathrm{Re}\{\nu_y\}}{\nu_y}\tau\right] \\ I_C\left[\frac{\mathrm{Im}\{\nu_y\}}{\nu_y}\tau\right] \end{bmatrix} + \frac{1}{2\pi}\begin{bmatrix} \mathrm{Re}\{I_H[\cdot]\} \\ \mathrm{Im}\{I_H[\cdot]\} \end{bmatrix} \otimes \begin{bmatrix} \mathrm{Re}\{z\} \\ \mathrm{Im}\{z\} \end{bmatrix}\begin{bmatrix} \mathrm{Re}\{\tau\} \\ \mathrm{Im}\{\tau\} \end{bmatrix}.$$

(2.40)

This representation involves singular and hypersingular contour integrals. Other Stokes layer potentials $\boldsymbol{S}'$, $\boldsymbol{D}'$, S^p, and D^p are written as follows:

$$\boldsymbol{S}'[\tau](z_x) = \frac{1}{2\pi}\mathrm{Im}\{I_C[\nu_x\overline{\nu_y}\cdot]\}\begin{bmatrix} \mathrm{Re}\{\tau\} \\ \mathrm{Im}\{\tau\} \end{bmatrix}$$

$$+ \frac{1}{2\pi}\begin{bmatrix} \mathrm{Im}\{I_H[\mathrm{Re}\{z\overline{\nu_x}\}\,\overline{\nu_y}\cdot]\} & \mathrm{Re}\{I_H[\mathrm{Re}\{z\overline{\nu_x}\}\,\overline{\nu_y}\cdot]\} \\ \mathrm{Re}\{I_H[\mathrm{Re}\{z\overline{\nu_x}\}\,\overline{\nu_y}\cdot]\} & -\mathrm{Im}\{I_H[\mathrm{Re}\{z\overline{\nu_x}\}\,\overline{\nu_y}\cdot]\} \end{bmatrix}\begin{bmatrix} \mathrm{Re}\{\tau\} \\ \mathrm{Im}\{\tau\} \end{bmatrix},$$

(2.41)

$$\frac{\pi}{\mu}\boldsymbol{D}'[\tau](z_x) = -\frac{1}{2}\mathrm{Re}\{\nu_x\overline{\nu_y}\}\,\overline{\nu_y}\begin{bmatrix} \mathrm{Im}\{I_H[\cdot]\} & \mathrm{Re}\{I_H[\cdot]\} \\ \mathrm{Re}\{I_H[\cdot]\} & -\mathrm{Im}\{I_H[\cdot]\} \end{bmatrix}\begin{bmatrix} \mathrm{Re}\{\tau\} \\ \mathrm{Im}\{\tau\} \end{bmatrix}$$

$$+ \frac{1}{2}\nu_x\overline{\nu_y}\left[\boldsymbol{n}_y \otimes \begin{bmatrix} \mathrm{Im}\{I_H[\cdot]\} \\ \mathrm{Re}\{I_H[\cdot]\} \end{bmatrix}\right]\begin{bmatrix} \mathrm{Re}\{\tau\} \\ \mathrm{Im}\{\tau\} \end{bmatrix}$$

$$+ \frac{1}{2}\begin{bmatrix} 0 & 1 \\ 1 & 0 \end{bmatrix}\left[\boldsymbol{n}_x \otimes \begin{bmatrix} \mathrm{Re}\{I_H[\cdot]\} \\ \mathrm{Im}\{I_H[\cdot]\} \end{bmatrix}\right]\begin{bmatrix} \mathrm{Re}\{\tau\} \\ \mathrm{Im}\{\tau\} \end{bmatrix} - \left[\boldsymbol{n}_x \otimes \begin{bmatrix} \mathrm{Im}\{I_H[\cdot]\} \\ \mathrm{Re}\{I_H[\cdot]\} \end{bmatrix}\right]\begin{bmatrix} \mathrm{Re}\{\tau\} \\ \mathrm{Im}\{\tau\} \end{bmatrix}$$

$$+ \left(\boldsymbol{n}_x \cdot \begin{bmatrix} \mathrm{Im}\{I_H[\cdot]\} \\ \mathrm{Re}\{I_H[\cdot]\} \end{bmatrix}\right)\begin{bmatrix} \mathrm{Re}\{\tau\} \\ \mathrm{Im}\{\tau\} \end{bmatrix} + 2\left[\begin{bmatrix} n_{x2} & n_{x1} \\ n_{x1} & n_{x2} \end{bmatrix}\begin{bmatrix} \mathrm{Re}\{I_S[\cdot]\} \\ \mathrm{Im}\{I_S[\cdot]\} \end{bmatrix} \otimes \boldsymbol{r}\right]\begin{bmatrix} \mathrm{Re}\{\tau\} \\ \mathrm{Im}\{\tau\} \end{bmatrix},$$

(2.42)

$$S^p[\tau](z_x) = -\frac{1}{2\pi}\begin{bmatrix} \mathrm{Im}\left\{I_C\left[\frac{\cdot}{\nu_y}\right]\right\} \\ \mathrm{Re}\left\{I_C\left[\frac{\cdot}{\nu_y}\right]\right\} \end{bmatrix} \cdot \begin{bmatrix} \mathrm{Re}\{\tau\} \\ \mathrm{Im}\{\tau\} \end{bmatrix},$$

(2.43)

$$D^p[\tau](z_x) = \frac{\mu}{\pi}\begin{bmatrix} \mathrm{Im}\{I_H[\cdot]\} \\ \mathrm{Re}\{I_H[\cdot]\} \end{bmatrix} \cdot \begin{bmatrix} \mathrm{Re}\{\tau\} \\ \mathrm{Im}\{\tau\} \end{bmatrix}.$$

(2.44)

Note that the representation in Equation (2.42) involves a supersingular contour integral.

2.2.4 Categorization of quadrature evaluations

The three options available for layer potential evaluation are (1) kernel-split quadrature on fine grid panels Γ_{fin}, (2) kernel-split quadrature on coarse grid panels Γ_{coa}, and (3) standard composite Gauss-Legendre quadrature on the coarse grid Γ_{coa}. We maximize efficiency while maintaining accuracy by choosing the quadrature type based on both the distance of the target point z_t from the interface Γ as well as its separation from a boundary transition point $\boldsymbol{s}$. When the target point is close to $\boldsymbol{s}$, the largest contribution to the layer potentials comes from source points near $\boldsymbol{s}$ where the Green's function has a maximum. Since layer densities have complicated (nonpolynomial-like) asymptotics near boundary transition points which require refined meshes to resolve, we use quadrature option (1) for this case. More precisely, if $d(z_t, \Gamma)/L_{fin} < 3.0$ where L_{fin} is the length of the panel on Γ_{fin} closest to z_t and $d(\cdot, \cdot)$ is the minimum distance function, then z_t is grouped in the first category. If the above condition is false but $d(z_t, \Gamma)/L_{coa} < 0.6$ where L_{coa} is the length of the coarse panel on Γ_{coa} that is closest to z_t, then z_t is placed in the second category. The remaining points are put into the third category for evaluation with standard composite Gauss-Legendre quadrature on the coarse grid. We determine the thresholds of 0.6 and 3.0 that are used in the above conditions via numerical experiments in representative geometries.

2.2.5 The Stokes Fast Multipole Method (FMM)

The solution of the linear system (2.23) using GMRES as well as evaluation of velocities, pressure, and traction forces in $\overline{\Omega}$ involve matrix-vector products in which the matrices are composed of the discretized kernels of the Stokes layer potentials

and associated quadrature weights. A naive implementation of these matrix-vector products would give a complexity of $O(N_{coa}^2)$ for layer potential evaluations on Γ and $O(n_{it}N_{coa}^2)$ to solve the linear system (2.23), where n_{it} is the number of GMRES iterations and we recall that N_{coa} is the number of gridpoints in the discretization of Γ in the coarsest grid level. We note that the use of refined grids in the RCIP computation at target points that are close to a corner or boundary transition point involve an inappreciable operation count and does not affect the overall complexity of the algorithm. Similarly, the complexity of the area evaluation of velocities, pressure, and traction forces in $\overline{\Omega}$ at M_t target points scales quadratically as $O(M_t N_{coa})$. One additional difficulty is that the size of the matrix in the linear system for solving (2.23) increases as the number of discretized Gauss-Legendre nodes on the boundary grows. Indeed, the memory allocation for constructing the matrix could exceed a typical laptop computer's capacity in some large-scale problems.

We significantly reduce the complexity of layer potential evaluations on Γ to linear scaling $O(N_{coa})$ (so that the GMRES solve takes $O(n_{it}N_{coa})$ operations) and evaluations of velocities, etc. in $\overline{\Omega}$ to $O(M_t + N_{coa})$ by incorporating a Stokes FMM. The use of the Stokes FMM combined with GMRES also helps reduce memory requirements and avoids out-of-memory issues. We use the Fortran library FMM2D written by Leslie Greengard and Manas Rachh, which is specifically tailored to 2D geometries.

2.2.6 Superhydrophobic flow

The discussion up to now has concentrated on the boundary value problem for mixed Dirichlet-Neumann data. We now consider the more complicated boundary conditions for SH flow.

Theoretical and numerical studies of liquid flow about superhydrophobic surfaces tend to concentrate on two geometries. These are (1) externally imposed

shear flow over a single SH surface, as depicted in Figure 2.11, and (2) pressure driven flow within a superhydrophobic channel, illustrated in Figures 2.12 and 2.13. The SH boundary is modeled as a microstructured surface that is patterned with a collection of grooves or air pockets, such that when a fluid of viscosity μ flows over it, a stable Cassie state is attained in which a gas bubble is trapped in each groove. The SH boundary therefore consists of an alternating array of liquid-gas interfaces (bubbles) and liquid-solid interfaces (solid ridges which separate the bubbles). The gas bubble is taken to be a passive fluid with a spatially constant pressure, and hence in the absence of surface contaminants the gas-liquid meniscus is shear-stress free.

A common assumption in studies of SH flow is that the capillary number is small, $Ca = \mu U/\sigma \ll 1$. Here U is a characteristic flow velocity and σ is the surface tension coefficient. The smallness of the capillary number implies that the bubble or groove meniscus is essentially a static circular cap with constant curvature κ. We shall employ this constant curvature assumption in our model, which replaces the usual normal stress boiudnary condition at the bubble interface.

Denote the collection of liquid-gas interfaces by Γ_C, no-slip solid and other boundaries in which a velocity Dirichlet condition is imposed by Γ_D, and surfaces in which a pressure boundary condition is given by Γ_P. The governing equations for our model consist of the incompressible Stokes equations (2.1) in Ω, along with boundary conditions

$$\boldsymbol{u} \cdot \boldsymbol{n} = 0, \quad \boldsymbol{t} \cdot \boldsymbol{\sigma} \boldsymbol{n} = 0 \quad \text{on } \Gamma_C, \tag{2.45}$$

$$\boldsymbol{u} = \boldsymbol{g}(\boldsymbol{x}) \quad \text{on } \Gamma_D, \tag{2.46}$$

$$p = h(\boldsymbol{x}) \quad \text{on } \Gamma_P, \tag{2.47}$$

where $\boldsymbol{t}$ and $\boldsymbol{n}$ are the surface tangent and normal (directed outward from the fluid domain), respectively. The first equation is a composite or hybrid Dirichlet-Neumann condition that enforces zero normal velocity and shear stress at the meniscus. The

second equation is a Dirichlet condition which represents the no-slip condition $\boldsymbol{u} = 0$ on solid interfaces and prescribed velocity on some surfaces of the outer (enclosing) boundary. The third equation represents a pressure condition which is prescribed on inlets/outlets in pressure driven flow within a superhydrophobic channel. The discussion below concentrates on the case in which there are liquid-gas interfaces Γ_c and boundaries Γ_D with a prescribed velocity. Modifications for pressure pressure driven flow are straight forward.

We employ a linear combination of the single- and double-layer potentials $\boldsymbol{S}_{\Gamma_C}$ and $\boldsymbol{D}_{\Gamma_C}$ to represent the fluid velocity perturbations in Ω that are induced by the presence of the boundary Γ_C, where the composite boundary condition is enforced. We use the traction single- and double-layer potential $\boldsymbol{D}'_{\Gamma_C}$ and $\boldsymbol{S}'_{\Gamma_C}$ to represent the force pertubations induced by Γ_C. The layer potential representations associated with the Dirichlet boundary condition on Γ_D are given by Equations (2.3) and (2.4). Combining these representations, we obtain the following layer potential characterization of the velocity and traction generated by the presence of the boundaries in our superhydrophobic flow problem:

$$\boldsymbol{u}(\boldsymbol{x}) = \boldsymbol{D}_{\Gamma_D}[\boldsymbol{\rho}](\boldsymbol{x}) + \boldsymbol{S}_{\Gamma_C}[\boldsymbol{\rho}](\boldsymbol{x}) + \boldsymbol{D}_{\Gamma_C}[\boldsymbol{\rho}](\boldsymbol{x}), \qquad (2.48)$$

$$\boldsymbol{f}(\boldsymbol{x}) = \boldsymbol{D}'_{\Gamma_D}[\boldsymbol{\rho}](\boldsymbol{x}) + \boldsymbol{S}'_{\Gamma_C}[\boldsymbol{\rho}](\boldsymbol{x}) + \boldsymbol{D}'_{\Gamma_C}[\boldsymbol{\rho}](\boldsymbol{x}), \qquad (2.49)$$

for $\boldsymbol{x} \in \Omega$. Compared with the previous formulation (Equations (2.3) and (2.4)) for the mixed Dirichlet-Neumann boundary value problem, there is an additional $\boldsymbol{D}_{\Gamma_C}[\boldsymbol{\rho}](\boldsymbol{x})$ and $\boldsymbol{D}'_{\Gamma_C}[\boldsymbol{\rho}](\boldsymbol{x})$ to account for the composite boundary condition on Γ_C. Jump conditions for the Dirichlet boundary condition on Γ_D induce the standard vector BIEs

$$-\frac{1}{2}\boldsymbol{\rho}(\boldsymbol{x}) + \boldsymbol{D}_{\Gamma_D}[\boldsymbol{\rho}](\boldsymbol{x}) + \boldsymbol{S}_{\Gamma_C}[\boldsymbol{\rho}](\boldsymbol{x}) + \boldsymbol{D}_{\Gamma_C}[\boldsymbol{\rho}](\boldsymbol{x}) = \boldsymbol{u} \quad \boldsymbol{x} \in \Gamma_D. \qquad (2.50)$$

On the other hand, we obtain two modified scalar BIEs for the jump conditions on Γ_C

$$\boldsymbol{n_x} \cdot \left(-\frac{1}{2}\boldsymbol{\rho}(\boldsymbol{x}) + \boldsymbol{D}_{\Gamma_D}[\boldsymbol{\rho}](\boldsymbol{x}) + \boldsymbol{S}_{\Gamma_C}[\boldsymbol{\rho}](\boldsymbol{x}) + \boldsymbol{D}_{\Gamma_C}[\boldsymbol{\rho}](\boldsymbol{x}) \right) = 0 \quad \boldsymbol{x} \in \Gamma_C, \qquad (2.51)$$

$$\boldsymbol{t_x} \cdot \left(\frac{1}{2}\boldsymbol{\rho}(\boldsymbol{x}) + \boldsymbol{D}'_{\Gamma_D}[\boldsymbol{\rho}](\boldsymbol{x}) + \boldsymbol{S}'_{\Gamma_C}[\boldsymbol{\rho}](\boldsymbol{x}) + \boldsymbol{D}'_{\Gamma_C}[\boldsymbol{\rho}](\boldsymbol{x}) \right) = 0 \quad \boldsymbol{x} \in \Gamma_C, \qquad (2.52)$$

where $\boldsymbol{n_x}$ and $\boldsymbol{t_x}$ are the outward normal and tangential unit vectors at $\boldsymbol{x}$, respectively.

As it stands, the two scalar BIEs (2.51) and (2.52) are not in a form that is consistent with the RCIP method, which requires discretization of the Equation (2.19), that is, consisting of the sum of an identity operator and a discrete integral operator. Thus, we must convert our boundary value problem into one of the proper form. This is done by multiplying the scalar equations (2.51) and (2.52) by the vectors $-2\boldsymbol{n_x}$ and $2\boldsymbol{t_x}$, respectively, then adding. It is easily verified that this gives an equation of the required type. Next, let $\boldsymbol{M} = (M_{i,j})_{i,j\in\{1,2\}}$ and $\boldsymbol{M}' = (M'_{i,j})_{i,j\in\{1,2\}}$ be block matrices obtained by discretizing two integral operators

$$-2\left(\boldsymbol{D}_{\Gamma_D} + \boldsymbol{D}_{\Gamma_C} + \boldsymbol{S}_{\Gamma_C} \right) \qquad (2.53)$$

and

$$2\left(\boldsymbol{D}'_{\Gamma_D} + \boldsymbol{D}'_{\Gamma_C} + \boldsymbol{S}'_{\Gamma_C} \right), \qquad (2.54)$$

respectively. Also, let $\boldsymbol{\Lambda}_{n1} = \mathrm{diag}(n_{x1})$ and $\boldsymbol{\Lambda}_{n2} = \mathrm{diag}(n_{x2})$ be diagonal matrices where n_{x1} and n_{x2} are the first and second components of $\boldsymbol{n_x}$, respectively; and let $\boldsymbol{\Lambda}_{t1} = \mathrm{diag}(t_{x1})$ and $\boldsymbol{\Lambda}_{t2} = \mathrm{diag}(t_{x2})$ be another set of diagonal matrices defined using the unit tangent vector. Then, construct the discrete matrix operators $\boldsymbol{K_1}$ and $\boldsymbol{K'_1}$

as

$$
K_1 = \begin{bmatrix} \Lambda_{n1}^2 M_{11} & \Lambda_{n1}^2 M_{12} \\ \Lambda_{n1}\Lambda^{n2} M_{11} & \Lambda_{n1}\Lambda_{n2} M_{12} \end{bmatrix} + \begin{bmatrix} \Lambda_{n1}\Lambda_{n2} M_{21} & \Lambda_{n1}\Lambda_{n2} M_{22} \\ \Lambda_{n2}^2 M_{21} & \Lambda_{n1}\Lambda_{n2} M_{12} \end{bmatrix} , \qquad (2.55)
$$

$$
K_1' = \begin{bmatrix} \Lambda_{t1}^2 M_{11}' & \Lambda_{t1}^2 M_{12}' \\ \Lambda_{t1}\Lambda_{t2} M_{11}' & \Lambda_{t1}\Lambda_{t2} M_{12}' \end{bmatrix} + \begin{bmatrix} \Lambda_{t1}\Lambda_{t2} M_{21}' & \Lambda_{t1}\Lambda_{t2} M_{22}' \\ \Lambda_{t2}^2 M_{21}' & \Lambda_{t1}\Lambda_{t2} M_{12}' \end{bmatrix} . \qquad (2.56)
$$

It is shown in appendix A.3 that the linear system corresponding to Equations (2.51) and (2.52) can be discretized as

$$
(I + K_1 + K_1') \rho_1 = 0 \qquad (2.57)
$$

which is the desired form that is compatible with the RCIP method.

2.2.7 Computation of effective and intrinsic slip length

Computing the effective slip length is an important subject as a practical application to fluid dynamics simulations. The effective slip length denoted by λ hereafter is defined as the distance underneath the bottom where the extrapolated horizontal velocity becomes zero. Some SH flow problems with mixed boundary conditions are discussed and the exact solutions are given as the stream function in Philip [68]. Recent studies of analytical and numerical methods to compute λ can be seen in some literature such as Davis and Lauga [22] and Teo and Khoo [77]. The mixed boundary conditions imposed on meniscus interfaces can be interpreted as composite boundary conditions described in the previous section. We present some methods to numerically compute λ for problems that have been discussed in preexisting literature and one with a slightly different setting.

Shear flow over a plate with meniscus interfaces Here, we focus on the problem in section 11 of Philip [68]. In the original problem, shear flow passes through in the horizontal direction over entirely flat and periodic compositions of solid plates

and meniscus interfaces at the bottom. Rigorously, the domain of the original problem is semi-infinite because the upper side is open. We close the open upper side of the domain at a finite positive height H with the horizontal line segment far enough from the bottom to obtain the finite computational domain. Since the problem is periodic we also restrict the computational domain to one period or a finite number of periods in the horizontal direction shown as Figure 2.11.
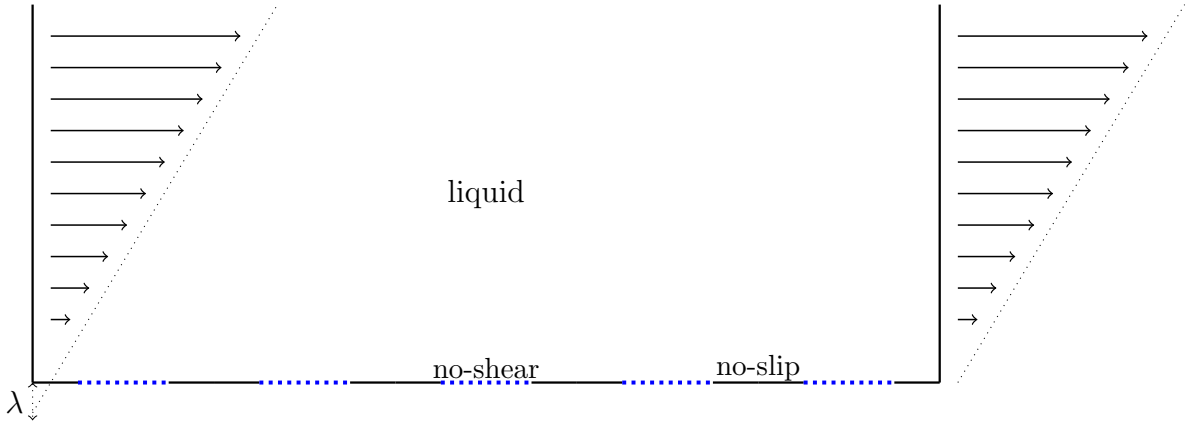
Figure 2.11 Superhydrophobic flow over periodic plates and menisci in the same situation as section 11 in Philip [68] except for the artificial ceiling.

Assuming H is large enough, λ in the domain satisfies the equation of the velocity $\boldsymbol{u} = (u_1, u_2)$

$$\boldsymbol{u} = (u_1, u_2) \simeq (\dot{\gamma}(x_2 + \lambda), 0) \tag{2.58}$$

which implies that $\dot{\gamma} \simeq \frac{\partial u_1}{\partial x_2}$, $\frac{\partial u_1}{\partial x_1} \simeq 0$, and $u_2 \simeq 0$. Then we apply the above approximation (2.58) to the stress tensor $\boldsymbol{\sigma} = (\sigma_{ij})_{1 \leq i,j \leq 2} = -P\delta_{ij} + \mu \left(\frac{\partial u_i}{\partial x_j} + \frac{\partial u_j}{\partial x_i} \right)$ on the ceiling.

$$\boldsymbol{\sigma} \simeq \begin{bmatrix} -P & \frac{\partial u_1}{\partial x_2} \\ \mu \frac{\partial u_1}{\partial x_2} & -P \end{bmatrix}. \tag{2.59}$$

Thus, noting the unit normal vector on the ceiling is $\boldsymbol{n} = (0,1)$, the surface force is

$$\boldsymbol{f} = \begin{bmatrix} f_1 \\ f_2 \end{bmatrix} = \boldsymbol{\sigma}\boldsymbol{n} \simeq \begin{bmatrix} \mu\frac{\partial u_1}{\partial x_2} \\ -P \end{bmatrix}. \tag{2.60}$$

$$\therefore \frac{\partial u_1}{\partial x_2} \simeq \frac{1}{\mu}f_1. \tag{2.61}$$

Since $\dot{\gamma}$ is not necessarily constant in the restricted finite domain in general, we compute an approximated $\dot{\gamma}$ as the averaged value over one horizontal period L

$$\dot{\gamma} \simeq \frac{1}{L}\left[\int_{x=0}^{L} \frac{\partial u_1}{\partial x_2}(x, H)dx\right] = \frac{1}{\mu L}\int_{x=0}^{L} f_1(x, H)dx. \tag{2.62}$$

f_1 can be numerically computed with the BIE method and the above approximation leads to

$$\lambda \simeq \frac{\mu L u_1}{\int_{x=0}^{L} f_1(x, H)dx} - H \tag{2.63}$$

The imposed boundary conditions on the ceiling and the vertical sides can be Dirichlet condition since the exact solution is available as derived in Philip [68]. As for the boundary conditions at the bottom, Dirichlet condition on the flat plates and the composite conditions on meniscus interfaces are imposed. The method with the approximation above to compute λ is validated in the numerical example in the later section.

Poiseuile channel flow Here we introduce another approach to compute λ for problems with genuinely bounded domains in the vertical direction. The problems discussed here can be regarded as flow through some channel structure. The structure of periodic plates and meniscus interfaces can be placed not only at the bottom but also on the top boundary here. In the case of the flat structure on the ceiling, the boundary condition is Dirichlet with zero velocity (Figure 2.12). If we set the symmetric structure on the ceiling and the bottom, the composite boundary

conditions are imposed on both parts (Figure 2.13). Also, we impose another combination of composite boundary conditions on both vertical sides: zero velocity in the vertical direction and pressure.
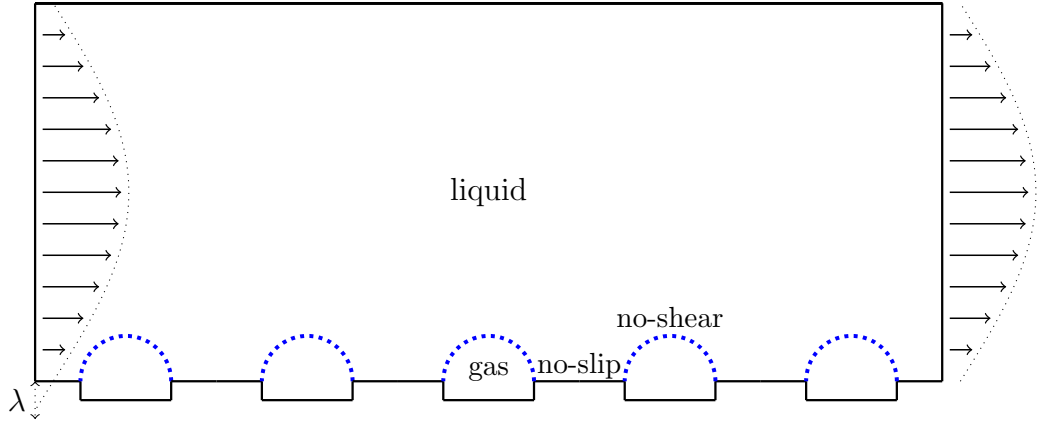
Figure 2.12 Superhydrophobic flow over periodic plates and menisci with 90 degrees of protrusion angles. The protrusion angle is defined as the angle between the meniscus tangent and horizontal line.

Since the computational domain is bounded, we use another formulation on λ defined at the bottom

$$u_1 = \dot{\gamma}\lambda = \frac{\partial u_1}{\partial x_2}\lambda \qquad (2.64)$$

whereas the previous approximation (2.58) is valid at large enough height x_2 for the semi-infinite domain.

Here we take another approach compared with the previous problem. We determine λ of Poiseuile channel flow with the numerical results of the boundary value problems discussed above. In the case of a flat ceiling, $u_1(H) = 0$, and assuming the velocity can be written in the following form

$$u_1(x_2) = \frac{1}{2}Ax_2^2 + Bx_2 + C \qquad (2.65)$$

where A, B, and C are some constants eliminated or determined below. The boundary conditions are

$$u(H) = \frac{1}{2}AH^2 + BH + C = 0, \tag{2.66}$$

$$u(0) = C = \lambda \frac{\partial u_1}{\partial x_2}. \tag{2.67}$$

Noting $\frac{\partial u_1}{\partial x_2}(x_2) = Ax_2 + B$, we eliminate $B = -\frac{AH^2}{2(\lambda+H)}$ and $C = \lambda B$ and $u_1(x_2)$ and rewrite $u_1(x_2)$ only with A, H, and λ as follows:

$$\frac{A}{2}\left(x_2^2 - H^2\frac{x_2 + \lambda}{H + \lambda}\right). \tag{2.68}$$

A direct calculation of the flux $F := \int_0^H u_1(x_2)dx_2$ leads to

$$F = -\frac{AH^3(H + 4\lambda)}{12(H + \lambda)} \Leftrightarrow \lambda = -\frac{H(AH^3 - 12F)}{4(AH^3 + 3F)}. \tag{2.69}$$

λ can be numerically determined by computing F with the BIE method and composite boundary conditions imposed.

In case we set the plates and meniscus boundary on the ceiling the same way as the bottom, we can derive a similar formula for λ taking the symmetry in the vertical direction into account.
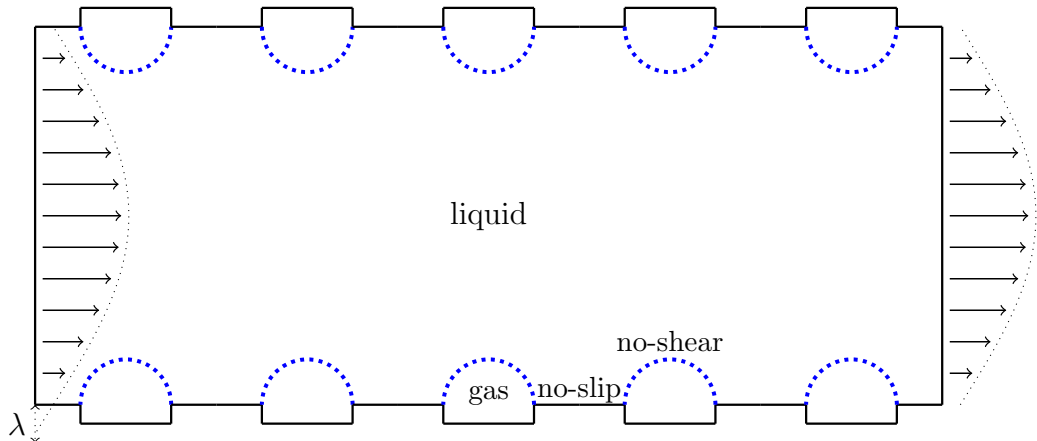
Figure 2.13 Superhydrophobic flow through a symmetric channel composed of periodic plates and menisci with 90 degrees of protrusion angles.

2.3 Numerical Examples

In this section, we demonstrate the performance of the numerical method with some numerical experiments. The code implementation is in MATLAB release 2020a, and the Stokes FMM library developed in Fortran by Leslie Greengard and Manas Rachh is also used via MEX API. We carried out the numerical experiments on a 64-bit laptop with 3 GHz dual-core Intel Core i7 and the memory size is 16 GB. The OS of the laptop is MacOS Catalina (Version 10.15.7).

The following parameters are commonly used in the numerical experiments unless mentioned otherwise. The viscosity is taken as $\mu = 1$, the deepest level of refinement for the RCIP method is $n_{sub} = 40$, and the residual threshold to stop GMRES iterations eps = 2.2204e-16 set by MATLAB.

2.3.1 Validation

We first illustrate the accuracy of our numerical method in evaluating the velocities, forces (cf. Equation (2.4)), and pressure for interior flow with mixed boundary conditions in three types of domains: a smooth star-shaped domain, a rectangular domain, and an arch-shaped domain.

The boundary of the star-shaped domain contains two boundary transition points, at locations shown in Figure 2.2. Dirichlet boundary condition on the dashed line on the lower left part and Neumann condition on the remaining part. The rectangular domain contains four corners and alternating boundary conditions, i.e., Dirichlet condition on the top and bottom, and Neumann condition on the left and right sides. The arch-shaped domain contains two boundary transition points at two bottom corners, and we impose a Dirichlet boundary condition on the bottom and Neumann condition on the remaining arch-shaped curve. The computational domains of these examples are shown in Figure 2.2.

Quantities (e.g., velocity) are evaluated at interior target points on a lattice of 300×300 equispaced points. To generate flow, we put $20,000$ point forces outside the boundary to generate artificial (i.e., synthetic) boundary data. The exact solution inside a given domain and the boundary data are available via exact formulas for the velocity, pressure, and stress induced by stokeslet or stresslet point forces. We apply our numerical method to compute the desired quantities inside the domain from the boundary data, and compare the results with the exact solutions. The force $\boldsymbol{f} = \boldsymbol{\sigma n}$ is evaluated using Equation (2.4) with the direction of the normal vector $\boldsymbol{n}$ at the target chosen randomly. The pointwise absolute errors of velocities, forces, and pressure are plotted in Figures 2.14, 2.15, and 2.16. Evaluations at $23,814$ interior target points for the star-shape case are categorized as follows: close-evaluations with the refined density $\boldsymbol{\rho}_{\text{fin}}$ are activated at 115 points, close-evaluations without the refined density at $1,360$ points, and normal evaluations at the rest of $22,339$ points. The boundary is discretized $N_{coa} = 3,840$ points, and is surrounded by a square lattice with its both height and width equal to 3.5. The minimum distance between the evaluation points inside and the boundary is 5.208e-04. In the case of the rectangular boundary, evaluations at $29,651$ interior target points in total are categorized as follows: close-evaluations with the refined density are activated at 267 points, close-evaluations without the refined density at $1,600$ points, and normal evaluations at the rest of $27,794$ points. The boundary is discretized $N_{coa} = 2,880$ points, and is surrounded by a square lattice with its height 2 and width 3. The minimum distance between the evaluation points inside and the boundary is 3.67e-03. In the case of the arch boundary, evaluations at $14,164$ interior target points in total are categorized as follows: close-evaluations with the refined density are activated at 69 points, close-evaluations without the refined density at 624 points, and normal evaluations at the rest of $13,471$ points. The method in this work achieves at least 9-10 digits of accuracy for all evaluations of velocities, surface forces, and pressure.

The boundary is discretized $N_{coa} = 3,168$ points, and is surrounded by a square lattice with its both height and width equal to 2. The minimum distance between the evaluation points inside and the boundary is 3.465e-04.
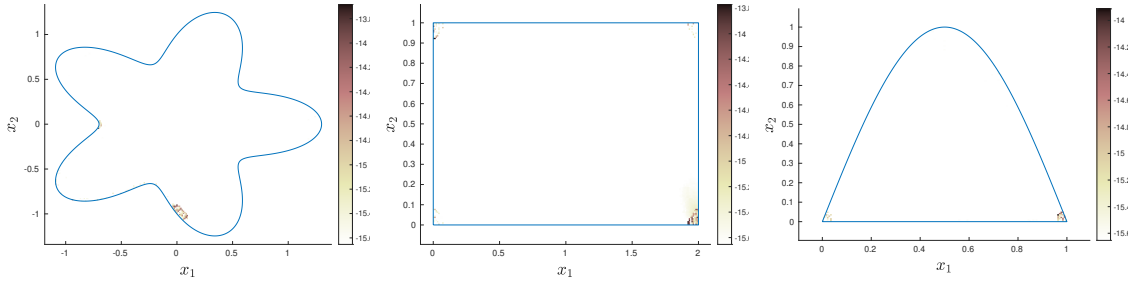
Figure 2.14 Pointwise error of computed velocity field inside of a smooth star-shape, a rectangular domain, and an arch-shaped domain.
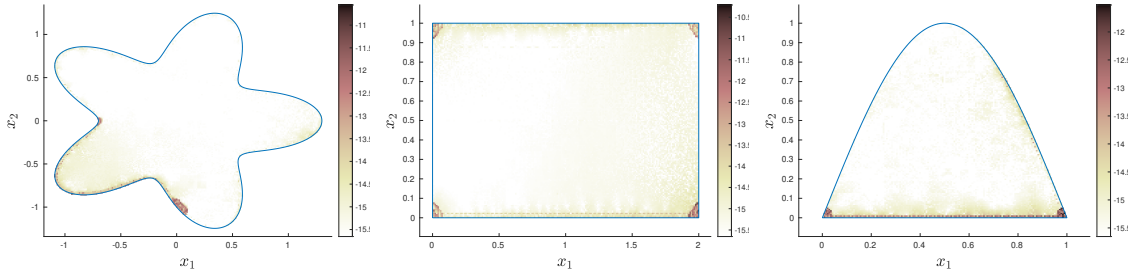
Figure 2.15 Pointwise error of computed force field inside of a smooth star-shape, a rectangular domain, and an arch-shaped domain.
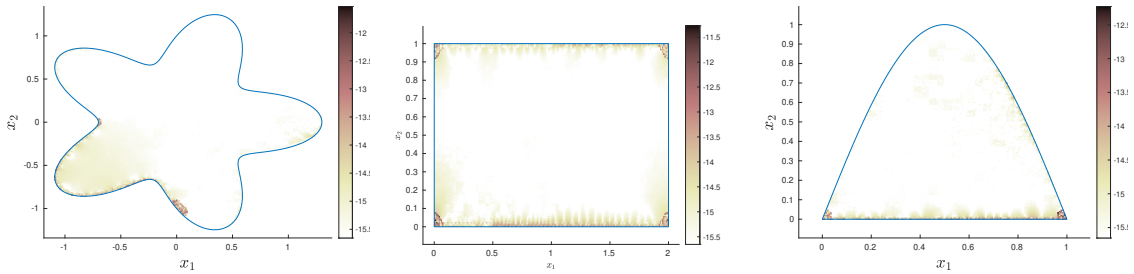
Figure 2.16 Pointwise error of computed pressure field inside of a smooth star-shape, a rectangular domain, and an arch-shaped domain.

2.3.2 Computational cost

Here we focus on CPU-time cost because the memory limit is not a dominant issue. In particular, we discuss the space complexity of our method. Incorporating the Stokes FMM, the dominant computational cost includes

1. $O(n_{it}N_{coa})$ for GMRES iterations,

2. $O(N_{coa} + M_t)$ for evaluations over $\overline{\Omega}$,

where N_{coa} is the number of discretized points on the boundary, n_{it} is the number of GMRES iterations, and M_t is the number of target points in the interior. The cost of the RCIP method is negligible as discussed in Remark (2.2.2). The cost of applying kernel-split quadrature and the interpolation method is also negligible since the number of evaluations to which these methods are applied is a small part of the total evaluations. The elapsed wall-clock time is measured using 'tic' and 'toc' built-in MATLAB functions. In the first example of the star-shaped boundary with $N_{coa} = 3,840$, the GMRES converged with 45 iterations and took 4.12 seconds, and the $M_t = 23,814$ evaluations of velocity, forces, and pressure took 10.7 seconds. In the second example of the rectangular boundary with $N_{coa} = 2,880$, the GMRES converged with 32 iterations and took 2.89 seconds, and the $M_t = 29,651$ evaluations of velocity, forces, and pressure took 20.13 seconds. In the third example of the arch-shaped boundary with $N_{coa} = 3,168$, the GMRES converged with 30 iterations and took 2.78 seconds, and the $M_t = 29,651$ evaluations of velocity, forces, and pressure took 6.43 seconds.

2.3.3 Applications to SH flow

The numerical examples in this section are associated with Section 2.2.6; the boundary conditions include the composite conditions due to the boundary being made up of solid surfaces alternating with bubble or groove menisci. First, we validate by comparing with the exact solutions of Philip [68].

We consider transverse shear flow over a plate containing a no-shear slot with width $2a$, for which an exact analytical solution is derived in section 10 of [68]. The mixed conditions on the plate $x_2 = 0$ are $\frac{\partial u_1}{\partial x_2} = u_2 = 0$ for $|x_1| < a$ (zero shear stress), and $u_1 = u_2 = 0$ for $|x_1| > a$ (no-slip). We use a complex variable $z = \frac{1}{a}(x_1 + ix_2)$ to describe the solution where (x_1, x_2) is the position in the original two-dimensional space. The exact solution for the stream function is given in [68]:

$$\psi = \phi_1 + a^2 \tau_\infty \Phi_2/\mu \qquad (2.70)$$

where $\phi_1 = \frac{1}{2}\tau_\infty x_2^2/\mu$ and $\Phi_2 = \frac{1}{4}\mathrm{Re}\left\{(\bar{z} - z)\left((z^2 - 1)^{1/2} - z\right)\right\}$ with given parameters τ_∞ (the constant shear stress as $x_2 \to \infty$) and μ. Physical quantities such as velocities are derived from the stream function taking partial derivatives with respect to real variables, following the method of Klinteberg et al. [51]. The computed and analytical solutions are shown in Figures 2.17 and 2.18. Comparison of these two solutions show that we obtain 11-digit accuracy of the velocity evaluations.
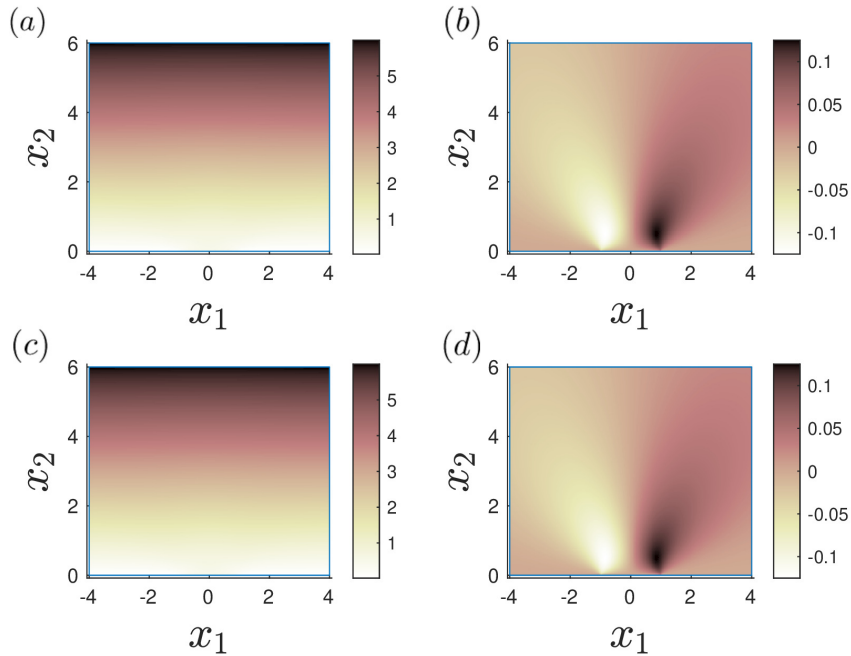
Figure 2.17 Velocities $\boldsymbol{u} = (u_1, u_2)$. (a): exact solution of u_1 from [68], (b): exact solution of u_2, (c): numerical solution of u_1, (d): numerical solution of u_2.
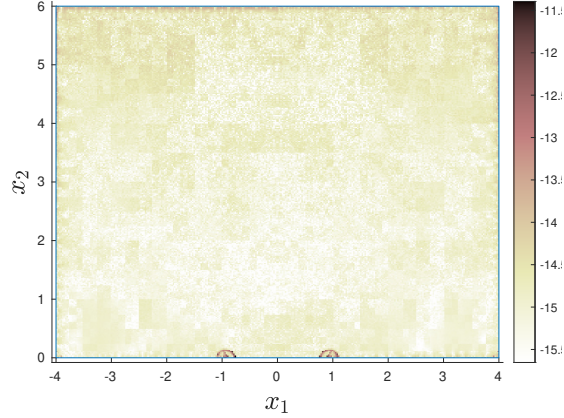
Figure 2.18 Pointwise absolute error in velocity for $a = 1$ in Figure 2.17.

Next, we consider transverse shear flow over a plate with a regular periodic arrangement of no-shear slots, as discussed in section 11 of Philip [68]. All the slots have the same width $2a$ centered at multiples of $2b$ $(a < b)$. The exact solution of the stream function is given as [68]:

$$\psi = \phi_1 + a^2 \tau_\infty \Phi_3 / \mu \tag{2.71}$$

where $\phi_1 = \frac{1}{2}\tau_\infty x_2^2/\mu$ and $\Phi_3 = \frac{1}{4}\text{Re}\left\{(\bar{z} - z)\left(\frac{1}{\alpha}\arccos\frac{\cos(\alpha z)}{\cos\alpha} - z\right)\right\}$ with given parameters τ_∞ and μ. The parameter α is defined by $\alpha = \frac{\pi}{2}\frac{a}{b}$.

We show three numerical examples related to this problem. First, we compute the velocity field in the case of $b/a = 4$. Second, we change the parameters a and b to make each solid plate narrower (equivalently each slot wider) to $a : b = 99 : 100$. This corresponds to small solid fraction. Finally, we increase the number of slots to 101 with the same parameters $b/a = 4$. Figure 2.19 shows the x_1 and x_2 component of the exact solution (top) and the computational results from our BIE method (bottom). We find 11-digit accuracy is achieved for the velocity evaluations in Figure 2.20.
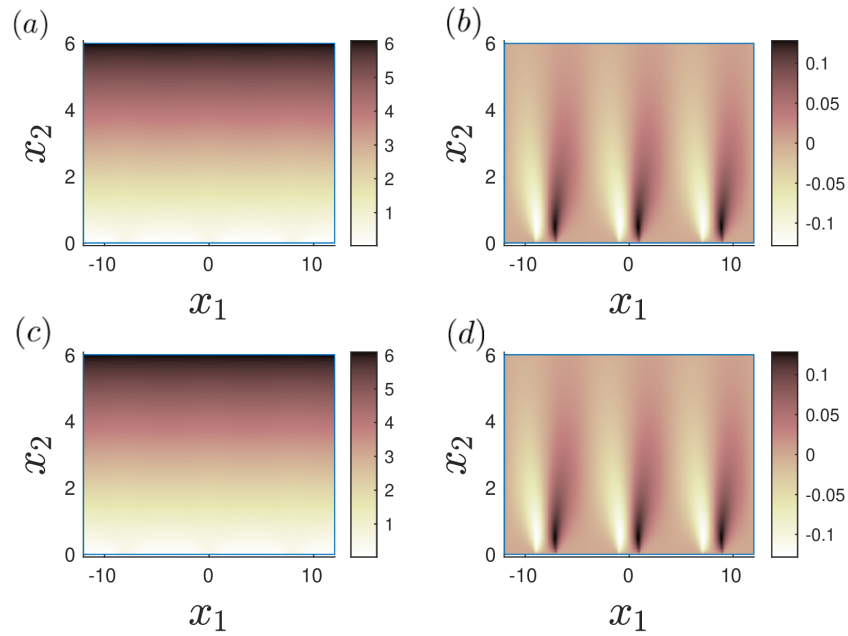
Figure 2.19 Velocities $\boldsymbol{u} = (u_1, u_2)$ with three slots. (a): exact solution of u_1, (b): exact solution of u_2, (c): numerical solution of u_1, (d): numerical solution of u_2.
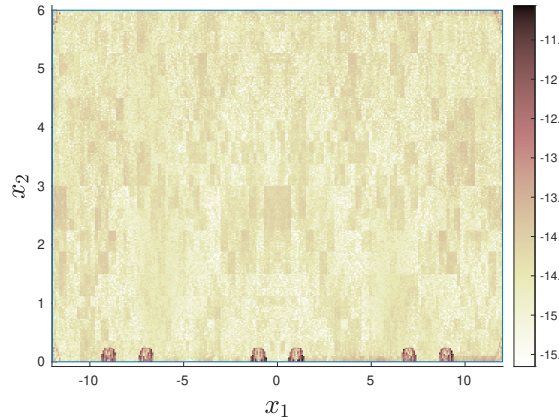
Figure 2.20 Pointwise absolute error with three slots in Figure 2.19.

The following two figures show the results with $a : b = 99 : 100$ so that the solid plates become wider and the slots narrower. This corresponds to small solid fraction, which is a particularly challenging case for numerical simulation, since the distance between each pair of adjacent singular points is small. The numerical results, however, show our method achieves 13-digit accuracy in the velocity as shown in Figure 2.22.

49
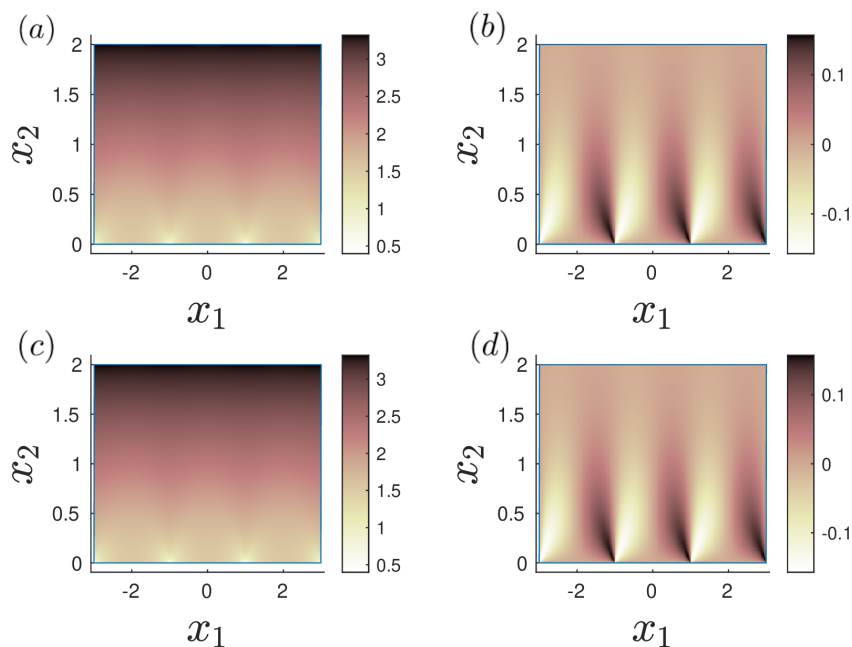
Figure 2.21 Velocities $\boldsymbol{u} = (u_1, u_2)$ for small solid fraction $a : b = 99 : 100$. (a): exact solution of u_1, (b): exact solution of u_2, (c): numerical solution of u_1, (d): numerical solution of u_2.
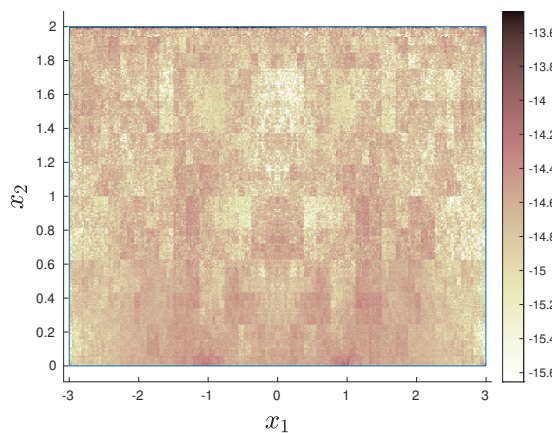
Figure 2.22 Pointwise absolute error for the parameter values in Figure 2.21.

In the third example, the number of slots is increased to 101 with the other parameters the same as in Figure 2.19. Since we consider a regular array of slots with periodic boundary conditions, the solution is the same as Figure 2.19. However, we now place 101 slots in our one root periodic box, to show that the method is capable of computing the solution to high accuracy over a very large number of solid-groove

cells. We have chosen 10^{-11} for the GMRES tolerance to speed up the computation. The result in Figure 2.27 shows 10-digit accuracy.
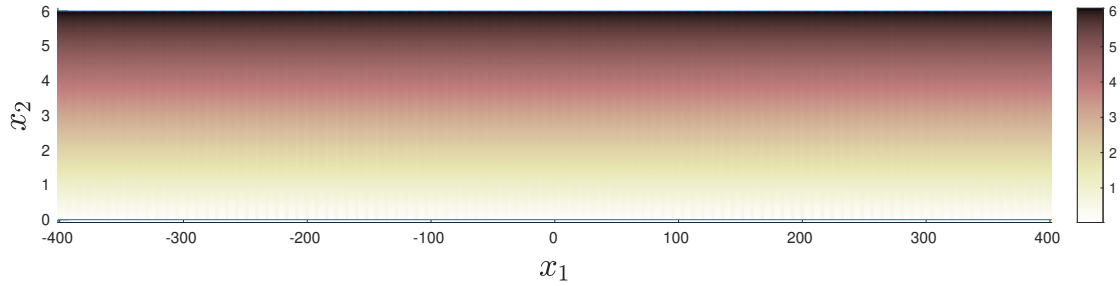
Figure 2.23 u_1 of exact velocities with 101 slots.
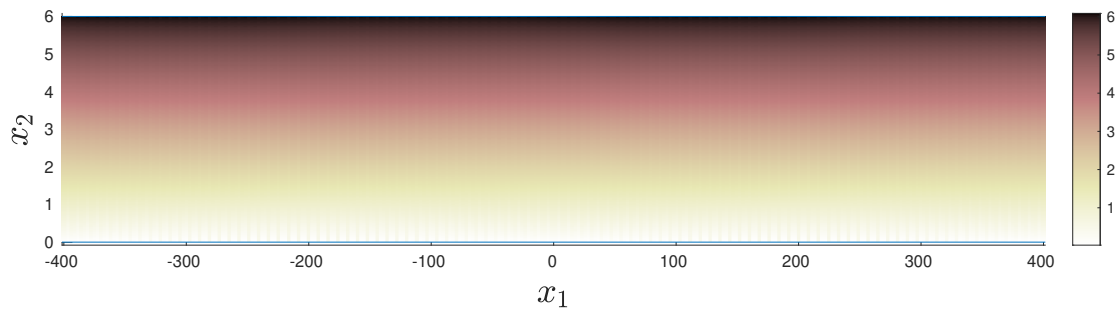
Figure 2.24 u_1 of simulated velocities with 101 slots.
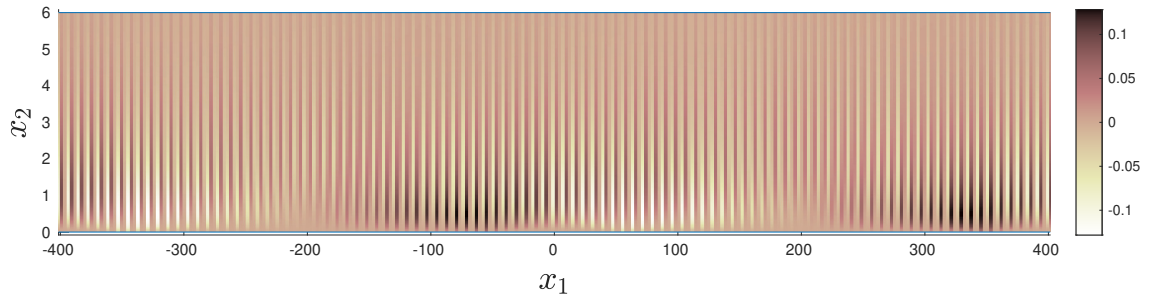
Figure 2.25 u_2 of exact velocities with 101 slots.
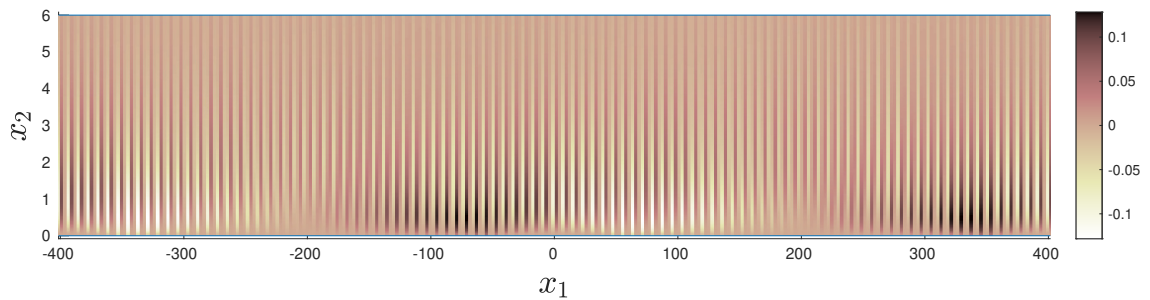
Figure 2.26 u_2 of simulated velocities with 101 slots.
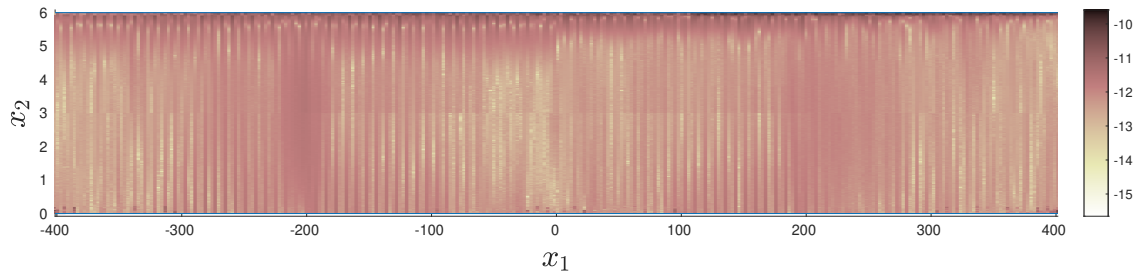
Figure 2.27 Pointwise numerical error in velocities with 101 slots.

2.3.4   Effective slip length computations

So far, we have shown the numerical results from computing velocity fields, forces, and pressure for problems with various boundary conditions and geometries. We now show our numerical results for the intrinsic and effective slip length λ (cf. Section 2.2.7).

First, we compare the numerically computed λ with the exact value derived in [68]. This example involves a periodic geometry with a flat interface, i.e., the bubble menisci are undeformed. The coarse-grained quantity λ is the intrinsic slip length, defined in Equation (2.58) and computed as described in Section 2.2.7. The result of our method agrees with the exact solution as shown in Figure 2.28.
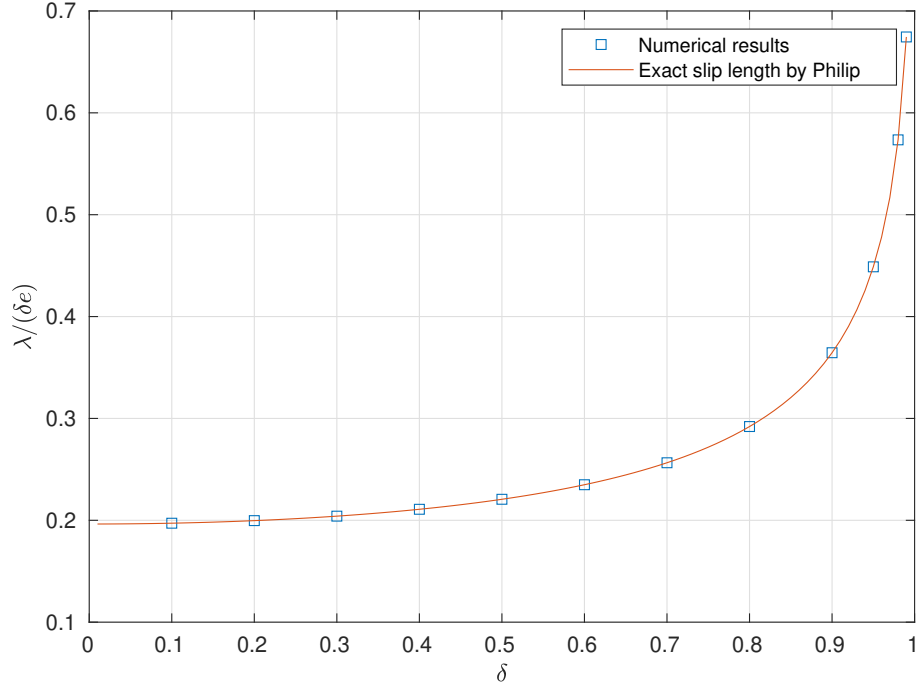
Figure 2.28 Numerical results of normalized effective slip length $\lambda/(\delta e)$ compared with the exact value from Philip [68]. Here $\delta := e/E$ where e is the slot width and E is the length of one period. The slip length is made dimensionless by e and scaled by the slot fraction δ. The height of the computational domain is set to $8E$.

Next, we show the behavior of λ in the case of deformed menisci with nonzero protrusion angles. For this test we consider pressure driven flow in a channel, for which λ is the effective slip length. This is defined as the value of λ at which a comparison channel with uniform slip $u_1 = \lambda \frac{\partial u_1}{\partial x_2}$ on the SH wall has equivalent flux $F := \int_0^H u_1(x_2)dx_2$, for the same pressure forcing. This quantity is computed in two different geometries. One is for pressure driven flow with one SH bottom wall and one entirely solid (top) wall. We refer to this as 'one-sided' SH channel flow. The second geometry involves a channel with two SH walls. This is called 'symmetric' SH channel flow. The computation of λ in both cases in discussed in Section 2.2.7. Schematics of the flow geometries are shown in Figures 2.12 and 2.13. The pressure boundary conditions are an imposed unit pressure pressure jump between the left inlet and right outlet, and no vertical velocity ($u_2 = 0$) on the inlet/outlet boundaries. Exact solutions to the problems are unavailable because the protrusion angles are nonzero.

Thus, we can only give a qualitative comparison with preexisting computations of λ in periodic geometries. The numerical results for λ with our method are shown in Figure 2.29 for one period and Figure 2.30 for 21 periods. Both results show the same qualitative behavior to the ones shown in preexisting literature. Note the two results in Figures 2.29 and 2.30 look similar (they differ by less than 10^{-3} relatively). This is to be expected, since in Figure 2.30 we take a uniform array of slot menisci, for which the average slip per cell is similar to the one cell slip in Figure 2.29. Our method is able to compute for a large number of cells with irregular spacing and protrusion angles. In future work, we can explore the effect of cell geometry on λ. Figures 2.31 and 2.32 show the computed velocity field in the interior domain for the two different geometries, incorporating 21 solid-groove cells and meniscus angle of 15 degrees.
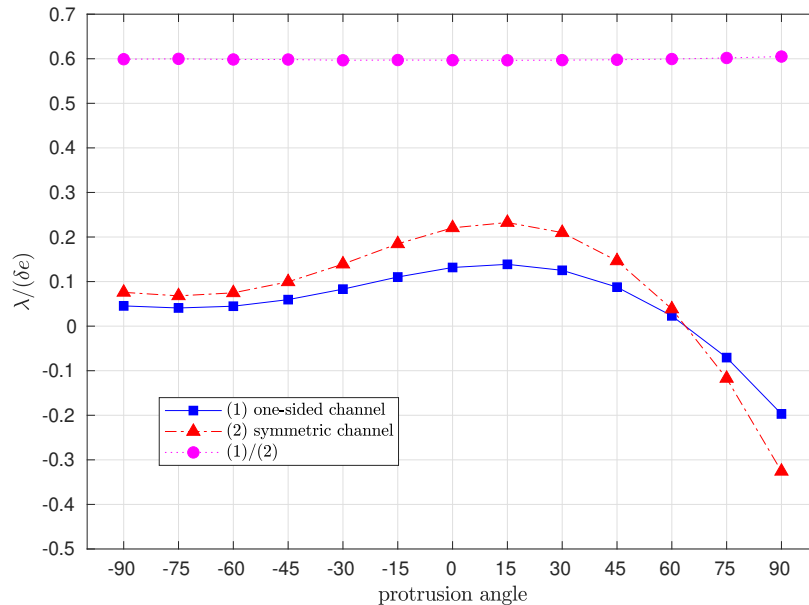
Figure 2.29 Numerical results of non-dimensionalized $\lambda/(\delta e)$ in the case of one meniscus with protrusion angles between -90 and 90 degrees. In a similar manner to Figure 2.28, we use the same notation as Figure 3 in Teo and Khoo [77]; e and E are defined as the length of one meniscus and the length of one period, and $\delta := e/E$ is the slot fraction. In the numerical results, we set e to 2 and E to 4. The hight of the computational domain is set to $8E = 64$.
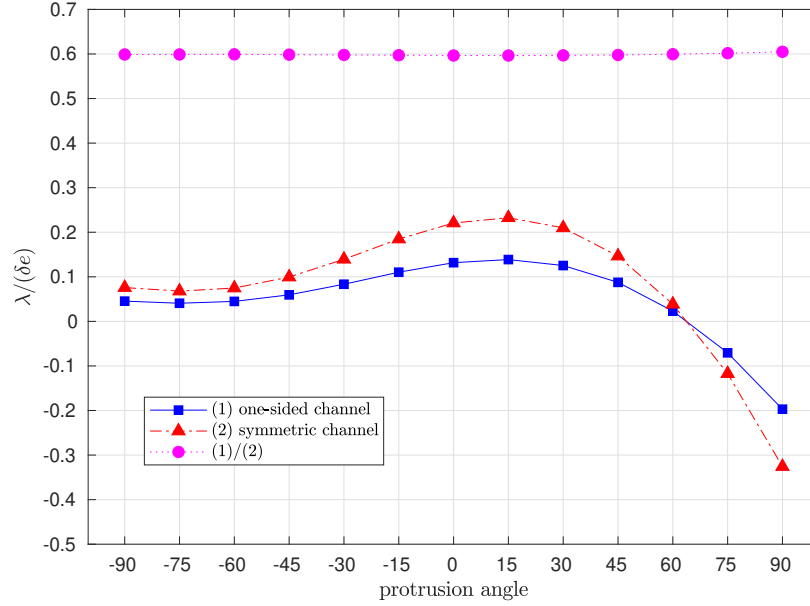
Figure 2.30 Numerical results of effective slip length in the case of $n_p := 21$ menisci with protrusion angles between -90 and 90 degrees. e and E are defined as the length of one meniscus and the length of one period, E_{tot} is the total length of n_p periods, and $\delta := (n_p e)/(E_{tot})$ is the slot fraction. In the numerical results, we set e to 2, E to 4, and E_{tot} to $n_p E = 84$. The hight of the computational domain is set to $8E = 64$.
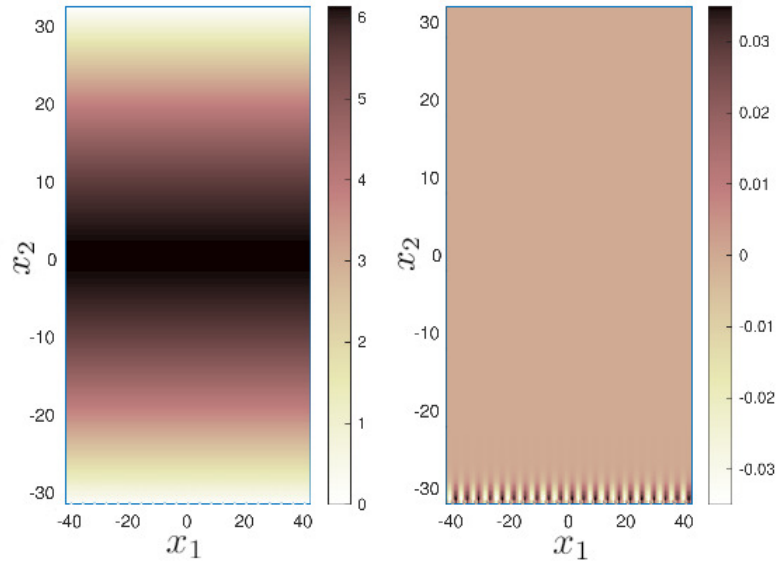
Figure 2.31 Plots of the velocity field in the case of 21 menisci in a one-sided SH channel and protrusion angles of 15 degrees.
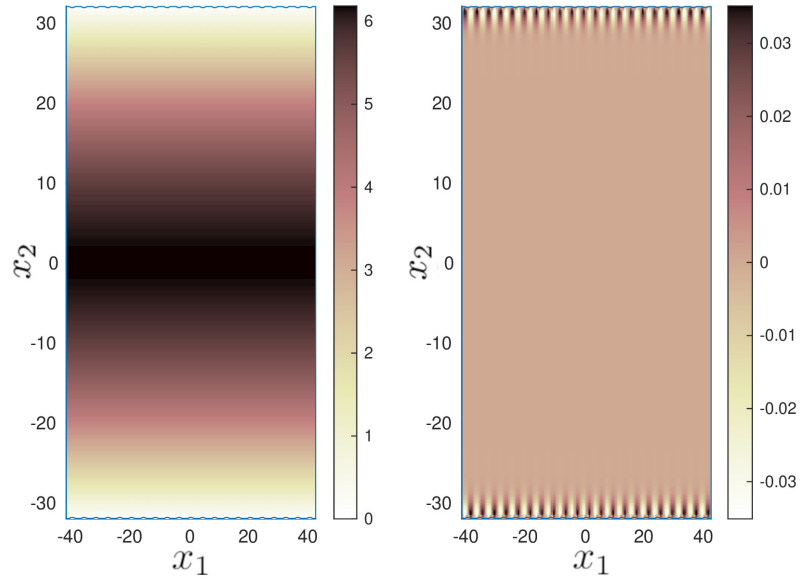
Figure 2.32 Plots of the velocity field in the case of 21 menisci in a symmetric SH channel and protrusion angles of 15 degrees.

CHAPTER 3

SCATTERING MATRIX FORMULATION FOR INTEGRATED PHOTONICS

3.1 Background

We now turn our attention to computational electromagnetics and its applications to integrated photonics. As is well known, transmission of information by electric interconnects is limited in latency by power concerns and in bandwidth by the amount of resources (e.g. parallel wires) devoted to port. In addition, long-range electric interconnects are subject to substantial losses. On the other hand, electric interconnects are easy to design, and substantial automation for the design of such circuits is available. Photonic interconnects, by contrast, are virtually unconstrained in bandwidth and offer minimal latency, but they pose far greater design challenges, for which to date little design automation is available. As the miniaturization of electronic devices progresses, the disadvantages of electric interconnects are being felt acutely, and photonic circuits are becoming economically viable in many everyday applications.

As a result, the photonic industry is growing rapidly. Compared with the integrated electronic circuits industry, the integrated optical circuits industry is still in its infancy. Indeed, for the electronic circuits industry, Moore's law has mostly reached the limit of its validity, and a single integrated electronic circuit (IC) chip may contain billions of transistors and other electronic components, while the current state-of-art integrated optical circuits chip contains photonic components such as various waveguides, couplers and arrayed waveguide gratings only on the order of one hundred. One major cause of this substantial difference is the lack of reliable tools for the design of integrated optical circuits. Existing numerical methods face

difficulties in obtaining satisfactory resolutions solving boundary value problems of three-dimensional Maxwell's equations as the fundamentally governing equations for photonics. Thus, an efficient and accurate simulation tool for photonics is in urgent need.

In this chapter, we study in detail the scattering matrix formulation for waveguide structures whose mathematical model is the interior Dirichlet Helmholtz problem in two dimensions. Admittedly, this is a much simplified model than Maxwell's equations in dielectric layered media in three dimensions. However, the model problem retains all critical building blocks: the mode calculation, the calculation of the scattering matrix of a single component, and the merging of the modularized scattering matrices. Therefore, our study provides useful insights towards our target application. Computationally, we rely again on the boundary integral equation formulation for dimension reduction, fast multipole methods for linear complexity, the RCIP method for point singularities, and the high-order kernel-split quadrature for accurate evaluation of singular and nearly singular layer potentials.

3.1.1 Existing numerical methods

We provide a brief review of widely used existing numerical methods for photonics simulation, concentrating on the difficulties those methods encounter. Okamoto [66] is an overview reference. One common issue among the existing methods is that those methods need unrealistically large-scale discretizations due to the following reason. The wavelength of the incident optical wave in typical devices is usually on the order of micrometers, while the sizes of devices themselves are of millimeters in at least two dimensions. Hence, the size of the entire simulation domain for a single device can be approximately $1,000 \times 1,000 \times 10$ in terms of incident wavelength.

Finite element method. The finite element method (FEM) is one of the standard methods for mainly mode calculation of waveguides (Brenner and Scott [14], Itoh et al. [47], Koshiba [53], Yamashita [81], Yeh et al. [85], Young [89], Zienkiewicz [91]). The FEM has the following disadvantages to integrated photonics simulations. Initially, discretization of the entire computational volume domain becomes extremely large scale, resulting in significant space complexity. Also, applying the FEM to large-scale problems tends to suffer from poor conditioning, which requires extra effort of preconditioning or using a direct solver method. Practically, the FEM is mostly applied to mode calculations of waveguides with small uniform cross-sections due to the limitation above.

Beam propagation method. Another widely-used type of method is the beam propagation method (Antoine et al. [2], Antoine et al. [3], Bamberger et al. [5], Fan et al. [27], Kragl [54], Kumbhakar [56], Jinbiao et al. [87]). Beam propagation method uses a simplified model for solving the Helmholtz equations by simplifications of Maxwell's equations. The propagating waves are assumed to be highly oscillating plane waves. Also, the refraction index contrast between the cladding and the core in the waveguide is assumed to be small, which can be a limitation of this type of method. The computational domain has to be large rectangular so that the waves fade away at infinity, which leads to the extreme large volume discretization.

Finite difference time domain method. The finite difference time domain (FDTD) method belongs to finite difference based methods (Yee [84], Mur [64], Higdon [45], Berenger [8]). The FDTD directly solves Maxwell's equations with respect to both space and time variables. This type of method also requires significantly large-scale discretization for the whole computational domain. In addition, some artificial boundary conditions called absorbing boundary conditions are imposed at the edge of the computational domain to avoid undesirable reflections.

Overall, the existing methods mentioned above encounter difficulties in discretizing the entire computational domain and often need to add some artificial assumptions to carry out numerical simulations even for obtaining minimum resolution of the simulation.

3.1.2 BIE methods and fast algorithms

The proposed method in this dissertation is based on the boundary integral equation (BIE) methods to resolve the most serious common issue of large-scale volume discretization with the existing methods collected above. In short, the BIE methods are a type of methods that utilizes layer potential representations for the associated partial differential equations (PDEs). Layer potentials are integral operators acting on some unknown density which needs to be determined with by solving the linear system derived from the discretized BIE. Since the density is defined on the boundary, we only need to discretize the boundary, via the surface integral in $\mathbb{R}^3$ or the line integral in $\mathbb{R}^2$. Once we determine the unknown density values, we again apply the discretized layer potentials acting on the density to evaluate the solution, its gradient, or Hessian, etc. Being able to focusing only on the boundary helps us avoid the entire volume discretization of the computational domain, reducing the dimension of the discretization by one.

The BIE methods have been extensively applied to numerical solvers for elliptic partial differential equations because of the ability to deal with complex geometry (Banerjee [6], Boriskina et al. [12], Biros et al. [9]), and owing to the compatibility with fast algorithms such as the fast multipole method (FMM) (Greengard and Rokhlin [35], Ying et al. [86], Greengard et al. [33], Rachh et al. [26], Ruqi et al. [67]), uniform/non-uniform Fast Fourier Transform (FFT) (Cooley and Tukey [19], Dutt and Rokhlin [23], Barnett et al. [7], Greengard and Lee [32], Ruiz-Antolin and Townsend [75]), and modern linear system solvers such as GMRES (Saad and

Schultz [76]) and fast direct solvers (Bremer [13], Ho and Greengard [46], Gillman et al. [28], Greengard et al. [31], Kong et al. [52], Martinsson and Rokhlin [62, 63], Martinsson [61]). We also would like to mention that the recent study to obtain high resolutions dealing with the singularities due to the intrinsic property of layer potentials in both $\mathbb{R}^2$ and $\mathbb{R}^3$. Selective work includes the RCIP method (Helsing and Ojala [42], Helsing [36]), kernel-split quadratures (Helsing [37], Helsing and Holst [38], Helsing and Jiang [39]), and other approaches (Wu et al. [80], Zhu and Veerapaneni [90] and Greengard et al. [33]). The above citations are a handful of representative or closely related existing work among a vast literature on BIE methods coupled with fast algorithms. In this dissertation, we incorporate some of the methods to be able to modularize the entire large-scale computations efficiently.

3.2 Mathematical Formulations

3.2.1 Notation and nomenclature

In a similar manner to the previous chapter, the common notation used in this chapter is as follows. We denote the computational domain of interest by Ω in $\mathbb{R}^2$, and the boundary by $\Gamma := \partial\Omega$. In the subsequent sections, we will define the two-dimensional Helmholtz Green's function denoted by $G(\boldsymbol{x}, \boldsymbol{y})$ and associated boundary integral kernels in the form $K(\boldsymbol{x}, \boldsymbol{y})$, where $\boldsymbol{x} = (x_1, x_2)$ and $\boldsymbol{y} = (y_1, y_2)$ are referred to as the *target* point and *source* point, respectively. We also use $\boldsymbol{r} := \boldsymbol{x} - \boldsymbol{y}$ and $r := |\boldsymbol{r}|$. If a target and source point are on Γ, $\boldsymbol{n_x}$ and $\boldsymbol{n_y}$ are defined as the unit normal vectors pointing outward at $\boldsymbol{x}$ and $\boldsymbol{y}$, respectively. Again in a slight abuse of notation, we use the same boldface letter to denote an integral operator, its kernel, and the associated matrix after discretization, as long as the meaning is clear from context.

We also use complex variables as equivalent notation, especially for kernel-split quadratures, as the target point $z_x := x_1 + ix_2$, source point $z_y := y_1 + iy_2$, $z := (y_1 - x_1) + i(y_2 - x_2)$ (equivalent to $-\boldsymbol{r} = -(\boldsymbol{x} - \boldsymbol{y})$), unit normal vector $\nu_x := n_{x,1} + in_{x,2}$

at z_x, unit normal vector $\nu_y := n_{y,1} + i n_{y,2}$ at z_y, The conjugation of $z \in \mathbb{C}$ is denoted by $\bar{z}$.

3.2.2   A model problem

An open waveguide component is often considered as a natural model problem for the research investigation into integrated photonics (Epstein [25], Bonnet-Bendhia et al. [11, 10], and Chandler-wilde et al. [15]). The domain of such an open waveguide is semi-infinite, i.e., the waveguide path of the propagation modes is stretched infinitely in x_1 direction, and the bounded in x_2 direction in $\boldsymbol{x} = (x_1, x_2) \in \mathbb{R}^2$. This means that the input/output channels extend all the way to infinity. The waveguide is assumed to be dielectric in the existing work mentioned above. An image example we frequently use in the following discussion is shown in Figure 3.1.
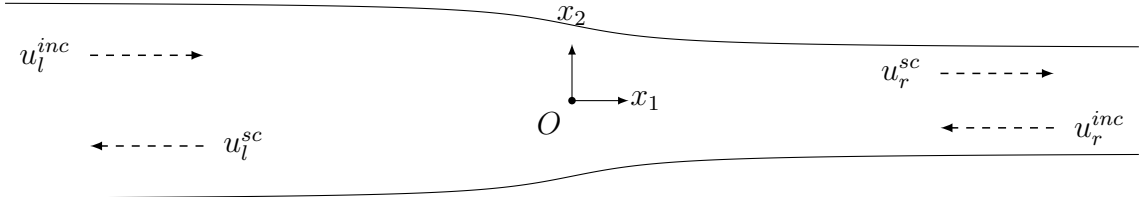
Figure 3.1 A two-dimensional semi-infinite waveguide with propagation modes along x_1 direction. The waveguide has two channels (interfaces) with different thicknesses. u_l^{inc} and u_r^{inc} indicate the incident waves, and u_l^{sc} and u_r^{sc} indicate the scattered waves on two sides, respectively.

Here, we study a somewhat simpler model. That is, the waves satisfy the Helmholtz equation inside the waveguide and zero Dirichlet condition on the waveguide boundary:

$$\begin{aligned} \Delta u(\boldsymbol{x}) + k^2 u(\boldsymbol{x}) = 0, \qquad & \boldsymbol{x} \in \Omega \\ u(\boldsymbol{x}) = 0, \qquad & \boldsymbol{x} \in \partial\Omega. \end{aligned} \tag{3.1}$$

3.2.3   General numerical procedure

We outline the numerical procedure of constructing scattering matrices for a large waveguide structure. First, we study the decomposition of the waves inside the

waveguide structure. We have shown that the waves can be decomposed into two parts: a set of propagating modes and evanescent waves that decay exponentially fast along the propagating directions. This enables us to modify the original problem as follows. Instead of trying to solve the original problem on an infinite domain, we solve the Helmholtz Dirichlet problem in a closed bounded domain by placing, say, vertical line segments at both ends as shown Figure 3.2. The field satisfies zero Dirichlet condition on the original boundary of the waveguide and some artificial nonzero data on those artificially introduced vertical line segments. By a clever set of linear algebraic operations, we show that one can compute the scattering matrix of the original infinite waveguide structure to high accuracy. The critical fact that we rely on is, of course, the exponential decay of the evanescent waves. We will quantify this in section 3.2.4.
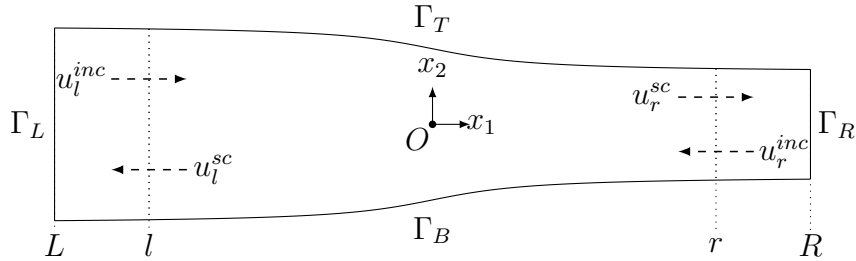
Figure 3.2 A simplified waveguide model of perfect conductor with bounded closed boundary.

3.2.4   Propagating modes

Before we introduce our definition and application of the scattering matrix to our problem, we would like to discuss the propagation modes denoted by $(\beta_m)_{m=1}^M$ whose existence depends on the structure of a given waveguide. Given the information of a waveguide such as the geometric structure and composed materials, to determine how many propagation modes are allowed and what are the exact values of such modes are not only intrinsically important but also non-trivial, while such mode calculation step is necessary procedure to develop a numerical method for integrated photonics. For

example, Lai and Jiang [57] Jiang and Lai [48] propose numerical methods for the mode calculations of photonic crystal fibers and rectangular waveguides in layered medium, both of which are tailored to obtain the second-kind boundary integral equations. In our case, however, not numerically but explicitly, we are able to compute the propagation modes that are admitted in the locally straight structure because of the simple assumptions we make. In this section, we show some mathematical conditions under which how many propagation modes can exist and explicit formulas for the modes with detailed derivations in appendix B.4.

In the local subdomain far away with respect to x_1 of the open waveguide 3.1 where the top and bottom boundary curves become completely parallel straight lines, the solution to the Helmholtz equation (3.12) in the subdomain can be written as

$$u(x_1, x_2) = \sum_{m=1}^{\infty} \left(c_m^+ e^{i\beta_m x_1} + c_m^- e^{-i\beta_m x_1} \right) g_m(x_2), \tag{3.2}$$

where $(c_m^\pm)_{m=1}^\infty$ are constant coefficients, $(g_m(x_2))_{m=1}^\infty$ are normalized eigenfunctions

$$g_m(x_2) = \sqrt{\frac{2}{h}} \sin\left(m\frac{\pi}{h}(x_2 + \frac{h}{2}) \right), \tag{3.3}$$

and $(\beta_m)_{m=1}^\infty$ are generally complex numbers satisfying

$$\beta^2 = k^2 - \left(m\frac{\pi}{h} \right)^2. \tag{3.4}$$

The derivation of Equation (3.4) is given in appendix B.4. In Equation (3.4), $k > 0$ is the given wavenumber inside the domain, and $h > 0$ is the thickness of the waveguide in the local subdomain. The solution can be understood as the linear combination of waves coming from 'left' (in the direction of increasing x_1), and from 'right' (decreasing x_1). If the incident wave u^{inc} comes only from the left, $u^{inc} = \sum_{m=1}^\infty c_m^- e^{-i\beta_m x_1} g_m(x_2)$ and $u^{sc} = \sum_{m=1}^\infty c_m^+ e^{i\beta_m x_1} g_m(x_2)$ hold as the scattered wave u^{sc} propagates in the opposite direction.

Depending on k and h, there exists a non-negative integer M such that β_m for any $m \leq M$ is a non-negative number (Equation (3.4) is non-negative) and that β_m for any $m > M$ is i (the imaginary unit) times a positive number ((3.4) is negative). The finite positive numbers $(\beta_m)_{m=1}^M$ are called *propagating modes* admitted for the given waveguide.

In the subdomain with an exactly straight structure allowing only M modes $(\beta_m)_{m=1}^M$, the solution (3.2) can be split into terms: ones with the propagating modes $e^{\pm i\beta_m x_1}$ where β_m is non-negative, and the other evanescent ones exponentially decaying $e^{-|\beta_m x_1|}$. We will discuss a quantitative estimation of the evanescent terms in the next section.

Also, we are able to derive the condition for the thickness h to allow exactly M modes as

$$M\frac{\pi}{k} < h < (M+1)\frac{\pi}{k}. \tag{3.5}$$

The derivations of inequalities (3.5) are given in appendix B.4.

Properties of the evanescent waves Here, we show an estimation of the convergence of propagation modes taking the evanescent terms with $(\beta_m)_{m=M+1}^\infty$ into account.

As we have briefly explained above, in the subdomain with a locally straight structure, if the incident wave comes from left, then the solution (3.2) at $\boldsymbol{x} = (x_1, x_2)$ is the superposition of

$$u^{inc}(x_1, x_2) = \sum_{m=1}^\infty c_m^+ e^{i\beta_m x_1} g_m(x_2) \tag{3.6}$$

and

$$u^{sc}(x_1, x_2) = \sum_{m=1}^\infty c_m^- e^{-i\beta_m x_1} g_m(x_2). \tag{3.7}$$

Suppose $u^{inc}(x_1 - \delta, x_2)$ and $u^{sc}(x_1 + \delta, x_2)$ are given for some positive number δ where $[x_1 - \delta, x_1 + \delta]$ is in the local subdomain. We also assume the subdomain admits M modes for a given wavenumber $k > 0$ and the thickness of the waveguide $h > 0$.

Initially, we focus on the evanescence of Equation (3.6). Noting $e^{i\beta_m \delta} = \exp\left[-\left(m\frac{\pi}{h} - k\right)\delta\right] > 0$ for $m > M$, the higher order terms for $m > M$ can be bounded as

$$
\left| \sum_{m=M+1}^{\infty} c_m^+ e^{i\beta_m(x_1)} g_m(x_2) \right| = \left| \sum_{m=M+1}^{\infty} c_m^+ e^{i\beta_m(x_1-\delta+\delta)} g_m(x_2) \right|
$$

$$
\leq e^{i\beta_{M+1}\delta} \left| \sum_{m=M+1}^{\infty} c_m^+ e^{i\beta_m(x_1-\delta)} g_m(x_2) \right|
$$

$$
= \exp\left[-\left((M+1)\frac{\pi}{h} - k\right)\delta\right] \left| \sum_{m=M+1}^{\infty} c_m^+ e^{i\beta_m(x_1-\delta)} g_m(x_2) \right|
$$

$$
= \exp\left[-\left((M+1)\frac{\pi}{h} - k\right)\delta\right] \left| \left(\sum_{m=1}^{\infty} - \sum_{m=1}^{M}\right) c_m^+ e^{i\beta_m(x_1-\delta)} g_m(x_2) \right|
$$

$$
(3.8)
$$

The last term $\left|\left(\sum_{m=1}^{\infty} - \sum_{m=1}^{M}\right) c_m^+ e^{i\beta_m(x_1-\delta)} g_m(x_2)\right|$ is finite since $u^{inc}(x_1 - \delta, x_2)$ is given as a finite number. Hence, the series of evanescent terms is bounded from above by some positive constant times $\exp\left[-\left((M+1)\frac{\pi}{h} - k\right)\delta\right]$. The logarithm of the upper bound is proportional to

$$
-\left[\frac{\pi}{h}(M+1) - k\right]\delta. \tag{3.9}
$$

Thus, the truncation of the solution $u^{inc}(x_1, x_2) \simeq \sum_{m=1}^{M} c_m^+ e^{i\beta_m x_1} g_m(x_2)$ with M terms is convergent exponentially to the original series as the modes propagate in the direction of increasing x_1.

The same argument still applies to the evanescence of u^{sc} coming from $x_1 + \delta$ because of the exponential decay of $e^{-i\beta_m(-\delta)} = e^{i\beta_m \delta}$.

Therefore, $u(x_1, x_2) = u^{inc} + u^{sc}$ can be well approximated as the superposition of finite terms up to order M in the local subdomain with the upper bound estimation (3.9).

3.2.5 Scattering matrices

The scattering matrix is an extremely useful mathematical tool and concept for studying any system that exhibits the linear relationship between its input and output data. There is a long history of research on the scattering theory in mathematical physics, including the classic book "Scattering Theory" by Lax and Phillips [60], Colton and Kress [17, 18], Bonnet-Bendhia and Tillequin [11], Bonnet-Bendhia et al. [10], Chandler-wilde et al. [15], and Chandler-Wilde and Zhang [16]. The scattering matrix has been used by researchers and engineers in electronic engineering to design and develop communication devices. See, for example, Rao [73] on the application of the scattering matrix to the study of microwave network systems. One example is the four-channel network shown in Figure 3.3. In the system, the scattering matrix $\boldsymbol{S} = (S_{i,j})_{1 \leq i,j \leq 4}$ is a four times four matrix satisfying

$$\boldsymbol{S}\boldsymbol{u}^{inc} = \boldsymbol{u}^{sc} \tag{3.10}$$

where $\boldsymbol{u}^{inc} = (u_1^{inc}, u_2^{inc}, u_3^{inc}, u_4^{inc})^T$ and $\boldsymbol{u}^{sc} = (u_1^{sc}, u_2^{sc}, u_3^{sc}, u_4^{sc})^T$ represent the incident and scattered wave vectors at all channels, respectively. The diagonal terms of $\boldsymbol{S}$ correspond to the reflection effects that quantify the amount of the incident wave reflected back into the originating channel, and the off-diagonal terms exhibit the transmission coefficients where each element determines the amount of the incident wave transmitted from one channel into the other channel. The scattering matrix $\boldsymbol{S}$ describes a microwave network system and provides a complete description of the network at its channels. The determination of the scattering matrix eliminates the need to know the network's internal components, providing the required information

to determine the output $\boldsymbol{u}^{sc}$ at all channels for any input $\boldsymbol{u}^{inc}$, making it convenient for complex systems.
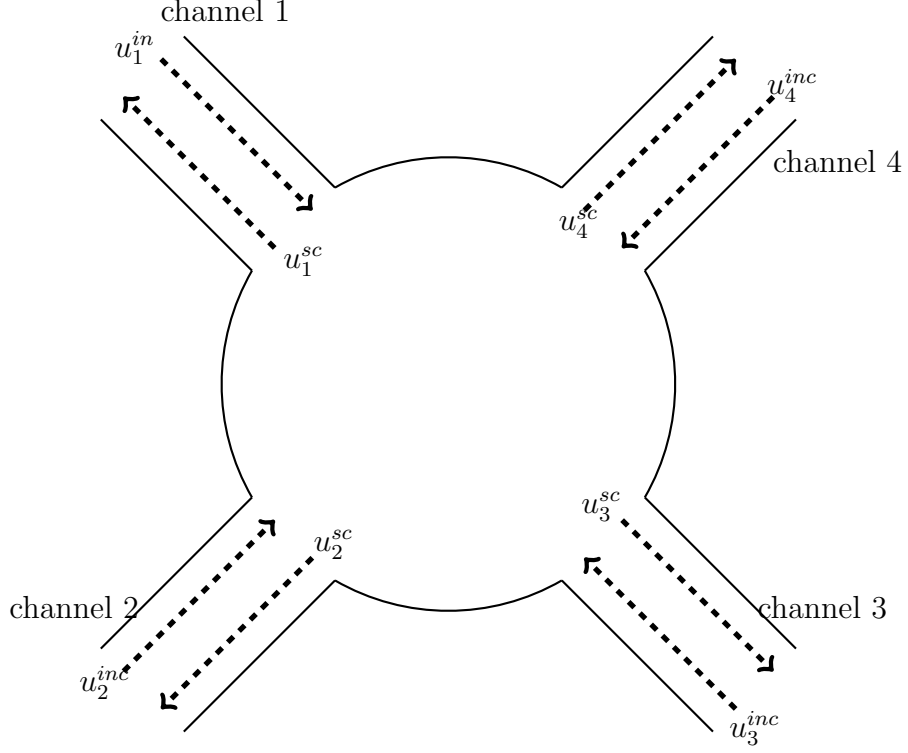
Figure 3.3 A microwave network system with 4 channels from Rao [73].

For integrated photonics in this dissertation, we define the scattering matrix as follows.

Definition 3.2.1 (Scattering matrix). *Suppose a waveguide with P input/output channels is modeled as the semi-infinite open Dirichlet boundary value problem of the Helmholtz equation (3.1). Also suppose pth channel admits M_p modes $(\beta_{p,m})_{m=1}^{M_p}$ ($1 \leq p \leq P$) as*

$$u(x_1, x_2) = u^{inc}(x_1, x_2) + u^{sc}(x_1, x_2)$$

$$\simeq \sum_{m=1}^{M_p} \left(c_{p,m}^+ e^{i\beta_{p,m}x_1} + c_{p,m}^- e^{-i\beta_{p,m}x_1} \right) g_{p,m}(x_2),$$

or

$$u(x_1, x_2) = u^{inc}(x_1, x_2) + u^{sc}(x_1, x_2)$$

$$\simeq \sum_{m=1}^{M_p} \left(c_{p,m}^- e^{-i\beta_{p,m}x_1} + c_{p,m}^+ e^{i\beta_{p,m}x_1} \right) g_{p,m}(x_2)$$

depending on the direction of the propagating modes associated with pth channel.

The scattering matrix of the waveguide is defined as the following matrix $\boldsymbol{S}$

$$\boldsymbol{S}\boldsymbol{c}^{inc} = \boldsymbol{c}^{sc} \tag{3.11}$$

where $\boldsymbol{c}^{inc}$ is the vector comprising coefficients for all channels and modes ($c_{p,m}^+$ or $c_{p,m}^-$) of propagating modes of the incident wave u^{inc}, and $\boldsymbol{c}^{sc}$ is the vector of coefficients of scattered wave u^{sc}, respectively.

Example 3.2.1. *If the number of channels P is two such as the case of Figure 3.1, and $Mp = 1$ for both $p = 1$ and $p = 2$ admitting only one single mode, then the scattering matrix is a two by two matrix mapping from $\boldsymbol{c^{inc}} = (c_{1,1}^+, c_{2,1}^-)^T$ to $\boldsymbol{c^{sc}} = (c_{1,1}^-, c_{2,1}^+)^T$. If the number of modes at each channel $Mp = 2$ for both $p = 1$ and $p = 2$, then the scattering matrix is a four by four matrix mapping from $\boldsymbol{c^{inc}} = (c_{1,1}^+, c_{1,2}^+, c_{2,1}^-, c_{2,2}^-)^T$ to $\boldsymbol{c^{sc}} = (c_{1,1}^-, c_{1,2}^-, c_{2,1}^+, c_{2,2}^+)^T$.*

3.2.6 The interior Dirichlet Helmholtz problem

Assuming that a waveguide is composed of perfect conductor and that the domain Ω is closed, piecewise smooth enough, and more or less straight in the direction of the propagation modes shown in Figure 3.2, the behavior of the electromagnetic waves inside can be modeled as an interior Dirichlet boundary value problem of the Helmholtz equation in the two-dimensional space. The solution u at $\boldsymbol{x}$ inside the domain satisfies

$$\Delta u(\boldsymbol{x}) + k^2 u(\boldsymbol{x}) = 0 \quad \boldsymbol{x} = (x_1, x_2) \in \Omega, \tag{3.12}$$

where k is assumed to be a positive wavenumber. We denote the wavenumber in a vacuum by k_v and the refractive index along a vertical cross-section by n so that $k = nk_v$. Also, let n_e be the effective index of propagation mode β along the same cross-section satisfying $\beta = n_e k_v$. We denote the top and bottom part of the boundary by Γ_T and Γ_B, and the left and right sides by Γ_L and Γ_R, respectively satisfying $\partial\Omega = \Gamma_T \cup \Gamma_B \cup \Gamma_L \cup \Gamma_R$. Homogeneous Dirichlet condition are imposed on the top and bottom $\Gamma_T \cup \Gamma_B$, and we assume some smooth functions $f(L, x_2)$ and $f(R, x_2)$ on left and right $\Gamma_L \cup \Gamma_R$;

$$u(\boldsymbol{x}) = \begin{cases} 0 & \boldsymbol{x} \in \Gamma_T \cup \Gamma_B, \\ f(x_2) & \boldsymbol{x} \in \Gamma_L \cup \Gamma_R. \end{cases} \tag{3.13}$$

3.2.7 The Helmholtz potential theory

To apply the BIE method to our problem in the following discussions, we need to choose an appropriate layer potential representation as the solution u to the Helmholtz boundary value problem satisfying (3.12) and (3.13). Here, we collect the definitions of Green's function, layer potentials, integral equations, and some identities associated with the two-dimensional Helmholtz equation. We follow conventional definitions often used in the preexisting work such as Colton and Kress [17, 18] and Neédélec [65].

3.2.8 The Helmholtz Green's function

Let $\boldsymbol{x}$ and $\boldsymbol{y}$ be arbitrary distinct points in $\mathbb{R}^2$. The fundamental solution to the Helmholtz equation $\Delta u(\boldsymbol{x}) + k^2 u(\boldsymbol{x}) = \delta(\boldsymbol{y})$ where δ is the delta distribution, is

$$G_k(\boldsymbol{x}, \boldsymbol{y}) = \frac{i}{4} H_0^{(1)}(kr) \tag{3.14}$$

where $H_0^{(1)}$ is the zeroth order of Hankel function of the first kind, k is the wavenumber, and $r := |\boldsymbol{x} - \boldsymbol{y}|$.

3.2.9 The Helmholtz layer potentials

The BIE methods involves various layer potentials associated with the underlying partial differential equations. In our problem, the Helmholtz single and double layer potentials and their normal derivatives are defined as follows.

$$S_k[\rho](\boldsymbol{x}) := \int_\Gamma G_k(\boldsymbol{x}, \boldsymbol{y})\rho(\boldsymbol{y})dS_{\boldsymbol{y}}, \qquad \text{(single-layer potential)} \tag{3.15}$$

$$D_k[\rho](\boldsymbol{x}) := \int_\Gamma \frac{\partial G}{\partial n_y}(\boldsymbol{x}, \boldsymbol{y})\rho(\boldsymbol{y})dS_{\boldsymbol{y}}, \qquad \text{(double-layer potential)} \tag{3.16}$$

$$S_k'[\rho](\boldsymbol{x}) := \int_\Gamma \frac{\partial G}{\partial n_x}(\boldsymbol{x}, \boldsymbol{y})\rho(\boldsymbol{y})dS_{\boldsymbol{y}}, \tag{3.17}$$

$$D_k'[\rho](\boldsymbol{x}) := \int_\Gamma \frac{\partial^2 G}{\partial n_x \partial n_y}(\boldsymbol{x}, \boldsymbol{y})\rho(\boldsymbol{y})dS_{\boldsymbol{y}}, \tag{3.18}$$

where $dS_{\boldsymbol{y}}$ is the arclength differential on Γ. It is well known that the layer potentials can be log-singular, singular, hyper-singular and near singularities of these, which may lead to loss of accuracy for numerical simulations. The single layer potential S has log-singularity on and off boundary Γ. The double layer potential D and S' have log-singularity on and off Γ and near singularity off Γ. D' has log-singularity and hyper-singularity off Γ while near log-singularity, near singularity, and near hyper-singularity off Γ. Summarized explanations about which layer potentials of the two-dimensional Helmholtz equation have which singularities are given in Helsing and Karlsson [41].

3.2.10 Jump relations of the Helmholtz layer potentials

Layer potentials S' and D satisfy the following jump relations at $\boldsymbol{x} \in \Gamma$ depending whether the domain of interest is interior or exterior:

$$\pm\frac{1}{2}\rho(\boldsymbol{x}) + S_k'[\rho](\boldsymbol{x}) = \lim_{h \to 0+} S_k'[\rho](\boldsymbol{x} \mp h\boldsymbol{n_x}), \tag{3.19}$$

$$\mp\frac{1}{2}\rho(\boldsymbol{x}) + D_k[\rho](\boldsymbol{x}) = \lim_{h \to 0+} D_k[\rho](\boldsymbol{x} \mp h\boldsymbol{n_x}). \tag{3.20}$$

Note that S_k and D'_k are known to be continuous across the boundary.

3.2.11 Calderon identities

The following four equations in the sense of integral operators involving the Helmholtz layer potentials are called Calderon identities.

$$S'_k S_k - S_k D'_k = 0, \tag{3.21}$$

$$D'_k S'_k - D_k D'_k = 0, \tag{3.22}$$

$$(S'_k)^2 - S_k D'_k = \frac{1}{4}I, \tag{3.23}$$

$$D_k^2 - D'_k S_k = \frac{1}{4}I. \tag{3.24}$$

Although we do not explicitly use the above identities in our discussions, these Calderon identities are known to be useful equations in a case that we are able to apply the identities to pre-conditioning of the linear system obtained by the discretization of the BIE to be solved for the unknown density. For example, Greengard et al. [33] rewrite an integral equation for a three-dimensional sound-hard scattering problem using the last identity to remove the hyper-singularity.

3.2.12 Integral representation and boundary integral equation

We choose the following combined layer potential representation from Colton and Kress [17] for the solution to our problem:

$$u(\boldsymbol{x}) = D_k[\rho](\boldsymbol{x}) + \frac{i}{2}kS_k[\rho](\boldsymbol{x}), \qquad \boldsymbol{x} \in \Omega. \tag{3.25}$$

Then the normal derivative of the solution $\frac{\partial u}{\partial n}$ can be written as

$$\frac{\partial u}{\partial n_x}(\boldsymbol{x}) = D'_k[\rho](\boldsymbol{x}) + \frac{i}{2}kS'_k[\rho](\boldsymbol{x}), \qquad \boldsymbol{x} \in \Omega, \tag{3.26}$$

assuming $\boldsymbol{n}_x$ is given. For the Dirichlet boundary value problem, by the interior jump relation of the double-layer potential (3.20), the unknown density ρ satisfies the

following second-kind boundary integral equation

$$-\frac{1}{2}\rho(\boldsymbol{x}) + D_k[\rho](\boldsymbol{x}) + \frac{i}{2}kS_k[\rho](\boldsymbol{x}) = f(\boldsymbol{x}), \qquad \boldsymbol{x} \in \Gamma. \tag{3.27}$$

3.3 Numerical Method

3.3.1 The BIE method for the Dirichlet Helmholtz BVP

Here we describe how we discretize and evaluate the layer potentials (3.15)-(3.18), the solution u (3.25) and the normal derivative (3.25) (or gradient) as necessary. Since this section somewhat overlaps with previous sections, we repeat important ingredients of the standard procedure of the BIE methods, the RCIP method, and kernel-split quadratures, skipping some redundant parts that have already explained.

3.3.2 Discretization of the BIE

To evaluate the solution u and its partial derivatives, we need to discretize the BIE (3.27) on the boundary Γ to construct a linear system to solve for the unknown density. We apply a standard panel-based Nyström discretization scheme via composite Gauss-Legendre quadrature with n_p panels. See Kress [55] for an introductory explanations. The total number of the discretization points is $N := n_{gl}n_p$. We set n_{gl} to 16 for double-precision floating point arithmetic. As a result, the linear system obtained by the discretization of BIEs (3.27) on Γ can be written as

$$(\boldsymbol{I} + \boldsymbol{K})\,\boldsymbol{\rho} = \boldsymbol{b}, \tag{3.28}$$

where $\boldsymbol{I}$ is the N times N identity matrix, $\boldsymbol{K}$ is the N times N square matrix involving the discretized combined layer potential representation $-2(D + \frac{1}{2}ikS)$, $\boldsymbol{\rho}$ is the vector of the unknown density values at the discretized points, and $\boldsymbol{b} = -2\boldsymbol{f}$ is a given Dirichlet boundary data vector with N entries.

In our problem formulation, the boundary Γ contains corners involving singularities and near-singularities which cause loss of accuracy and instability of the linear

system. Instead of a standard refinement around the corner, which often ends up with growing size and ill-conditioning of the linear system and failing to obtain satisfactory accuracy, we apply the RCIP method ([42, 36, 39, 40], also described in section 2.2.2) to avoid such loss of accuracy handling the linear system with the same size as the original one. The essential differences between applying the RCIP method in this chapter and Chapter 2 for the SH flow problem is that $n_{eq} = 1$ for the discretization of BIE (3.27) whereas $n_{eq} = 2$ in Chapter 2 because the solution of the Helmholtz equation and unknown density have scalar values, and that BIE (3.27) causes near log-singularity and singularity off the boundary Γ and log-singularity on Γ without hyper singularity since the BIE does not involve D'. Applying the RCIP method to (3.28) with the decomposition of $\boldsymbol{K} = \boldsymbol{K}^\circ + \boldsymbol{K}^*$ as described in section 2.2.2, we obtain the same form of linear system as (2.23)

$$(\boldsymbol{I} + \boldsymbol{K}^\circ \boldsymbol{R})\, \tilde{\boldsymbol{\rho}} = \boldsymbol{b}, \tag{3.29}$$

with a different block size (This linear system is merely a single block as a whole since $n_{eq} = 1$ while the corresponding block size in Chapter 2 is two by two as $n_{eq} = 2$.)

We also incorporate kernel-split quadratures referred in section 2.2.3 into the process of constructing the linear system via the RCIP method to deal with such singularities. The representative references are [37, 39, 80, 51]. When the discretized Gauss-Legendre panel of the target point $\boldsymbol{x}$ coincides with (or resides adjacent to) the panel of the source point $\boldsymbol{y}$, we substitute an appropriate kernel-split quadrature for the standard Gauss-Legendre quadrature over the panel of $\boldsymbol{y}$ affected by the (near) singularity. Helsing and Karlsson [41] also gives us the explicit formulas for splitting the Helmholtz kernels in the form of equation (2.33).

Once we construct the linear system to be solved for the unknown density with the combination of above techniques, we use GMRES [76] to determine the density values each target points $(\boldsymbol{x}_i)_{i=1}^N$ on Γ.

3.3.3 Layer potential evaluations along cross-sections

The construction of the scattering matrix requires evaluations of the solution u and partial derivative $\frac{\partial u}{\partial x_1}$ along some chosen cross-sections in the x_2 direction, orthogonal to the wave propagation. For the simple model problem in Figure (3.2), for example, we choose two cross-sections indicated as dotted lines at $x_1 = l$ and $x_1 = r$ on the left and right. As to the target points away from the boundary, we simply apply a standard composite Gauss-Legendre quadrature to evaluate the layer potentials as desired quantities for satisfactory enough resolutions. In the case of the target points close to the boundary, we again apply the kernel-split quadratures to avoid the loss of accuracy caused by near singularities.

3.3.4 Construction of the scattering matrix for a single waveguide component

We describe our method to construct scattering matrix and derive some mathematical identities that relate scattering matrices and propagation modes in this section. Consider a rectangular neighborhood of a cross-section $x_1 = l$:

$$\{\boldsymbol{x} = (x_1, x_2) \in \Omega \,|\, x_1 \in [l - \delta, l + \delta]\} \tag{3.30}$$

with some small enough $\delta > 0$ in Figure 3.2 and assume $L \ll l \ll O$. We also assume the waveguide admits a single propagation mode β_l along the cross-section $x = l$ for now $(M = 1)$. Then, recalling the exponential decay of higher order modes than M described in section 3.2.4, the solution $u(l, x_2)$ to equation (3.12) along the cross-section can be well approximated as

$$u(l, x_2) = u^{inc}(l, x_2) + u^{sc}(l, x_2) \simeq (c_l^+ e^{i\beta_l l} + c_l^- e^{-i\beta_l l}) g_l(x_2) \tag{3.31}$$

where

$$g_l(x_2) = \sqrt{\frac{2}{d_l}} \sin\left(\frac{\pi}{d_l}(x_2 + d_l/2)\right) \tag{3.32}$$

and d_l is the thickness of the cross-section. The coefficient $\sqrt{\frac{2}{d_l}}$ is set to have g_l normalized with respect to the standard L_2 norm over $[-d_l/2, d_l/2]$. The approximation is valid if the device components consist of function modules with straight waveguide structures and support a single mode along each cross-section. In cases of multiple modes, the approximation can be generalized to the summation with respect to the distinct modes, while we focus on the case of a single mode for simplicity here.

Along the right cross-section $x_1 = r$ with $O \ll r \ll R$, similarly assuming another mode β_r,

$$u(r, x_2) = u^{sc}(r, x_2) + u^{inc}(r, x_2) \simeq (c_r^+ e^{i\beta_r r} + c_r^- e^{-i\beta_r r}) g_r(x_2) \tag{3.33}$$

where

$$g_r(x_2) = \sqrt{\frac{2}{d_r}} \sin\left(\frac{\pi}{d_r}(x_2 + d_r/2)\right) \tag{3.34}$$

where d_r is the thickness of the right cross-section.

Remark 3.3.1. *In the case of a completely straight waveguide, we can use the same coordinates as $\boldsymbol{x} = (x_1, x_2)$ with the initially fixed origin for the neighborhood of the cross-section (3.30). However, the structure of the waveguide can be more complicated even if we decompose the waveguide into simpler components. Components can have multiple paths for the wave propagations or can be bent. In such cases, we abuse the notation (x_1, x_2) to construct scattering matrices along cross-sections as follows. Initially, we fix the origin inside the waveguide component on the propagation path(s). The x_1 coordinate for a cross-section is defined as the relative displacement along the propagation path from the origin. Then, the x_2 coordinate along the cross-section is locally defined as the displacement perpendicular to the path at x_1. We define such local coordinates (x_1, x_2) for each cross-section. For example, in*

Figure 3.4 for the case of Y-coupler shaped component, we can define the coordinates of the cross-sections as

- $\{\boldsymbol{x} = (x_1, x_2) \in \Omega \,|\, x_1 = -l, x_2 \in [-d_l/2, d_l/2]\}$,

- $\{\boldsymbol{x} = (x_1, x_2) \in \Omega \,|\, x_1 = r_1, x_2 \in [-d_{r_1}/2, d_{r_1}/2]\}$,

- $\{\boldsymbol{x} = (x_1, x_2) \in \Omega \,|\, x_1 = r_2, x_2 \in [-d_{r_2}/2, d_{r_2}/2]\}$

for the left, top-right, and bottom-right cross-sections respectively with some positive numbers l, r_1, r_2, d_l, d_{r_1}, and d_{r_2}.
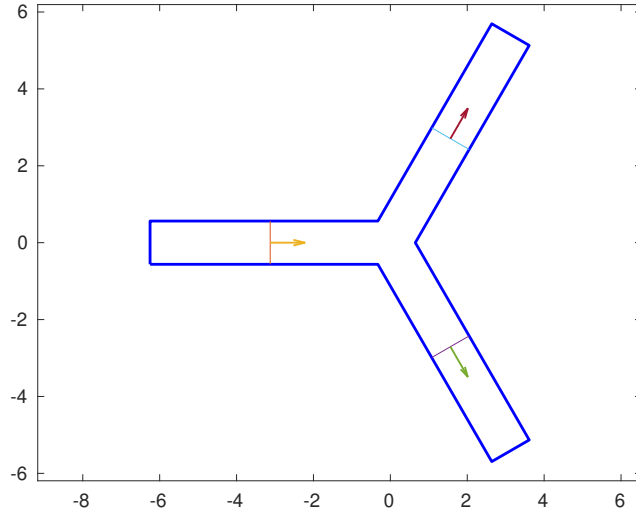
Figure 3.4 A computational domain modeled for a Y-coupler-shaped components.

In the currently discussed simple case, the scattering matrix $\boldsymbol{S}$ is 2×2 since the total number of admitted modes for all cross-sections are two, distinguishing β_l and β_r even if their values are the same. By definition, $\boldsymbol{S}$ satisfies [1]

$$\boldsymbol{S} \begin{bmatrix} c_l^+ \\ c_r^- \end{bmatrix} = \begin{bmatrix} c_l^- \\ c_r^+ \end{bmatrix}. \tag{3.35}$$

---

[1]We can change the alignment of the right-hand side as $\begin{bmatrix} c_r^+ \\ c_l^- \end{bmatrix}$ that makes $\boldsymbol{S}$ the identity matrix in the case of a completely rectangular waveguide ($h_l = h_r$).

The construction of the scattering matrix $\boldsymbol{S}$ is the following. Assuming that we have two solutions of u_1 and u_2 with some linearly independent boundary data, let $u_j(1 \le j \le 2)$ be

$$u_j(l, x_2) \simeq \left(c^+_{l,j} e^{i\beta_l l} + c^-_{l,j} e^{-i\beta_l l} \right) g_{l,j}(x_2), \tag{3.36}$$

$$u_j(r, x_2) \simeq \left(c^+_{r,j} e^{i\beta_r r} + c^-_{r,j} e^{-i\beta_r r} \right) g_{r,j}(x_2). \tag{3.37}$$

Then we construct the linear system

$$\boldsymbol{S} \begin{bmatrix} c^+_{l,1} & c^+_{l,2} \\ c^-_{r,1} & c^-_{r,2} \end{bmatrix} = \begin{bmatrix} c^-_{l,1} & c^-_{l,2} \\ c^+_{r,1} & c^+_{r,2} \end{bmatrix} \tag{3.38}$$

We denote the matrices of coefficients on the left-hand and right-hand sides by

$$\boldsymbol{C}_{inc} := \begin{bmatrix} c^+_{l,1} & c^+_{l,2} \\ c^-_{r,1} & c^-_{r,2} \end{bmatrix}, \tag{3.39}$$

$$\boldsymbol{C}_{sc} := \begin{bmatrix} c^-_{l,1} & c^-_{l,2} \\ c^+_{r,1} & c^+_{r,2} \end{bmatrix}. \tag{3.40}$$

and if $\boldsymbol{C}_{inc}$ is invertible, then we obtain the scattering matrix as

$$\boldsymbol{S} = \boldsymbol{C}_{sc} \boldsymbol{C}^{-1}_{inc}. \tag{3.41}$$

We determine the unknown coefficients

$$\left(c^+_{l,1}, c^-_{l,1}, c^+_{r,1}, c^-_{r,1} \right) \tag{3.42}$$

and

$$\left(c^+_{l,2}, c^-_{l,2}, c^+_{r,2}, c^-_{r,2} \right) \tag{3.43}$$

separately for each $j = \{1, 2\}$ to obtain M_{inc} and M_{sc}.

We omit j in the following discussion since we only need to repeat the same algorithm with distinct boundary data with for $j = 1$ and $j = 2$. We use the following two equations to determine c_l^+ c_l^-:

$$u(l, x_2) \simeq \left(c_l^+ e^{i\beta_l l} + c_l^- e^{-i\beta_l l} \right) g_l(x_2), \tag{3.44}$$

$$u_x(l, x_2) := \frac{\partial u}{\partial x}(l, x_2) \simeq i\beta_l \left(c_l^+ e^{i\beta_l l} - c_l^- e^{-i\beta_l l} \right) g_l(x_2), \tag{3.45}$$

Taking the inner products $\langle u, g_l \rangle$ and $\langle \frac{\partial u}{\partial x}, g_l \rangle$ with respect to x_2 over $[-d_l/2, d_l/2]$ using a normalized eigenfunction $g_l(x_2)$, we have

$$c_l^+ e^{i\beta_l l} + c_l^- e^{-i\beta_l l} = \langle u, g_l \rangle = \int_{-d_l/2}^{d_l/2} u(l, x_2') \overline{g(x_2')} dx_2', \tag{3.46}$$

$$i\beta_l \left(c_l^+ e^{i\beta_l l} - c_l^- e^{-i\beta_l l} \right) = \left\langle \frac{\partial u}{\partial x} g_l \right\rangle = \int_{-d_l/2}^{d_l/2} \frac{\partial u}{\partial x}(l, x_2') \overline{g(x_2')} dx_2'. \tag{3.47}$$

Then, we obtain

$$c_l^+ = \frac{1}{2} e^{-i\beta_l l} \left(I_1 + \frac{1}{i\beta_l} I_2 \right), \tag{3.48}$$

$$c_l^- = \frac{1}{2} e^{i\beta_l l} \left(I_1 - \frac{1}{i\beta_l} I_2 \right). \tag{3.49}$$

where $I_1 := \int_{-d_l/2}^{d_l/2} u(l, x_2') \overline{g(x_2')} dx_2'$ and $I_2 := \int_{-d_l/2}^{d_l/2} u_x(l, x_2') \overline{g(x_2')} dx_2'$.

We apply a BIE method with the mathematical formulations described in Subsection 3.3.3 for the evaluations I_1 and I_2.

Once we obtain the coefficients $(c_{l,1}^+, c_{l,1}^-, c_{r,1}^+, c_{r,1}^-)$, for the first set of data, we repeat the same procedure for the second data ($j = 2$) with distinct boundary data. Then $\boldsymbol{C}_{inc}$ and $\boldsymbol{C}_{sc}$ are constructed having the entries of these vectors for $\boldsymbol{S} = \boldsymbol{C}_{sc}\boldsymbol{C}_{inc}^{-1}$.

So far, we discussed the construction of the scattering matrix with only two ports and a single propagation mode on each channel. This method can be generalized for cases of more ports and more modes allowed in a straightforward manner, because the unknown coefficients C^+ and C^- can be separately computed for each channel, as long as that enough distinct boundary data are provided. In the cases of multiple

modes allowed for one channel, we note that the corresponding equations such as (3.31) and (3.32) have to be replaced with an appropriate linear combination

$$u(x_p, x_2) \simeq \sum_{m=1}^{M} (c_{x_p,m}^{+} e^{i\beta_{x_p,m} x_p} + c_{x_p}^{-} e^{-i\beta_{x_p,m} x_p}) g_{x_p,m}(x_2), \qquad (3.50)$$

and

$$g_{x_p,m}(x_2) = \sqrt{\frac{2}{d_{x_p}}} \sin \left(m \frac{\pi}{d_{x_p}} (x_2 + d_{x_p}/2) \right) \qquad (3.51)$$

where x_p is the x coordinate of the cross-section assigned to the channel with M modes. The most dominant part of the method is to compute the unknown density ρ where we use an iterative method such as GMRES to solve the linear system. This part can be accelerated by incorporating the two dimensional Fast Multipole Method (Rachh et al. [26]).

3.3.5 Merging two scattering matrices

In the previous section, we discussed how to compute the single scattering matrix which corresponds to an individual component of the waveguide. Our goal is the modularization of photonic device simulation in such a way that the whole device can be divided into multiple scattering matrices representing separated structures, and that the information of the whole device can be reconstructed from those scattering matrices already available. Once we managed to construct a modular scattering matrix, we do not have to repeat computing the scattering matrix of the same component or other components with the same structures. Merging multiple scattering matrices into one is done via divide-and-conquer; starting with the two smallest adjacent components, we repeat constructions of larger matrices recursively until the single matrix for the whole structure is obtained. In the following section, we describe how to merge a scattering matrix from two components in the next

section. Although some technical adjustment needs to be taken care of when multiple scattering matrices are merged, we provide the details in appendix B.3.

Merge of two scattering matrices. We discuss how to obtain the scattering matrix of the merged component in this section. Merging two scattering matrices into one matrix illustrates the essential idea and we can merge multiple matrices recursively. Hence, we focus the discussion on the merge of two components. Suppose we have two waveguide components and the associated scattering matrices $\boldsymbol{S}_l$ for the 'left' component and $\boldsymbol{S}_r$ for the 'right' one, respectively. As an example, consider connecting two components shown in Figure 3.5. Figure 3.6 shows the schematic image of the merged component.
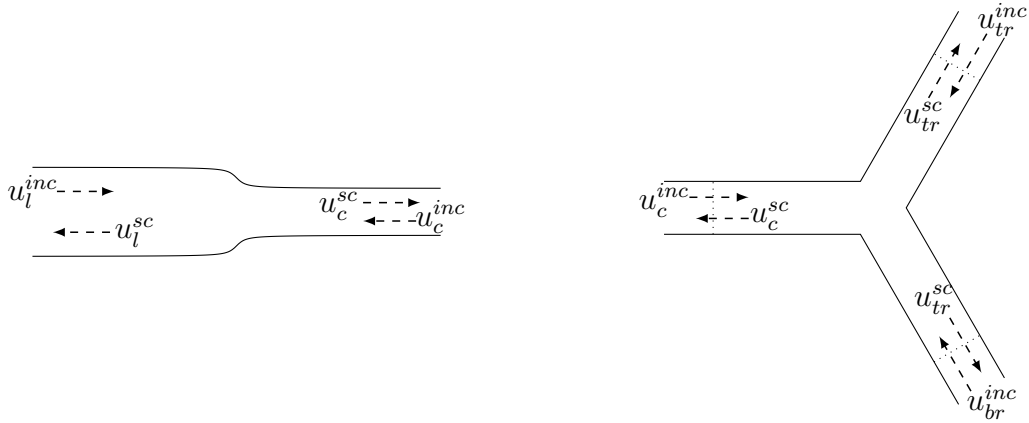
Figure 3.5 Two components of a waveguide before merging. Two scattering matrices $\boldsymbol{S}_l$ and $\boldsymbol{S}_r$ represent corresponding components.
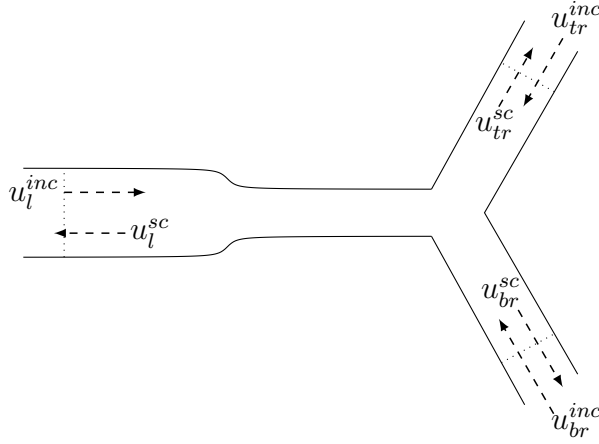
Figure 3.6 The merged component of two parts of Figure 3.5. The scattering matrix $\boldsymbol{S}_t$ representing the whole structure can be constructed from $\boldsymbol{S}_l$ and $\boldsymbol{S}_r$.

Let $(x_{1,l}, x_2)$ and $(x_{1,c}, x_2)$ be cross-sections of the left component, and $(x_{1,c}, x_2)$ and $(x_{1,r}, x_2)$ be cross-sections of the right one, where we intend to merge components along two cross-sections commonly denoted by $(x_{1,c}, x_2)$. Assuming cross-sections allow M_l, M_c, and M_r propagation modes respectively, we approximate the solution $u(x, x_2)$ along the cross-sections as follows.

$$u(x_{1,l}, x_2) \simeq \sum_{m=1}^{M_l} u_{l,m}(x_{1,l}, x_2), \tag{3.52}$$

$$u(x_{1,c}, x_2) \simeq \sum_{m=1}^{M_c} u_{c,m}(x_{1,c}, x_2), \tag{3.53}$$

$$u(x_{1,r}, x_2) \simeq \sum_{m=1}^{M_r} u_{r,m}(x_{1,r}, x_2), \tag{3.54}$$

where

$$u_{l,m}(x_{1,l}, x_2) = \left[c_{l,m}^+ e^{i\beta_{l,m} x_{1,l}} + c_{l,m}^- e^{-i\beta_{l,m} x_{1,l}} \right] g_{l,m}(x_2) \quad m \in \{1, 2, \ldots, M_l\}, \tag{3.55}$$

$$u_{c,m}(x_{1,c}, x_2) = \left[c_{c,m}^+ e^{i\beta_{c,m} x_{1,c}} + c_{c,m}^- e^{-i\beta_{c,m} x_{1,c}} \right] g_{c,m}(x_2) \quad m \in \{1, 2, \ldots, M_c\}, \tag{3.56}$$

$$u_{r,m}(x_{1,r}, x_2) = \left[c_{r,m}^+ e^{i\beta_{r,m} x_{1,r}} + c_{r,m}^- e^{-i\beta_{r,m} x_{1,r}} \right] g_{r,m}(x_2) \quad m \in \{1, 2, \ldots, M_r\}. \tag{3.57}$$

then, the scattering matrices $\boldsymbol{S}_l$ and $\boldsymbol{S}_r$ for two waveguide components satisfy the following linear systems.

$$\boldsymbol{S}_l \begin{bmatrix} \boldsymbol{c}_l^+ \\ \boldsymbol{c}_c^- \end{bmatrix} = \begin{bmatrix} \boldsymbol{S}_{l,11} & \boldsymbol{S}_{l,12} \\ \boldsymbol{S}_{l,21} & \boldsymbol{S}_{l,22} \end{bmatrix} \begin{bmatrix} \boldsymbol{c}_l^+ \\ \boldsymbol{c}_c^- \end{bmatrix} = \begin{bmatrix} \boldsymbol{c}_l^- \\ \boldsymbol{c}_c^+ \end{bmatrix}, \tag{3.58}$$

$$\boldsymbol{S}_r \begin{bmatrix} \boldsymbol{c}_c^+ \\ \boldsymbol{c}_r^- \end{bmatrix} = \begin{bmatrix} \boldsymbol{S}_{r,11} & \boldsymbol{S}_{r,12} \\ \boldsymbol{S}_{r,21} & \boldsymbol{S}_{r,22} \end{bmatrix} \begin{bmatrix} \boldsymbol{c}_c^+ \\ \boldsymbol{c}_r^- \end{bmatrix} = \begin{bmatrix} \boldsymbol{c}_c^- \\ \boldsymbol{c}_r^+ \end{bmatrix}. \tag{3.59}$$

since the two components are connected with some ports where the same propagation modes are admitted, the two linear systems share the same propagation coefficients $\boldsymbol{c}_c^\pm$. $\boldsymbol{c}_l^\pm$ and $\boldsymbol{c}_r^\pm$ correspond to the other coefficient vectors of the left component and the right one, respectively. For example, if we have two components shown in Figure 3.5 and if both components allow only one mode respectively, then $\boldsymbol{c}_l^\pm$, $\boldsymbol{c}_c^\pm$, and $\boldsymbol{c}_r^\pm$ have 1, 1, and 2 entries respectively. If the two waveguide components allow two modes respectively, then $\boldsymbol{c}_l^\pm$, $\boldsymbol{c}_c^\pm$, and $\boldsymbol{c}_r^\pm$ have 2, 2, and 4 entries respectively. We also assume the phase adjustment described in the previous section has been already applied to $\boldsymbol{S}_r$ to share the same origin as $\boldsymbol{S}_l$. The two linear systems of separated components give us four vector equations.

$$\begin{cases} \boldsymbol{S}_{l,11}\boldsymbol{c}_l^+ + \boldsymbol{S}_{l,12}\boldsymbol{c}_c^- = \boldsymbol{c}_l^-, \\ \boldsymbol{S}_{l,21}\boldsymbol{c}_l^+ + \boldsymbol{S}_{l,22}\boldsymbol{c}_c^- = \boldsymbol{c}_c^+, \\ \boldsymbol{S}_{r,11}\boldsymbol{c}_c^+ + \boldsymbol{S}_{r,12}\boldsymbol{c}_r^- = \boldsymbol{c}_c^-, \\ \boldsymbol{S}_{r,21}\boldsymbol{c}_c^+ + \boldsymbol{S}_{r,22}\boldsymbol{c}_r^- = \boldsymbol{c}_r^+ \end{cases} \tag{3.60}$$

Substituting $\boldsymbol{c}_c^+$ of the second equation into the third one,

$$\boldsymbol{S}_{r,11}\left(\boldsymbol{S}_{l,21}\boldsymbol{c}_l^+ + \boldsymbol{S}_{22}^l\boldsymbol{c}_c^-\right) + \boldsymbol{S}_{r,12}\boldsymbol{c}_r^- = \boldsymbol{c}_c^-. \tag{3.61}$$

Let $\boldsymbol{T} := \boldsymbol{I} - \boldsymbol{S}_{r,11}\boldsymbol{S}_{l,22}$ and assume it is invertible. Then the above equation leads to

$$\boldsymbol{S}_{r,11}\boldsymbol{S}_{l,21}\boldsymbol{c}_l^+ + \boldsymbol{S}_{12}^r\boldsymbol{c}_r^- = \boldsymbol{T}^{-1}\boldsymbol{c}_c^- \tag{3.62}$$

$$\Leftrightarrow \boldsymbol{c}_c^- = \boldsymbol{T}^{-1}\left(\boldsymbol{S}_{r,11}\boldsymbol{S}_{l,21}\boldsymbol{c}_l^+ + \boldsymbol{S}_{r,12}\boldsymbol{c}_r^-\right). \tag{3.63}$$

Eliminating $\boldsymbol{c}_c^-$ in the first equation using the equation above,

$$\boldsymbol{S}_{l,11}\boldsymbol{c}_l^+ + \boldsymbol{S}_{l,12}\boldsymbol{T}^{-1}\boldsymbol{S}_{r,11}\boldsymbol{S}_{l,21}\boldsymbol{c}_l^+ + \boldsymbol{S}_{l,12}\boldsymbol{T}^{-1}\boldsymbol{S}_{r,12}\boldsymbol{c}_r^- = \boldsymbol{c}_l^-. \tag{3.64}$$

Substituting $\boldsymbol{c}_c^+$ in the second equation into the fourth one,

$$\boldsymbol{c}_r^+ = \boldsymbol{S}_{r,21}\left(\boldsymbol{S}_{l,21}\boldsymbol{c}_l^+ + \boldsymbol{S}_{l,22}\boldsymbol{c}_c^-\right) + \boldsymbol{S}_{r,22}\boldsymbol{c}_r^-. \tag{3.65}$$

Eliminating $\boldsymbol{c}_l^-$ in the above equation,

$$\boldsymbol{S}_{r,21}\boldsymbol{S}_{l,21}\boldsymbol{c}_l^+ + \boldsymbol{S}_{r,21}\boldsymbol{S}_{l,22}\boldsymbol{T}^{-1}\boldsymbol{S}_{r,11}\boldsymbol{S}_{l,21}\boldsymbol{c}_l^+ + \boldsymbol{S}_{r,21}\boldsymbol{S}_{l,22}\boldsymbol{T}^{-1}\boldsymbol{S}_{r,12}\boldsymbol{c}_r^- + \boldsymbol{S}_{r,22}\boldsymbol{c}_r^- = \boldsymbol{c}_r^+. \tag{3.66}$$

Since we obtained the equations (3.64) and (3.66) involving only $\boldsymbol{c}_l^\pm$ and $\boldsymbol{c}_r^\pm$, we can construct the 'total' scattering matrix $\boldsymbol{S}_t$ such that

$$\begin{bmatrix} \boldsymbol{S}_{t,11} & \boldsymbol{S}_{t,12} \\ \boldsymbol{S}_{t,21} & \boldsymbol{S}_{t,22} \end{bmatrix} \begin{bmatrix} \boldsymbol{c}_l^+ \\ \boldsymbol{c}_r^- \end{bmatrix} = \begin{bmatrix} \boldsymbol{c}_l^- \\ \boldsymbol{c}_r^+ \end{bmatrix}, \tag{3.67}$$

where

$$\begin{cases} \boldsymbol{S}_{t,11} = \boldsymbol{S}_{l,11} + \boldsymbol{S}_{l,12}\boldsymbol{T}^{-1}\boldsymbol{S}_{r,11}\boldsymbol{S}_{l,21}, \\[2mm] \boldsymbol{S}_{t,12} = \boldsymbol{S}_{l,12}\boldsymbol{T}^{-1}\boldsymbol{S}_{r,12}, \\[2mm] \boldsymbol{S}_{t,21} = \boldsymbol{S}_{r,21}\left(\boldsymbol{S}_{l,21} + \boldsymbol{S}_{l,22}\boldsymbol{T}^{-1}\boldsymbol{S}_{r,11}\boldsymbol{S}_{l,21}\right), \\[2mm] \boldsymbol{S}_{t,22} = \boldsymbol{S}_{r,21}\boldsymbol{S}_{l,22}\boldsymbol{T}^{-1}\boldsymbol{S}_{r,12} + \boldsymbol{S}_{r,22}. \end{cases} \tag{3.68}$$

Merging two or more scattering matrices into one can be done by applying the same step as above recursively.

3.3.6 Some useful identities on scattering matrices

In this section, we show some identities that relate scattering matrices to the propagation modes. These identities can be used to verify numerical experiments presented in the later section.

Lemma 3.3.1. *Suppose $u(x, x_2)$ satisfies $\Delta u + k^2 u = 0$ in a simply connected domain Ω with piecewise smooth boundary $\partial\Omega$, where k is a real number. Then the following equation holds.*

$$\text{Im} \int_{\partial\Omega} u \frac{\overline{\partial u}}{\partial n} dS = 0. \tag{3.69}$$

(Proof.) Recalling Green's first identity

$$\int_{\Omega} \left(\Delta u v + \nabla u \cdot \nabla v \right) dV = \int_{\partial\Omega} \frac{\partial u}{\partial n} u dS, \tag{3.70}$$

with $v := \overline{u}$, we have

$$\int_{\Omega} \left(-k^2 |u|^2 + |\nabla u|^2 \right) dV = \int_{\partial\Omega} \frac{\partial u}{\partial n} \overline{u} dS = \overline{\int_{\partial\Omega} u \frac{\overline{\partial u}}{\partial n} dS}. \tag{3.71}$$

Since the left-hand side is a real number, taking the imaginary part of the equation leads to

$$\text{Im} \int_{\partial\Omega} u \frac{\overline{\partial u}}{\partial n} dS = 0, \tag{3.72}$$

which is the desired identity. $\qquad\qquad\square$

This identity and similar inequalities appear in the existing literature. For example, see the proof of lemma 3.11 in Kress and Colton [18] (the proof is given by Rellich), and the proof of lemma 3.2.1 in Nédélec [65].

Theorem 3.3.1. *Let $\boldsymbol{\beta}$ be the column vector with length M of the propagation modes of a waveguide component, and $\boldsymbol{S}$ be the corresponding M times M scattering matrix. Then, the following identity holds.*

$$\boldsymbol{D_\beta} = \boldsymbol{S}^* \boldsymbol{D_\beta} \boldsymbol{S} \tag{3.73}$$

where $\boldsymbol{D_\beta} := diag(\boldsymbol{\beta})$.

More specifically, $\beta_j = \sum_{k=1}^{M} |S_{k,j}|^2 \beta_k$ for all $j \in \{1, 2, \ldots, M\}$.

The proof is in appendix B.1.

Corollary 3.3.1. *In addition to the assumptions of the theorem above, if each channel admits the same single mode, then the scattering matrix is unitary.*

(Proof) Let the single mode be $\beta > 0$. Since $\boldsymbol{D_\beta} = \beta\boldsymbol{I}$,

$$\boldsymbol{S}^*\boldsymbol{D_\beta} = \boldsymbol{S}^*(\beta\boldsymbol{I}) = (\beta\boldsymbol{I})\boldsymbol{S}^*. \tag{3.74}$$

Therefore, the equation is equivalent to

$$\beta\boldsymbol{I} = \beta\boldsymbol{S}^*\boldsymbol{S} \Leftrightarrow \boldsymbol{I} = \boldsymbol{S}^*\boldsymbol{S}. \tag{3.75}$$

$\square$

On the other hand, it turns out that even if a scattering matrix is unitary, it does not necessarily implies that the set of allowed propagation modes for each channel are identical. An example can be seen in appendix B.2.

3.4 Numerical Examples

We confirm the mathematical results discussed so far with numerical examples in this section. The codes are implemented in MATLAB release 2020b. We carried out the numerical experiments on a standard 64-bit laptop with 11th Gen Intel(R) Core(TM) i7-1185G7 CPU, with 32 GB RAM. The OS on the laptop is Ubuntu 20.04.5 LTS.

3.4.1 Calculation of a single scattering matrix

Initially, we show numerical examples in three cases of computational domains shown in Figure 3.7. The boundary of the top left figure has the same boundary as Figure 3.2; the structure is piecewise smooth and more or less straight in the direction of

the propagation modes. The top right one has a uniform thickness but is bent in the middle by $\frac{1}{4}\pi$ radian. The bottom one has a symmetric structure of a Y-coupler.
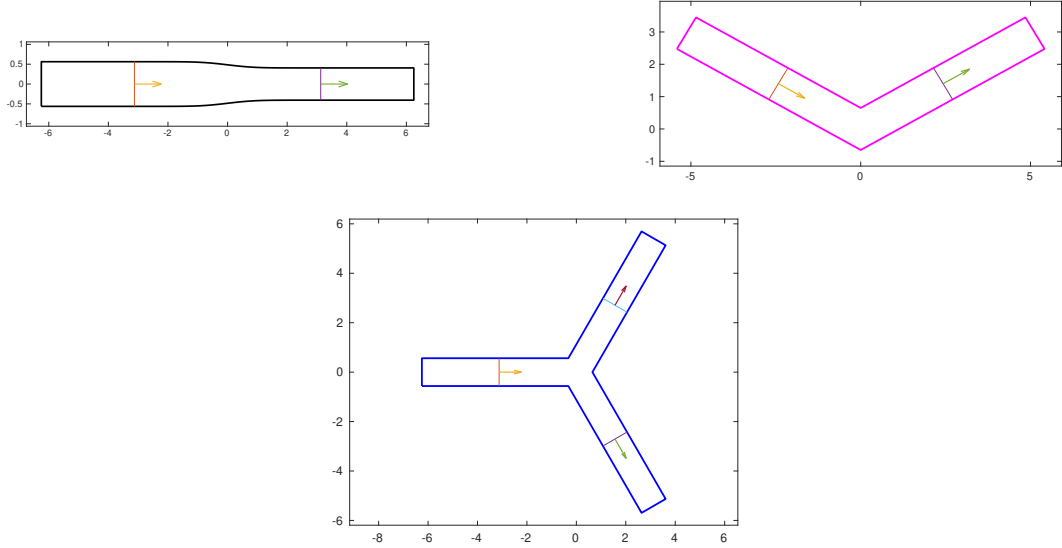
Figure 3.7 Three computational domains for numerical examples of single scattering matrix validations.

The parameters commonly set for the examples are as follows. The wavelength λ is 1.5 with the wavenumber in vacuum $k_v = 2\pi/\lambda \simeq 4.18879$. The refractive index in the domains n is 1.2 with the wavenumber $k = k_v n \simeq 5.02655$. For the top left waveguide, the thicknesses (d_l, d_r) of cross-sections on the left and right sides are $(1.8\pi/k, 1.3\pi/k) = (1.125, 0.8125)$ for a single mode, and $(2.8\pi/k, 2.3\pi/k) = (1.75, 1.4375)$ for two modes on each side, respectively. For the other two domains, the thicknesses of all cross-sections denoted by h are set to $1.8\pi/k = 1.125$ for a single mode, and $2.8\pi/k = 1.4375$ for two modes on each side, respectively.

Concerning the numerical method we apply to the computations of scattering matrices, We discretize the boundary curves with standard panel-based Gauss-Legendre nodes. Each panel has 16 nodes and we place two panels per wavelength on the boundary curves. Then, imposing distinct smooth boundary data on the channels of the waveguides, we compute the propagation coefficients applying the BIE method

based on the formulations described in section 3.2.7 coupled with the RCIP method and kernel-split quadratures on the discretized boundary. We repeatedly compute the propagation coefficients an adequate number of times to construct the scattering matrices with distinct smooth boundary data.

The convergence of the scattering matrices and identity (3.73) is measured in terms of the relative error norms. The plots are shown in Figure 3.8. We observe that the relative errors are convergent as the paths of propagation become longer in each case. The length of path for each case seems to be long enough between 20 and 40 times wavelength from the results.
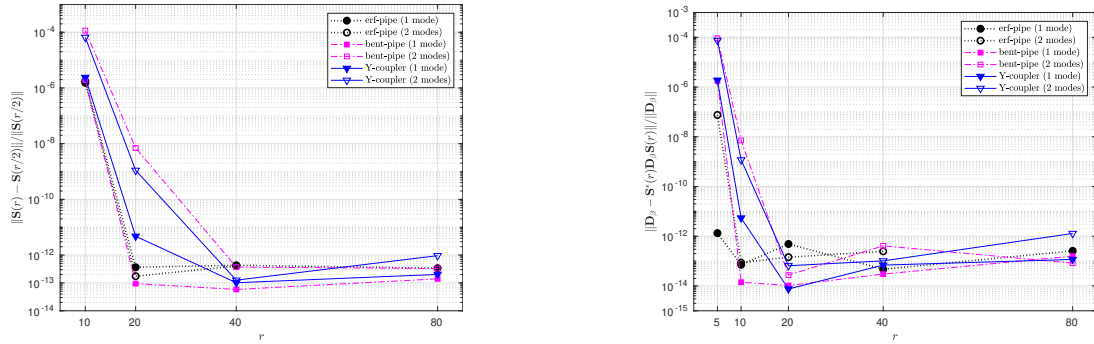
Figure 3.8 Numerical results of single components using three computational domains in Figure 3.7. r for the horizontal axes in these figures indicates the maximum distance between the channels and the center of the domain divided by the wavelength λ. e.g., if r equals 10, the distance between the center and the outermost channel along the propagation is 10λ.
Left: self-convergence tests. The vertical axis corresponds to the relative error norms $\|\boldsymbol{S}(r) - \boldsymbol{S}(r/2)\|_2/\|\boldsymbol{S}(r/2)\|_2$ for $r \in \{10, 20, 40, 80\}$.
Right: validations of identity (3.73). The horizontal axis corresponds to the same definition of r of the left figure. The vertical axis corresponds to the relative error norms $\|\boldsymbol{S}^*(r)\boldsymbol{D}[\boldsymbol{\beta}]\boldsymbol{S}(r) - \boldsymbol{D}[\boldsymbol{\beta}]\|_2/\|\boldsymbol{D}[\boldsymbol{\beta}]\|_2$ for $r \in \{5, 10, 20, 40, 80\}$.

3.4.2   Accuracy of the merging formula

As the next set of numerical examples, we confirm equation (3.68) and identity (3.73) for merging two scattering matrices. Here, we choose two computational domains shown in Figure 3.9. The domain on the left is constructed by connecting the erf-pipe and the Y-coupler in Figure 3.7, and the right one is obtained by connecting two bent pipes.
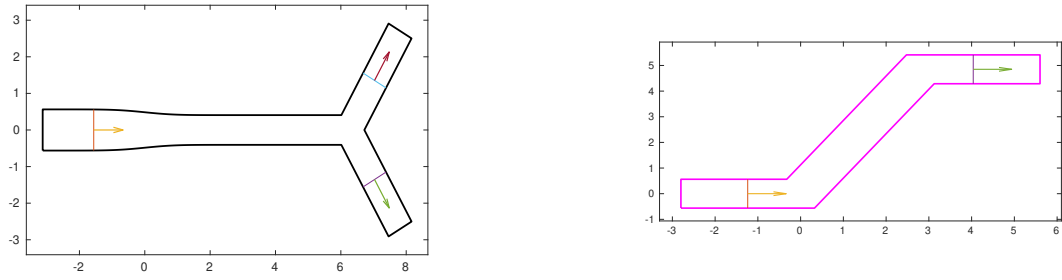
Figure 3.9 Two computational domains by merging individual components.

The results are shown in Figure 3.10. We also see the convergent relative errors as increasing the distance between two centers of components before they are merged.
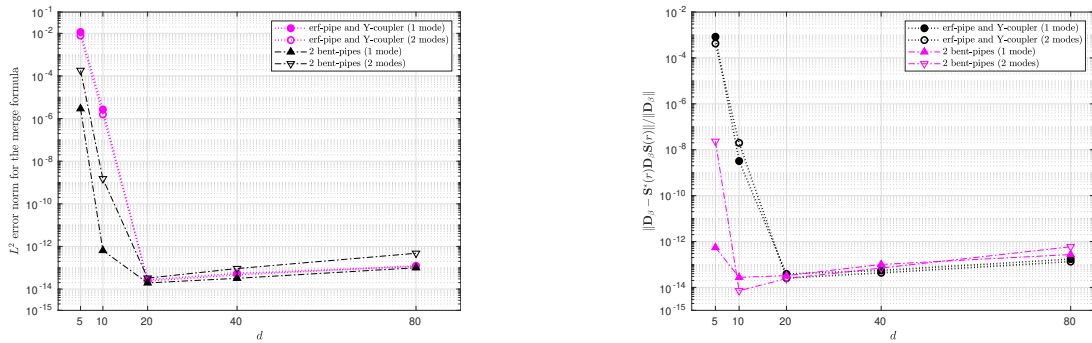
Figure 3.10 Numerical results of merged components using two computational domains in Figure 3.7. d for the horizontal axis in these figures indicates the distance divided by the wavelength λ between two centers of components along the path of the propagation before they are merged. Left: self-convergence tests. The vertical axis corresponds to relative error norms of two scattering matrices for each d. One is computed with the merged computational domain in Figure 3.9, and the other is the scattering matrix constructed via equation (3.68) and the scattering matrices computed individually before they merged.
Right: validations of identity (3.73) the same way as Figure 3.8, with merged computational domain in Figure 3.9.

Finally, we examine our method for modularization merging more components. We show an example with merging four components: two bent-pipes and two Y-couplers, as shown in the Figure 3.11. We use parameter d defined as the length of the propagation path between the left and right junctions. The cross-sections on the left and right sides are places at fixed $x_1 = 14\lambda$ where $\lambda = 1.25$ is the given wavelength. The relative error norms $\|\boldsymbol{S}(d) - \boldsymbol{S}(d-2)\|/\|\boldsymbol{S}(d-2)\|$ are measured and summarized on the Table 3.1. We observe that the relative errors attain some

89

lower bound around 10^{-12} once d is greater than equal to 20 in our experiments. The relative error norms compared with upper bound estimation (3.9) are shown in Figure 3.12. The convergence rate agrees with the upper bound estimation until it attain some lower bound around 10^{-12}.
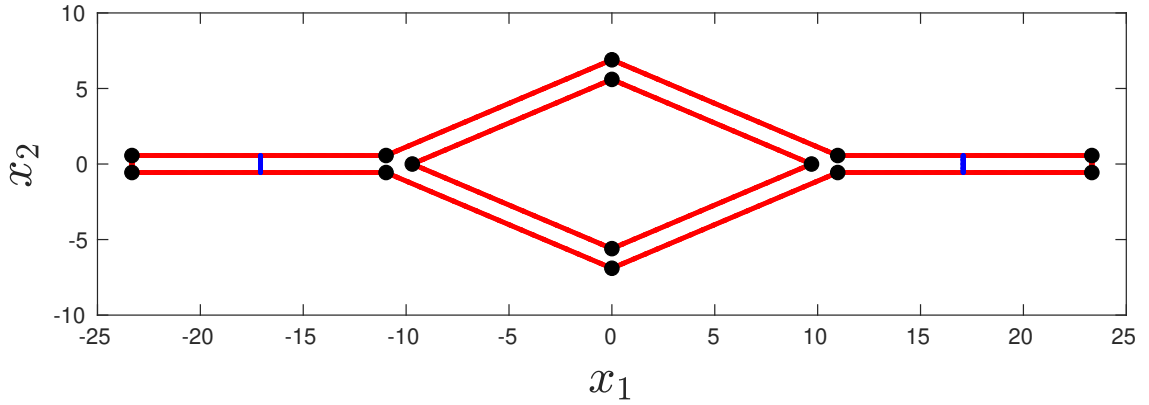
Figure 3.11 Merged computational domain obtained from four objects (two Y-couplers and two bent-pipes). Two bent-pipes are placed in the middle and connected between two Y-couplers on the left and right. Black dots indicate the corners of the merged objects, and blue line segments are the cross-sections where the evaluations are carried out to compute the merged scattering matrix.

Table 3.1 Relative Error Norms $\|\boldsymbol{S}(d) - \boldsymbol{S}(d-2)\|/\|\boldsymbol{S}(d-2)\|$

d/λ	$\|\boldsymbol{S}(d) - \boldsymbol{S}(d-2)\|/\|\boldsymbol{S}(d-2)\|$
4	2.54925e-02
6	1.90989e-03
8	4.55863e-05
10	2.63197e-06
12	2.11041e-07
14	5.04391e-09
16	2.86362e-10
18	2.23167e-11
20	3.75420e-12
22	1.64128e-12
24	3.40560e-12
26	3.05768e-12
28	1.62932e-12

Parameter d (the leftmost number in each row) is the distance of the propagation path between junction from the left to right. The distance between each cross-section and its closest junction is set to 14 times wavelength $\lambda = 1.25$.
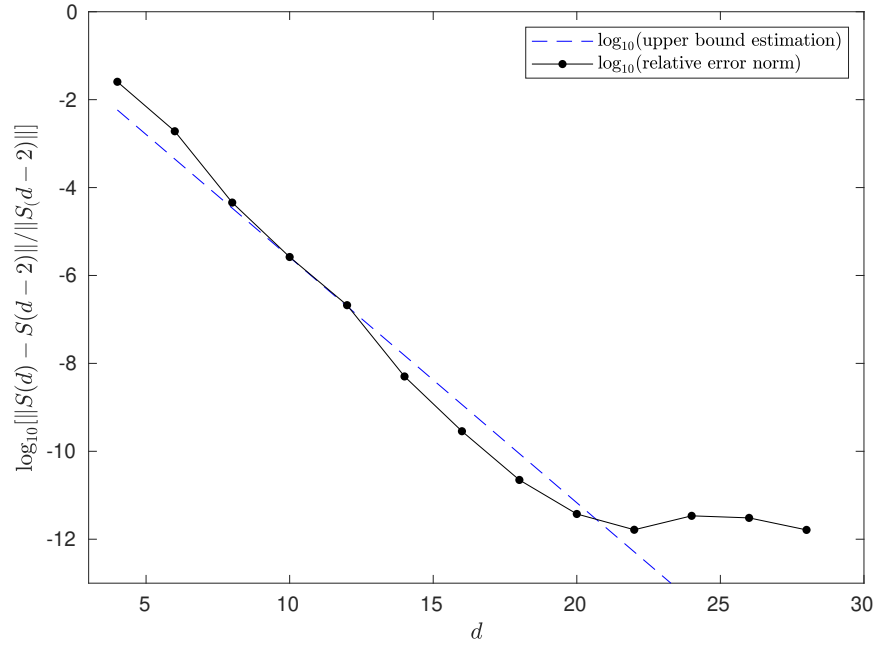
Figure 3.12 Plots of $\log_{10}\left[\|\boldsymbol{S}(d) - \boldsymbol{S}(d-2)\|/\|\boldsymbol{S}(d-2)\|\right]$ compared with upper bound estimation (3.9)

CHAPTER 4

CONCLUSIONS

In this dissertation, we have presented the development of numerical methods based on BIE methods for two types of boundary value problems of partial differential equations that arise from mathematical physics. In the first half of this dissertation, we have developed an accurate and fast numerical method based on the BIE methods for the interior mixed boundary value problems for Stokes equations and for applications to SH flow. We have chosen a layer potential representation for the solution to a given problem in terms of boundary integral equations. Then, we have incorporated a set of state-of-the-art numerical methods into our method: the RCIP method, the scaling technique, the kernel-split quadratures, and the Stokes FMM. Our method can achieve high accuracy since it can handle singular behavior in the neighborhood of corners and boundary transition points, and the algorithm is efficient in terms of both time and space complexities. As the future work, solving the linear system can be accelerated with preconditioning the BIEs utilizing the Calderon identities, as we observe that the convergence of GMRES iterations become slower when we impose the composite boundary conditions for the SH flow. Also, the extensions of our method to problems with surfactant and the three-dimensional problems can be desired.

In the second half of this dissertation, we have proposed a numerical method to construct scattering matrices for the large-scale simulation for integrated photonics development. We have chosen a divide-and-conquer approach taking advantage of two key facts. One is that integrated photonic devices locally consist of function modules with straight waveguides as input/output channels. The other is that each straight waveguide supports only a small number of propagating modes. Utilizing these key

facts, we have developed a numerical method to construct scattering matrices for pre-computable and reusable modularizations, instead of computing in the whole domain every time. We also have incorporated a state-of-art boundary integral equation (BIE) method, the RCIP method [36], and the high-order kernel-split quadratures [37, 38, 41] together to obtain high resolutions. We have observed our method works well for the two-dimensional cases with Dirichlet boundary conditions. The future work includes the extension of our method to the dielectric cases, i.e., more difficult cases with transmission boundary conditions in the two-dimensional space, and then to the three-dimensional cases ultimately.

APPENDIX A

SUPPLEMENTS TO SUPERHYDROPHOBIC FLOW

A.1 Derivations of Stokes Layer Potentials in $\mathbb{R}^2$

Following equation (2.1.8) in Pozrikidis [69], the Green's function associated with Stokes equations is given by

$$G_{ij}(\boldsymbol{x}, \boldsymbol{y}) := -\delta_{ij} \ln(r) + \frac{1}{r^2} r_i r_j, \tag{A.1}$$

where $\boldsymbol{r} := \boldsymbol{x} - \boldsymbol{y}$, $r := |\boldsymbol{r}|$, and $r_i := (\boldsymbol{x} - \boldsymbol{y})_i$ $(i, j \in \{1, 2\})$. (We use $r_i = \boldsymbol{x} - \boldsymbol{y}$ instead of $\hat{x} = \boldsymbol{y} - \boldsymbol{x}$ to obtain the same layer-potential representations as Wu et al. [80] so that the coefficients of the identity operators of the boundary integral equations are commonly 1/2.)

The pressure vector $\boldsymbol{p}$ is given as

$$\boldsymbol{p} = p_i := \frac{2}{r^2} r_i. \tag{A.2}$$

Let

$$\sigma[G]_{ijk}(\boldsymbol{x}, \boldsymbol{y}) := -\delta_{ik} p_j(\boldsymbol{x}, \boldsymbol{y}) + \mu \left(\frac{\partial G_{ij}}{\partial x_k}(\boldsymbol{x}, \boldsymbol{y}) + \frac{\partial G_{kj}}{\partial x_i}(\boldsymbol{x}, \boldsymbol{y}) \right), \tag{A.3}$$

$$\sigma[G]_{ijk}(\boldsymbol{y}, \boldsymbol{x}) := -\delta_{ik} p_j(\boldsymbol{y}, \boldsymbol{x}) + \mu \left(\frac{\partial G_{ij}}{\partial y_k}(\boldsymbol{y}, \boldsymbol{x}) + \frac{\partial G_{kj}}{\partial y_i}(\boldsymbol{y}, \boldsymbol{x}) \right) \tag{A.4}$$

$$= \delta_{ik} p_j(\boldsymbol{x}, \boldsymbol{y}) + \mu \left(\frac{\partial G_{ij}}{\partial y_k}(\boldsymbol{x}, \boldsymbol{y}) + \frac{\partial G_{kj}}{\partial y_i}(\boldsymbol{x}, \boldsymbol{y}) \right) \tag{A.5}$$

Then the stress tensor $\boldsymbol{\sigma} = \boldsymbol{T} = T_{ijk}(\boldsymbol{x}, \boldsymbol{y})$ is defined as

$$T_{ijk}(\boldsymbol{x}, \boldsymbol{y}) := -\sigma[\frac{1}{\mu} G_{ij}(\boldsymbol{x}, \boldsymbol{y})] = \delta_{ik} p_j(\boldsymbol{x}, \boldsymbol{y}) - \frac{\partial G_{ij}}{\partial x_k}(\boldsymbol{x}, \boldsymbol{y}) - \frac{\partial G_{kj}}{\partial x_i}(\boldsymbol{x}, \boldsymbol{y}) \tag{A.6}$$

$(i, j, k \in \{1, 2\})$. It turns out that

$$T_{ijk}(\boldsymbol{x}, \boldsymbol{y}) = \frac{1}{r^4} r_i r_j r_k, \tag{A.7}$$

which can be proven as follows. Noting the equations below,

$$\frac{\partial}{\partial x_i} \ln r = \frac{1}{r} \frac{\partial r}{\partial x_i} = \frac{1}{r^2} r_i, \tag{A.8}$$

$$\frac{\partial}{\partial y_i} \ln r = \frac{1}{r} \frac{\partial r}{\partial y_i} = -\frac{1}{r^2} r_i, \tag{A.9}$$

$$\frac{\partial}{\partial x_i}[r^{-n}] = -nr^{-n-2}r_i, \tag{A.10}$$

$$\frac{\partial}{\partial y_i}[r^{-n}] = nr^{-n-2}r_i, \tag{A.11}$$

$$\frac{\partial G_{ij}}{\partial x_k} = \delta_{ij}r^{-2}r_k - 2r^{-4}r_k r_i r_j + r^{-2}\delta_{ik}r_j + r^{-2}r_i \delta_{jk}, \tag{A.12}$$

$$\frac{\partial G_{kj}}{\partial x_i} = \delta_{kj}r^{-2}r_i - 2r^{-4}r_i r_j r_k + r^{-2}\delta_{ki}r_j + r^{-2}r_k \delta_{ji}. \tag{A.13}$$

$$\therefore T_{ijk}(\boldsymbol{x}, \boldsymbol{y}) = \delta_{ik}p_j - \frac{\partial G_{ij}}{\partial x_k} - \frac{\partial G_{kj}}{\partial x_i} \tag{A.14}$$

$$= 2\delta_{ik}r^{-2}r_j + 4r^{-4}r_i r_j r_k - 2\delta_{ik}r^{-2}r_j \tag{A.15}$$

$$= 4r^{-4}r_i r_j r_k. \quad \square \tag{A.16}$$

The surface force (traction) $\boldsymbol{f}$ at $\boldsymbol{y} \in \Gamma$ is defined as

$$\boldsymbol{f} := \boldsymbol{\sigma}(\boldsymbol{x}, \boldsymbol{y})\boldsymbol{n}(\boldsymbol{y}) = T_{ijk}(\boldsymbol{x}, \boldsymbol{y})n_{y,k}. \tag{A.17}$$

where $n_{y,k} := \boldsymbol{n}(\boldsymbol{y})$ is a unit normal vector at $\boldsymbol{y}$ pointing outwards.

The single-layer potential is defined as

$$\boldsymbol{S}[\boldsymbol{\rho}](\boldsymbol{x}) := \frac{1}{4\pi\mu} \int_{\Gamma} G_{ij}(\boldsymbol{x}, \boldsymbol{y})\rho_j(\boldsymbol{y})n_k(\boldsymbol{y})dS_y. \tag{A.18}$$

$\boldsymbol{S}'$ which appears for Neumann boundary condition is defined as

$$\boldsymbol{S}'_i := \frac{1}{4\pi\mu} \int_\Gamma \sigma[G]_{ijk}(\boldsymbol{x}, \boldsymbol{y}) n_{x,k} \rho_j dS_y \tag{A.19}$$

$$= \frac{1}{4\pi} \int_\Gamma \sigma[\frac{1}{\mu} G_{ij}]_k(\boldsymbol{x}, \boldsymbol{y}) n_{x,k} \rho_j dS_y \tag{A.20}$$

$$= -\frac{1}{4\pi} \int_\Gamma -\sigma[\frac{1}{\mu} G_{ij}]_k(\boldsymbol{x}, \boldsymbol{y}) \rho_j n_{x,k} dS_y \tag{A.21}$$

$$= -\frac{1}{4\pi} \int_\Gamma T_{ijk}(\boldsymbol{x}, \boldsymbol{y}) \rho_j n_{x,k} dS_y. \tag{A.22}$$

As for the double-layer potential $\boldsymbol{D}[\boldsymbol{\rho}](\boldsymbol{x})$, noting

$$\sigma[\frac{1}{\mu} G]_{jik}(\boldsymbol{y}, \boldsymbol{x}) = -\delta_{jk} p_i(\boldsymbol{y}, \boldsymbol{x}) + \mu \left(\frac{1}{\mu} \frac{\partial G_{ji}}{\partial y_k}(\boldsymbol{y}, \boldsymbol{x}) + \frac{1}{\mu} \frac{\partial G_{ki}}{\partial y_j}(\boldsymbol{y}, \boldsymbol{x}) \right) \tag{A.23}$$

$$= -\delta_{jk}(-p_i(\boldsymbol{x}, \boldsymbol{y})) + \left(\frac{\partial G_{ji}}{\partial y_k}(\boldsymbol{x}, \boldsymbol{y}) + \frac{\partial G_{ki}}{\partial y_j}(\boldsymbol{x}, \boldsymbol{y}) \right) \tag{A.24}$$

$$= 2r^{-2} \delta_{jk} r_i \tag{A.25}$$

$$- \delta_{ji}(-r^{-2} r_k) + 2r^{-4} r_k r_j r_i - r^{-2} \delta_{jk} r_i - r^{-2} r_j \delta_{ik} \tag{A.26}$$

$$- \delta_{ki}(-r^{-2} r_j) + 2r^{-4} r_j r_k r_i - r^{-2} \delta_{kj} r_i - r^{-2} r_k \delta_{ij} \tag{A.27}$$

$$= 4r^{-4} r_i r_j r_k \tag{A.28}$$

$$= T_{ijk}(\boldsymbol{x}, \boldsymbol{y}), \tag{A.29}$$

$\boldsymbol{D}[\boldsymbol{\rho}](\boldsymbol{x})$ is defined as

$$\boldsymbol{D}[\boldsymbol{\rho}](\boldsymbol{x}) := \frac{1}{4\pi\mu} \int_\Gamma \sigma[G]_{jik}(\boldsymbol{y}, \boldsymbol{x}) \rho_j n_{y,k} dS_y \tag{A.30}$$

$$= \frac{1}{4\pi} \int_\Gamma \sigma[\frac{1}{\mu} G]_{jik}(\boldsymbol{y}, \boldsymbol{x}) \rho_j n_{y,k} dS_y \tag{A.31}$$

$$= \frac{1}{4\pi} \int_\Gamma T_{ijk}(\boldsymbol{x}, \boldsymbol{y}) \rho_j n_{y,k} dS_y. \tag{A.32}$$

This matches equation (4) in Wu et al. [80]. Also, by definition, $\sigma[\frac{1}{\mu} G]_{jik}(\boldsymbol{y}, \boldsymbol{x}) = T_{jik}(\boldsymbol{y}, \boldsymbol{x}) = T_{ijk}(\boldsymbol{x}, \boldsymbol{y})$ holds and the above definition of $\boldsymbol{D}$ matches equation (4.3.1) in Pozrikidis [69].

The single-layer potential of pressure P^S is defined as

$$P^S[\boldsymbol{\rho}](\boldsymbol{x}) := \frac{1}{4\pi} \int_\Gamma p_j(\boldsymbol{x}, \boldsymbol{y}) \rho_j dS_y = \frac{1}{4\pi} \int_\Gamma \frac{2}{r^2} r_j(\boldsymbol{x}, \boldsymbol{y}) \rho_j dS_y = \frac{1}{2\pi} \int_\Gamma \frac{1}{r^2} (\boldsymbol{r} \cdot \boldsymbol{\rho}) \, dS_y,$$

(A.33)

and the double-layer potential of pressure P^D is defined as

$$P^D[\boldsymbol{\rho}](\boldsymbol{x}) := \frac{\mu}{4\pi} \int_\Gamma \Pi_{jk}(\boldsymbol{x}, \boldsymbol{y}) \rho_j n_{y,k} dS_y$$

(A.34)

where

$$\Pi_{jk}(\boldsymbol{x}, \boldsymbol{y}) := -\left(\frac{\partial p_j}{\partial x_k} + \frac{\partial p_k}{\partial x_j} \right)$$

(A.35)

$$= -\frac{\partial}{\partial x_k}[2r^{-2}]r_j - \frac{\partial}{\partial x_j}[2r^{-2}]r_k$$

(A.36)

$$= -2(-2r^{-4}r_k r_j + r^{-2}\delta_{jk}) + -2(-2r^{-4}r_j r_k + r^{-2}\delta_{kj})$$

(A.37)

$$= 4(-r^{-2}\delta_{jk} + 2r^{-4}r_j r_k).$$

(A.38)

$$\therefore P^S[\boldsymbol{\rho}](\boldsymbol{x}) = \frac{\mu}{4\pi} \int_\Gamma 4(r^{-2}\delta_{jk} - 2r^{-4}r_j r_k) \rho_j n_{y,k} dS_y$$

(A.39)

$$= \frac{\mu}{4\pi} \int_\Gamma (r^{-2}\delta_{jk} - 2r^{-4}r_j r_k) \rho_j n_{y,k} dS_y.$$

(A.40)

Here we derive $\boldsymbol{D}'$. The kernel of $\boldsymbol{D}'$ is defined as

$$\boldsymbol{K}^{\boldsymbol{D}'} := \left(\frac{\partial T_{ijk}}{\partial x_l}(\boldsymbol{x}, \boldsymbol{y}) + \frac{\partial T_{ljk}}{\partial x_i}(\boldsymbol{x}, \boldsymbol{y}) \right) n_{y,k} n_{x,l} - \Pi_{jk} n_{y,k} n_{x,i}(\boldsymbol{x}, \boldsymbol{y})$$

(A.41)

with four indices i, j, k, and l $(i, j, k, l \in \{1, 2\})$.

$$\frac{\partial T_{ijk}}{\partial x_l}(\boldsymbol{x}, \boldsymbol{y}) = \frac{\partial}{\partial x_l}[4r^{-4}r_i r_j r_k]$$

(A.42)

$$= 4[-4r^{-6}r_l r_i r_j r_k + r^{-4}\delta_{il}r_j r_k + r^{-4}r_i\delta_{jl}r_k + r^{-4}r_i r_j\delta_{kl}],$$

(A.43)

$$\frac{\partial T_{ljk}}{\partial x_i}(\boldsymbol{x}, \boldsymbol{y}) = \frac{\partial}{\partial x_i}[4r^{-4}r_l r_j r_k]$$

(A.44)

$$= 4[-4r^{-6}r_i r_l r_j r_k + r^{-4}\delta_{li}r_j r_k + r^{-4}r_l\delta_{ji}r_k + r^{-4}r_l r_j\delta_{ki}].$$

(A.45)

$$\therefore \frac{1}{4} \left[\frac{\partial T_{ijk}}{\partial x_l}(\boldsymbol{x}, \boldsymbol{y}) + \frac{\partial T_{ljk}}{\partial x_i}(\boldsymbol{x}, \boldsymbol{y}) \right] n_{y,k} n_{x,l} \tag{A.46}$$

$$= -8r^{-6} r_i r_j (r_k n_{y,k})(r_l n_{x,l}) + 2r^{-4}(\delta_{il} n_{x,l}) r_j (r_k n_{y,k}) \tag{A.47}$$

$$+ r^{-4} r_i (\delta_{jl} n_{x,l})(r_k n_{y,k}) + r^{-4} r_i r_j \delta_{kl} n_{x,l} n_{y,k} \tag{A.48}$$

$$+ r^{-4} \delta_{ij}(r_k n_{y,k})(r_l n_{x,l}) + r^{-4} r_j (\delta_{ki} n_{y,k})(r_l n_{x,l}) \tag{A.49}$$

$$= -8r^{-6} (\boldsymbol{r} \cdot \boldsymbol{n_y}) (\boldsymbol{r} \cdot \boldsymbol{n_x}) [r \otimes r] + 2r^{-4} (\boldsymbol{r} \cdot \boldsymbol{n_y}) [n_x \otimes r] \tag{A.50}$$

$$+ r^{-4} (\boldsymbol{r} \cdot \boldsymbol{n_y}) [r \otimes n_x] + r^{-4} (\boldsymbol{n_x} \cdot \boldsymbol{n_y}) [r \otimes r] \tag{A.51}$$

$$+ r^{-4} (\boldsymbol{r} \cdot \boldsymbol{n_x}) (\boldsymbol{r} \cdot \boldsymbol{n_y}) I + r^{-4} (\boldsymbol{r} \cdot \boldsymbol{n_x}) [n_y \otimes r] . \tag{A.52}$$

As for the pressure term $\Pi_{jk} n_{y,k} n_{x,i}$,

$$\frac{1}{4} \Pi_{jk} n_{y,k} n_{x,i} = -(r^{-2} \delta_{jk} - 2r^{-4} r_j r_k) n_{y,k} n_{x,i} \tag{A.53}$$

$$= -r^{-2}(n_{x,i} n_{y,j}) + 2r^{-4}(r_k n_{y,k})(n_{x,i} r_j) \tag{A.54}$$

$$= -r^{-2} [n_x \otimes n_y] + 2r^{-4} (\boldsymbol{r} \cdot \boldsymbol{n_y}) [n_x \otimes r] . \tag{A.55}$$

$$\therefore \frac{1}{4} \boldsymbol{K^{D'}} = \frac{1}{4} \left(\frac{\partial T_{ijk}}{\partial x_l}(\boldsymbol{x}, \boldsymbol{y}) + \frac{\partial T_{ljk}}{\partial x_i}(\boldsymbol{x}, \boldsymbol{y}) \right) n_{y,k} n_{x,l} - \Pi_{jk} n_{y,k} n_{x,i}(\boldsymbol{x}, \boldsymbol{y}) \tag{A.56}$$

$$= -8r^{-6} (\boldsymbol{r} \cdot \boldsymbol{n_y}) (\boldsymbol{r} \cdot \boldsymbol{n_x}) [r \otimes r] + \underset{\nearrow 0}{2r^{-4} (\boldsymbol{r} \cdot \boldsymbol{n_y}) [n_x \otimes r]} \tag{A.57}$$

$$+ r^{-4} (\boldsymbol{r} \cdot \boldsymbol{n_y}) [r \otimes n_x] + r^{-4} (\boldsymbol{n_x} \cdot \boldsymbol{n_y}) [r \otimes r] \tag{A.58}$$

$$+ r^{-4} (\boldsymbol{r} \cdot \boldsymbol{n_x}) (\boldsymbol{r} \cdot \boldsymbol{n_y}) I + r^{-4} (\boldsymbol{r} \cdot \boldsymbol{n_x}) [n_y \otimes r] \tag{A.59}$$

$$+ r^{-2} [n_x \otimes n_y] - \underset{\nearrow 0}{2r^{-4} (\boldsymbol{r} \cdot \boldsymbol{n_y}) [n_x \otimes r]} \tag{A.60}$$

$$= -8r^{-6} (\boldsymbol{r} \cdot \boldsymbol{n_y}) (\boldsymbol{r} \cdot \boldsymbol{n_x}) [r \otimes r] + r^{-4} (\boldsymbol{r} \cdot \boldsymbol{n_y}) [r \otimes n_x] \tag{A.61}$$

$$+ r^{-4} (\boldsymbol{n_x} \cdot \boldsymbol{n_y}) [r \otimes r] + r^{-4} (\boldsymbol{r} \cdot \boldsymbol{n_x}) (\boldsymbol{r} \cdot \boldsymbol{n_y}) I \tag{A.62}$$

$$+ r^{-4} (\boldsymbol{r} \cdot \boldsymbol{n_x}) [n_y \otimes r] + r^{-2} [n_x \otimes n_y] . \tag{A.63}$$

D' is defined as

$$D'[\rho](x) = \frac{\mu}{4\pi} \int_\Gamma K_{ij}^{D'} \rho_j dS_y = \frac{\mu}{\pi} \int_\Gamma \frac{1}{4} K_{ij}^{D'} \rho_j dS_y \tag{A.64}$$

$$= \frac{\mu}{\pi} \int_\Gamma \left(-8r^{-6} (\boldsymbol{r} \cdot \boldsymbol{n_y}) (\boldsymbol{r} \cdot \boldsymbol{n_x}) [r \otimes r] + r^{-4} (\boldsymbol{r} \cdot \boldsymbol{n_y}) [r \otimes n_x] \right) \rho_j dS_y$$

$$\tag{A.65}$$

$$+ \frac{\mu}{\pi} \int_\Gamma \left(r^{-4} (\boldsymbol{n_x} \cdot \boldsymbol{n_y}) [r \otimes r] + r^{-4} (\boldsymbol{r} \cdot \boldsymbol{n_x}) (\boldsymbol{r} \cdot \boldsymbol{n_y}) I \right) \rho_j dS_y \tag{A.66}$$

$$+ \frac{\mu}{\pi} \int_\Gamma \left(r^{-4} (\boldsymbol{r} \cdot \boldsymbol{n_x}) [n_y \otimes r] + r^{-2} [n_x \otimes n_y] \right) \rho_j dS_y \tag{A.67}$$

the same as equation (54) in Wu et al. [80].

A.2 Derivations of Stokes Layer Potentials in $\mathbb{C}$

A.2.1 Some partial derivatives in complex variables

In general, for an analytic complex variable function $f(z, \bar{z}) = f(x, y)$ where $z \in \mathbb{C}$ and $x, y \in \mathbb{R}$, the partial derivative of f with respect to real x

$$\frac{\partial f}{\partial x} = \begin{cases} \mathrm{Re}\left\{\frac{\partial f}{\partial x}\right\} + \mathrm{Im}\left\{\frac{\partial f}{\partial x}\right\}, \\ \frac{\partial}{\partial x} \left(\mathrm{Re}\left\{f\right\} + i\mathrm{Im}\left\{f\right\} \right) = \frac{\partial}{\partial x}\mathrm{Re}\left\{f\right\} + i\frac{\partial}{\partial x}\mathrm{Im}\left\{f\right\} \end{cases} \tag{A.68}$$

holds by definition.

$$\therefore \begin{cases} \mathrm{Re}\left\{\frac{\partial f}{\partial x}\right\} = \frac{\partial}{\partial x}\left[\mathrm{Re}\left\{f\right\}\right], \\ \mathrm{Im}\left\{\frac{\partial f}{\partial x}\right\} = \frac{\partial}{\partial x}\left[\mathrm{Im}\left\{f\right\}\right]. \end{cases} \tag{A.69}$$

These hold similarly for the partial derivative with respect to y.

Let $z := (y_1 - x_1) + i(y_2 - x_2) \in \mathbb{C}$ corresponding to $-\boldsymbol{r} = \boldsymbol{y} - \boldsymbol{x} \in \mathbb{R}^2$. Also let $\forall \boldsymbol{v} = (v_1, v_2)^T \in \mathbb{R}^2$ and $c = v_1 + iv_2 \in \mathbb{C}$.

Now we consider the partial derivatives of $\frac{\partial}{\partial x_1}[r^{-2} (\boldsymbol{r} \cdot \boldsymbol{v})]$ with respect to the variables of $\boldsymbol{x} = (x_1, x_2)^T$. Since $\frac{c}{z}$ depends only on z (independent of $\bar{z}$), the first

order derivative with respect to x_1 is

$$\frac{\partial}{\partial x_1}[r^{-2}(\boldsymbol{r}\cdot\boldsymbol{v})] = \frac{\partial}{\partial x_1}\left[-\mathrm{Re}\left\{\frac{c}{z}\right\}\right] \tag{A.70}$$

$$= -\mathrm{Re}\left\{\frac{\partial}{\partial x_1}\left(\frac{c}{z}\right)\right\} \tag{A.71}$$

$$= -\mathrm{Re}\left\{\frac{\partial}{\partial z}\left(\frac{c}{z}\right)\frac{\partial z}{\partial x_1}\right\} \tag{A.72}$$

$$= -\mathrm{Re}\left\{-\frac{c}{z^2}(-1)\right\} \tag{A.73}$$

$$= -\mathrm{Re}\left\{\frac{c}{z^2}\right\}. \tag{A.74}$$

The first equality is because of the identity we have already seen, the second equality is because of the just above discussion, and the third equality is because of the chain rule. We can compute other partial derivatives similarly using

$$\frac{\partial z}{\partial x_1} = -1, \frac{\partial z}{\partial x_2} = -i, \frac{\partial z}{\partial y_1} = 1, \frac{\partial z}{\partial y_2} = i, \tag{A.75}$$

$$\frac{\partial \overline{z}}{\partial x_1} = -1, \frac{\partial \overline{z}}{\partial x_2} = -i, \frac{\partial \overline{z}}{\partial y_1} = 1, \frac{\partial \overline{z}}{\partial y_2} = i. \tag{A.76}$$

For example, the partial derivatives with respect to the variables of $\boldsymbol{x} = (x_1, x_2)^T$ up to the second order can be written as

$$\frac{\partial}{\partial x_1}[r^{-2}(\boldsymbol{r}\cdot\boldsymbol{v})] = \frac{\partial}{\partial x_1}\left[-\mathrm{Re}\left\{\frac{c}{z}\right\}\right] = -\mathrm{Re}\left\{\frac{c}{z^2}\right\}, \tag{A.77}$$

$$\frac{\partial}{\partial x_2}[r^{-2}(\boldsymbol{r}\cdot\boldsymbol{v})] = \frac{\partial}{\partial x_2}\left[-\mathrm{Re}\left\{\frac{c}{z}\right\}\right] = -\mathrm{Re}\left\{i\frac{c}{z^2}\right\} = \mathrm{Im}\left\{\frac{c}{z^2}\right\}, \tag{A.78}$$

$$\frac{\partial^2}{\partial x_1^2}[r^{-2}(\boldsymbol{r}\cdot\boldsymbol{v})] = \frac{\partial^2}{\partial x_1^2}\left[-\mathrm{Re}\left\{\frac{c}{z}\right\}\right] = -2\mathrm{Re}\left\{\frac{c}{z^3}\right\}, \tag{A.79}$$

$$\frac{\partial^2}{\partial x_2^2}[r^{-2}(\boldsymbol{r}\cdot\boldsymbol{v})] = \frac{\partial^2}{\partial x_2^2}\left[-\mathrm{Re}\left\{\frac{c}{z}\right\}\right] = 2\mathrm{Im}\left\{i\frac{c}{z^3}\right\} = 2\mathrm{Re}\left\{\frac{c}{z^3}\right\} \tag{A.80}$$

$$\frac{\partial^2}{\partial x_1\partial x_2}[r^{-2}(\boldsymbol{r}\cdot\boldsymbol{v})] = \frac{\partial^2}{\partial x_1\partial x_2}\left[-\mathrm{Re}\left\{\frac{c}{z}\right\}\right] = -2\mathrm{Re}\left\{i\frac{c}{z^3}\right\} = 2\mathrm{Im}\left\{\frac{c}{z^3}\right\}. \tag{A.81}$$

A.2.2 Laplace layer potentials

We recall the layer potentials $\mathcal{S}$ and $\mathcal{D}$ for the Laplace equation. They can be written in $\mathbb{C}$ as

$$\mathcal{S}[\tau](z_x) := \int_\Gamma \log \frac{1}{r} \tau(z_y)|dz_y|, \tag{A.82}$$

$$\mathcal{D}[\tau](z_x) := \int_\Gamma \frac{\partial}{\partial \boldsymbol{n}_y} \left(\log \frac{1}{r} \right) \tau(z_y)|dz_y| = \int_\Gamma \frac{\boldsymbol{r} \cdot \boldsymbol{n}_y}{r^2} \tau(z_y)|dz_y|. \tag{A.83}$$

By the definitions of I_L, I_C, and the identity

$$\frac{\boldsymbol{r} \cdot \boldsymbol{n}_y}{r^2} = -\mathrm{Re}\left[\frac{\nu_y}{z}\right], \tag{A.84}$$

$$\mathcal{S}[\tau](z_x) = -I_L[\tau](z_x), \tag{A.85}$$

$$\mathcal{D}[\tau](z_x) = \mathrm{Re}\left[iI_C[\tau]\right]. \tag{A.86}$$

A.2.3 Stokes layer potentials

Stokes layer potentials are written as compositions of the singular integrals and Laplace layer potentials in $\mathbb{C}$. Now we convert the single and double layer potentials $\boldsymbol{S}$ and $\boldsymbol{D}$ for Stokes flow equations into complex forms.

A.2.4 Stokes single-layer potential S

As to Stokes single layer potential S, we rewrite S as the following form

$$\begin{aligned}
\boldsymbol{S}[\tau](z_x) = \boldsymbol{S}[\boldsymbol{\rho}](\boldsymbol{x}) &= \int_\Gamma G_{ij}(\boldsymbol{x}, \boldsymbol{y})\rho_j(\boldsymbol{y})ds_y \\
&= \int_\Gamma \left[-\delta_{ij} \log(r) + \frac{1}{r^2} r_i r_j \right] \rho_j(\boldsymbol{y})ds_y \\
&= \mathcal{S}[\boldsymbol{\rho}](\boldsymbol{x}) + \int_\Gamma \frac{[\boldsymbol{r} \otimes \boldsymbol{r}]}{r^2} \boldsymbol{\rho} ds_y \\
&= \mathcal{S}[\boldsymbol{\rho}](\boldsymbol{x}) + \int_\Gamma (\boldsymbol{r} \cdot \boldsymbol{\rho}) \nabla_x \left[\log(r)\right] ds_y \\
&= \mathcal{S}[\boldsymbol{\rho}] - \int_\Gamma \mathrm{Re}[\overline{z}\tau]\nabla_x \left[\log(r)\right] |dz_y|.
\end{aligned} \tag{A.87}$$

We used another identity below to obtain the fourth line

$$\frac{[\boldsymbol{r} \otimes \boldsymbol{r}]}{r^2} \boldsymbol{\rho} = (\boldsymbol{r} \cdot \boldsymbol{\rho}) \frac{\boldsymbol{r}}{r^2} = (\boldsymbol{r} \cdot \boldsymbol{\rho}) \nabla_x \log(r). \tag{A.88}$$

Noting $z = (y_1 - x_1) + i(y_2 - x_2)$ and $\tau = \rho_1 + i\rho_2$,

$$\int_\Gamma \mathrm{Re}[\bar{z}\tau] \nabla_x [\log(r)] \, |dz_y| \tag{A.89}$$

$$= \int_\Gamma [(y_1 - x_1)\rho_1 + (y_2 - x_2)\rho_2] \nabla_x [\log(r)] \, |dz_y|$$

$$= \int_\Gamma (\boldsymbol{y} \cdot \boldsymbol{\rho}) \nabla_x [\log(r)] \, |dz_y| - x_1 \int_\Gamma \rho_1 \nabla_x [\log(r)] \, |dz_y| - x_2 \int_\Gamma \rho_2 \nabla_x [\log(r)] \, |dz_y|$$

$$= -\nabla_x \int_\Gamma (\boldsymbol{y} \cdot \boldsymbol{\rho}) \log \frac{1}{r} |dz_y| + x_1 \nabla_x \int_\Gamma \rho_1 \log \frac{1}{r} |dz_y| + x_2 \nabla_x \int_\Gamma \rho_2 \log \frac{1}{r} |dz_y|$$

$$= -\nabla_x \mathcal{S}[(\boldsymbol{y} \cdot \boldsymbol{\rho})] + x_1 \nabla_x \mathcal{S}[\rho_1] + x_2 \nabla_x \mathcal{S}[\rho_2]. \tag{A.90}$$

$$\therefore S[\tau] = \mathcal{S}[\boldsymbol{\rho}] - \int_\Gamma \mathrm{Re}[\bar{z}\tau] \nabla_x [\log(r)] \, |dz_y|$$

$$= \mathcal{S}[\boldsymbol{\rho}] + \nabla_x \mathcal{S}[(\boldsymbol{y} \cdot \boldsymbol{\rho})] - x_1 \nabla_x \mathcal{S}[\rho_1] - x_2 \nabla_x \mathcal{S}[\rho_2]. \tag{A.91}$$

This matches the derivation in Wu et al. [80].

To compute this more explicitly, we need the gradient of $\log r$ in complex variable.

$$\frac{\partial}{\partial x_1} \log(r) = \frac{\partial}{\partial x_1} \mathrm{Re} \left\{ \log(z_y - z_x) \right\}$$

$$= \mathrm{Re} \left\{ \frac{\partial}{\partial x_1} \log(z_y - z_x) \right\} = \mathrm{Re} \left\{ \frac{-1}{z_y - z_x} \right\} = -\mathrm{Re} \left\{ \frac{1}{z} \right\}, \tag{A.92}$$

$$\frac{\partial}{\partial x_2} \log(r) = \frac{\partial}{\partial x_2} \mathrm{Re} \left\{ \log(z_y - z_x) \right\}$$

$$= \mathrm{Re} \left\{ \frac{\partial}{\partial x_2} \log(z_y - z_x) \right\} = \mathrm{Re} \left\{ \frac{-i}{z_y - z_x} \right\} = \mathrm{Im} \left\{ \frac{1}{z} \right\}. \tag{A.93}$$

$$\therefore \nabla_x \log(r) = \begin{pmatrix} -\mathrm{Re} \left\{ \frac{1}{z} \right\} \\ \mathrm{Im} \left\{ \frac{1}{z} \right\} \end{pmatrix}. \tag{A.94}$$

$$S[\tau] = \mathcal{S}[\boldsymbol{\rho}] - \oint_\Gamma \mathrm{Re}[\bar{z}\tau]\nabla_x\left[\log(r)\right]|dz_y|$$

$$= \mathcal{S}[\boldsymbol{\rho}] + \nabla_x\mathcal{S}[(\boldsymbol{y}\cdot\boldsymbol{\rho})] - x_1\nabla_x\mathcal{S}[\rho_1] - x_2\nabla_x\mathcal{S}[\rho_2]. \qquad (\mathrm{A.95})$$

$$\therefore \nabla_x\mathcal{S}[\rho] = \nabla_x \oint_\Gamma \rho\log\frac{1}{r}|dz_y|$$

$$= -\oint_\Gamma \rho\nabla_x\log\frac{1}{r}|dz_y|$$

$$= -\oint_\Gamma \rho \begin{pmatrix} -\mathrm{Re}\left\{\frac{1}{z}\right\} \\ \mathrm{Im}\left\{\frac{1}{z}\right\} \end{pmatrix} |dz_y|$$

$$= \begin{pmatrix} \mathrm{Re}\left\{\int \frac{\rho}{z}\frac{dz}{i\nu_y}\right\} \\ -\mathrm{Im}\left\{\int \frac{\rho}{z}\frac{dz}{i\nu_y}\right\} \end{pmatrix}$$

$$= \begin{pmatrix} \mathrm{Re}\left\{I_C[\frac{\rho}{i\nu_y}]\right\} \\ -\mathrm{Im}\left\{I_C[\frac{\rho}{i\nu_y}]\right\} \end{pmatrix}. \qquad (\mathrm{A.96})$$

for $\rho \in \mathbb{R}$.

$$\therefore S[\tau] = \mathcal{S}[\boldsymbol{\rho}] + \nabla_x \mathcal{S}[(\boldsymbol{y} \cdot \boldsymbol{\rho})] - x_1 \nabla_x \mathcal{S}[\rho_1] - x_2 \nabla_x \mathcal{S}[\rho_2] \tag{A.97}$$

$$= - \begin{pmatrix} I_L[\rho_1] \\ I_L[\rho_2] \end{pmatrix} + \begin{pmatrix} \operatorname{Re}\left\{ I_C[\frac{(\boldsymbol{y} \cdot \boldsymbol{\rho})}{i\nu_y}] \right\} \\ -\operatorname{Im}\left\{ I_C[\frac{(\boldsymbol{y} \cdot \boldsymbol{\rho})}{i\nu_y}] \right\} \end{pmatrix} \tag{A.98}$$

$$- x_1 \begin{pmatrix} \operatorname{Re}\left\{ I_C[\frac{\rho_1}{i\nu_y}] \right\} \\ -\operatorname{Im}\left\{ I_C[\frac{\rho_1}{i\nu_y}] \right\} \end{pmatrix} - x_2 \begin{pmatrix} \operatorname{Re}\left\{ I_C[\frac{\rho_2}{i\nu_y}] \right\} \\ -\operatorname{Im}\left\{ I_C[\frac{\rho_2}{i\nu_y}] \right\} \end{pmatrix} \tag{A.99}$$

$$= - \begin{pmatrix} I_L[\rho_1] \\ I_L[\rho_2] \end{pmatrix} + \begin{pmatrix} \operatorname{Re}\left\{ I_C[\frac{1}{i\nu_y}\left((y_1 - x_1)\rho_1 + (y_2 - x_2)\rho_2\right)] \right\} \\ -\operatorname{Im}\left\{ I_C[\frac{1}{i\nu_y}\left((y_1 - x_1)\rho_1 + (y_2 - x_2)\rho_2\right)] \right\} \end{pmatrix} \tag{A.100}$$

$$= - \begin{pmatrix} I_L[\rho_1] \\ I_L[\rho_2] \end{pmatrix} + \left[\begin{pmatrix} \operatorname{Re}\left\{ I_C[\frac{1}{i\nu_y} \cdot] \right\} \\ -\operatorname{Im}\left\{ I_C[\frac{1}{i\nu_y} \cdot] \right\} \end{pmatrix} \otimes \begin{pmatrix} y_1 - x_1 \\ y_2 - x_2 \end{pmatrix} \right] \begin{pmatrix} \rho_1 \\ \rho_2 \end{pmatrix} \tag{A.101}$$

$$= - \begin{pmatrix} I_L[\rho_1] \\ I_L[\rho_2] \end{pmatrix} + \left[\begin{pmatrix} \operatorname{Im}\left\{ I_C[\overline{\nu_y} \cdot] \right\} \\ \operatorname{Re}\left\{ I_C[\overline{\nu_y} \cdot] \right\} \end{pmatrix} \otimes \begin{pmatrix} \operatorname{Re}\left\{ z \right\} \\ \operatorname{Im}\left\{ z \right\} \end{pmatrix} \right] \begin{pmatrix} \rho_1 \\ \rho_2 \end{pmatrix}. \tag{A.102}$$

A.2.5 Stokes double-layer potential D

Next, we convert Stokes double layer potential D. Here we use another identity

$$\nabla_x \left[\frac{(\boldsymbol{r} \cdot \boldsymbol{n_y})}{r^2} \right] = \frac{\boldsymbol{n_y}}{r^2} - 2(\boldsymbol{r} \cdot \boldsymbol{n_y}) \frac{\boldsymbol{r}}{r^4}. \tag{A.103}$$

Then

$$\boldsymbol{D}[\tau](z_x) = \boldsymbol{D}[\boldsymbol{\rho}](\boldsymbol{x}) = \int_\Gamma T_{ijk}(\boldsymbol{x}, \boldsymbol{y}) n_k(\boldsymbol{y}) \rho_j(\boldsymbol{y}) ds_y$$

$$= \int_\Gamma \frac{(\boldsymbol{r} \cdot \boldsymbol{n_y})}{r^2} \frac{[\boldsymbol{r} \otimes \boldsymbol{r}]}{r^2} \boldsymbol{\rho}(\boldsymbol{y}) ds_y$$

$$= \frac{1}{2} \int_\Gamma (\boldsymbol{r} \cdot \boldsymbol{\rho}) \left(\frac{\boldsymbol{n_y}}{r^2} - \nabla_x \left[\frac{(\boldsymbol{r} \cdot \boldsymbol{n_y})}{r^2} \right] \right) ds_y$$

$$= -\frac{1}{2} \int_\Gamma \mathrm{Re}\left\{ \frac{\tau}{z} \right\} \begin{pmatrix} \nu_{y,1} \\ \nu_{y,2} \end{pmatrix} |dz_y| + \frac{1}{2} \int_\Gamma \mathrm{Re}\left[\bar{z}\tau \right] \begin{pmatrix} -\mathrm{Re}\left\{ \frac{\nu_y}{z^2} \right\} \\ \mathrm{Im}\left\{ \frac{\nu_y}{z^2} \right\} \end{pmatrix} |dz_y|$$

$$= -\frac{1}{2}\mathrm{Im} \left[\int_\Gamma \begin{pmatrix} \nu_{y,1}/\nu_y \\ \nu_{y,2}/\nu_y \end{pmatrix} \otimes \begin{pmatrix} 1/z \\ i/z \end{pmatrix} \begin{pmatrix} \mathrm{Re}\left\{ \tau \right\} \\ \mathrm{Im}\left\{ \tau \right\} \end{pmatrix} dz_y \right]$$

$$+ \frac{1}{2} \int_\Gamma \begin{pmatrix} \mathrm{Im}\left\{ \frac{\cdot}{z^2} \right\} \\ \mathrm{Re}\left\{ \frac{\cdot}{z^2} \right\} \end{pmatrix} \otimes \begin{pmatrix} -\mathrm{Re}\left\{ z \right\} \\ -\mathrm{Im}\left\{ z \right\} \end{pmatrix} \begin{pmatrix} -\mathrm{Re}\left\{ \tau \right\} \\ -\mathrm{Im}\left\{ \tau \right\} \end{pmatrix} dz_y$$

$$= -\frac{1}{2}\mathrm{Im} \begin{bmatrix} I_C\left[\frac{\nu_{y,1}}{\nu_y}\tau \right] \\ I_C\left[\frac{\nu_{y,2}}{\nu_y}\tau \right] \end{bmatrix} + \frac{1}{2} \begin{pmatrix} \mathrm{Re}\left\{ I_H[\cdot] \right\} \\ \mathrm{Im}\left\{ I_H[\cdot] \right\} \end{pmatrix} \otimes \begin{pmatrix} -\mathrm{Re}\left\{ z \right\} \\ -\mathrm{Im}\left\{ z \right\} \end{pmatrix} \begin{pmatrix} -\mathrm{Re}\left\{ \tau \right\} \\ -\mathrm{Im}\left\{ \tau \right\} \end{pmatrix}.$$

$$\text{(A.104)}$$

A.2.6 S'

$$S'[\boldsymbol{\rho}] = -\int_\Gamma \frac{1}{r^4} [r \otimes r] (\boldsymbol{r} \cdot \boldsymbol{n_x}) \boldsymbol{\rho_y} ds_y$$

$$= -\int_\Gamma \frac{1}{r^4} r_i r_j r_k n_{x,k} \rho_{y,j} ds_y$$

$$= -\int_\Gamma \left(\frac{1}{r^4} r_j \rho_{y,j} r_i \right) (r_k n_{x,k}) ds_y. \tag{A.105}$$

We substitute the following identity into the first term of the integrand

$$\nabla_x \left[\frac{(\boldsymbol{r} \cdot \boldsymbol{\rho})}{r^2} \right] = \frac{\boldsymbol{\rho}}{r^2} - \frac{2}{r^4} (\boldsymbol{r} \cdot \boldsymbol{\rho}) \boldsymbol{r}$$

$$\Leftrightarrow \quad \frac{(\boldsymbol{r} \cdot \boldsymbol{\rho})}{r^4} \boldsymbol{r} = \frac{1}{2} \left[\frac{\boldsymbol{\rho}}{r^2} - \nabla_x \left[\frac{(\boldsymbol{r} \cdot \boldsymbol{\rho})}{r^2} \right] \right]. \tag{A.106}$$

Then

$$S'[\boldsymbol{\rho}] = -\int_\Gamma \frac{1}{2}\left[\frac{\boldsymbol{\rho}}{r^2} - \nabla_x\left[\frac{(\boldsymbol{r}\cdot\boldsymbol{\rho})}{r^2}\right]\right](\boldsymbol{r}\cdot\boldsymbol{n_x})\,ds_y$$

$$= -\frac{1}{2}\int_\Gamma \frac{(\boldsymbol{r}\cdot\boldsymbol{n_x})}{r^2}\boldsymbol{\rho}\,ds_y + \frac{1}{2}\int_\Gamma \nabla_x\left[\frac{(\boldsymbol{r}\cdot\boldsymbol{\rho})}{r^2}\right](\boldsymbol{r}\cdot\boldsymbol{n_x})\,ds_y$$

$$= \underbrace{-\frac{1}{2}\int_\Gamma \frac{(\boldsymbol{r}\cdot\boldsymbol{n_x})}{r^2}\boldsymbol{\rho}\,ds_y}_{(I)} + \underbrace{\frac{1}{2}(\boldsymbol{x}\cdot\boldsymbol{n_x})\int_\Gamma \nabla_x\frac{(\boldsymbol{r}\cdot\boldsymbol{\rho})}{r^2}\,ds_y}_{(II)} - \underbrace{\frac{1}{2}\int_\Gamma (\boldsymbol{y}\cdot\boldsymbol{n_x})\nabla_x\frac{(\boldsymbol{r}\cdot\boldsymbol{\rho})}{r^2}\,ds_y}_{(III)}.$$

$$(A.107)$$

$\underline{(I) - \frac{1}{2}\int_\Gamma \frac{(\boldsymbol{r}\cdot\boldsymbol{n_x})}{r^2}\boldsymbol{\rho}\,ds_y}$: Using the following identity

$$\frac{(\boldsymbol{r}\cdot\boldsymbol{n_x})}{r^2} = -\mathrm{Re}\left\{\frac{\nu_x}{z}\right\} \tag{A.108}$$

where $\nu_x = n_{x,1} + i n_{x,2}$ and $\boldsymbol{n_x} = (n_{x,1}, n_{x,2})$,

$$\underline{(I)} = \int -\mathrm{Re}\left\{\frac{\nu_x}{z}\right\}\boldsymbol{\rho}|dz_y|$$

$$= -\mathrm{Re}\left\{\int \frac{1}{z}\nu_x\boldsymbol{\rho}|dz_y|\right\}$$

$$= -\mathrm{Re}\left\{\int \frac{1}{z}\frac{\nu_x}{i\nu_y}\boldsymbol{\rho}\,dz_y\right\}$$

$$= -\mathrm{Re}\left\{I_C\left[\frac{\nu_x}{i\nu_y}\boldsymbol{\rho}\right]\right\}$$

$$= -\mathrm{Re}\left\{-iI_C\left[\frac{\nu_x}{\nu_y}\boldsymbol{\rho}\right]\right\}$$

$$= -\mathrm{Im}\left\{I_C\left[\frac{\nu_x}{\nu_y}\boldsymbol{\rho}\right]\right\}. \tag{A.109}$$

$\underline{(II) \int_\Gamma \nabla_x\frac{(\boldsymbol{r}\cdot\boldsymbol{\rho})}{r^2}\,ds_y}$: Here using the identity below

$$\nabla_x\left[\frac{(\boldsymbol{r}\cdot\boldsymbol{\rho})}{r^2}\right] = \nabla_x\left[-\mathrm{Re}\left\{\frac{\nu_x}{z}\right\}\right] = \left(-\mathrm{Re}\left\{\frac{\tau}{z^2}\right\}, \mathrm{Im}\left\{\frac{\tau}{z^2}\right\}\right) \tag{A.110}$$

where $\tau = \rho_1 + i\rho_2$,

$$
\begin{aligned}
\underline{(II)} &= \int \begin{pmatrix} -\mathrm{Re}\left\{\frac{\tau}{z^2}\right\} \\ \mathrm{Im}\left\{\frac{\tau}{z^2}\right\} \end{pmatrix} |dz_y| \\
&= \begin{pmatrix} -\mathrm{Re}\left\{\int \frac{\tau}{z^2}|dz_y|\right\} \\ \mathrm{Im}\left\{\int \frac{\tau}{z^2}|dz_y|\right\} \end{pmatrix} \\
&= \begin{pmatrix} -\mathrm{Re}\left\{\int \frac{\tau}{z^2}\frac{dz_y}{i\nu_y}\right\} \\ \mathrm{Im}\left\{\int \frac{\tau}{z^2}\frac{dz_y}{i\nu_y}\right\} \end{pmatrix} \\
&= \begin{pmatrix} -\mathrm{Re}\left\{I_H\left[\frac{\tau}{i\nu_y}\right]\right\} \\ \mathrm{Im}\left\{I_H\left[\frac{\tau}{i\nu_y}\right]\right\} \end{pmatrix} \\
&= \begin{pmatrix} -\mathrm{Re}\left\{I_H\left[-i\overline{\nu_y}(\rho_1 + i\rho_2)\right]\right\} \\ \mathrm{Im}\left\{I_H\left[-i\overline{\nu_y}(\rho_1 + i\rho_2)\right]\right\} \end{pmatrix} \\
&= \begin{pmatrix} -\mathrm{Im}\left\{I_H\left[\overline{\nu_y}\rho_1\right]\right\} - \mathrm{Re}\left\{I_H\left[\overline{\nu_y}\rho_2\right]\right\} \\ -\mathrm{Re}\left\{I_H\left[\overline{\nu_y}\rho_1\right]\right\} + \mathrm{Im}\left\{I_H\left[\overline{\nu_y}\rho_2\right]\right\} \end{pmatrix} \\
&= \begin{bmatrix} -\mathrm{Im}\left\{I_H\left[\overline{\nu_y}\cdot\right]\right\}, & -\mathrm{Re}\left\{I_H\left[\overline{\nu_y}\cdot\right]\right\} \\ -\mathrm{Re}\left\{I_H\left[\overline{\nu_y}\cdot\right]\right\}, & \mathrm{Im}\left\{I_H\left[\overline{\nu_y}\cdot\right]\right\} \end{bmatrix} \begin{pmatrix} \rho_1 \\ \rho_2 \end{pmatrix}.
\end{aligned}
\tag{A.111}
$$

$\underline{(III) \int_\Gamma (\boldsymbol{y} \cdot \boldsymbol{n_x}) \nabla_x \frac{(\boldsymbol{r} \cdot \boldsymbol{\rho})}{r^2} ds_y}$:

$$
\begin{aligned}
(III) &= \int (y_1 n_{x,1} + y_2 n_{x,2})\nabla_x\left[\frac{(\boldsymbol{r} \cdot \boldsymbol{\rho})}{r^2}\right] ds_y \\
&= n_{x,1}\int y_1 \nabla_x\left[\frac{(\boldsymbol{r} \cdot \boldsymbol{\rho})}{r^2}\right] ds_y + n_{x,2}\int y_2 \nabla_x\left[\frac{(\boldsymbol{r} \cdot \boldsymbol{\rho})}{r^2}\right] ds_y \\
&= n_{x,1}\int y_1 \begin{pmatrix} -\mathrm{Re}\left\{\frac{\tau}{z^2}\right\} \\ \mathrm{Im}\left\{\frac{\tau}{z^2}\right\} \end{pmatrix} |dz_y| + n_{x,2}\int y_2 \begin{pmatrix} -\mathrm{Re}\left\{\frac{\tau}{z^2}\right\} \\ \mathrm{Im}\left\{\frac{\tau}{z^2}\right\} \end{pmatrix} |dz_y|.
\end{aligned}
\tag{A.112}
$$

$$-\int y_1 \mathrm{Re}\left\{\frac{\tau}{z^2}\right\}|dz_y| = -\mathrm{Re}\left\{\int y_1 \frac{\tau}{z^2}\frac{dz_y}{i\nu_y}\right\}$$

$$= -\mathrm{Re}\left\{\int \frac{1}{z^2}y_1(-i\overline{\nu_y})(\rho_1+i\rho_2)dz_y\right\}$$

$$= \mathrm{Re}\left\{i\int \frac{1}{z^2}y_1\overline{\nu_y}\rho_1 dz_y\right\} - \mathrm{Re}\left\{\int \frac{1}{z^2}y_1\overline{\nu_y}\rho_2 dz_y\right\}$$

$$= -\mathrm{Im}\left\{\int \frac{1}{z^2}y_1\overline{\nu_y}\rho_1 dz_y\right\} - \mathrm{Re}\left\{\int \frac{1}{z^2}y_1\overline{\nu_y}\rho_2 dz_y\right\}$$

$$= \begin{pmatrix} -\mathrm{Im}\left\{I_H\left[y_1\overline{\nu_y}\cdot\right]\right\} \\ -\mathrm{Re}\left\{I_H\left[y_1\overline{\nu_y}\cdot\right]\right\} \end{pmatrix} \cdot \begin{pmatrix} \rho_1 \\ \rho_2 \end{pmatrix}. \tag{A.113}$$

Other terms involving $\mathrm{Im}\left\{\frac{\tau}{z^2}\right\}$ and y_2 in the integrals give similar forms. As a result,

$$(III) = \sum_{j=1}^{2} n_{x,j} \begin{bmatrix} -\mathrm{Im}\left\{I_H\left[y_j\overline{\nu_y}\cdot\right]\right\}, & -\mathrm{Re}\left\{I_H\left[y_j\overline{\nu_y}\cdot\right]\right\} \\ -\mathrm{Re}\left\{I_H\left[y_j\overline{\nu_y}\cdot\right]\right\}, & \mathrm{Im}\left\{I_H\left[y_j\overline{\nu_y}\cdot\right]\right\} \end{bmatrix} \begin{pmatrix} \rho_1 \\ \rho_2 \end{pmatrix}. \tag{A.114}$$

Noting $z = (y_1 - x_1) + i(y_2 - x_2)$, we summarize S' as

$$S'[\boldsymbol{\rho}] = \frac{1}{2}\mathrm{Im}\left\{I_C\left[\frac{\nu_x}{\nu_y}\boldsymbol{\rho}\right]\right\} + \frac{(\boldsymbol{x}\cdot\boldsymbol{n_x})}{2}\begin{bmatrix} -\mathrm{Im}\left\{I_H\left[\overline{\nu_y}\cdot\right]\right\}, & -\mathrm{Re}\left\{I_H\left[\overline{\nu_y}\cdot\right]\right\} \\ -\mathrm{Re}\left\{I_H\left[\overline{\nu_y}\cdot\right]\right\}, & \mathrm{Im}\left\{I_H\left[\overline{\nu_y}\cdot\right]\right\} \end{bmatrix}\boldsymbol{\rho}$$

$$- \frac{1}{2}\sum_{j=1}^{2} n_{x,j}\begin{bmatrix} -\mathrm{Im}\left\{I_H\left[y_j\overline{\nu_y}\cdot\right]\right\}, & -\mathrm{Re}\left\{I_H\left[y_j\overline{\nu_y}\cdot\right]\right\} \\ -\mathrm{Re}\left\{I_H\left[y_j\overline{\nu_y}\cdot\right]\right\}, & \mathrm{Im}\left\{I_H\left[y_j\overline{\nu_y}\cdot\right]\right\} \end{bmatrix}\boldsymbol{\rho}$$

$$= \frac{1}{2}\mathrm{Im}\left\{I_C\left[\nu_x\overline{\nu_y}\boldsymbol{\rho}\right]\right\}$$

$$+ \frac{1}{2}\begin{bmatrix} -\mathrm{Im}\left\{I_H\left[(\boldsymbol{r}\cdot\boldsymbol{n_x})\overline{\nu_y}\cdot\right]\right\}, & -\mathrm{Re}\left\{I_H\left[(\boldsymbol{r}\cdot\boldsymbol{n_x})\overline{\nu_y}\cdot\right]\right\} \\ -\mathrm{Re}\left\{I_H\left[(\boldsymbol{r}\cdot\boldsymbol{n_x})\overline{\nu_y}\cdot\right]\right\}, & \mathrm{Im}\left\{I_H\left[(\boldsymbol{r}\cdot\boldsymbol{n_x})\overline{\nu_y}\cdot\right]\right\} \end{bmatrix}\boldsymbol{\rho} \tag{A.115}$$

here we can compute $(\boldsymbol{r}\cdot\boldsymbol{n_x})$ as $-\mathrm{Re}\left\{z\overline{\nu_x}\right\}$.

A.2.7 D'

Let $\boldsymbol{n}(\boldsymbol{x}) := \boldsymbol{n_x} = (n_{x,1}, n_{x,2})$, $\boldsymbol{n}(\boldsymbol{y}) := \boldsymbol{n_y} = (n_{y,1}, n_{y,2})$, $\nu_x := n_{x,1} + in_{x,2}$, and $\nu_y := n_{y,1} + in_{y,2}$. ν The kernel $K_{ij}^{\boldsymbol{D}'}$ of $D'_{\Gamma_1}[\boldsymbol{\rho}](\boldsymbol{x}) = \int_{\Gamma_1} K_{ij}^{D'}(\boldsymbol{x}, \boldsymbol{y})\rho(\boldsymbol{y})_j ds_{\boldsymbol{y}}$ $(\boldsymbol{x} \in \Gamma_2)$

109

is given by

$$\left[\nabla\left(T_{ijk}n_{y_k}\right) + \left\{\nabla\left(T_{ijk}n_{y_k}\right)\right\}^T - \Pi_{ik}(\boldsymbol{x},\boldsymbol{y})n_{y_k}\right]\boldsymbol{n_x}$$

$$= \left[\frac{\partial}{\partial x_l}T_{ijk} + \frac{\partial}{\partial x_i}T_{ljk}\right]n_{y_k}n_{xl} - \Pi_{ik}(\boldsymbol{x},\boldsymbol{y})n_{xj}n_{y_k} \quad (i,j,k,l \in \{1,2\}) \qquad \text{(A.116)}$$

where $T_{ijk}n_{y_k}$ is the kernel of the double layer potential, and $\Pi_{ik}n_{y_k}$ is defined as

$\frac{1}{\pi}\left(-\frac{1}{2r^2}\delta_{ik} + \frac{1}{r^4}\hat{x}_i\hat{x}_k\right)n_{y_k}$ (2.6.21) in Pozrikidis [69].

The first term of (A.116) is computed as

$$\nabla\left(T_{ijk}n_{y_k}\right)\boldsymbol{n}(\boldsymbol{x}) = \frac{\partial}{\partial x_l}\left(\frac{1}{\pi r^4}\hat{x}_i\hat{x}_j\hat{x}_k n_{y_k}\right)n_{xl}$$

$$= \left\{\frac{1}{\pi r^4}\left(\delta_{il}\hat{x}_j\hat{x}_k + \hat{x}_i\delta_{jl}\hat{x}_k + \hat{x}_i\hat{x}_j\delta_{kl}\right) - 4\frac{1}{\pi r^6}\hat{x}_i\hat{x}_j\hat{x}_k\hat{x}_l\right\}n_{y_k}n_{xl}$$

$$= \frac{1}{\pi r^4}\left\{n_{xi}\hat{x}_j\left(\boldsymbol{r}\cdot\boldsymbol{n_y}\right) + \hat{x}_i n_{xj}\left(\boldsymbol{r}\cdot\boldsymbol{n_y}\right) + \hat{x}_i\hat{x}_j\left(\boldsymbol{n_x}\cdot\boldsymbol{n_y}\right)\right\}$$

$$- 4\frac{1}{\pi r^6}\hat{x}_i\hat{x}_j\left(\boldsymbol{r}\cdot\boldsymbol{n_x}\right)\left(\boldsymbol{r}\cdot\boldsymbol{n_y}\right)$$

$$= \frac{1}{\pi r^4}\left\{\left(\left[n_x\otimes r\right] + \left[r\otimes n_x\right]\right)\left(\boldsymbol{r}\cdot\boldsymbol{n_y}\right) + \left[r\otimes r\right]\left(\boldsymbol{n_x}\cdot\boldsymbol{n_y}\right)\right\}$$

$$- 4\frac{1}{\pi r^6}\left[r\otimes r\right]\left(\boldsymbol{r}\cdot\boldsymbol{n_x}\right)\left(\boldsymbol{r}\cdot\boldsymbol{n_y}\right). \qquad \text{(A.117)}$$

Similarly, noting the transpose is about indices i and l, the second term is

$$\left\{\nabla\left(T_{ijk}n_{y_k}\right)\right\}^T\boldsymbol{n}(\boldsymbol{x}) = \frac{\partial}{\partial x_i}\left(\frac{1}{\pi r^4}\hat{x}_l\hat{x}_j\hat{x}_k n_{y_k}\right)n_{xl}$$

$$= \left\{\frac{1}{\pi r^4}\left(\delta_{li}\hat{x}_j\hat{x}_k + \hat{x}_l\delta_{ji}\hat{x}_k + \hat{x}_l\hat{x}_j\delta_{ki}\right) - 4\frac{1}{\pi r^6}\hat{x}_l\hat{x}_j\hat{x}_k\hat{x}_i\right\}n_{y_k}n_{xl}$$

$$= \frac{1}{\pi r^4}\left\{n_{xi}\hat{x}_j\left(\boldsymbol{r}\cdot\boldsymbol{n_y}\right) + \delta_{ij}\left(\boldsymbol{r}\cdot\boldsymbol{n_x}\right)\left(\boldsymbol{r}\cdot\boldsymbol{n_y}\right) + n_{yi}\hat{x}_j\left(\boldsymbol{r}\cdot\boldsymbol{n_x}\right)\right\}$$

$$- 4\frac{1}{\pi r^6}\hat{x}_i\hat{x}_j\left(\boldsymbol{r}\cdot\boldsymbol{n_x}\right)\left(\boldsymbol{r}\cdot\boldsymbol{n_y}\right)$$

$$= \frac{1}{\pi r^4}\left\{\left[n_x\otimes r\right]\left(\boldsymbol{r}\cdot\boldsymbol{n_y}\right) + \left[r\otimes n_x\right]\left(\boldsymbol{r}\cdot\boldsymbol{n_y}\right)\boldsymbol{I} + \left[n_y\otimes r\right]\left(\boldsymbol{r}\cdot\boldsymbol{n_x}\right)\right\}$$

$$- 4\frac{1}{\pi r^6}\left[r\otimes r\right]\left(\boldsymbol{r}\cdot\boldsymbol{n_x}\right)\left(\boldsymbol{r}\cdot\boldsymbol{n_y}\right). \qquad \text{(A.118)}$$

The third term $\Pi_{ik}(\boldsymbol{x}, \boldsymbol{y})n_{xj}n_{yk}$ is

$$
\begin{aligned}
\Pi_{ik}(\boldsymbol{x}, \boldsymbol{y})n_{xj}n_{yk} =& \frac{1}{2\pi} \cdot 2 \left(-\delta_{ik}\frac{1}{r^2} + \frac{2}{r^4}\hat{x}_i\hat{x}_k \right) n_{xj}n_{yk} \\
=& \frac{1}{\pi} \left(-\frac{1}{r^2}n_{y_i}n_{xj} + \frac{2}{r^4}(\hat{x}_k n_{yk})\hat{x}_i n_{xj} \right) \\
=& \frac{1}{\pi} \left(-\frac{1}{r^2}\left[n_y \otimes n_x \right] + \frac{2}{r^4}\left(\boldsymbol{r} \cdot \boldsymbol{n_y} \right)\left[r \otimes n_x \right] \right).
\end{aligned} \tag{A.119}
$$

Therefore, we have the kernel of $\boldsymbol{D'}$ below

$$
\begin{aligned}
& \left[\nabla \left(T_{ijk}n_{yk} \right) + \left\{ \nabla \left(T_{ijk}n_{yk} \right) \right\}^T - \Pi_{ik}(\boldsymbol{x}, \boldsymbol{y})n_{yk} \right] \boldsymbol{n}(\boldsymbol{x}) \\
=& \quad \frac{1}{\pi r^2} \left(\boldsymbol{n_y} \otimes \boldsymbol{n_x} \right) \\
& + \frac{1}{\pi r^4} \left\{ \left(\boldsymbol{n_y} \otimes \boldsymbol{r} \right)\left(\boldsymbol{r} \cdot \boldsymbol{n_x} \right) + \left(\boldsymbol{r} \otimes \boldsymbol{r} \right)\left(\boldsymbol{n_x} \cdot \boldsymbol{n_y} \right) + \left(\boldsymbol{r} \cdot \boldsymbol{n_x} \right)\left(\boldsymbol{r} \cdot \boldsymbol{n_y} \right)I + \left(\boldsymbol{r} \cdot \boldsymbol{n_y} \right)\left(\boldsymbol{r} \otimes \boldsymbol{n_x} \right) \right\} \\
& - \frac{8}{\pi r^6} \left(\boldsymbol{r} \cdot \boldsymbol{n_x} \right)\left(\boldsymbol{r} \cdot \boldsymbol{n_y} \right)\left(\boldsymbol{r} \otimes \boldsymbol{r} \right).
\end{aligned} \tag{A.120}
$$

This result matches equation (54) in Wu et al. [80]

We want to apply the special quadrature technique for close evaluations. For this purpose, we need to change the expression (A.120) into a form of complex variables.

Converting D' into another form in $\mathbb{C}$.

At first, the following equation holds for $\forall \boldsymbol{v} \in \mathbb{R}^2$.

$$\nabla_x \left[r^{-2} \left(\boldsymbol{r} \cdot \boldsymbol{v} \right) \right] = r^{-2} \boldsymbol{v} - 2r^{-4} \left(\boldsymbol{r} \cdot \boldsymbol{v} \right) \boldsymbol{r} \Leftrightarrow r^{-4} \left(\boldsymbol{r} \cdot \boldsymbol{v} \right) \boldsymbol{r} = \frac{1}{2} \left\{ r^{-2} \boldsymbol{v} - \nabla_x \left[r^{-2} \left(\boldsymbol{r} \cdot \boldsymbol{v} \right) \right] \right\}$$

(A.121)

So, the kernel of the double layer potential can be written as

$$\boldsymbol{K}^D \boldsymbol{\rho} = r^{-4} r_i r_j r_k \rho_j n_{yk} = r^{-4} \left(\boldsymbol{r} \cdot \boldsymbol{n_y} \right) \left(\boldsymbol{r} \cdot \boldsymbol{\rho} \right) \boldsymbol{r} = \left(\boldsymbol{r} \cdot \boldsymbol{\rho} \right) r^{-4} \left(\boldsymbol{r} \cdot \boldsymbol{n_y} \right) \boldsymbol{r}$$

$$= \left(\boldsymbol{r} \cdot \boldsymbol{\rho} \right) \frac{1}{2} \left\{ r^{-2} \boldsymbol{n_y} - \nabla_x \left[r^{-2} \left(\boldsymbol{r} \cdot \boldsymbol{n_y} \right) \right] \right\}$$

$$= \frac{1}{2} \left\{ r^{-2} \left(\boldsymbol{r} \cdot \boldsymbol{\rho} \right) \boldsymbol{n_y} - \left(\left(\boldsymbol{x} - \boldsymbol{y} \right) \cdot \boldsymbol{\rho} \right) \nabla_x \left[r^{-2} \left(\boldsymbol{r} \cdot \boldsymbol{n_y} \right) \right] \right\}$$

$$= \frac{1}{2} \left\{ r^{-2} \left(\boldsymbol{r} \cdot \boldsymbol{\rho} \right) \boldsymbol{n_y} - \left(\boldsymbol{x} \cdot \boldsymbol{\rho} \right) \nabla_x \left[r^{-2} \left(\boldsymbol{r} \cdot \boldsymbol{n_y} \right) \right] + \left(\boldsymbol{y} \cdot \boldsymbol{\rho} \right) \nabla_x \left[r^{-2} \left(\boldsymbol{r} \cdot \boldsymbol{n_y} \right) \right] \right\}$$

(A.122)

where $\boldsymbol{x} = (x_1, x_2)^T$ and $\boldsymbol{y} = (y_1, y_2)^T$ are the target point and a source point respectively, $\boldsymbol{r} = \boldsymbol{x} - \boldsymbol{y}$, $\boldsymbol{\rho} = (\rho_1, \rho_2)^T$ the density vector, $\boldsymbol{n_y} = (n_{y1}, n_{y2})^T$ the unit normal vector at $\boldsymbol{y}$. Also let $\boldsymbol{n_x} = (n_{x1}, n_{x2})^T$ be the unit normal vector at $\boldsymbol{x}$. We use this to compute the first two terms of

$$\boldsymbol{K}^{D'} \boldsymbol{\rho} = \left\{ \nabla_x \left[\boldsymbol{K}^D \boldsymbol{\rho} \right] + \left(\nabla_x \left[\boldsymbol{K}^D \boldsymbol{\rho} \right] \right)^T - \left(\boldsymbol{\Pi}^D \cdot \boldsymbol{\rho} \right) \right\} \boldsymbol{n_x}. \qquad \text{(A.123)}$$

$$\nabla_{\boldsymbol{x}}\left[\boldsymbol{K}^D\boldsymbol{\rho}\right] = \frac{1}{2}\left\{\nabla_{\boldsymbol{x}}\left[r^{-2}\left(\boldsymbol{r}\cdot\boldsymbol{\rho}\right)\boldsymbol{n}_y\right] + \nabla_{\boldsymbol{x}}\nabla_{\boldsymbol{x}}\left[r^{-2}\left(\boldsymbol{r}\cdot\boldsymbol{n}_y\right)\right]\left(\boldsymbol{y}\cdot\boldsymbol{\rho}\right)\right\}$$

$$+ \frac{1}{2}\left\{-\left[\nabla_{\boldsymbol{x}}\left[\left(\boldsymbol{x}\cdot\boldsymbol{\rho}\right)\right]\otimes\nabla_{\boldsymbol{x}}\left[r^{-2}\left(\boldsymbol{r}\cdot\boldsymbol{n}_y\right)\right]\right] - \left(\boldsymbol{x}\cdot\boldsymbol{\rho}\right)\nabla_{\boldsymbol{x}}\nabla_{\boldsymbol{x}}\left[r^{-2}\left(\boldsymbol{r}\cdot\boldsymbol{n}_y\right)\right]\right\}$$

$$= \frac{1}{2}\left\{\nabla_{\boldsymbol{x}}\left[r^{-2}\left(\boldsymbol{r}\cdot\boldsymbol{\rho}\right)\boldsymbol{n}_y\right] + \nabla_{\boldsymbol{x}}\nabla_{\boldsymbol{x}}\left[r^{-2}\left(\boldsymbol{r}\cdot\boldsymbol{n}_y\right)\right]\left(\boldsymbol{y}\cdot\boldsymbol{\rho}\right)\right\}$$

$$+ \frac{1}{2}\left\{-\left[\boldsymbol{\rho}\otimes\nabla_{\boldsymbol{x}}\left[r^{-2}\left(\boldsymbol{r}\cdot\boldsymbol{n}_y\right)\right]\right] - \left(\boldsymbol{x}\cdot\boldsymbol{\rho}\right)\nabla_{\boldsymbol{x}}\nabla_{\boldsymbol{x}}\left[r^{-2}\left(\boldsymbol{r}\cdot\boldsymbol{n}_y\right)\right]\right\}$$

$$= \frac{1}{2}\left\{\left[\nabla_{\boldsymbol{x}}\left[r^{-2}\left(\boldsymbol{r}\cdot\boldsymbol{\rho}\right)\right]\otimes\boldsymbol{n}_y\right] + \nabla_{\boldsymbol{x}}\nabla_{\boldsymbol{x}}\left[r^{-2}\left(\boldsymbol{r}\cdot\boldsymbol{n}_y\right)\right]\left(\boldsymbol{y}\cdot\boldsymbol{\rho}\right)\right\}$$

$$+ \frac{1}{2}\left\{-\left[\boldsymbol{\rho}\otimes\nabla_{\boldsymbol{x}}\left[r^{-2}\left(\boldsymbol{r}\cdot\boldsymbol{n}_y\right)\right]\right] - \left(\boldsymbol{x}\cdot\boldsymbol{\rho}\right)\nabla_{\boldsymbol{x}}\nabla_{\boldsymbol{x}}\left[r^{-2}\left(\boldsymbol{r}\cdot\boldsymbol{n}_y\right)\right]\right\}.$$

$$(A.124)$$

$$\left(\nabla_{\boldsymbol{x}}\left[\boldsymbol{K}^D\boldsymbol{\rho}\right]\right)^T = \frac{1}{2}\left\{\left[\boldsymbol{n}_y\otimes\nabla_{\boldsymbol{x}}\left[r^{-2}\left(\boldsymbol{r}\cdot\boldsymbol{\rho}\right)\right]\right] + \left(\nabla_{\boldsymbol{x}}\nabla_{\boldsymbol{x}}\left[r^{-2}\left(\boldsymbol{r}\cdot\boldsymbol{u}_y\right)\right]\right)^T\left(\boldsymbol{y}\cdot\boldsymbol{\rho}\right)\right\}$$

$$= \frac{1}{2}\left\{-\left[\nabla_{\boldsymbol{x}}\left[r^{-2}\left(\boldsymbol{r}\cdot\boldsymbol{n}_y\right)\right]\otimes\boldsymbol{\rho}\right] - \left(\boldsymbol{x}\cdot\boldsymbol{\rho}\right)\left(\nabla_{\boldsymbol{x}}\nabla_{\boldsymbol{x}}\left[r^{-2}\left(\boldsymbol{r}\cdot\boldsymbol{n}_y\right)\right]\right)^T\right\}.$$

$$(A.125)$$

Also, we write the last term as

$$\boldsymbol{\Pi}^D\cdot\boldsymbol{\rho} = \left(r^{-2}\boldsymbol{n}_y - 2r^{-4}\left(\boldsymbol{r}\cdot\boldsymbol{n}_y\right)\boldsymbol{r}\right)\cdot\boldsymbol{\rho} = -\nabla_{\boldsymbol{x}}\left[r^{-2}\left(\boldsymbol{r}\cdot\boldsymbol{n}_y\right)\right]\cdot\boldsymbol{\rho}. \qquad (A.126)$$

Hence, we write (A.123) as

$$\nabla_{\boldsymbol{x}}\left[\boldsymbol{K}^D\boldsymbol{\rho}\right] + \left(\nabla_{\boldsymbol{x}}\left[\boldsymbol{K}^D\boldsymbol{\rho}\right]\right)^T - \left(\boldsymbol{\Pi}^D\cdot\boldsymbol{\rho}\right)$$

$$= \frac{1}{2}\left\{\left[\nabla_{\boldsymbol{x}}\left[r^{-2}\left(\boldsymbol{r}\cdot\boldsymbol{\rho}\right)\right]\otimes\boldsymbol{n}_y\right] + \left[\boldsymbol{n}_y\otimes\nabla_{\boldsymbol{x}}\left[r^{-2}\left(\boldsymbol{r}\cdot\boldsymbol{\rho}\right)\right]\right]\right\}$$

$$+ \frac{1}{2}\left\{\nabla_{\boldsymbol{x}}\nabla_{\boldsymbol{x}}\left[r^{-2}\left(\boldsymbol{r}\cdot\boldsymbol{n}_y\right)\right] + \left(\nabla_{\boldsymbol{x}}\nabla_{\boldsymbol{x}}\left[r^{-2}\left(\boldsymbol{r}\cdot\boldsymbol{n}_y\right)\right]\right)^T\right\}\left(\left(\boldsymbol{y}-\boldsymbol{x}\right)\cdot\boldsymbol{\rho}\right)$$

$$- \frac{1}{2}\left\{\left[\boldsymbol{\rho}\otimes\nabla_{\boldsymbol{x}}\left[r^{-2}\left(\boldsymbol{r}\cdot\boldsymbol{n}_y\right)\right]\right] + \left[\nabla_{\boldsymbol{x}}\left[r^{-2}\left(\boldsymbol{r}\cdot\boldsymbol{n}_y\right)\right]\otimes\boldsymbol{\rho}\right]\right\}$$

$$+ \left(\nabla_{\boldsymbol{x}}\left[r^{-2}\left(\boldsymbol{r}\cdot\boldsymbol{n}_y\right)\right]\cdot\boldsymbol{\rho}\right)$$

$$= \frac{1}{2}\left\{\left[\nabla_{\boldsymbol{x}}\left[r^{-2}\left(\boldsymbol{r}\cdot\boldsymbol{\rho}\right)\right]\otimes\boldsymbol{n}_y\right] + \left[\boldsymbol{n}_y\otimes\nabla_{\boldsymbol{x}}\left[r^{-2}\left(\boldsymbol{r}\cdot\boldsymbol{\rho}\right)\right]\right]\right\}$$

$$- \frac{1}{2}\left\{\nabla_{\boldsymbol{x}}\nabla_{\boldsymbol{x}}\left[r^{-2}\left(\boldsymbol{r}\cdot\boldsymbol{n}_y\right)\right] + \left(\nabla_{\boldsymbol{x}}\nabla_{\boldsymbol{x}}\left[r^{-2}\left(\boldsymbol{r}\cdot\boldsymbol{n}_y\right)\right]\right)^T\right\}\left(\boldsymbol{r}\cdot\boldsymbol{\rho}\right)$$

$$- \frac{1}{2}\left\{\left[\boldsymbol{\rho}\otimes\nabla_{\boldsymbol{x}}\left[r^{-2}\left(\boldsymbol{r}\cdot\boldsymbol{n}_y\right)\right]\right] + \left[\nabla_{\boldsymbol{x}}\left[r^{-2}\left(\boldsymbol{r}\cdot\boldsymbol{n}_y\right)\right]\otimes\boldsymbol{\rho}\right]\right\}$$

$$+ \left(\nabla_{\boldsymbol{x}}\left[r^{-2}\left(\boldsymbol{r}\cdot\boldsymbol{n}_y\right)\right]\cdot\boldsymbol{\rho}\right). \qquad (A.127)$$

We compute each term separately or similar terms together using the complex variable expressions in the following sections.

The first term of (A.127)

Let $\tau := \rho_1 + i\rho_2 \in \mathbb{C}$ correspond to the density vector of the boundary integral equations $\rho = (\rho_1, \rho_2)^T \in \mathbb{R}^2$. Noting $[\boldsymbol{a_1} \otimes \boldsymbol{a_2}]\,\boldsymbol{a_3} = (\boldsymbol{a_2} \cdot \boldsymbol{a_3})\,\boldsymbol{a_1}$,

$$\left[\left[\boldsymbol{\nabla_x}\left[r^{-2}\left(\boldsymbol{r} \cdot \boldsymbol{\rho}\right)\right] \otimes n_y\right]\right] n_x = \left[\begin{pmatrix} -\mathrm{Re}\left\{\tau z^{-2}\right\} \\ \mathrm{Im}\left\{\tau z^{-2}\right\} \end{pmatrix} \otimes n_y\right] n_x = (\boldsymbol{n_y} \cdot \boldsymbol{n_x}) \begin{pmatrix} -\mathrm{Re}\left\{\tau z^{-2}\right\} \\ \mathrm{Im}\left\{\tau z^{-2}\right\} \end{pmatrix}.$$

$$(\mathrm{A.128})$$

$$\int_\Gamma \left[\boldsymbol{\nabla_x} \left[r^{-2} \left(\boldsymbol{r} \cdot \boldsymbol{\rho} \right) \right] \otimes n_y \right] n_x dS_y$$

$$= \begin{pmatrix} -\int_\Gamma \left(\boldsymbol{n_x} \cdot \boldsymbol{n_y} \right) \mathrm{Re} \left\{ \tau z^{-2} \right\} dS_y \\ \int_\Gamma \left(\boldsymbol{n_x} \cdot \boldsymbol{n_y} \right) \mathrm{Im} \left\{ \tau z^{-2} \right\} dS_y \end{pmatrix}$$

$$= \begin{pmatrix} -\mathrm{Re} \left\{ \int_\Gamma \left(\boldsymbol{n_x} \cdot \boldsymbol{n_y} \right) \tau z^{-2} dS_y \right\} \\ \mathrm{Im} \left\{ \int_\Gamma \left(\boldsymbol{n_x} \cdot \boldsymbol{n_y} \right) \tau z^{-2} dS_y \right\} \end{pmatrix} \qquad (\because \text{The integrand except } \tau z^{-2} \text{ is real.})$$

$$= \begin{pmatrix} -\mathrm{Re} \left\{ \int_\Gamma \mathrm{Re} \left\{ n_x \overline{\nu_y} \right\} \tau z^{-2} \frac{-i}{n_y} dz_y \right\} \\ \mathrm{Im} \left\{ \int_\Gamma \mathrm{Re} \left\{ n_x \overline{\nu_y} \right\} \tau z^{-2} \frac{-i}{n_y} dz_y \right\} \end{pmatrix} \qquad (\because dS_y = |dz_y| = \frac{-i}{\nu_y} dz_y, \ \left(\boldsymbol{n_x} \cdot \boldsymbol{n_y} \right) = \mathrm{Re} \left\{ \nu_x \overline{\nu_y} \right\}.)$$

$$= \begin{pmatrix} \mathrm{Re} \left\{ i \int_\Gamma \mathrm{Re} \left\{ \nu_x \overline{\nu_y} \right\} \tau z^{-2} \overline{\nu_y} dz_y \right\} \\ -\mathrm{Im} \left\{ i \int_\Gamma \mathrm{Re} \left\{ \nu_x \overline{\nu_y} \right\} \tau z^{-2} \overline{\nu_y} dz_y \right\} \end{pmatrix} \qquad (\because \nu_y \overline{\nu_y} = 1.)$$

$$= \begin{pmatrix} -\mathrm{Im} \left\{ \int_\Gamma \mathrm{Re} \left\{ \nu_x \overline{\nu_y} \right\} \tau z^{-2} \overline{\nu_y} dz_y \right\} \\ -\mathrm{Re} \left\{ \int_\Gamma \mathrm{Re} \left\{ \nu_x \overline{\nu_y} \right\} \tau z^{-2} \overline{\nu_y} dz_y \right\} \end{pmatrix} \qquad (\because \mathrm{Re} \left\{ ic \right\} = -\mathrm{Im} \left\{ c \right\}, \ \mathrm{Im} \left\{ ic \right\} = \mathrm{Re} \left\{ c \right\} \ \text{for } \forall c \in \mathbb{C}.)$$

$$= \begin{pmatrix} -\mathrm{Im} \left\{ \int_\Gamma \mathrm{Re} \left\{ \nu_x \overline{\nu_y} \right\} (\rho_1 + i\rho_2) z^{-2} \overline{\nu_y} dz_y \right\} \\ -\mathrm{Re} \left\{ \int_\Gamma \mathrm{Re} \left\{ \nu_x \overline{\nu_y} \right\} (\rho_1 + i\rho_2) z^{-2} \overline{\nu_y} dz_y \right\} \end{pmatrix}$$

$$= \begin{pmatrix} -\mathrm{Im} \left\{ \int_\Gamma \mathrm{Re} \left\{ \nu_x \overline{\nu_y} \right\} \rho_1 z^{-2} \overline{\nu_y} dz_y \right\} - \mathrm{Im} \left\{ i \int_\Gamma \mathrm{Re} \left\{ \nu_x \overline{\nu_y} \right\} \rho_2 z^{-2} \overline{\nu_y} dz_y \right\} \\ -\mathrm{Re} \left\{ \int_\Gamma \mathrm{Re} \left\{ \nu_x \overline{\nu_y} \right\} \rho_1 z^{-2} \overline{\nu_y} dz_y \right\} - \mathrm{Re} \left\{ i \int_\Gamma \mathrm{Re} \left\{ \nu_x \overline{\nu_y} \right\} \rho_2 z^{-2} \overline{\nu_y} dz_y \right\} \end{pmatrix}$$

$$= \begin{pmatrix} -\mathrm{Im} \left\{ \int_\Gamma \mathrm{Re} \left\{ \nu_x \overline{\nu_y} \right\} \rho_1 z^{-2} \overline{\nu_y} dz_y \right\} - \mathrm{Re} \left\{ \int_\Gamma \mathrm{Re} \left\{ \nu_x \overline{\nu_y} \right\} \rho_2 z^{-2} \overline{\nu_y} dz_y \right\} \\ -\mathrm{Re} \left\{ \int_\Gamma \mathrm{Re} \left\{ \nu_x \overline{\nu_y} \right\} \rho_1 z^{-2} \overline{\nu_y} dz_y \right\} + \mathrm{Im} \left\{ \int_\Gamma \mathrm{Re} \left\{ \nu_x \overline{\nu_y} \right\} \rho_2 z^{-2} \overline{\nu_y} dz_y \right\} \end{pmatrix}$$

$$= \begin{pmatrix} -\mathrm{Im} \left\{ I_H \left[\mathrm{Re} \left\{ \nu_x \overline{\nu_y} \right\} \overline{\nu_y} \rho_1 \right] \right\} - \mathrm{Re} \left\{ I_H \left[\mathrm{Re} \left\{ \nu_x \overline{\nu_y} \right\} \overline{\nu_y} \rho_2 \right] \right\} \\ -\mathrm{Re} \left\{ I_H \left[\mathrm{Re} \left\{ \nu_x \overline{\nu_y} \right\} \overline{\nu_y} \rho_1 \right] \right\} + \mathrm{Im} \left\{ I_H \left[\mathrm{Re} \left\{ \nu_x \overline{\nu_y} \right\} \overline{\nu_y} \rho_2 \right] \right\} \end{pmatrix}, \qquad \text{(A.129)}$$

here and after this section we use the notations of following these.

$$I_H \left[f \right] (x) := \int_\Gamma \frac{f}{z^2} dz_y, \qquad \text{(A.130)}$$

$$I_S \left[f \right] (x) := \int_\Gamma \frac{f}{z^3} dz_y \qquad \text{(A.131)}$$

<u>The second term of (A.127)</u>

Since $r^{-2} (\boldsymbol{r} \cdot \boldsymbol{\rho}) = -\mathrm{Re}\left\{\frac{\tau}{z}\right\}$,

$$\frac{\partial}{\partial x_1} \left[r^{-2} (\boldsymbol{r} \cdot \boldsymbol{\rho}) \right] = -\mathrm{Re}\left\{ (-1)z^{-2}(-1)\tau \right\} = -\mathrm{Re}\left\{ \frac{\tau}{z^2} \right\}, \tag{A.132}$$

$$\frac{\partial}{\partial x_2} \left[r^{-2} (\boldsymbol{r} \cdot \boldsymbol{\rho}) \right] = -\mathrm{Re}\left\{ (-1)z^{-2}(-i)\tau \right\} = -\mathrm{Re}\left\{ i\frac{\tau}{z^2} \right\} = \mathrm{Im}\left\{ \frac{\tau}{z^2} \right\}. \tag{A.133}$$

Also, noting $[\boldsymbol{a_1} \otimes \boldsymbol{a_2}]\, \boldsymbol{a_3} = (\boldsymbol{a_2} \cdot \boldsymbol{a_3})\, \boldsymbol{a_1}$ for $\boldsymbol{a_1}, \boldsymbol{a_2}, \boldsymbol{a_3} \in \mathbb{R}^2$,

$$\begin{aligned}
\left\{ \left[\boldsymbol{n_y} \otimes \boldsymbol{\nabla_x} \left[r^{-2} (\boldsymbol{r} \cdot \boldsymbol{\rho}) \right] \right] \right\} \boldsymbol{n_x} &= \left\{ \left(\boldsymbol{\nabla_x} \left[\boldsymbol{r^{-2}} (\boldsymbol{r} \cdot \boldsymbol{\rho}) \right] \cdot \boldsymbol{n_x} \right) \right\} \boldsymbol{n_y} \\
&= \left[\begin{pmatrix} -\mathrm{Re}\left\{ \tau z^{-2} \right\} \\ \mathrm{Im}\left\{ \tau z^{-2} \right\} \end{pmatrix} \cdot \begin{pmatrix} n_{x1} \\ n_{x2} \end{pmatrix} \right] \boldsymbol{n_y} \\
&= \left(-\mathrm{Re}\left\{ \tau z^{-2} \right\} n_{x1} + \mathrm{Im}\left\{ \tau z^{-2} \right\} n_{x2} \right) \boldsymbol{n_y} \\
&= -\mathrm{Re}\left\{ \tau z^{-2} n_x \right\} \boldsymbol{n_y} \\
&= -\mathrm{Re}\left\{ (\rho_1 + i\rho_2) z^{-2} \nu_x \right\} \boldsymbol{n_y} \\
&= -\left(\rho_1 \mathrm{Re}\left\{ z^{-2} \nu_x \right\} + \rho_2 \mathrm{Re}\left\{ i z^{-2} \nu_x \right\} \right) \boldsymbol{n_y} \\
&= -\left\{ \begin{pmatrix} \mathrm{Re}\left\{ z^{-2} \nu_x \right\} \\ \mathrm{Re}\left\{ i z^{-2} \nu_x \right\} \end{pmatrix} \cdot \boldsymbol{\rho} \right\} \boldsymbol{n_y} \\
&= \left\{ \begin{pmatrix} -\mathrm{Re}\left\{ z^{-2} \nu_x \right\} \\ \mathrm{Im}\left\{ z^{-2} \nu_x \right\} \end{pmatrix} \cdot \boldsymbol{\rho} \right\} \begin{pmatrix} n_{y1} \\ n_{y2} \end{pmatrix}
\end{aligned} \tag{A.134}$$

$$\int_{\Gamma} \left[\boldsymbol{n_y} \otimes \boldsymbol{\nabla_x} \left[r^{-2} \left(\boldsymbol{r} \cdot \boldsymbol{\rho} \right) \right] \right] \boldsymbol{n_x} dS_y = \int_{\Gamma} \left\{ \begin{pmatrix} -\mathrm{Re}\left\{ z^{-2}\nu_x \right\} \\ \mathrm{Im}\left\{ z^{-2}\nu_x \right\} \end{pmatrix} \cdot \boldsymbol{\rho} \right\} \boldsymbol{n_y} dS_y$$

$$= \int_{\Gamma} \begin{pmatrix} -n_{y1}\mathrm{Re}\left\{ z^{-2}\nu_x \right\} \rho_1 + n_{y1}\mathrm{Im}\left\{ z^{-2}\nu_x \right\} \rho_2 \\ -n_{y2}\mathrm{Re}\left\{ z^{-2}\nu_x \right\} \rho_1 + n_{y2}\mathrm{Im}\left\{ z^{-2}\nu_x \right\} \rho_2 \end{pmatrix} dS_y$$

$$= \begin{pmatrix} -\mathrm{Re}\left\{ \int_{\Gamma} n_{y1} z^{-2}\nu_x \rho_1 dS_y \right\} + \mathrm{Im}\left\{ \int_{\Gamma} n_{y1} z^{-2}\nu_x \rho_2 dS_y \right\} \\ -\mathrm{Re}\left\{ \int_{\Gamma} n_{y2} z^{-2}\nu_x \rho_1 dS_y \right\} + \mathrm{Im}\left\{ \int_{\Gamma} n_{y2} z^{-2}\nu_x \rho_2 dS_y \right\} \end{pmatrix}$$

$$= \begin{pmatrix} \mathrm{Re}\left\{ i \int_{\Gamma} n_{y1} z^{-2}\nu_x \overline{\nu_y} \rho_1 dz_y \right\} - \mathrm{Im}\left\{ i \int_{\Gamma} n_{y1} z^{-2}\nu_x \overline{\nu_y} \rho_2 dz_y \right\} \\ \mathrm{Re}\left\{ i \int_{\Gamma} n_{y2} z^{-2}\nu_x \overline{\nu_y} \rho_1 dz_y \right\} - \mathrm{Im}\left\{ i \int_{\Gamma} n_{y2} z^{-2}\nu_x \overline{\nu_y} \rho_2 dz_y \right\} \end{pmatrix}$$

$$= \begin{pmatrix} -\mathrm{Im}\left\{ \int_{\Gamma} n_{y1} z^{-2}\nu_x \overline{\nu_y} \rho_1 dz_y \right\} - \mathrm{Re}\left\{ \int_{\Gamma} n_{y1} z^{-2}\nu_x \overline{\nu_y} \rho_2 dz_y \right\} \\ -\mathrm{Im}\left\{ \int_{\Gamma} n_{y2} z^{-2}\nu_x \overline{\nu_y} \rho_1 dz_y \right\} - \mathrm{Re}\left\{ \int_{\Gamma} n_{y2} z^{-2}\nu_x \overline{\nu_y} \rho_2 dz_y \right\} \end{pmatrix}$$

$$= \begin{pmatrix} -\mathrm{Im}\left\{ I_H \left[n_{y1}\nu_x \overline{\nu_y} \rho_1 \right] \right\} - \mathrm{Re}\left\{ I_H \left[n_{y1}\nu_x \overline{\nu_y} \rho_2 \right] \right\} \\ -\mathrm{Im}\left\{ I_H \left[n_{y2}\nu_x \overline{\nu_y} \rho_1 \right] \right\} - \mathrm{Re}\left\{ I_H \left[n_{y2}\nu_x \overline{\nu_y} \rho_2 \right] \right\} \end{pmatrix}.$$

$$(A.135)$$

$$\therefore \int_{\Gamma} \frac{1}{2} \left\{ \left[\boldsymbol{\nabla_x} \left[r^{-2} \left(\boldsymbol{r} \cdot \boldsymbol{\rho} \right) \right] \otimes \boldsymbol{n_y} \right] + \left[\boldsymbol{n_y} \otimes \boldsymbol{\nabla_x} \left[r^{-2} \left(\boldsymbol{r} \cdot \boldsymbol{\rho} \right) \right] \right] \boldsymbol{n_x} \right\} dS_y$$

$$= \frac{1}{2} \begin{pmatrix} -\mathrm{Im}\left\{ I_H \left[\mathrm{Re}\left\{ n_x \overline{\nu_y} \right\} \overline{\nu_y} \rho_1 \right] \right\} - \mathrm{Re}\left\{ I_H \left[\mathrm{Re}\left\{ n_x \overline{\nu_y} \right\} \overline{\nu_y} \rho_2 \right] \right\} \\ -\mathrm{Re}\left\{ I_H \left[\mathrm{Re}\left\{ n_x \overline{\nu_y} \right\} \overline{\nu_y} \rho_1 \right] \right\} + \mathrm{Im}\left\{ I_H \left[\mathrm{Re}\left\{ n_x \overline{\nu_y} \right\} \overline{\nu_y} \rho_2 \right] \right\} \end{pmatrix}$$

$$+ \frac{1}{2} \begin{pmatrix} -\mathrm{Im}\left\{ I_H \left[n_{y1} n_x \overline{\nu_y} \rho_1 \right] \right\} - \mathrm{Re}\left\{ I_H \left[n_{y1} n_x \overline{\nu_y} \rho_2 \right] \right\} \\ -\mathrm{Im}\left\{ I_H \left[n_{y2} n_x \overline{\nu_y} \rho_1 \right] \right\} - \mathrm{Re}\left\{ I_H \left[n_{y2} n_x \overline{\nu_y} \rho_2 \right] \right\} \end{pmatrix}. \qquad (A.136)$$

The third and forth terms of (A.127) Here we compute

$$-\left[\boldsymbol{\nabla}_{\boldsymbol{x}}\boldsymbol{\nabla}_{\boldsymbol{x}}\left[r^{-2}\left(\boldsymbol{r}\cdot\boldsymbol{n_y}\right)\right]+\left(\boldsymbol{\nabla}_{\boldsymbol{x}}\boldsymbol{\nabla}_{\boldsymbol{x}}\left[r^{-2}\left(\boldsymbol{r}\cdot\boldsymbol{n_y}\right)\right]\right)^{T}\right]\left(\boldsymbol{r}\cdot\boldsymbol{\rho}\right)\boldsymbol{n_x}. \tag{A.137}$$

Since

$$\boldsymbol{\nabla}_{\boldsymbol{x}}\boldsymbol{\nabla}_{\boldsymbol{x}}\left[r^{-2}\left(\boldsymbol{r}\cdot\boldsymbol{n_y}\right)\right]=2\begin{bmatrix}-\mathrm{Re}\left\{\nu_y z^{-3}\right\} & \mathrm{Im}\left\{\nu_y z^{-3}\right\}\\ \mathrm{Im}\left\{\nu_y z^{-3}\right\} & \mathrm{Re}\left\{\nu_y z^{-3}\right\}\end{bmatrix}, \tag{A.138}$$

$$\boldsymbol{\nabla}_{\boldsymbol{x}}\boldsymbol{\nabla}_{\boldsymbol{x}}\left[r^{-2}\left(\boldsymbol{r}\cdot\boldsymbol{n_y}\right)\right]+\left(\boldsymbol{\nabla}_{\boldsymbol{x}}\boldsymbol{\nabla}_{\boldsymbol{x}}\left[r^{-2}\left(\boldsymbol{r}\cdot\boldsymbol{n_y}\right)\right]\right)^{T}=4\begin{bmatrix}-\mathrm{Re}\left\{\nu_y z^{-3}\right\} & \mathrm{Im}\left\{\nu_y z^{-3}\right\}\\ \mathrm{Im}\left\{\nu_y z^{-3}\right\} & \mathrm{Re}\left\{\nu_y z^{-3}\right\}\end{bmatrix}. \tag{A.139}$$

Also using $\left(\boldsymbol{r}\cdot\boldsymbol{\rho}\right)\boldsymbol{n_x}=\left[\boldsymbol{n_x}\otimes\boldsymbol{r}\right]\boldsymbol{\rho}$, we have

$$-\left[\boldsymbol{\nabla}_{\boldsymbol{x}}\boldsymbol{\nabla}_{\boldsymbol{x}}\left[r^{-2}\left(\boldsymbol{r}\cdot\boldsymbol{n_y}\right)\right]+\left(\boldsymbol{\nabla}_{\boldsymbol{x}}\boldsymbol{\nabla}_{\boldsymbol{x}}\left[r^{-2}\left(\boldsymbol{r}\cdot\boldsymbol{n_y}\right)\right]\right)^{T}\right]\left(\boldsymbol{r}\cdot\boldsymbol{\rho}\right)\boldsymbol{n_x}$$

$$=-4\begin{bmatrix}-\mathrm{Re}\left\{\nu_y z^{-3}\right\} & \mathrm{Im}\left\{\nu_y z^{-3}\right\}\\ \mathrm{Im}\left\{\nu_y z^{-3}\right\} & \mathrm{Re}\left\{\nu_y z^{-3}\right\}\end{bmatrix}\left[\boldsymbol{n_x}\otimes\boldsymbol{r}\right]\boldsymbol{\rho}$$

$$=-4\begin{bmatrix}-\mathrm{Re}\left\{\nu_y z^{-3}\right\} & \mathrm{Im}\left\{\nu_y z^{-3}\right\}\\ \mathrm{Im}\left\{\nu_y z^{-3}\right\} & \mathrm{Re}\left\{\nu_y z^{-3}\right\}\end{bmatrix}\begin{bmatrix}n_{x1}r_1 & n_{x1}r_2\\ n_{x2}r_1 & n_{x2}r_2\end{bmatrix}\boldsymbol{\rho}$$

$$=-4\begin{bmatrix}-\mathrm{Re}\left\{\nu_y z^{-3}\right\}n_{x1}r_1+\mathrm{Im}\left\{\nu_y z^{-3}\right\}n_{x2}r_1 & -\mathrm{Re}\left\{\nu_y z^{-3}\right\}n_{x1}r_2+\mathrm{Im}\left\{\nu_y z^{-3}\right\}n_{x2}r_2\\ \mathrm{Im}\left\{\nu_y z^{-3}\right\}n_{x1}r_1+\mathrm{Re}\left\{\nu_y z^{-3}\right\}n_{x2}r_1 & \mathrm{Im}\left\{\nu_y z^{-3}\right\}n_{x1}r_2+\mathrm{Re}\left\{\nu_y z^{-3}\right\}n_{x2}r_2\end{bmatrix}\boldsymbol{\rho}$$

$$=-4\begin{bmatrix}-\mathrm{Re}\left\{\nu_y z^{-3}\right\}n_{x1}r_1 & -\mathrm{Re}\left\{\nu_y z^{-3}\right\}n_{x1}r_2\\ \mathrm{Im}\left\{\nu_y z^{-3}\right\}n_{x1}r_1 & \mathrm{Im}\left\{\nu_y z^{-3}\right\}n_{x1}r_2\end{bmatrix}\boldsymbol{\rho}-4\begin{bmatrix}\mathrm{Im}\left\{\nu_y z^{-3}\right\}n_{x2}r_1 & \mathrm{Im}\left\{\nu_y z^{-3}\right\}n_{x2}r_2\\ \mathrm{Re}\left\{\nu_y z^{-3}\right\}n_{x2}r_1 & \mathrm{Re}\left\{\nu_y z^{-3}\right\}n_{x2}r_2\end{bmatrix}\boldsymbol{\rho}$$

$$=-4\begin{pmatrix}-\mathrm{Re}\left\{\nu_y z^{-3}\right\}n_{x1}r_1\rho_1-\mathrm{Re}\left\{\nu_y z^{-3}\right\}n_{x1}r_2\rho_2\\ \mathrm{Im}\left\{\nu_y z^{-3}\right\}n_{x1}r_1\rho_1+\mathrm{Im}\left\{\nu_y z^{-3}\right\}n_{x1}r_2\rho_2\end{pmatrix}$$

$$-4\begin{pmatrix}\mathrm{Im}\left\{\nu_y z^{-3}\right\}n_{x2}r_1\rho_1+\mathrm{Im}\left\{\nu_y z^{-3}\right\}n_{x2}r_2\rho_2\\ \mathrm{Re}\left\{\nu_y z^{-3}\right\}n_{x2}r_1\rho_1+\mathrm{Re}\left\{\nu_y z^{-3}\right\}n_{x2}r_2\rho_2\end{pmatrix} \tag{A.140}$$

The integral of each element along the boundary can be written like below.

$$\int_\Gamma \text{Re}\left\{\nu_y z^{-3}\right\} n_{x1} r_1 \rho_1 dS_y = \text{Re}\left\{\int_\Gamma \nu_y z^{-3} n_{x1} r_1 \rho_1 dS_y\right\}$$

$$= \text{Re}\left\{\int_\Gamma \nu_y z^{-3} n_{x1} r_1 \rho_1 \frac{-i}{\nu_y} dz_y\right\}$$

$$= -\text{Re}\left\{i \int_\Gamma z^{-3} n_{x1} r_1 \rho_1 dz_y\right\} \qquad \text{(A.141)}$$

$$\therefore \int_\Gamma -\left[\boldsymbol{\nabla_x}\boldsymbol{\nabla_x}\left[r^{-2}\left(\boldsymbol{r}\cdot\boldsymbol{\nu_y}\right)\right] + \left(\boldsymbol{\nabla_x}\boldsymbol{\nabla_x}\left[r^{-2}\left(\boldsymbol{r}\cdot\boldsymbol{\nu_y}\right)\right]\right)^T\right]\left(\boldsymbol{r}\cdot\boldsymbol{\rho}\right)\boldsymbol{n_x}dS_y$$

$$= -4\begin{pmatrix} \text{Re}\left\{i\int_\Gamma n_{x1}r_1\rho_1 z^{-3}dz_y\right\} + \text{Re}\left\{i\int_\Gamma n_{x1}r_2\rho_2 z^{-3}dz_y\right\} \\ -\text{Im}\left\{i\int_\Gamma n_{x1}r_1\rho_1 z^{-3}dz_y\right\} - \text{Im}\left\{i\int_\Gamma n_{x1}r_2\rho_2 z^{-3}dz_y\right\} \end{pmatrix}$$

$$-4\begin{pmatrix} -\text{Im}\left\{i\int_\Gamma n_{x2}r_1\rho_1 z^{-3}dz_y\right\} - \text{Im}\left\{i\int_\Gamma n_{x2}r_2\rho_2 z^{-3}dz_y\right\} \\ -\text{Re}\left\{i\int_\Gamma n_{x2}r_1\rho_1 z^{-3}dz_y\right\} - \text{Re}\left\{i\int_\Gamma n_{x2}r_2\rho_2 z^{-3}dz_y\right\} \end{pmatrix}$$

$$= -4\begin{pmatrix} -\text{Im}\left\{\int_\Gamma n_{x1}r_1\rho_1 z^{-3}dz_y\right\} - \text{Im}\left\{\int_\Gamma n_{x1}r_2\rho_2 z^{-3}dz_y\right\} \\ -\text{Re}\left\{\int_\Gamma n_{x1}r_1\rho_1 z^{-3}dz_y\right\} - \text{Re}\left\{\int_\Gamma n_{x1}r_2\rho_2 z^{-3}dz_y\right\} \end{pmatrix}$$

$$-4\begin{pmatrix} -\text{Re}\left\{\int_\Gamma n_{x2}r_1\rho_1 z^{-3}dz_y\right\} - \text{Re}\left\{\int_\Gamma n_{x2}r_2\rho_2 z^{-3}dz_y\right\} \\ \text{Im}\left\{\int_\Gamma n_{x2}r_1\rho_1 z^{-3}dz_y\right\} + \text{Im}\left\{\int_\Gamma n_{x2}r_2\rho_2 z^{-3}dz_y\right\} \end{pmatrix}$$

$$= 4\begin{pmatrix} \text{Im}\left\{I_S\left[n_{x1}r_1\rho_1\right]\right\} + \text{Im}\left\{I_S\left[n_{x1}r_2\rho_2\right]\right\} \\ \text{Re}\left\{I_S\left[n_{x1}r_1\rho_1\right]\right\} + \text{Re}\left\{I_S\left[n_{x1}r_2\rho_2\right]\right\} \end{pmatrix} + 4\begin{pmatrix} \text{Re}\left\{I_S\left[n_{x2}r_1\rho_1\right]\right\} + \text{Re}\left\{I_S\left[n_{x2}r_2\rho_2\right]\right\} \\ -\text{Im}\left\{I_S\left[n_{x2}r_1\rho_1\right]\right\} - \text{Im}\left\{I_S\left[n_{x2}r_2\rho_2\right]\right\} \end{pmatrix}$$

$$\text{(A.142)}$$

$$\therefore -\frac{1}{2}\int_\Gamma\left[\boldsymbol{\nabla_x}\boldsymbol{\nabla_x}\left[r^{-2}\left(\boldsymbol{r}\cdot\boldsymbol{\nu_y}\right)\right] + \left(\boldsymbol{\nabla_x}\boldsymbol{\nabla_x}\left[r^{-2}\left(\boldsymbol{r}\cdot\boldsymbol{\nu_y}\right)\right]\right)^T\right]\left(\boldsymbol{r}\cdot\boldsymbol{\rho}\right)\boldsymbol{n_x}dS_y$$

$$= 2\begin{pmatrix} \text{Im}\left\{I_S\left[n_{x1}r_1\rho_1\right]\right\} + \text{Im}\left\{I_S\left[n_{x1}r_2\rho_2\right]\right\} \\ \text{Re}\left\{I_S\left[n_{x1}r_1\rho_1\right]\right\} + \text{Re}\left\{I_S\left[n_{x1}r_2\rho_2\right]\right\} \end{pmatrix} + 2\begin{pmatrix} \text{Re}\left\{I_S\left[n_{x2}r_1\rho_1\right]\right\} + \text{Re}\left\{I_S\left[n_{x2}r_2\rho_2\right]\right\} \\ -\text{Im}\left\{I_S\left[n_{x2}r_1\rho_1\right]\right\} - \text{Im}\left\{I_S\left[n_{x2}r_2\rho_2\right]\right\} \end{pmatrix}$$

$$\text{(A.143)}$$

The fifth and sixth terms of (A.127) Noting

$$\left[\boldsymbol{\rho} \otimes \boldsymbol{\nabla}_{\boldsymbol{x}}\left[r^{-2}\left(\boldsymbol{r} \cdot \boldsymbol{n}_{\boldsymbol{y}}\right)\right]\right] \boldsymbol{n}_{\boldsymbol{x}}=\left(\boldsymbol{\nabla}_{\boldsymbol{x}}\left[r^{-2}\left(\boldsymbol{r} \cdot \boldsymbol{n}_{\boldsymbol{y}}\right)\right] \cdot \boldsymbol{\nu}_{\boldsymbol{x}}\right) \boldsymbol{\rho},\tag{A.144}$$

$$\left[\boldsymbol{\nabla}_{\boldsymbol{x}}\left[r^{-2}\left(\boldsymbol{r} \cdot \boldsymbol{n}_{\boldsymbol{y}}\right)\right] \otimes \boldsymbol{\rho}\right] \boldsymbol{n}_{\boldsymbol{x}}=\left[\boldsymbol{\nabla}_{\boldsymbol{x}}\left[r^{-2}\left(\boldsymbol{r} \cdot \boldsymbol{n}_{\boldsymbol{y}}\right)\right] \otimes \boldsymbol{n}_{\boldsymbol{x}}\right] \boldsymbol{\rho}.\tag{A.145}$$

$$\begin{aligned}
\therefore -&\left\{\left[\boldsymbol{\rho} \otimes \boldsymbol{\nabla}_{\boldsymbol{x}}\left[r^{-2}\left(\boldsymbol{r} \cdot \boldsymbol{n}_{\boldsymbol{y}}\right)\right]\right]+\left[\boldsymbol{\nabla}_{\boldsymbol{x}}\left[r^{-2}\left(\boldsymbol{r} \cdot \boldsymbol{n}_{\boldsymbol{y}}\right)\right] \otimes \boldsymbol{\rho}\right]\right\} \boldsymbol{n}_{\boldsymbol{x}} \\
=-&\left\{\left(\boldsymbol{\nabla}_{\boldsymbol{x}}\left[r^{-2}\left(\boldsymbol{r} \cdot \boldsymbol{n}_{\boldsymbol{y}}\right)\right] \cdot \boldsymbol{n}_{\boldsymbol{x}}\right)+\left[\boldsymbol{\nabla}_{\boldsymbol{x}}\left[r^{-2}\left(\boldsymbol{r} \cdot \boldsymbol{n}_{\boldsymbol{y}}\right)\right] \otimes \boldsymbol{n}_{\boldsymbol{x}}\right]\right\} \boldsymbol{\rho} \\
=-&\left\{\binom{-\operatorname{Re}\left\{\nu_{y} z^{-2}\right\}}{\operatorname{Im}\left\{\nu_{y} z^{-2}\right\}} \cdot \boldsymbol{n}_{\boldsymbol{x}}+\binom{-\operatorname{Re}\left\{\nu_{y} z^{-2}\right\}}{\operatorname{Im}\left\{\nu_{y} z^{-2}\right\}} \otimes \boldsymbol{n}_{\boldsymbol{x}}\right\} \boldsymbol{\rho}.\tag{A.146}
\end{aligned}$$

The integral of the first term on the boundary is

$$\begin{aligned}
\int_{\Gamma}-&\left\{\binom{-\operatorname{Re}\left\{\nu_{y} z^{-2}\right\}}{\operatorname{Im}\left\{\nu_{y} z^{-2}\right\}} \cdot \boldsymbol{n}_{\boldsymbol{x}}\right\} \boldsymbol{\rho}\, dS_{y}=\int_{\Gamma}\left(\operatorname{Re}\left\{\nu_{y} z^{-2}\right\} n_{x1}-\operatorname{Im}\left\{\nu_{y} z^{-2}\right\} n_{x2}\right) \boldsymbol{\rho}\, dS_{y} \\
&=\int_{\Gamma} \operatorname{Re}\left\{\nu_{y} z^{-2}\right\} n_{x1} \boldsymbol{\rho}\, dS_{y}-\int_{\Gamma} \operatorname{Im}\left\{\nu_{y} z^{-2}\right\} n_{x2} \boldsymbol{\rho}\, dS_{y} \\
&=\operatorname{Re}\left\{\int_{\Gamma} \nu_{y} z^{-2} n_{x1} \boldsymbol{\rho}\, dS_{y}\right\}-\operatorname{Im}\left\{\int_{\Gamma} \nu_{y} z^{-2} n_{x2} \boldsymbol{\rho}\, dS_{y}\right\} \\
&=\operatorname{Re}\left\{\int_{\Gamma} \nu_{y} z^{-2} n_{x1} \boldsymbol{\rho} \frac{-i}{\nu_{y}} dz_{y}\right\}-\operatorname{Im}\left\{\int_{\Gamma} \nu_{y} z^{-2} n_{x2} \boldsymbol{\rho} \frac{-i}{\nu_{y}} dz_{y}\right\} \\
&=-\operatorname{Re}\left\{i \int_{\Gamma} z^{-2} n_{x1} \boldsymbol{\rho}\, dz_{y}\right\}+\operatorname{Im}\left\{i \int_{\Gamma} z^{-2} n_{x2} \boldsymbol{\rho}\, dz_{y}\right\} \\
&=+\operatorname{Im}\left\{\int_{\Gamma} z^{-2} n_{x1} \boldsymbol{\rho}\, dz_{y}\right\}+\operatorname{Re}\left\{\int_{\Gamma} z^{-2} n_{x2} \boldsymbol{\rho}\, dz_{y}\right\} \\
&=\operatorname{Im}\left\{I_{H}\left[n_{x1} \boldsymbol{\rho}\right]\right\}+\operatorname{Re}\left\{I_{H}\left[n_{x2} \boldsymbol{\rho}\right]\right\} \\
&=\binom{\operatorname{Im}\left\{I_{H}\left[n_{x1} \rho_{1}\right]\right\}+\operatorname{Re}\left\{I_{H}\left[n_{x2} \rho_{1}\right]\right\}}{\operatorname{Im}\left\{I_{H}\left[n_{x1} \rho_{2}\right]\right\}+\operatorname{Re}\left\{I_{H}\left[n_{x2} \rho_{2}\right]\right\}}
\end{aligned}$$
$$\tag{A.147}$$

The second term of (A.146) is

$$
-\left\{ \begin{pmatrix} -\mathrm{Re}\left\{\nu_y z^{-2}\right\} \\ \mathrm{Im}\left\{\nu_y z^{-2}\right\} \end{pmatrix} \otimes \boldsymbol{n_x} \right\} \boldsymbol{\rho} = \begin{bmatrix} \mathrm{Re}\left\{\nu_y z^{-2}\right\} n_{x1} & \mathrm{Re}\left\{\nu_y z^{-2}\right\} n_{x2} \\ -\mathrm{Im}\left\{\nu_y z^{-2}\right\} n_{x1} & -\mathrm{Im}\left\{\nu_y z^{-2}\right\} n_{x2} \end{bmatrix} \boldsymbol{\rho} \quad (\mathrm{A}.148)
$$

$$
= \begin{pmatrix} \mathrm{Re}\left\{\nu_y z^{-2}\right\} n_{x1}\rho_1 + \mathrm{Re}\left\{\nu_y z^{-2}\right\} n_{x2}\rho_2 \\ -\mathrm{Im}\left\{\nu_y z^{-2}\right\} n_{x1}\rho_1 - \mathrm{Im}\left\{\nu_y z^{-2}\right\} n_{x2}\rho_2 \end{pmatrix}
$$

$$(\mathrm{A}.149)$$

Hence, we write the integral of the second term of (A.146) as

$$
\int_\Gamma -\left\{ \begin{pmatrix} -\mathrm{Re}\left\{\nu_y z^{-2}\right\} \\ \mathrm{Im}\left\{\nu_y z^{-2}\right\} \end{pmatrix} \otimes \boldsymbol{n_x} \right\} \boldsymbol{\rho}\, dS_y
$$

$$
= \begin{pmatrix} \int_\Gamma \mathrm{Re}\left\{\nu_y z^{-2}\right\} n_{x1}\rho_1 dS_y + \int_\Gamma \mathrm{Re}\left\{\nu_y z^{-2}\right\} n_{x2}\rho_2 dS_y \\ -\int_\Gamma \mathrm{Im}\left\{\nu_y z^{-2}\right\} n_{x1}\rho_1 dS_y - \int_\Gamma \mathrm{Im}\left\{\nu_y z^{-2}\right\} n_{x2}\rho_2 dS_y \end{pmatrix}
$$

$$
= \begin{pmatrix} \mathrm{Re}\left\{\int_\Gamma \nu_y z^{-2} n_{x1}\rho_1 dS_y\right\} + \mathrm{Re}\left\{\int_\Gamma \nu_y z^{-2} n_{x2}\rho_2 dS_y\right\} \\ -\mathrm{Im}\left\{\int_\Gamma \nu_y z^{-2} n_{x1}\rho_1 dS_y\right\} - \mathrm{Im}\left\{\int_\Gamma \nu_y z^{-2} n_{x2}\rho_2 dS_y\right\} \end{pmatrix}
$$

$$
= \begin{pmatrix} \mathrm{Re}\left\{\int_\Gamma \nu_y z^{-2} n_{x1}\rho_1 \frac{-i}{\nu_y} dz_y\right\} + \mathrm{Re}\left\{\int_\Gamma \nu_y z^{-2} n_{x2}\rho_2 \frac{-i}{\nu_y} dz_y\right\} \\ -\mathrm{Im}\left\{\int_\Gamma \nu_y z^{-2} n_{x1}\rho_1 \frac{-i}{\nu_y} dz_y\right\} - \mathrm{Im}\left\{\int_\Gamma \nu_y z^{-2} n_{x2}\rho_2 \frac{-i}{\nu_y} dz_y\right\} \end{pmatrix}
$$

$$
= \begin{pmatrix} -\mathrm{Re}\left\{i\int_\Gamma z^{-2} n_{x1}\rho_1 dz_y\right\} - \mathrm{Re}\left\{i\int_\Gamma z^{-2} n_{x2}\rho_2 dz_y\right\} \\ \mathrm{Im}\left\{i\int_\Gamma z^{-2} n_{x1}\rho_1 dz_y\right\} + \mathrm{Im}\left\{i\int_\Gamma z^{-2} n_{x2}\rho_2 dz_y\right\} \end{pmatrix}
$$

$$
= \begin{pmatrix} \mathrm{Im}\left\{\int_\Gamma z^{-2} n_{x1}\rho_1 dz_y\right\} + \mathrm{Im}\left\{\int_\Gamma z^{-2} n_{x2}\rho_2 dz_y\right\} \\ \mathrm{Re}\left\{\int_\Gamma z^{-2} n_{x1}\rho_1 dz_y\right\} + \mathrm{Re}\left\{\int_\Gamma z^{-2} n_{x2}\rho_2 dz_y\right\} \end{pmatrix}
$$

$$
= \begin{pmatrix} \mathrm{Im}\left\{I_H\left[n_{x1}\rho_1\right]\right\} + \mathrm{Im}\left\{I_H\left[n_{x2}\rho_2\right]\right\} \\ \mathrm{Re}\left\{I_H\left[n_{x1}\rho_1\right]\right\} + \mathrm{Re}\left\{I_H\left[n_{x2}\rho_2\right]\right\} \end{pmatrix} \quad (\mathrm{A}.150)
$$

The last term of (A.127) We write the last term of (A.127) as

$$
\left(\boldsymbol{\nabla}_{\boldsymbol{x}}\left[r^{-2}\left(\boldsymbol{r}\cdot\boldsymbol{n_y}\right)\right]\cdot\boldsymbol{\rho}\right)\boldsymbol{n_x} = \left[\boldsymbol{n_x}\otimes\boldsymbol{\nabla}_{\boldsymbol{x}}\left[r^{-2}\left(\boldsymbol{r}\cdot\boldsymbol{n_y}\right)\right]\right]\boldsymbol{\rho}
$$

$$
= \left[\boldsymbol{n_x}\otimes\begin{pmatrix}-\mathrm{Re}\left\{\nu_y z^{-2}\right\}\\ \mathrm{Im}\left\{\nu_y z^{-2}\right\}\end{pmatrix}\right]\boldsymbol{\rho}
$$

$$
= \begin{bmatrix}-n_{x1}\mathrm{Re}\left\{\nu_y z^{-2}\right\} & n_{x1}\mathrm{Im}\left\{\nu_y z^{-2}\right\}\\ -n_{x2}\mathrm{Re}\left\{\nu_y z^{-2}\right\} & n_{x2}\mathrm{Im}\left\{\nu_y z^{-2}\right\}\end{bmatrix}\begin{pmatrix}\rho_1\\ \rho_2\end{pmatrix}
$$

$$
= \begin{pmatrix}-n_{x1}\mathrm{Re}\left\{\nu_y z^{-2}\right\}\rho_1 + n_{x1}\mathrm{Im}\left\{\nu_y z^{-2}\right\}\rho_2\\ -n_{x2}\mathrm{Re}\left\{\nu_y z^{-2}\right\}\rho_1 + n_{x2}\mathrm{Im}\left\{\nu_y z^{-2}\right\}\rho_2\end{pmatrix} \qquad (A.151)
$$

The integral on the boundary is

$$
\int_\Gamma\left[\boldsymbol{n_x}\otimes\begin{pmatrix}-\mathrm{Re}\left\{\nu_y z^{-2}\right\}\\ \mathrm{Im}\left\{\nu_y z^{-2}\right\}\end{pmatrix}\right]\boldsymbol{\rho}\,dS_y
$$

$$
= \begin{pmatrix}-\int_\Gamma n_{x1}\rho_1\mathrm{Re}\left\{\nu_y z^{-2}\right\}dS_y + \int_\Gamma n_{x1}\rho_2\mathrm{Im}\left\{\nu_y z^{-2}\right\}dS_y\\ -\int_\Gamma n_{x2}\rho_1\mathrm{Re}\left\{\nu_y z^{-2}\right\}dS_y + \int_\Gamma n_{x2}\rho_2\mathrm{Im}\left\{\nu_y z^{-2}\right\}dS_y\end{pmatrix}
$$

$$
= \begin{pmatrix}-\mathrm{Re}\left\{\int_\Gamma n_{x1}\rho_1\nu_y z^{-2}dS_y\right\} + \mathrm{Im}\left\{\int_\Gamma n_{x1}\rho_2\nu_y z^{-2}dS_y\right\}\\ -\mathrm{Re}\left\{\int_\Gamma n_{x2}\rho_1\nu_y z^{-2}dS_y\right\} + \mathrm{Im}\left\{\int_\Gamma n_{x2}\rho_2\nu_y z^{-2}dS_y\right\}\end{pmatrix}
$$

$$
= \begin{pmatrix}\mathrm{Re}\left\{i\int_\Gamma n_{x1}\rho_1 z^{-2}dz_y\right\} - \mathrm{Im}\left\{i\int_\Gamma n_{x1}\rho_2 z^{-2}dz_y\right\}\\ \mathrm{Re}\left\{i\int_\Gamma n_{x2}\rho_1 z^{-2}dz_y\right\} - \mathrm{Im}\left\{i\int_\Gamma n_{x2}\rho_2 z^{-2}dz_y\right\}\end{pmatrix}
$$

$$
= -\begin{pmatrix}\mathrm{Im}\left\{\int_\Gamma n_{x1}\rho_1 z^{-2}dz_y\right\} + \mathrm{Re}\left\{\int_\Gamma n_{x1}\rho_2 z^{-2}dz_y\right\}\\ \mathrm{Im}\left\{\int_\Gamma n_{x2}\rho_1 z^{-2}dz_y\right\} + \mathrm{Re}\left\{\int_\Gamma n_{x2}\rho_2 z^{-2}dz_y\right\}\end{pmatrix}
$$

$$
= \begin{pmatrix}-\mathrm{Im}\left\{I_H\left[n_{x1}\rho_1\right]\right\} - \mathrm{Re}\left\{I_H\left[n_{x1}\rho_2\right]\right\}\\ -\mathrm{Im}\left\{I_H\left[n_{x2}\rho_1\right]\right\} - \mathrm{Re}\left\{I_H\left[n_{x2}\rho_2\right]\right\}\end{pmatrix} \qquad (A.152)
$$

The summary of another form of $\boldsymbol{D}'$

$$\int_\Gamma \left[\boldsymbol{\nabla_x} \left[\boldsymbol{K^D \rho} \right] - \left(\boldsymbol{\nabla_x} \left[\boldsymbol{K^D \rho} \right] \right)^T - \left(\boldsymbol{\Pi^D} \cdot \boldsymbol{\rho} \right) \right] \boldsymbol{n_x} dS_y$$

$$= \frac{1}{2} \int_\Gamma \left\{ \left[\boldsymbol{\nabla_x} \left[r^{-2} \left(\boldsymbol{r} \cdot \boldsymbol{\rho} \right) \right] \otimes \boldsymbol{n_y} \right] + \left[\boldsymbol{n_y} \otimes \boldsymbol{\nabla_x} \left[r^{-2} \left(\boldsymbol{r} \cdot \boldsymbol{\rho} \right) \right] \right] \boldsymbol{n_x} \right\} dS_y$$

$$- \frac{1}{2} \int_\Gamma \left[\boldsymbol{\nabla_x \nabla_x} \left[r^{-2} \left(\boldsymbol{r} \cdot \boldsymbol{n_y} \right) \right] + \left(\boldsymbol{\nabla_x \nabla_x} \left[r^{-2} \left(\boldsymbol{r} \cdot \boldsymbol{n_y} \right) \right] \right)^T \right] \left(\boldsymbol{r} \cdot \boldsymbol{\rho} \right) \boldsymbol{n_x} dS_y$$

$$- \frac{1}{2} \int_\Gamma \left[\left[\boldsymbol{\rho} \otimes \boldsymbol{\nabla_x} \left[r^{-2} \left(\boldsymbol{r} \cdot \boldsymbol{n_y} \right) \right] \right] + \left[\boldsymbol{\nabla_x} \left[r^{-2} \left(\boldsymbol{r} \cdot \boldsymbol{n_y} \right) \right] \otimes \boldsymbol{\rho} \right] \right] \boldsymbol{n_x} dS_y$$

$$+ \int_\Gamma \left(\boldsymbol{\nabla_x} \left[\boldsymbol{r^{-2}} \left(\boldsymbol{r} \cdot \boldsymbol{n_y} \right) \right] \cdot \boldsymbol{\rho} \right) \boldsymbol{n_x} dS_y$$

$$= \frac{1}{2} \begin{pmatrix} -\mathrm{Im}\left\{ I_H \left[\mathrm{Re}\left\{ \nu_x \overline{\nu_y} \right\} \overline{\nu_y} \rho_1 \right] \right\} - \mathrm{Re}\left\{ I_H \left[\mathrm{Re}\left\{ \nu_x \overline{\nu_y} \right\} \overline{\nu_y} \rho_2 \right] \right\} \\ -\mathrm{Re}\left\{ I_H \left[\mathrm{Re}\left\{ \nu_x \overline{\nu_y} \right\} \overline{\nu_y} \rho_1 \right] \right\} + \mathrm{Im}\left\{ I_H \left[\mathrm{Re}\left\{ \nu_x \overline{\nu_y} \right\} \overline{\nu_y} \rho_2 \right] \right\} \end{pmatrix}$$

$$+ \frac{1}{2} \begin{pmatrix} -\mathrm{Im}\left\{ I_H \left[n_{y1} \nu_x \overline{\nu_y} \rho_1 \right] \right\} - \mathrm{Re}\left\{ I_H \left[n_{y1} \nu_x \overline{\nu_y} \rho_2 \right] \right\} \\ -\mathrm{Im}\left\{ I_H \left[n_{y2} \nu_x \overline{\nu_y} \rho_1 \right] \right\} - \mathrm{Re}\left\{ I_H \left[n_{y2} \nu_x \overline{\nu_y} \rho_2 \right] \right\} \end{pmatrix}$$

$$+ 2 \begin{pmatrix} \mathrm{Im}\left\{ I_S \left[n_{x1} r_1 \rho_1 \right] \right\} + \mathrm{Im}\left\{ I_S \left[n_{x1} r_2 \rho_2 \right] \right\} \\ \mathrm{Re}\left\{ I_S \left[n_{x1} r_1 \rho_1 \right] \right\} + \mathrm{Re}\left\{ I_S \left[n_{x1} r_2 \rho_2 \right] \right\} \end{pmatrix} + 2 \begin{pmatrix} \mathrm{Re}\left\{ I_S \left[n_{x2} r_1 \rho_1 \right] \right\} + \mathrm{Re}\left\{ I_S \left[n_{x2} r_2 \rho_2 \right] \right\} \\ -\mathrm{Im}\left\{ I_S \left[n_{x2} r_1 \rho_1 \right] \right\} - \mathrm{Im}\left\{ I_S \left[n_{x2} r_2 \rho_2 \right] \right\} \end{pmatrix}$$

$$+ \frac{1}{2} \begin{pmatrix} \cancel{\mathrm{Im}\left\{ I_H \left[n_{x1} \rho_1 \right] \right\}}^0 + \mathrm{Re}\left\{ I_H \left[n_{x2} \rho_1 \right] \right\} \\ \mathrm{Im}\left\{ I_H \left[n_{x1} \rho_2 \right] \right\} + \cancel{\mathrm{Re}\left\{ I_H \left[n_{x2} \rho_2 \right] \right\}}_0 \end{pmatrix} + \frac{1}{2} \begin{pmatrix} \cancel{\mathrm{Im}\left\{ I_H \left[n_{x1} \rho_1 \right] \right\}}^0 + \mathrm{Im}\left\{ I_H \left[n_{x2} \rho_2 \right] \right\} \\ \mathrm{Re}\left\{ I_H \left[n_{x1} \rho_1 \right] \right\} + \cancel{\mathrm{Re}\left\{ I_H \left[n_{x2} \rho_2 \right] \right\}}_0 \end{pmatrix}$$

$$+ \begin{pmatrix} -\cancel{\mathrm{Im}\left\{ I_H \left[n_{x1} \rho_1 \right] \right\}}^0 - \mathrm{Re}\left\{ I_H \left[n_{x1} \rho_2 \right] \right\} \\ -\mathrm{Im}\left\{ I_H \left[n_{x2} \rho_1 \right] \right\} - \cancel{\mathrm{Re}\left\{ I_H \left[n_{x2} \rho_2 \right] \right\}}_0 \end{pmatrix}$$

$$= \underbrace{\frac{1}{2} \begin{pmatrix} -\mathrm{Im}\left\{ I_H \left[\mathrm{Re}\left\{ \nu_x \overline{\nu_y} \right\} \overline{\nu_y} \rho_1 \right] \right\} - \mathrm{Re}\left\{ I_H \left[\mathrm{Re}\left\{ \nu_x \overline{\nu_y} \right\} \overline{\nu_y} \rho_2 \right] \right\} \\ -\mathrm{Re}\left\{ I_H \left[\mathrm{Re}\left\{ \nu_x \overline{\nu_y} \right\} \overline{\nu_y} \rho_1 \right] \right\} + \mathrm{Im}\left\{ I_H \left[\mathrm{Re}\left\{ \nu_x \overline{\nu_y} \right\} \overline{\nu_y} \rho_2 \right] \right\} \end{pmatrix}}_{(H1)}$$

$$+ \underbrace{\frac{1}{2} \begin{pmatrix} -\mathrm{Im}\left\{ I_H \left[n_{y1} \nu_x \overline{\nu_y} \rho_1 \right] \right\} - \mathrm{Re}\left\{ I_H \left[n_{y1} \nu_x \overline{\nu_y} \rho_2 \right] \right\} \\ -\mathrm{Im}\left\{ I_H \left[n_{y2} \nu_x \overline{\nu_y} \rho_1 \right] \right\} - \mathrm{Re}\left\{ I_H \left[n_{y2} \nu_x \overline{\nu_y} \rho_2 \right] \right\} \end{pmatrix}}_{(H2)}$$

$$+ \underbrace{\frac{1}{2} \begin{pmatrix} \mathrm{Re}\left\{ I_H \left[n_{x2} \rho_1 \right] \right\} + \mathrm{Im}\left\{ I_H \left[n_{x2} \rho_2 \right] \right\} \\ \mathrm{Re}\left\{ I_H \left[n_{x1} \rho_1 \right] \right\} + \mathrm{Im}\left\{ I_H \left[n_{x1} \rho_2 \right] \right\} \end{pmatrix}}_{(H3)} + \underbrace{\begin{pmatrix} -\mathrm{Re}\left\{ I_H \left[n_{x1} \rho_{\color{red}2} \right] \right\} \\ -\mathrm{Im}\left\{ I_H \left[n_{x2} \rho_{\color{red}1} \right] \right\} \end{pmatrix}}_{(H4)}$$

$$+ \underbrace{2 \begin{pmatrix} \mathrm{Im}\left\{ I_S \left[n_{x1} r_1 \rho_1 \right] \right\} + \mathrm{Im}\left\{ I_S \left[n_{x1} r_2 \rho_2 \right] \right\} \\ \mathrm{Re}\left\{ I_S \left[n_{x1} r_1 \rho_1 \right] \right\} + \mathrm{Re}\left\{ I_S \left[n_{x1} r_2 \rho_2 \right] \right\} \end{pmatrix}}_{(S1)} + \underbrace{2 \begin{pmatrix} \mathrm{Re}\left\{ I_S \left[n_{x2} r_1 \rho_1 \right] \right\} + \mathrm{Re}\left\{ I_S \left[n_{x2} r_2 \rho_2 \right] \right\} \\ -\mathrm{Im}\left\{ I_S \left[n_{x2} r_1 \rho_1 \right] \right\} - \mathrm{Im}\left\{ I_S \left[n_{x2} r_2 \rho_2 \right] \right\} \end{pmatrix}}_{(S2)}$$

$$(A.153)$$

We rearrange each term as matrix-vector products of corresponding kernels and densities.

$$
\begin{aligned}
(H1) &= - \begin{bmatrix} \operatorname{Im}\{I_H\,[\,\cdot\,]\} & \operatorname{Re}\{I_H\,[\,\cdot\,]\} \\ \operatorname{Re}\{I_H\,[\,\cdot\,]\} & -\operatorname{Im}\{I_H\,[\,\cdot\,]\} \end{bmatrix} \begin{bmatrix} \operatorname{Re}\{\nu_x\overline{\nu_y}\}\,\overline{\nu_y}\rho_1 \\ \operatorname{Re}\{\nu_x\overline{\nu_y}\}\,\overline{\nu_y}\rho_2 \end{bmatrix} \\
&= \begin{bmatrix} \operatorname{Im}\{I_H\,[\,\cdot\,]\} & \operatorname{Re}\{I_H\,[\,\cdot\,]\} \\ \operatorname{Re}\{I_H\,[\,\cdot\,]\} & -\operatorname{Im}\{I_H\,[\,\cdot\,]\} \end{bmatrix} \operatorname{Re}\{\nu_x\overline{\nu_y}\}\,\overline{\nu_y}\boldsymbol{\rho}
\end{aligned}
\tag{A.154}
$$

$$
\begin{aligned}
(H2) &= - \begin{bmatrix} \operatorname{Im}\{I_H\,[n_{y1}\,\cdot\,]\} & \operatorname{Re}\{I_H\,[n_{y1}\,\cdot\,]\} \\ \operatorname{Im}\{I_H\,[n_{y2}\,\cdot\,]\} & \operatorname{Re}\{I_H\,[n_{y2}\,\cdot\,]\} \end{bmatrix} \begin{bmatrix} \nu_x\overline{\nu_y}\rho_1 \\ \nu_x\overline{\nu_y}\rho_2 \end{bmatrix} \\
&= \left[\begin{bmatrix} n_{y1} \\ n_{y2} \end{bmatrix} \otimes \begin{bmatrix} \operatorname{Im}\{I_H\,[\,\cdot\,]\} \\ \operatorname{Re}\{I_H\,[\,\cdot\,]\} \end{bmatrix} \right] \begin{bmatrix} \nu_x\overline{\nu_y}\rho_1 \\ \nu_x\overline{\nu_y}\rho_2 \end{bmatrix} \\
&= \left[\begin{bmatrix} n_{y1} \\ n_{y2} \end{bmatrix} \otimes \begin{bmatrix} \operatorname{Im}\{I_H\,[\,\cdot\,]\} \\ \operatorname{Re}\{I_H\,[\,\cdot\,]\} \end{bmatrix} \right] \nu_x\overline{\nu_y}\boldsymbol{\rho}
\end{aligned}
\tag{A.155}
$$

$$
\begin{aligned}
(H3) &= \begin{bmatrix} 0 & 1 \\ 1 & 0 \end{bmatrix} \begin{bmatrix} \operatorname{Re}\{I_H\,[n_{x1}\cdot]\} & \operatorname{Im}\{I_H\,[n_{x1}\cdot]\} \\ \operatorname{Re}\{I_H\,[n_{x2}\cdot]\} & \operatorname{Im}\{I_H\,[n_{x2}\cdot]\} \end{bmatrix} \begin{bmatrix} \rho_1 \\ \rho_2 \end{bmatrix} \\
&= \begin{bmatrix} 0 & 1 \\ 1 & 0 \end{bmatrix} \begin{bmatrix} \operatorname{Im}\{I_H\,[n_{x1}\cdot]\} & \operatorname{Re}\{I_H\,[n_{x1}\cdot]\} \\ \operatorname{Im}\{I_H\,[n_{x2}\cdot]\} & \operatorname{Re}\{I_H\,[n_{x2}\cdot]\} \end{bmatrix} \begin{bmatrix} 0 & 1 \\ 1 & 0 \end{bmatrix} \begin{bmatrix} \rho_1 \\ \rho_2 \end{bmatrix} \\
&= \begin{bmatrix} 0 & 1 \\ 1 & 0 \end{bmatrix} \left[\boldsymbol{n}_x \otimes \begin{bmatrix} \operatorname{Im}\{I_H\,[\,\cdot\,]\} \\ \operatorname{Re}\{I_H\,[\,\cdot\,]\} \end{bmatrix} \right] \begin{bmatrix} 0 & 1 \\ 1 & 0 \end{bmatrix} \boldsymbol{\rho}
\end{aligned}
\tag{A.156}
$$

$$(H4) = \begin{bmatrix} 0 & -\mathrm{Re}\left\{I_H\left[n_{x1}\cdot\right]\right\} \\ -\mathrm{Im}\left\{I_H\left[n_{x2}\cdot\right]\right\} & 0 \end{bmatrix} \begin{bmatrix} \rho_1 \\ \rho_2 \end{bmatrix}$$

$$= -\left[\begin{bmatrix} n_{x1} \\ n_{x2} \end{bmatrix} \otimes \begin{bmatrix} \mathrm{Im}\left\{I_H\left[\cdot\right]\right\} \\ \mathrm{Re}\left\{I_H\left[\cdot\right]\right\} \end{bmatrix}\right] \begin{bmatrix} \rho_1 \\ \rho_2 \end{bmatrix} + \begin{bmatrix} \mathrm{Im}\left\{I_H\left[n_{x1}\cdot\right]\right\} & 0 \\ 0 & \mathrm{Re}\left\{I_H\left[n_{x2}\cdot\right]\right\} \end{bmatrix} \begin{bmatrix} \rho_1 \\ \rho_2 \end{bmatrix}$$

$$= -\left[\boldsymbol{n}_x \otimes \begin{bmatrix} \mathrm{Im}\left\{I_H\left[\cdot\right]\right\} \\ \mathrm{Re}\left\{I_H\left[\cdot\right]\right\} \end{bmatrix}\right]\boldsymbol{\rho} + \begin{bmatrix} n_{x1} & 0 \\ 0 & n_{x2} \end{bmatrix} \begin{bmatrix} \mathrm{Im}\left\{I_H\left[\cdot\right]\right\} \\ \mathrm{Re}\left\{I_H\left[\cdot\right]\right\} \end{bmatrix}\boldsymbol{\rho}$$

$$= -\left[\boldsymbol{n}_x \otimes \begin{bmatrix} \mathrm{Im}\left\{I_H\left[\cdot\right]\right\} \\ \mathrm{Re}\left\{I_H\left[\cdot\right]\right\} \end{bmatrix}\right]\boldsymbol{\rho} + \left(\boldsymbol{n}_x \cdot \begin{bmatrix} \mathrm{Im}\left\{I_H\left[\cdot\right]\right\} \\ \mathrm{Re}\left\{I_H\left[\cdot\right]\right\} \end{bmatrix}\right)\boldsymbol{I}\boldsymbol{\rho} \qquad (A.157)$$

$$(S1) = n_{x1}\left[\begin{bmatrix} \mathrm{Im}\left\{I_S\left[\cdot\right]\right\} \\ \mathrm{Re}\left\{I_S\left[\cdot\right]\right\} \end{bmatrix} \otimes \begin{bmatrix} r_1 \\ r_2 \end{bmatrix}\right]\begin{bmatrix} \rho_1 \\ \rho_2 \end{bmatrix} = n_{x1}\left[\begin{bmatrix} \mathrm{Im}\left\{I_S\left[\cdot\right]\right\} \\ \mathrm{Re}\left\{I_S\left[\cdot\right]\right\} \end{bmatrix} \otimes \boldsymbol{r}\right]\boldsymbol{\rho} \quad (A.158)$$

$$(S2) = n_{x2}\left[\begin{bmatrix} \mathrm{Re}\left\{I_S\left[\cdot\right]\right\} \\ -\mathrm{Im}\left\{I_S\left[\cdot\right]\right\} \end{bmatrix} \otimes \begin{bmatrix} r_1 \\ r_2 \end{bmatrix}\right]\begin{bmatrix} \rho_1 \\ \rho_2 \end{bmatrix} = n_{x2}\left[\begin{bmatrix} \mathrm{Re}\left\{I_S\left[\cdot\right]\right\} \\ \mathrm{Im}\left\{I_S\left[\cdot\right]\right\} \end{bmatrix} \otimes \boldsymbol{r}\right]\boldsymbol{\rho} \quad (A.159)$$

$$\therefore (A.153) = \frac{1}{2}(H1) + \frac{1}{2}(H2) + \frac{1}{2}(H3) + (H4) + 2(S1) + 2(S2)$$

$$= -\frac{1}{2}\begin{bmatrix} \operatorname{Im}\{I_H[\cdot]\} & \operatorname{Re}\{I_H[\cdot]\} \\ \operatorname{Re}\{I_H[\cdot]\} & -\operatorname{Im}\{I_H[\cdot]\} \end{bmatrix} \operatorname{Re}\{\nu_x \overline{\nu_y}\}\,\overline{\nu_y}\boldsymbol{\rho}$$

$$+ \frac{1}{2}\left[\begin{bmatrix} n_{y1} \\ n_{y2} \end{bmatrix} \otimes \begin{bmatrix} \operatorname{Im}\{I_H[\cdot]\} \\ \operatorname{Re}\{I_H[\cdot]\} \end{bmatrix}\right]\nu_x \overline{\nu_y}\boldsymbol{\rho}$$

$$+ \frac{1}{2}\begin{bmatrix} 0 & 1 \\ 1 & 0 \end{bmatrix}\left[\boldsymbol{n}_x \otimes \begin{bmatrix} \operatorname{Im}\{I_H[\cdot]\} \\ \operatorname{Re}\{I_H[\cdot]\} \end{bmatrix}\right]\begin{bmatrix} 0 & 1 \\ 1 & 0 \end{bmatrix}\boldsymbol{\rho}$$

$$- \left[\boldsymbol{n}_x \otimes \begin{bmatrix} \operatorname{Im}\{I_H[\cdot]\} \\ \operatorname{Re}\{I_H[\cdot]\} \end{bmatrix}\right]\boldsymbol{\rho} + \left(\boldsymbol{n}_x \cdot \begin{bmatrix} \operatorname{Im}\{I_H[\cdot]\} \\ \operatorname{Re}\{I_H[\cdot]\} \end{bmatrix}\right)\boldsymbol{I}\boldsymbol{\rho}$$

$$+ 2n_{x1}\left[\begin{bmatrix} \operatorname{Im}\{I_S[\cdot]\} \\ \operatorname{Re}\{I_S[\cdot]\} \end{bmatrix} \otimes \boldsymbol{r}\right]\boldsymbol{\rho} + 2n_{x2}\left[\begin{bmatrix} \operatorname{Re}\{I_S[\cdot]\} \\ \operatorname{Im}\{I_S[\cdot]\} \end{bmatrix} \otimes \boldsymbol{r}\right]\boldsymbol{\rho}. \quad (A.160)$$

A.2.8 Pressure P

$$P(\boldsymbol{x}, \boldsymbol{y}) = \frac{1}{2\pi} \int_\Gamma \frac{(\boldsymbol{r} \cdot \boldsymbol{\rho})}{r^2} ds_y \tag{A.161}$$

$$= \frac{1}{2\pi} \int_\Gamma -\text{Re}\left\{\frac{\sigma}{z}\right\} |dz_y| \tag{A.162}$$

$$= -\frac{1}{2\pi} \text{Re}\left\{\int_\Gamma \frac{\sigma}{z} |dz_y|\right\} \tag{A.163}$$

$$= -\frac{1}{2\pi} \text{Re}\left\{\int_\Gamma \frac{\rho_1 + i\rho_2}{z} \left(-\frac{i}{\nu_y}\right) dz_y\right\} \tag{A.164}$$

$$= -\frac{1}{2\pi} \text{Re}\left\{i \int_\Gamma \frac{\rho_1}{\nu_y} \frac{1}{z} dz_y - \int_\Gamma \frac{\rho_2}{\nu_y} \frac{1}{z} dz_y\right\} \tag{A.165}$$

$$= \frac{1}{2\pi} \left(-\text{Im}\left\{I_C\left[\frac{\rho_1}{\nu_y}\right]\right\} - \text{Re}\left\{I_C\left[\frac{\rho_2}{\nu_y}\right]\right\}\right) \tag{A.166}$$

$$= -\frac{1}{2\pi} \begin{pmatrix} \text{Im}\left\{I_C\left[\frac{\cdot}{\nu_y}\right]\right\} \\ \text{Re}\left\{I_C\left[\frac{\cdot}{\nu_y}\right]\right\} \end{pmatrix} \cdot \begin{pmatrix} \rho_1 \\ \rho_2 \end{pmatrix}. \tag{A.167}$$

A.2.9 P'

Here we compute

$$P' = \int_\Gamma \frac{\mu}{\pi} \left[-\frac{\boldsymbol{n_y}}{r^2} + \frac{2}{r^4} (\boldsymbol{r} \cdot \boldsymbol{n_y}) \boldsymbol{r}\right] \cdot \boldsymbol{\rho} ds_y. \tag{A.168}$$

Recalling an identity

$$\nabla_x \left[\frac{(\boldsymbol{r} \cdot \boldsymbol{n_y})}{r^2}\right] = \frac{\boldsymbol{n_y}}{r^2} - \frac{2}{r^4} (\boldsymbol{r} \cdot \boldsymbol{n_y}) \boldsymbol{r} \tag{A.169}$$

and

$$\frac{(\boldsymbol{r} \cdot \boldsymbol{n_y})}{r^2} = -\text{Re}\left\{\frac{\nu_y}{z}\right\}, \tag{A.170}$$

the integrand of P' is

$$-\frac{n_{y,j}}{r^2} + \frac{2}{r^4}\left(\boldsymbol{r} \cdot \boldsymbol{n_y}\right)r_j = -\nabla_x\left[\frac{\left(\boldsymbol{r} \cdot \boldsymbol{n_y}\right)}{r^2}\right]$$

$$= \nabla_x \text{Re}\left\{\frac{\nu_y}{z}\right\}$$

$$= \begin{pmatrix} \text{Re}\left\{\frac{\nu_y}{z^2}\right\} \\ -\text{Im}\left\{\frac{\nu_y}{z^2}\right\} \end{pmatrix}. \tag{A.171}$$

$$\therefore P' = \frac{\mu}{\pi}\int_\Gamma \begin{pmatrix} \text{Re}\left\{\frac{\nu_y}{z^2}\right\} \\ -\text{Im}\left\{\frac{\nu_y}{z^2}\right\} \end{pmatrix} \cdot \boldsymbol{\rho}|dz_y|$$

$$= \frac{\mu}{\pi}\int_\Gamma\left[\text{Re}\left\{\frac{\nu_y\rho_1}{z^2}\right\} - \text{Im}\left\{\frac{\nu_y\rho_2}{z^2}\right\}\right]|dz_y|$$

$$= \frac{\mu}{\pi}\left[\text{Re}\left\{\int_\Gamma\frac{\nu_y\rho_1}{z^2}|dz_y|\right\} - \text{Im}\left\{\int_\Gamma\frac{\nu_y\rho_2}{z^2}|dz_y|\right\}\right]$$

$$= \frac{\mu}{\pi}\left[\text{Re}\left\{\int_\Gamma\frac{\nu_y\rho_1}{z^2}\frac{dz_y}{i\nu_y}\right\} - \text{Im}\left\{\int_\Gamma\frac{\nu_y\rho_2}{z^2}\frac{dz_y}{i\nu_y}\right\}\right]$$

$$= \frac{\mu}{\pi}\left[\text{Re}\left\{-i\int_\Gamma\frac{\rho_1}{z^2}dz_y\right\} - \text{Im}\left\{-i\int_\Gamma\frac{\rho_2}{z^2}dz_y\right\}\right]$$

$$= \frac{\mu}{\pi}\left[\text{Im}\left\{\int_\Gamma\frac{\rho_1}{z^2}dz_y\right\} + \text{Re}\left\{\int_\Gamma\frac{\rho_2}{z^2}dz_y\right\}\right]$$

$$= \frac{\mu}{\pi}\begin{pmatrix} \text{Im}\left\{I_H\left[\,\cdot\,\right]\right\} \\ \text{Re}\left\{I_H\left[\,\cdot\,\right]\right\} \end{pmatrix} \cdot \begin{pmatrix} \rho_1 \\ \rho_2 \end{pmatrix}. \tag{A.172}$$

A.3   A Derivation of Equation (2.57)

The aim of this section is to obtain a linear system (2.57)

$$\left(\boldsymbol{I} + \boldsymbol{K} + \boldsymbol{K'}\right)\boldsymbol{\rho} = \boldsymbol{0} \tag{A.173}$$

with the identity to be able to the RCIP method for the composite boundary conditions in section 2.2.6.

Let $(\boldsymbol{x}_i)_{i=0}^N$ be the target discretization points on the boundary Γ. First, we consider the following $(2N \times 1)$ vectors equivalent to matrix-vector products involving

$(N \times N)$ diagonal matrices $\mathbf{\Lambda}_{nj}$ $(j \in \{1, 2\})$ and the density $(2N \times 1)$ vector $\boldsymbol{\rho}$. We denote $\boldsymbol{x}_i$ by (i) for the simplicity of the following equations.

$$
\begin{bmatrix}
(\boldsymbol{\rho}(1) \cdot \boldsymbol{n}(1))n_1(1) \\
\vdots \\
(\boldsymbol{\rho}(N) \cdot \boldsymbol{n}(N))n_1(N) \\
\hline
(\boldsymbol{\rho}(1) \cdot \boldsymbol{n}(1))n_2(1) \\
\vdots \\
(\boldsymbol{\rho}(N) \cdot \boldsymbol{n}(N))n_2(N)
\end{bmatrix}
=
\begin{bmatrix}
\mathbf{\Lambda}_{n1}^2 & \mathbf{\Lambda}_{n1}\mathbf{\Lambda}_{n2} \\
\hline
\mathbf{\Lambda}_{n1}\mathbf{\Lambda}_{n2} & \mathbf{\Lambda}_{n2}^2
\end{bmatrix}
\boldsymbol{\rho}
\tag{A.174}
$$

$$
\begin{bmatrix}
(\boldsymbol{\rho}(1) \cdot \boldsymbol{t}(1))n_1(1) \\
\vdots \\
(\boldsymbol{\rho}(N) \cdot \boldsymbol{t}(N))n_1(N) \\
\hline
(\boldsymbol{\rho}(1) \cdot \boldsymbol{t}(1))n_2(1) \\
\vdots \\
(\boldsymbol{\rho}(N) \cdot \boldsymbol{t}(N))n_2(N)
\end{bmatrix}
=
\begin{bmatrix}
\mathbf{\Lambda}_{t1}^2 & \mathbf{\Lambda}_{t1}\mathbf{\Lambda}_{t2} \\
\hline
\mathbf{\Lambda}_{t1}\mathbf{\Lambda}_{t2} & \mathbf{\Lambda}_{t2}^2
\end{bmatrix}
\boldsymbol{\rho}
\tag{A.175}
$$

We see that

$$
(A.174) + (A.175) = \boldsymbol{I}\boldsymbol{\rho}
\tag{A.176}
$$

by the orthogonality of $\boldsymbol{n}(\boldsymbol{x})$ and $\boldsymbol{t}(\boldsymbol{x})$.

Next, we focus on one target discretization point $\boldsymbol{x}_i$ $(1 \le i \le N)$ for the moment. Let

$$
\boldsymbol{M} =
\begin{bmatrix}
\boldsymbol{M}_{11} & \boldsymbol{M}_{12} \\
\hline
\boldsymbol{M}_{21} & \boldsymbol{M}_{22}
\end{bmatrix}
\tag{A.177}
$$

be the $(2N \times 2N)$ block matrix composed of four $(N \times N)$ matrices, and define

$$
\boldsymbol{M}_i =
\begin{bmatrix}
\boldsymbol{M}_{i,11} & \boldsymbol{M}_{i,12} \\
\hline
\boldsymbol{M}_{i,21} & \boldsymbol{M}_{i,22}
\end{bmatrix}
\tag{A.178}
$$

129

as the $2 \times 2N$ block matrix composed of the ith and $(N+i)$th rows of $\boldsymbol{M}$ for arbitrary $i \in \{1, \ldots, N\}$. We also denote the (2×1) vector obtained by taking the dot product of ith and $(N+i)$th rows of $\boldsymbol{M\rho}$ and $\boldsymbol{n}(i)$ by $(\boldsymbol{M\rho})_i$. Then,

$$[(\boldsymbol{M\rho})_i \cdot \boldsymbol{n}(\boldsymbol{x_i})]\,\boldsymbol{n}(i) \tag{A.179}$$

$$= \begin{bmatrix} (\boldsymbol{M}_{i,11}\boldsymbol{\rho}_1 + \boldsymbol{M}_{i,12}\boldsymbol{\rho}_2)n_1^2(i) + (\boldsymbol{M}_{i,21}\boldsymbol{\rho}_1 + \boldsymbol{M}_{i,22}\boldsymbol{\rho}_2)n_1(i)n_2(i) \\ (\boldsymbol{M}_{i,11}\boldsymbol{\rho}_1 + \boldsymbol{M}_{i,12}\boldsymbol{\rho}_2)n_2(i)n_1(i) + (\boldsymbol{M}_{i,21}\boldsymbol{\rho}_1 + \boldsymbol{M}_{i,22}\boldsymbol{\rho}_2)n_2^2(i) \end{bmatrix} \tag{A.180}$$

$$= \begin{bmatrix} (\boldsymbol{M}_{i,11}n_{i,1}^2 + \boldsymbol{M}_{i,21}n_{i,1}n_{i,2})\boldsymbol{\rho}_1 + (\boldsymbol{M}_{i,12}n_{i,1}^2 + \boldsymbol{M}_{i,22}n_{i,1}n_{i,2})\boldsymbol{\rho}_2 \\ (\boldsymbol{M}_{i,11}n_{i,1}n_{i,2} + \boldsymbol{M}_{i,21}n_{i,2}^2)\boldsymbol{\rho}_1 + (\boldsymbol{M}_{i,12}n_{i,1}n_{i,2} + \boldsymbol{M}_{i,22}n_{i,2}^2)\boldsymbol{\rho}_2 \end{bmatrix} \tag{A.181}$$

$$= \left[\begin{array}{c|c} n_{i,1}^2\boldsymbol{M}_{i,11} + n_{i,1}n_{i,2}\boldsymbol{M}_{i,21} & n_{i,1}^2\boldsymbol{M}_{i,12} + n_{i,1}n_{i,2}\boldsymbol{M}_{i,22} \\ \hline n_{i,1}n_{i,2}\boldsymbol{M}_{i,11} + n_{i,2}^2\boldsymbol{M}_{i,21} & n_{i,1}n_{i,2}\boldsymbol{M}_{i,12} + n_{i,2}^2\boldsymbol{M}_{i,22} \end{array} \right] \boldsymbol{\rho} \tag{A.182}$$

holds for each $\boldsymbol{x}_i \in \Gamma$. The alignment of the $2N$ equations $([(\boldsymbol{M\rho})_1 \cdot \boldsymbol{n}(1)]\,\boldsymbol{n}(1))_{i=1}^N$ leads to

$$\begin{bmatrix} [(\boldsymbol{M\rho})_1 \cdot \boldsymbol{n}(1)]\,n_1(1) \\ \vdots \\ [(\boldsymbol{M\rho})_N \cdot \boldsymbol{n}(N)]\,n_1(N) \\ \hline [(\boldsymbol{M\rho})_1 \cdot \boldsymbol{n}(1)]\,n_2(1) \\ \vdots \\ [(\boldsymbol{M\rho})_N \cdot \boldsymbol{n}(N)]\,n_2(N) \end{bmatrix} = \left[\begin{array}{c|c} \boldsymbol{\Lambda}_{n1}^2\boldsymbol{M}_{11} + \boldsymbol{\Lambda}_{n1}\boldsymbol{\Lambda}_{n2}\boldsymbol{M}_{21} & \boldsymbol{\Lambda}_{n1}^2\boldsymbol{M}_{12} + \boldsymbol{\Lambda}_{n1}\boldsymbol{\Lambda}_{n2}\boldsymbol{M}_{22} \\ \hline \boldsymbol{\Lambda}_{n1}\boldsymbol{\Lambda}_{n2}\boldsymbol{M}_{11} + \boldsymbol{\Lambda}_{n2}^2\boldsymbol{M}_{21} & \boldsymbol{\Lambda}_{n1}\boldsymbol{\Lambda}_{n2}\boldsymbol{M}_{12} + \boldsymbol{\Lambda}_{n2}^2\boldsymbol{M}_{22} \end{array} \right] \boldsymbol{\rho}$$

$$\tag{A.183}$$

Similarly,

$$
\begin{bmatrix}
[(\boldsymbol{M'\rho})_1 \cdot \boldsymbol{t}(1)]\, t_1(1) \\
\vdots \\
[(\boldsymbol{M'\rho})_N \cdot \boldsymbol{t}(N)]\, t_1(N) \\
[(\boldsymbol{M'\rho})_1 \cdot \boldsymbol{t}(1)]\, t_2(1) \\
\vdots \\
[(\boldsymbol{M'\rho})_N \cdot \boldsymbol{t}(N)]\, t_2(N)
\end{bmatrix}
=
\left[
\begin{array}{c|c}
\boldsymbol{\Lambda}_{t1}^2 \boldsymbol{M'}_{11} + \boldsymbol{\Lambda}_{t1}\boldsymbol{\Lambda}_{t2}\boldsymbol{M'}_{21} & \boldsymbol{\Lambda}_{t1}^2 \boldsymbol{M'}_{12} + \boldsymbol{\Lambda}_{t1}\boldsymbol{\Lambda}_{t2}\boldsymbol{M'}_{22} \\
\hline
\boldsymbol{\Lambda}_{t1}\boldsymbol{\Lambda}_{t2}\boldsymbol{M'}_{11} + \boldsymbol{\Lambda}_{t2}^2 \boldsymbol{M'}_{21} & \boldsymbol{\Lambda}_{t1}\boldsymbol{\Lambda}_{t2}\boldsymbol{M'}_{12} + \boldsymbol{\Lambda}_{t2}^2 \boldsymbol{M'}_{22}
\end{array}
\right] \boldsymbol{\rho}.
$$

(A.184)

Noting $(A.174) + (A.175) = \boldsymbol{I\rho}$ as we have seen in (A.176),

$$(A.174) + (A.175) + (A.183) + (A.184) \tag{A.185}$$

$$
= \boldsymbol{I\rho} +
\left[
\begin{array}{c|c}
\boldsymbol{\Lambda}_{n1}^2 \boldsymbol{M}_{11} + \boldsymbol{\Lambda}_{n1}\boldsymbol{\Lambda}_{n2}\boldsymbol{M}_{21} & \boldsymbol{\Lambda}_{n1}^2 \boldsymbol{M}_{12} + \boldsymbol{\Lambda}_{n1}\boldsymbol{\Lambda}_{n2}\boldsymbol{M}_{22} \\
\hline
\boldsymbol{\Lambda}_{n1}\boldsymbol{\Lambda}_{n2}\boldsymbol{M}_{11} + \boldsymbol{\Lambda}_{n2}^2 \boldsymbol{M}_{21} & \boldsymbol{\Lambda}_{n1}\boldsymbol{\Lambda}_{n2}\boldsymbol{M}_{12} + \boldsymbol{\Lambda}_{n2}^2 \boldsymbol{M}_{22}
\end{array}
\right] \boldsymbol{\rho}
\tag{A.186}
$$

$$
+
\left[
\begin{array}{c|c}
\boldsymbol{\Lambda}_{t1}^2 \boldsymbol{M'}_{11} + \boldsymbol{\Lambda}_{t1}\boldsymbol{\Lambda}_{t2}\boldsymbol{M'}_{21} & \boldsymbol{\Lambda}_{t1}^2 \boldsymbol{M'}_{12} + \boldsymbol{\Lambda}_{t1}\boldsymbol{\Lambda}_{t2}\boldsymbol{M'}_{22} \\
\hline
\boldsymbol{\Lambda}_{t1}\boldsymbol{\Lambda}_{t2}\boldsymbol{M'}_{11} + \boldsymbol{\Lambda}_{t2}^2 \boldsymbol{M'}_{21} & \boldsymbol{\Lambda}_{t1}\boldsymbol{\Lambda}_{t2}\boldsymbol{M'}_{12} + \boldsymbol{\Lambda}_{t2}^2 \boldsymbol{M'}_{22}
\end{array}
\right] \boldsymbol{\rho}
\tag{A.187}
$$

Now we set $\boldsymbol{M}$ and $\boldsymbol{M'}$ to

$$\boldsymbol{M} := -\left(\boldsymbol{D}_{\Gamma_{\mathrm{D}}} + \boldsymbol{D}_{\Gamma_{\mathrm{C}}} + \boldsymbol{S}_{\Gamma_{\mathrm{C}}}\right) \tag{A.188}$$

$$\boldsymbol{M'} := \boldsymbol{D'}_{\Gamma_{\mathrm{D}}} + \boldsymbol{D'}_{\Gamma_{\mathrm{C}}} + \boldsymbol{S'}_{\Gamma_{\mathrm{C}}} \tag{A.189}$$

The ith element and $(N+i)$th element of vector $(A.174)+(A.183)$ are $[(\boldsymbol{I\rho})_i + (\boldsymbol{M\rho})_i] \cdot \boldsymbol{n}(i)n_1(i)$ and $[(\boldsymbol{I\rho})_i + (\boldsymbol{M\rho})_i] \cdot \boldsymbol{n}(i)n_2(i)$. Both of them are zero because of the boundary condition of zero normal velocity (2.51). The same argument applies to $(A.175) + (A.184)$. Therefore, $(A.174) + (A.175) + (A.183) + (A.184)$ are a zero vector. In conclusion, we see the construction of

$$\left(\boldsymbol{I} + \boldsymbol{K} + \boldsymbol{K'}\right)\boldsymbol{\rho} = \boldsymbol{0} \tag{A.190}$$

where $\boldsymbol{K}$ and $\boldsymbol{K}'$ are the second and third matrices in (A.187) for the composite boundary conditions.

APPENDIX B

SUPPLEMENTS TO INTEGRATED PHOTONICS

B.1   Proof of Theorem 3.3.1

Let the number of ports be P. Let m_p be the number of modes on the interface of pth port $(1 \leq p \leq P)$. Let $h > 0$ be the width of the cross-section. Along a cross-section $\{(x_p, y)| - h/2 < y < h/2\}$ near pth port,

$$u(x, y) \simeq \sum_{j=1}^{m_p} \sigma_{p,j} \left(c_{p,j}^{inc} \phi_{p,j}^{inc} + c_{p,j}^{sc} \phi_{p,j}^{sc} \right) \tag{B.1}$$

where

$$\phi_{p,j}^{inc}(x_p, y) = e^{i\beta_{p,j} x_p} g_{p,j}(y), \tag{B.2}$$

$$\phi_{p,j}^{sc}(x_p, y) = e^{i\beta_{p,j} x_p} g_{p,j}(y), \tag{B.3}$$

$$g_{p,j}(y) := \sqrt{\frac{2}{h}} \int_{-h/2}^{h/2} \sin\left(j\frac{\pi}{h}(y + h/2) \right) \tag{B.4}$$

with $\|g\| = 1$,

$$\sigma_{p,j} = \begin{cases} 1 & (\phi_{p,j}^{inc} = e^{i\beta_{p,j} x_p} g_{p,j}(y)), \\ -1 & (\phi_{p,j}^{inc} = e^{-i\beta_{p,j} x_p} g_{p,j}(y)). \end{cases} \tag{B.5}$$

The sign $\sigma_{p,j}$ is determined by an arbitrary choice of the pth port being set to an input or output channel, and by the direction of propagation modes depending on the local coordinate we choose. Once we fix all the ports, then the set of signs $\{\sigma_{p,j}\}_{1 \leq p \leq P, 1 \leq j \leq m_p}$ is also uniquely fixed.

We focus our attention on the cross-section of the pth port for a while, and construct a mathematical identity by some equation derived later and the definition of the scattering matrix. We fix the x-coordinate to be x_p.

$$\frac{\partial u}{\partial x}(x_p, y) = \sum_{j=1}^{m_p} \sigma_{p,j}(i\beta) \left(c_{p,j}^{inc} \phi_{p,j}^{inc} - c_{p,j}^{sc} \phi_{p,j}^{sc} \right) \tag{B.6}$$

$$
\begin{aligned}
\left\langle u, \frac{u}{x} \right\rangle_{\Gamma_p} &= \left\langle \sum_{j=1}^{m_p} \sigma_{p,j} \left(c_{p,j}^{inc} \phi_{p,j}^{inc} + c_{p,j}^{sc} \phi_{p,j}^{sc} \right), \sum_{k=1}^{m_p} \sigma_{p,k}(i\beta_{p,k}) \left(c_{p,k}^{inc} \phi_{p,k}^{inc} - c_{p,k}^{sc} \phi_{p,k}^{sc} \right) \right\rangle_{\Gamma_p} \\
&= \sum_{j=1}^{m_p} \sum_{k=1}^{m_p} \delta_{j,k} \sigma_{p,j}^2 (-i\beta_{p,k}) \left\langle c_{p,j}^{inc} \phi_{p,j}^{inc} + c_{p,j}^{sc} \phi_{p,j}^{sc}, c_{p,k}^{inc} \phi_{p,k}^{inc} - c_{p,k}^{sc} \phi_{p,k}^{sc} \right\rangle_{\Gamma_p} \\
&= -i \sum_{j=1}^{m_p} \beta_{p,j} \left\langle c_{p,j}^{inc} \phi_{p,j}^{inc} + c_{p,j}^{sc} \phi_{p,j}^{sc}, c_{p,j}^{inc} \phi_{p,j}^{inc} - c_{p,j}^{sc} \phi_{p,j}^{sc} \right\rangle_{\Gamma_p}.
\end{aligned} \tag{B.7}
$$

The cross terms with respect to j and k vanish because of the orthogonality of $g_{p,j}$ and $g_{p,k}$. Also, $\{\sigma_{p,j}\}_{1 \le j \le m_p}$ by the arbitrary choice do not affect the following calculations.

Each dot product inside the summation of the last equation is

$$
\begin{aligned}
&\left\langle c_{p,j}^{inc} \phi_{p,j}^{inc} + c_{p,j}^{sc} \phi_{p,j}^{sc}, c_{p,j}^{inc} \phi_{p,j}^{inc} - c_{p,j}^{sc} \phi_{p,j}^{sc} \right\rangle \\
&= |c_{p,j}^{inc}|^2 \|\phi_{p,j}^{inc}\|^2 - c_{p,j}^{inc} \overline{c_{p,j}^{sc}} \langle \phi_{p,j}^{inc}, \phi_{p,j}^{sc} \rangle + c_{p,j}^{sc} \overline{c_{p,j}^{inc}} \langle \phi_{p,j}^{sc}, \phi_{p,j}^{inc} \rangle - |c_{p,j}^{sc}|^2 \|\phi_{p,j}^{sc}\|^2.
\end{aligned} \tag{B.8}
$$

Noting $\phi_{p,j}^{inc}(x_p, y) = e^{i\beta_{p,j}x_p} g_{p,j}(y)$, $\phi_{p,j}^{sc}(x_p, y) = e^{i\beta_{p,j}x_p} g_{p,j}(y)$, and $\|g_{p,j}\| = 1$, the first term equals $|c_{p,j}^{inc}|^2$. Other terms can be simplified similarly. As a result, we obtain

$$
\begin{aligned}
&\left\langle c_{p,j}^{inc} \phi_{p,j}^{inc} + c_{p,j}^{sc} \phi_{p,j}^{sc}, c_{p,j}^{inc} \phi_{p,j}^{inc} - c_{p,j}^{sc} \phi_{p,j}^{sc} \right\rangle \\
&= |c_{p,j}^{inc}|^2 - c_{p,j}^{inc} \overline{c_{p,j}^{sc}} e^{2i\beta_{p,j}x_p} + c_{p,j}^{sc} \overline{c_{p,j}^{inc}} e^{-2i\beta_{p,j}x_p} - |c_{p,j}^{sc}|^2.
\end{aligned} \tag{B.9}
$$

$$
\begin{aligned}
\therefore \left\langle u, \frac{\partial u}{\partial x} \right\rangle_{\Gamma_p} &= -i \sum_{j=1}^{m_p} \beta_{p,j} \left(|c_{p,j}^{inc}|^2 - |c_{p,j}^{sc}|^2 - c_{p,j}^{inc} \overline{c_{p,j}^{sc}} e^{2i\beta_{p,j}x_p} + c_{p,j}^{sc} \overline{c_{p,j}^{inc}} e^{-2i\beta_{p,j}x_p} \right) \\
&= -i \sum_{j=1}^{m_p} \beta_{p,j} \left(|c_{p,j}^{inc}|^2 - |c_{p,j}^{sc}|^2 \right) \tag{B.10} \\
&\quad - i \sum_{j=1}^{m_p} \beta_{p,j} \left(-c_{p,j}^{inc} \overline{c_{p,j}^{sc}} e^{2i\beta_{p,j}x_p} + c_{p,j}^{sc} \overline{c_{p,j}^{inc}} e^{-2i\beta_{p,j}x_p} \right). \tag{B.11}
\end{aligned}
$$

Now we take all of the pth ports ($1 \leq p \leq P$) into account to construct an identity involving the scattering matrix $\boldsymbol{S}$. We deal with (B.10) and (B.11) separately.

By the definition of the scattering matrix satisfying $\boldsymbol{S}\boldsymbol{c}^{inc} = \boldsymbol{c}^{sc}$ where $\boldsymbol{c}^{inc}$ and $\boldsymbol{c}^{sc}$ are column vectors that are alignments of all $(c_{p,j}^{inc})_{1 \leq p \leq P, 1 \leq j \leq m_p}$ and $(c_{p,j}^{sc})_{1 \leq p \leq P, 1 \leq j \leq m_p}$, equations (B.10) for all $(p,j)_{1 \leq p \leq P, 1 \leq j \leq m_p}$ give us

$$\sum_{1 \leq p \leq P, 1 \leq j \leq m_p} \beta_{p,j}(|c_{p,j}^{inc}|^2 - |c_{p,j}^{sc}|^2) = \sum_{1 \leq p \leq P, 1 \leq j \leq m_p} \left(c_{p,j}^{inc} \beta_{p,j} \overline{c_{p,j}^{inc}} - \overline{c_{p,j}^{sc}} \beta_{p,j} c_{p,j}^{sc} \right)$$

$$= (\boldsymbol{c}^{inc})^* \boldsymbol{D}[\boldsymbol{\beta}](\boldsymbol{c}^{inc}) - (\boldsymbol{S}\boldsymbol{c}^{inc})^* \boldsymbol{D}[\boldsymbol{\beta}]\boldsymbol{S}\boldsymbol{c}^{inc}$$

$$= (\boldsymbol{c}^{inc})^* \left(\boldsymbol{D}[\boldsymbol{\beta}] - \boldsymbol{S}^* \boldsymbol{D}[\boldsymbol{\beta}]\boldsymbol{S} \right) \boldsymbol{c}^{inc} \qquad \text{(B.12)}$$

where $\boldsymbol{\beta} := (\beta_{1,1}, \ldots, \beta_{1,m_p}, \ldots, \beta_{p,1}, \ldots, \beta_{p,m_p}, \ldots, \beta_{P,1}, \ldots, \beta_{P,m_P})^T$.

Next, we consider equations of (B.11) for all (p,j).

$$\sum_{1 \leq p \leq P, 1 \leq j \leq m_p} \beta_{p,j} c_{p,j}^{inc} \overline{c_{p,j}^{sc}} e^{2i\beta_{p,j}x_p} = \sum_{1 \leq p \leq P, 1 \leq j \leq m_p} c_{p,j}^{inc} \beta_{p,j} e^{2i\beta_{p,j}x_p} \overline{c_{p,j}^{sc}}$$

$$= (\boldsymbol{c}^{inc})^T \boldsymbol{D}[\boldsymbol{\beta}]\boldsymbol{D}[e^{2i\boldsymbol{\beta}\cdot\boldsymbol{x}_p}] \overline{\boldsymbol{S}\boldsymbol{c}^{inc}}$$

$$= \overline{(\boldsymbol{c}^{inc})^* \boldsymbol{D}[\boldsymbol{\beta}]\boldsymbol{D}[e^{-2i\boldsymbol{\beta}\cdot\boldsymbol{x}_p}]\boldsymbol{S}\boldsymbol{c}^{inc}} \qquad \text{(B.13)}$$

where $\boldsymbol{x}_p := (x_1, \ldots, x_1, \ldots, x_p, \ldots, x_p, \ldots, x_P, \ldots, x_P)^T$. Similarly, from the second terms in the summation (B.11) for all (p,j), we have

$$\sum_{1 \leq p \leq P, 1 \leq j \leq m_p} \beta_{p,j} c_{p,j}^{sc} \overline{c_{p,j}^{inc}} e^{-2i\beta_{p,j}x_p} = (\boldsymbol{c}^{inc})^* \boldsymbol{D}[\boldsymbol{\beta}]\boldsymbol{D}[e^{-2i\boldsymbol{\beta}\cdot\boldsymbol{x}_p}]\boldsymbol{S}\boldsymbol{c}^{inc}. \qquad \text{(B.14)}$$

Thus, the summation (B.11) for all (p,j) leads to

$$-\overline{(\boldsymbol{c}^{inc})^* \boldsymbol{D}[\boldsymbol{\beta}]\boldsymbol{D}[e^{-2i\boldsymbol{\beta}\cdot\boldsymbol{x}_p}]\boldsymbol{S}\boldsymbol{c}^{inc}} + (\boldsymbol{c}^{inc})^* \boldsymbol{D}[\boldsymbol{\beta}]\boldsymbol{D}[e^{-2i\boldsymbol{\beta}\cdot\boldsymbol{x}_p}]\boldsymbol{S}\boldsymbol{c}^{inc}$$

$$= 2i\text{Im}\left\{ (\boldsymbol{c}^{inc})^* \boldsymbol{D}[\boldsymbol{\beta}]\boldsymbol{D}[e^{-2i\boldsymbol{\beta}\cdot\boldsymbol{x}_p}]\boldsymbol{S}\boldsymbol{c}^{inc} \right\}. \qquad \text{(B.15)}$$

$$\therefore \left\langle u, \frac{\partial u}{\partial x} \right\rangle_\Gamma = \left\langle u, \frac{\partial u}{\partial x} \right\rangle_{\Gamma_p(1 \leq p \leq P)}$$

$$= -i \left[(B.12) + (B.15) \right]$$

$$= -i \left[(\boldsymbol{c}^{inc})^* \left(\boldsymbol{D}[\boldsymbol{\beta}] - \boldsymbol{S}^* \boldsymbol{D}[\boldsymbol{\beta}] \boldsymbol{S} \right) \boldsymbol{c}^{inc} + 2i \mathrm{Im} \left\{ (\boldsymbol{c}^{inc})^* \boldsymbol{D}[\boldsymbol{\beta}] \boldsymbol{D}[e^{-2i\boldsymbol{\beta} \cdot \boldsymbol{x}_p}] \boldsymbol{S} \boldsymbol{c}^{inc} \right\} \right]$$

$$= -i (\boldsymbol{c}^{inc})^* \left(\boldsymbol{D}[\boldsymbol{\beta}] - \boldsymbol{S}^* \boldsymbol{D}[\boldsymbol{\beta}] \boldsymbol{S} \right) \boldsymbol{c}^{inc} + 2 \mathrm{Im} \left\{ (\boldsymbol{c}^{inc})^* \boldsymbol{D}[\boldsymbol{\beta}] \boldsymbol{D}[e^{-2i\boldsymbol{\beta} \cdot \boldsymbol{x}_p}] \boldsymbol{S} \boldsymbol{c}^{inc} \right\} .$$

$$\text{(B.16)}$$

Noting the second term is a real number,

$$\mathrm{Im} \left\langle u, \frac{\partial u}{\partial x} \right\rangle_\Gamma = -\mathrm{Re} \left\{ (\boldsymbol{c}^{inc})^* \left(\boldsymbol{D}[\boldsymbol{\beta}] - \boldsymbol{S}^* \boldsymbol{D}[\boldsymbol{\beta}] \boldsymbol{S} \right) \boldsymbol{c}^{inc} \right\} = 0. \qquad \text{(B.17)}$$

Since $\boldsymbol{c}^{inc}$ can be chosen arbitrarily,

$$\boldsymbol{D}[\boldsymbol{\beta}] - \boldsymbol{S}^* \boldsymbol{D}[\boldsymbol{\beta}] \boldsymbol{S} = 0 \Leftrightarrow \boldsymbol{D}[\boldsymbol{\beta}] = \boldsymbol{S}^* \boldsymbol{D}[\boldsymbol{\beta}] \boldsymbol{S} \qquad \text{(B.18)}$$

holds. The diagonal entries on both sides lead to $\beta_j = \sum_{k=1}^{M} |S_{k,j}|^2 \beta_k$ for all $j \in \{1, 2, \ldots, M\}$. □

B.2 An Example of Non-unitary Scattering Matrix

Consider a straight waveguide with two ports each of which admits a single propagation mode β_l and β_r in the same manner as the previous discussion. In this case, the size of the scattering matrix is two by two. Assuming $\boldsymbol{S}$ is unitary,

$$\boldsymbol{S}^* \boldsymbol{S} = \begin{bmatrix} |S_{11}|^2 + |S_{21}|^2 & \overline{S_{11}} S_{12} + \overline{S_{21}} S_{22} \\ S_{11} \overline{S_{12}} + S_{12} \overline{S_{22}} & |S_{12}|^2 + |S_{22}|^2 \end{bmatrix} = \boldsymbol{I}, \qquad \text{(B.19)}$$

$$\boldsymbol{S} \boldsymbol{S}^* = \begin{bmatrix} |S_{11}|^2 + |S_{12}|^2 & S_{11} \overline{S_{21}} + S_{21} \overline{S_{22}} \\ S_{21} \overline{S_{11}} + S_{22} \overline{S_{12}} & |S_{21}|^2 + |S_{22}|^2 \end{bmatrix} = \boldsymbol{I}. \qquad \text{(B.20)}$$

These lead to the following conditions:

$$\begin{cases} |S_{11}|^2 + |S_{21}|^2 = 1, \\[2mm] |S_{12}|^2 + |S_{22}|^2 = 1, \\[2mm] S_{11}\overline{S_{12}} + S_{21}\overline{S_{22}} = 0, \\[2mm] |S_{11}|^2 + |S_{12}|^2 = 1, \\[2mm] |S_{21}|^2 + |S_{22}|^2 = 1, \\[2mm] S_{11}\overline{S_{21}} + S_{12}\overline{S_{22}} = 0, \\[2mm] |S_{11}| = |S_{22}|, \\[2mm] |S_{12}| = |S_{21}|. \end{cases} \qquad (B.21)$$

Consider the linear system with the scattering matrix and incident and scattered coefficients

$$\boldsymbol{S} \begin{bmatrix} c_l^+ \\ c_r^- \end{bmatrix} = \begin{bmatrix} c_r^+ \\ c_l^- \end{bmatrix} \Leftrightarrow \begin{cases} S_{11}c_l^+ + S_{12}c_r^- = c_r^+, \\[2mm] S_{21}c_l^+ + S_{22}c_r^- = c_l^-. \end{cases} \qquad (B.22)$$

We choose an arbitrary complex pair $(c_l^+, c_r^-) = (\alpha_1, \alpha_2)$. Then the identity (3.69) becomes

$$\operatorname{Im}\langle u, \frac{\partial u}{\partial n}\rangle = \beta_l \left(|c_l^+|^2 - |c_l^-|^2 \right) - \beta_r \left(|c_r^+|^2 - |c_r^-|^2 \right)$$

$$= \beta_l \left[|\alpha_1|^2 - |\alpha_1 S_{21} + \alpha_2 S_{22}|^2 \right] - \beta_r \left[|\alpha_1 S_{11} + \alpha_2 S_{12}|^2 - |\alpha_2|^2 \right] \quad (B.23)$$

The following expansions

$$|\alpha_1 S_{21} + \alpha_2 S_{22}|^2 = |\alpha_1|^2(1 - |S_{11}|^2) + |\alpha_2|^2|S_{11}|^2 + \alpha_1\overline{\alpha_2}S_{21}\overline{S_{22}} + \overline{\alpha_1}\alpha_2\overline{S_{21}}S_{22},$$

$$\qquad (B.24)$$

$$|\alpha_1 S_{11} + \alpha_2 S_{12}|^2 = |\alpha_1|^2|S_{11}|^2 + |\alpha_2|^2(1 - |S_{11}|^2) + \alpha_1\overline{\alpha_2}S_{11}\overline{S_{12}} + \overline{\alpha_1}\alpha_2\overline{S_{11}}S_{12} - |\alpha_2|^2,$$

$$\qquad (B.25)$$

lead to

$$\mathrm{Im}\langle u, \frac{\partial u}{\partial n}\rangle$$

$$= \beta_l \left[\cancel{|\alpha_1|^2}^{\;0} - \cancel{|\alpha_1|^2}^{\;0} + |\alpha_1|^2|S_{11}|^2 - |\alpha_2|^2|S_{22}|^2 - \alpha_1\overline{\alpha_2}S_{21}\overline{S_{22}} - \overline{\alpha_1}\alpha_2\overline{S_{21}}S_{22} \right]$$

$$- \beta_r \left[|\alpha_1|^2|S_{11}|^2 + \cancel{|\alpha_2|^2}^{\;0} - |\alpha_2|^2|S_{11}|^2 - \alpha_1\overline{\alpha_2}S_{11}\overline{S_{12}} - \overline{\alpha_1}\alpha_2\overline{S_{11}}S_{12} - \cancel{|\alpha_2|^2}^{\;0} \right]$$

$$= (\beta_l - \beta_r)(|\alpha_1|^2 - |\alpha_2|^2)|S_{11}|^2 - \beta_l\alpha_1\overline{\alpha_2}S_{21}\overline{S_{22}} - \beta_r\alpha_1\overline{\alpha_2}S_{11}\overline{S_{12}}$$

$$- \beta_l\overline{\alpha_1}\alpha_2\overline{S_{21}}S_{22} - \beta_l\overline{\alpha_1}\alpha_2\overline{S_{11}}S_{12}$$

$$= (\beta_l - \beta_r)(|\alpha_1|^2 - |\alpha_2|^2)|S_{11}|^2 + \beta_l\alpha_1\overline{\alpha_2}S_{11}\overline{S_{12}} - \beta_r\alpha_1\overline{\alpha_2}S_{11}\overline{S_{12}}$$

$$+ \beta_l\overline{\alpha_1}\alpha_2\overline{S_{11}}S_{12} - \beta_l\overline{\alpha_1}\alpha_2\overline{S_{11}}S_{12} \quad (\because S_{21}\overline{S_{22}} = -S_{11}\overline{S_{12}})$$

$$= (\beta_l - \beta_r)(|\alpha_1|^2 - |\alpha_2|^2)|S_{11}|^2 + (\beta_l - \beta_r)\alpha_1\overline{\alpha_2}S_{11}\overline{S_{12}}$$

$$+ (\beta_l - \beta_r)\overline{\alpha_1}\alpha_2\overline{S_{11}}S_{12}$$

$$= (\beta_l - \beta_r)\left[(|\alpha_1|^2 - |\alpha_2|^2)|S_{11}|^2 + \alpha_1\overline{\alpha_2}S_{11}\overline{S_{12}} + \overline{\alpha_1}\alpha_2\overline{S_{11}}S_{12} \right]$$

$$= 0. \tag{B.26}$$

If S_{11} is not zero, then we can conclude $\beta_l = \beta_r$ selecting $(\alpha_1, \alpha_2) = (1, 0)$. However, if S_{11} is zero, $\beta_l = \beta_r$ can be false. In such a case, the linear system with the scattering matrix is

$$S\begin{bmatrix} c_+^l \\ c_-^r \end{bmatrix} = \begin{bmatrix} 0 & \omega \\ \overline{\omega} & 0 \end{bmatrix} \begin{bmatrix} c_+^r \\ c_-^l \end{bmatrix} \Leftrightarrow \begin{cases} c_+^r = \omega c_-^r, \\ c_-^l = \overline{\omega} c_+^l \end{cases} \tag{B.27}$$

where ω is some complex number with a magnitude of one.

B.3   Phase Adjustment for The Merged Scattering Matrix

Here we discuss the phase term adjustments for the terms of $e^{\beta x}$ needed to be considered when modularized scattering matrices are merged. Once we determine the modularized scattering matrices separately, the next step is to merge the pieces into one matrix to obtain the representation of the whole structure. In the merging

process, we need to take the change of coordinates into account when multiple components are connected. Modularized scattering matrices are constructed by fixing local coordinates independently. When we merge multiple components, the coordinates for one component can remain the same, while the coordinates of the other merged components can be changed by translation, rotation, or both of them, depending on the original coordinates chosen before merging. For example, when we merge two components with the same structure, both represented by the same scattering matrices denoted by S, we can still use one S but the other S has to be adjusted appropriately because we need to choose one coordinate system after the merge.

Suppose we have two waveguide components represented by two scattering matrices S_1 and S_2. We assume the corresponding two components have two ports respectively and a single mode for each port. And we consider the situation in which the two components are merged by connecting one port to another. Let the origins of two coordinates be O_1 and O_2 respectively. Suppose we keep the origin O_1 of one component unchanged before and after the merge. Then the coordinates of the other component are affected. Before the merge, S_2 satisfies

$$S_2 \begin{bmatrix} c_l^+ \\ c_r^- \end{bmatrix} = \begin{bmatrix} c_l^- \\ c_r^+ \end{bmatrix} \tag{B.28}$$

with the origin O_2. As we see in (3.49), $C^\pm$ is independent of y. We only need to adjust the terms of $e^{\pm\beta x}$, more precisely, the distance of the path with respect to x from O_1 and O_2 after the merge. Let x be the first local coordinate for S_2 with the origin O_2, and define $d^\pm := \exp\left(\pm i\beta(O_2 - O_1)\right)$. Since

$$\exp(\pm i\beta(x - O_2)) = \exp\left(\pm i\beta(x - O_1 + O_1 - O_2)\right) \tag{B.29}$$

$$= \exp\left(\mp i\beta(O_2 - O_1)\right)\exp\left(\pm i\beta(x - O_1)\right) \tag{B.30}$$

$$= d^\mp \exp\left(\pm i\beta(x - O_1)\right), \tag{B.31}$$

(B.28) with the origin O_2 is equivalent to

$$\boldsymbol{S}_2 \begin{bmatrix} c_l^+ d^- \\ c_r^- d^+ \end{bmatrix} = \begin{bmatrix} c_l^- d^+ \\ c_r^+ d^- \end{bmatrix} \tag{B.32}$$

with the origin O_1. Assuming another set of coefficients $(c_{l,2}^\pm, c_{l,2}^\pm)$ which can be obtained by having distinct boundary data, we have

$$\boldsymbol{S}_2 \begin{bmatrix} c_{l,1}^+ d^- & c_{l,2}^+ d^- \\ c_{r,1}^- d^+ & c_{r,2}^- d^+ \end{bmatrix} = \begin{bmatrix} c_{l,1}^- d^+ & c_{l,2}^- d^+ \\ c_{r,1}^+ d^- & c_{r,2}^+ d^- \end{bmatrix}. \tag{B.33}$$

This equation is decomposed as follows

$$\boldsymbol{S}_2 \begin{bmatrix} d^- & 0 \\ 0 & d^+ \end{bmatrix} \begin{bmatrix} c_{l,1}^+ & c_{l,2}^+ \\ c_{r,1}^- & c_{r,2}^- \end{bmatrix} = \begin{bmatrix} d^+ & 0 \\ 0 & d^- \end{bmatrix} \begin{bmatrix} c_{r,1}^+ & c_{r,2}^+ \\ c_{l,1}^- & c_{l,2}^- \end{bmatrix} \tag{B.34}$$

$$\Leftrightarrow \boldsymbol{S}_2 \begin{bmatrix} d^- & 0 \\ 0 & d^+ \end{bmatrix} M_{inc} = \begin{bmatrix} d^+ & 0 \\ 0 & d^- \end{bmatrix} M_{sc} \tag{B.35}$$

With the same assumption that M_{inc} is invertible as section 3.3.4,

$$\boldsymbol{S}_2 = \begin{bmatrix} d^+ & 0 \\ 0 & d^- \end{bmatrix} M_{sc} M_{inc}^{-1} \begin{bmatrix} d^+ & 0 \\ 0 & d^- \end{bmatrix} \tag{B.36}$$

Adjustments for cases of multiple modes or more ports are similarly derived. For example, in the case of two ports each of which admits two propagation modes, The adjusted scattering matrix component $\boldsymbol{S}_{adj}$ is

$$\boldsymbol{S}_{adj} = \boldsymbol{DSD} \tag{B.37}$$

where $\boldsymbol{S}$ is the individually computed original scattering matrix and $\boldsymbol{D} := diag\left(d_{l,1}^+, d_{l,2}^+, d_{r,1}^-, d_{r,2}^-\right)$.

B.4 Derivations of Equations (3.4) and (3.5)

In this appendix, we give the detailed derivations of (3.4) and (3.5). Applying separation of variables $u(\boldsymbol{x}) = e^{\beta x_1} g(x_2)$ along the cross-section with the height $h > 0$, then the Helmholtz equation (3.12) leads to

$$\Delta u(\boldsymbol{x}) + k^2(\boldsymbol{x}) = e^{\beta x_1}\left[(k^2 + \beta^2)g(x_2) + g''(x_2)\right] \tag{B.38}$$

$$= e^{\beta x_1} k_v \left[(n^2 + n_e^2)g(x_2) + g''(x_2)\right] \tag{B.39}$$

$$= 0. \tag{B.40}$$

$$\therefore (n^2 + n_e^2)g(x_2) + g''(x_2) = 0. \tag{B.41}$$

We non-dimensionalize the above equation with $\tilde{h} := k_v h$ as follows.

$$g(\tilde{x}_2) = c_1 \cos(\sqrt{n^2 - n_e^2}(\tilde{x}_2 + \tilde{h}/2)) + c_2 \sin(\sqrt{n^2 - n_e^2}(\tilde{x}_2 + \tilde{h}/2)) \quad |\tilde{x}_2| < \tilde{h}/2 \tag{B.42}$$

where c_1 and c_2 are some constants.

The boundary conditions at $\tilde{x}_2 = \pm\tilde{h}/2$ to $c_1 = 0$ and

$$g(\tilde{h}/2) = c_2 \sin\left(\sqrt{n^2 - n_e^2}\,\tilde{h}\right) = 0 \tag{B.43}$$

which implies that $\sqrt{n^2 - n_e^2}\,\tilde{h} = m\pi$ with some positive integer m for some propagation mode β to exist. Then we obtain

$$(n^2 - n_e^2)\tilde{h}^2 = (m\pi)^2 \tag{B.44}$$

$$\Leftrightarrow \quad k_v^2(n^2 - n_e^2)\tilde{h}^2 = k_v^2(m\pi)^2 \tag{B.45}$$

$$\Leftrightarrow \quad (k^2 - \beta^2)\tilde{h}^2 = k_v^2(m\pi)^2 \tag{B.46}$$

$$\Leftrightarrow \quad \beta^2 = k^2 - \left(\frac{m\pi}{h}\right)^2 \tag{B.47}$$

since $k = k_v n$, $\beta = k_v n_e$ and $\tilde{h} = k_v h$.

In the case that M modes $(\beta_m)_{m=1}^M$ are allowed,

$$\beta^2 = k^2 - \left(\frac{m\pi}{h}\right)^2 > 0 \tag{B.48}$$

and

$$\beta^2 = k^2 - \left(\frac{(m+1)\pi}{h}\right)^2 < 0 \tag{B.49}$$

need to hold, which leads to

$$\frac{\pi}{k} < h < 2\frac{\pi}{k}. \tag{B.50}$$

As h increases, more integers of m satisfy Hence, we can restrict the number of modes with the adjustment of h.

Once h is fixed, we can also determine $\beta = n_e k_v$. For example, in the case of a single mode,

$$\sqrt{n^2 - n_e^2} k_v h = \pi \tag{B.51}$$

$$\Rightarrow \quad n^2 - n_e^2 = \left(\frac{\pi}{k_v h}\right)^2 \tag{B.52}$$

$$\Rightarrow \quad n_e = \sqrt{n^2 - \left(\frac{\pi}{k_v h}\right)^2}. \tag{B.53}$$

The inside of the square root is positive as long as the left inequality holds (**??**) since

$$\frac{\pi}{k} < h \Leftrightarrow \frac{\pi}{kh} = \frac{1}{n}\frac{\pi}{k_v h} < 1 \Rightarrow \frac{\pi}{k_v h} < n. \tag{B.54}$$

REFERENCES

[1] Mosquito eye 50:1 magnification stock photo. `https://www.istockphoto.com`. Accessed: June 26th, 2023.

[2] X. Antoine, P. Dreyfuss, and K. Ramdani. A construction of beam propagation methods for optical waveguides. *Communications in Computational Physics CiCP*, 6:565–576., 2009.

[3] X. Antoine, Y. Huang, and Y. Y. Lu. Computing high-frequency scattered fields by beam propagation methods: A prospective study. *Journal of Algorithms and Computational Technology*, 4(2):147–166, 2010.

[4] T. Askham and M. Rachh. A boundary integral equation approach to computing eigenvalues of the stokes operator. *Advances in Computational Mathematics*, 46(2), 2020.

[5] A. Bamberger, F. Coron, and J-M. Ghidaglia. An analysis of the b.p.m. approximation of the helmholtz equation in an optical fiber alain bamberger, françois coron and jean-michel ghidaglia. *RAIRO. Modélisation Mathématique et Analyse Numérique*, 21(3):405–424, 2017.

[6] P. K. Banerjee. *Boundary element methods in engineering science.* McGraw-Hill, New York City, 1981.

[7] A. Barnett, J. Magland, and L. Klinteberg. A parallel non-uniform fast fourier transform library based on an ëxponential of semicirclekernel. *SIAM Journal on Scientific Computing*, 41(5):479–504, 2019.

[8] J. P. Berenger. A perfectly matched layer for the absorption of electromagnetic waves. *Journal of Computational Physics*, 114(2):185–200, 1994.

[9] G. Biros, L. Ying, and D. Zorin. A fast solver for the stokes equations with distributed forces in complex geometries q. *Journal of Computational Physics*, 193(1):317–348, 2004.

[10] A. S. Bonnet-Bendhia, B. Goursaud, and C. Hazard. Mathematical analysis of the junction of two acoustic open waveguides. *SIAM Journal on Applied Mathematics*, 71:2048–2071, 2011.

[11] A. S. Bonnet-Bendhia and A. Tillequin. A limiting absorption principle for scattering problems with unbounded obstacles. *Mathematical Methods in the Applied Sciences*, 24:1089–1111, 2001.

[12] S. V. Boriskina, T. M. Benson, P. Sewell, and A. I. Nosich. Highly efficient full-vectorial integral equation solution for the bound, leaky, and complex modes of

dielectric waveguides. *IEEE Journal Selected Topics in Quantum Electronics*, 8(6):1225–1232, 2002.

[13] J. Bremer. A fast direct solver for the integral equations of scattering theory on planar curves with corners. *Journal of Computational Physics*, 231:1879–1899, 2012.

[14] S. C. Brenner and L. R. Scott. *The Mathematical Theory of Finite Element Methods.* Springer, New York City, 2007.

[15] S. Chandler-wilde, P. Monk, and M. Thomas. The mathematics of scattering by unbounded, rough, inhomogeneous layers. *Journal of Computational and Applied Mathematics*, 204:549–559, 2007.

[16] S. Chandler-Wilde and B. Zhang. Electromagnetic scattering by an inhomogeneous conducting or dielectric layer on a perfectly conducting plate. *R. Soc. Lond. Proc. Ser. A Math. Phys. Eng. Sci.*, 454:519–542, 1998.

[17] D. Colton and R. Kress. *Inverse Acoustic and Electromagnetic Scattering Theory.* Springer, New York City, 1998.

[18] D. Colton and R. Kress. *Integral Equation Methods in Scattering Theory.* SIAM, Philadelphia, 2013.

[19] J. Cooley and J. Tukey. An algorithm for the machine calculation of complex fourier series. *Mathematics of Computation*, 19(90), 1965.

[20] D. Crowdy. Effective slip lengths for longitudinal shear fow over partial-slip circular bubble mattresses. *Fluid Dynamics Research*, 47, 2015.

[21] S. Dash, M. T. Alt, and S. V. Garimella. Hybrid surface design for robust superhydrophobicity. *Langmuir*, 28(25):9606–15, 2012.

[22] A. Davis and E. Lauga. Geometric transition in friction for flow over a bubble mattress. *Physics of Fluids*, 21, 2008.

[23] A. Dutt and V. Rokhlin. Fast fourier transforms for nonequispaced data. *SIAM Journal on Scientific Computing*, 41(5):1369–1393, 1993.

[24] H. Ehlers, M. Biletzke, B. Kuhlow, G. Przyrembel, and U.H.P. Fischer. Optoelectronic packaging of arrayed-waveguide grating modules and their environmental stability tests. *Optical Fiber Technology*, 6(4):344–356, 2000.

[25] C. L. Epstein. Finding and representing solutions to transmission problems for open channels. *Arxiv*, 2023.

[26] M. Rachh et al. Fast multipole methods in two dimensions (fmm2d). `https://fmm2d.readthedocs.io/en/latest/`. Accessed: February 14th, 2023.

[27] K Fan, W. Cai, and X. Ji. A full vectorial generalized discontinuous galerkin beam propagation method (gdg–bpm) for nonsmooth electromagnetic fields in waveguides. *Journal of Computational Physics*, 227(15):7178–7191, 2008.

[28] A. Gillman, P. M. Young, and P-G. Martinsson. A direct solver with o(n) complexity for integral equations on one-dimensional domains. *Frontiers of Mathematics in China*, 7:217–247, 2012.

[29] Linden Gledhill. This is what butterfly wings look like up close, and it's kind of blowing our minds. `https://metro.co.uk`. Accessed: June 26th, 2023.

[30] G. H. Golub and C. F. V. Loan. *Matrix Computations, 3rd Edition.* Johns Hopkins University Press, Baltimore, 1996.

[31] L. Greengard, D. Gueyffier, P-G. Martinsson, and V. Rokhlin. A direct solver with o(n) complexity for integral equations on one-dimensional domains. *Acta Numerica.*, 18:243–275, 2009.

[32] L. Greengard and J-Y. Lee. Accelerating the nonuniform fast fourier transform. *SIAM Review*, 46(3):443–454, 2004.

[33] L. Greengard, M. O'Neil, M. Rachh, and F. Vico. Fast multipole methods for evaluation of layer potentials with locally-corrected quadratures. *Journal of Computational Physics*, 10, 2021.

[34] L. Greengard and V. Rokhlin. A fast algorithm for particle simulations. *Journal of Computational Physics*, 73(2), 1987.

[35] L. Greengard and V. Rokhlin. A fast algorithm for particle simulations. *Journal of Computational Physics*, 73(2):325–348, 1987.

[36] J. Helsing. Solving integral equations on piecewise smooth boundaries using the rcip method: a tutorial. `https://www.maths.lth.se/na/staff/helsing/Tutor/index.html`. Accessed: February 13th, 2023.

[37] J. Helsing. Integral equation methods for elliptic problems with boundary conditions of mixed type. *Journal of Computational Physics*, 228(23):8892–8907, 2009.

[38] J. Helsing and A. Holst. Variants of an explicit kernel-split panel-based nyström discretization scheme for helmholtz boundary value problems. *Advances in Computational Mathematics*, 41(3):691–708, 2015.

[39] J. Helsing and S. Jiang. On integral equation methods for the first dirichlet problem of the biharmonic and modified biharmonic equations. *SIAM Journal on Scientific Computing*, 40(4):A2609–A2630, 2018.

[40] J. Helsing and S. Jiang. Solving fredholm second-kind integral equations with singular right-hand sides on non-smooth boundaries. *Journal of Computational Physics*, 448, 2022.

[41] J. Helsing and A. Karlsson. On a helmholtz transmission problem in planar domains with corners. *Journal of Computational Physics*, 371, 2018.

[42] J. Helsing and R. Ojala. Corner singularities for elliptic problems: Integral equations, graded meshes, quadrature and compressed inverse preconditioning. *Journal of Computational Physics*, 227, 2008.

[43] J. Helsing and R. Ojala. Elastostatic computations on aggregates of grains with sharp interfaces, corners, and triple-junctions. *International Journal of Solids and Structures*, 46(25-26):4437–4450, 2009.

[44] H. V. Henderson and S. R. Searle. On deriving the inverse of a sum of matrices. *SIAM Review*, 23(1):53–60, 1981.

[45] R.L. Higdon. Absorbing boundary conditions for difference approximations to the multi-dimensional wave equation. *Mathematics of Computation*, 47(176):437–459, 1986.

[46] K. L. Ho and L. Greengard. A fast direct solver for structured linear systems by recursive skeletonization. *SIAM Journal on Scientific Computing*, 34(5):A2507–A2532, 2012.

[47] T. Itoh, G. Pelosi, and P. Silvester. *Finite Element Software for Microwave Engineering*. Wiley-Interscience, Hoboken, 1996.

[48] S. Jiang and J. Lai. A quantitative study of the effect of cladding thickness on modal confinement loss in photonic waveguides. *Optic Express*, 24(22):24872–24882, 2016.

[49] M. A. Kelmanson. An integral equation method for the solution of singular slow flow problems. *Journal of Computational Physics*, 51, 1983.

[50] T. L. Kirk, G. Karamanis, D. G. Crowdy, and M. Hodes. Thermocapillary stress and meniscus curvature effects on slip lengths in ridged microchannels. *Journal of Fluid Mechanics*, 894, 2020.

[51] L. Klinteberg, T. Askham, and M. C. Kropinski. A fast integral equation method for the two-dimensional navier-stokes equations. *Journal of Computational Physics*, 409, 2020.

[52] W. Y. Kong, J. Bremer, and V. Rokhlin. An adaptive fast direct solver for boundary integral equations in two dimensions. *Applied and Computational Harmonic Analysis*, 31(3):346–369, 2011.

[53] M. Koshiba. *Optical Waveguide Theory by the Finite Element Method*. Springer, Dordrecht, 1992.

[54] H. Kragl. Cases of structural equality between the scalar wave equations of optics and the quantum-mechanical schrödinger equation. *Journal of the Optical Society of America*, 9(6):964–973, 1992.

[55] R. Kress. *Linear Integral Equations, Third Edition.* Springer, Göttingen, 2014.

[56] D. Kumbhakar. Condensed matrix method for implicit type scheme in imaginary distance beam propagation method. *Journal of Computational Methods in Sciences and Engineering*, 8(1-2):139–146, 2008.

[57] J. Lai and S. Jiang. Second kind integral equation formulation for the mode calculation of optical waveguides. *Applied and Computational Harmonic Analysis*, 44:645–664, 2018.

[58] L. S. Lam, M Hodes, G. Karamanis, T. Kirk, and S. MacLachlan. Effect of meniscus curvature on apparent on apparent thermal slip. *Journal of Heat and Mass Transfer*, 138(12), 2016.

[59] E. Lauga and H. A. Stone. Effective slip in pressure-driven stokes flow. *Journal of Fluid Mechanics*, 489:55–77., 2003.

[60] P. D. Lax and R. S. Phillips. *Scattering Theory.* Academic Press, Cambridge, 1990.

[61] P. G. Martinsson. A fast direct solver for a class of elliptic partial differential equations. *Journal of Scientific Computing*, 38:316–330, 2009.

[62] P.G. Martinsson and V. Rokhlin. A fast direct solver for boundary integral equations in two dimensions. *Journal of Computational Physics*, 205:1–23, 2005.

[63] P.G. Martinsson and V. Rokhlin. A fast direct solver for scattering problems involving elongated structures. *Journal of Computational Physics*, 221(1):288–302, 2007.

[64] G. Mur. Absorbing boundary conditions for the finite-difference approximation of the time-domain electromagnetic field equations. *IEEE Transactions on Electromagnetic Compatibility*, 23(4):377–382, 1981.

[65] J. Neédélec. *Acoustic and Electromagnetic Equations.* Springer, New York City, 2001.

[66] K. Okamoto. *Fundamentals of Optical Wavuguides.* Academic Press, Cambridge, 2022.

[67] R. Pei, T. Askham, L. Greengard, and S. Jiang. Periodic fast multipole method. *SIAM Journal on Scientific Computing*, 2022.

[68] J. R. Philip. Flows satisfying mixed no-slip and no-shear conditions. *Journal of Applied Mathematics and Physics (ZAMP)*, 23, 1972.

[69] C. Pozrikidis. *Boundary integral and sigularity methods for linearized viscous flow.* Cambridge University Press, Cambridge, 1992.

[70] D. Quéré. Wetting and roughness. *Annual Review of Materials Research*, 38(1):71–99, 2008.

[71] M. Rachh and T. Askham. Integral equation formulation of the biharmonic dirichlet problem. *Journal of Scientific Computing*, 75(2):762–781, 2017.

[72] M. Rachh and K. Serkh. On the solution of stokes equation on regions with corners. *Communications on Pure and Applied Mathematics*, 73.11:2295–2369, 2020.

[73] S. Rao. *Time Domain Electromagnetics*. Academic Press, 1999.

[74] J. Rothstein. Slip on superhydrophobic surfaces. *Annual Review of Materials Research*, 42(1):89–109, 2010.

[75] D. Ruiz-Antolin and A. Townsend. A nonuniform fast fourier transform based on low rank approximation. *SIAM Journal on Scientific Computing*, 40(1):A529–A547, 2018.

[76] Y. Saad and M.H. Schultz. 'gmres: A generalized minimal residual algorithm for solving nonsymmetric linear systems'. *SIAM Journal on Scientific and Statistical Computing*, 7, 1986.

[77] C. J. Teo and B.C. Khoo. Effects of interface curvature on poiseuille flow through microchannels and microtubes containing superhydrophobic surfaces with transverse grooves and ribs. *Microfluid Nanofluidics*, 17, 2014.

[78] William Thielicke. Surface of a lotus leaf. `https://www.sci.news`. Accessed: June 26th, 2023.

[79] G. Verchota. Layer potentials and regularity for the Dirichlet problem for Laplace's equation in Lipschitz domains. *Journal of Functional Analysis*, 59(3):572–611, 1984.

[80] B. Wu, H. Zhu, A. Barnett, and S. Veerapaneni. Solution of stokes flow in complex nonsmooth 2d geometries via a linear-scaling high-order adaptive integral equation scheme. *Journal of Computational Physics*, 410, 2020.

[81] E. Yamashita. *Analysis Methods for Electromagnetic Wave Problems*. Artech House Publishers, London, 1990.

[82] E. Yariv and O. Schnitzer. Pressure-driven plug flows between superhydrophobic surfaces of closely spaced circular bubbles. *Journal of Engineering Mathematics*, 2018.

[83] E. Yariv and M. Siegel. Rotation of a superhydrophobic cylinder in a viscous liquid. *Journal of Fluid Mechanics*, 880, 2019.

[84] K. Yee. Numerical solution of initial boundary value problems involving maxwell's equations in isotropic media. *IEEE Trans. Antennas Propag.*, 14(3):302–307, 1966.

[85] C. Yeh, Kee Whan Ha, S. B. Dong, and W. P. Brown. Single-mode optical waveguides. *Applied Optics*, 18:1490–504, 1979.

[86] L. Ying, G. Biros, and D. Zorin. A kernel-independent adaptive fast multipole algorithm in two and three dimensions. *Journal of Computational Physics*, 196:591–626, 2004.

[87] T. V. Yioultsis, G. D. Ziogos, and E. E. Kriezis. Explicit finite-difference vector beam propagation method based on the iterated crank-nicolson scheme. *Journal of the Optical Society of America*, 26(10):2183–2191, 2009.

[88] K. Y. You. *Emerging Waveguide Technology*. IntechOpen, 2018.

[89] T. P. Young. Design of integrated optical circuits using finite elements. *Proceedings of the IEEE*, 135(3):135–144, 1988.

[90] H. Zhu and S. Veerapaneni. High-order close evaluation of laplace layer potentials: A differential geometric approach. *SIAM Journal on Scientific Computing*, 44(3):A1381–A1404, 2022.

[91] O. C. Zienkiewicz. *The Finite Element Method In Engineering Science*. Butterworth-Heinemann, Massachusetts, 2013.